Technische Universität München

Max-Planck-Institut für Physik
(Werner-Heisenberg-Institut)

Temporal and spectral characteristics of the active galactic nucleus Mkn 501 during a phase of high activity in the TeV range

Daniel Kranich

Vollständiger Abdruck der von der Fakultät für Physik der Technischen Universität München zur Erlangung des akademischen Grades eines Doktors der Naturwissenschaften genehmigten Dissertation.

Vorsitzender: Univ.-Prof. Dr. M. Lindner

Prüfer der Dissertation:

1. Hon.-Prof. Dr. N. Schmitz
2. Univ.-Prof. Dr. F. von Feilitzsch
3. Prof. O. C. de Jager, Potchefstroomse Universiteit / Südafrika (schriftliche Beurteilung)

Die Dissertation wurde am 05.07.2001 bei der Technischen Universität München eingereicht und durch die Fakultät für Physik am 04.12.2001 angenommen.

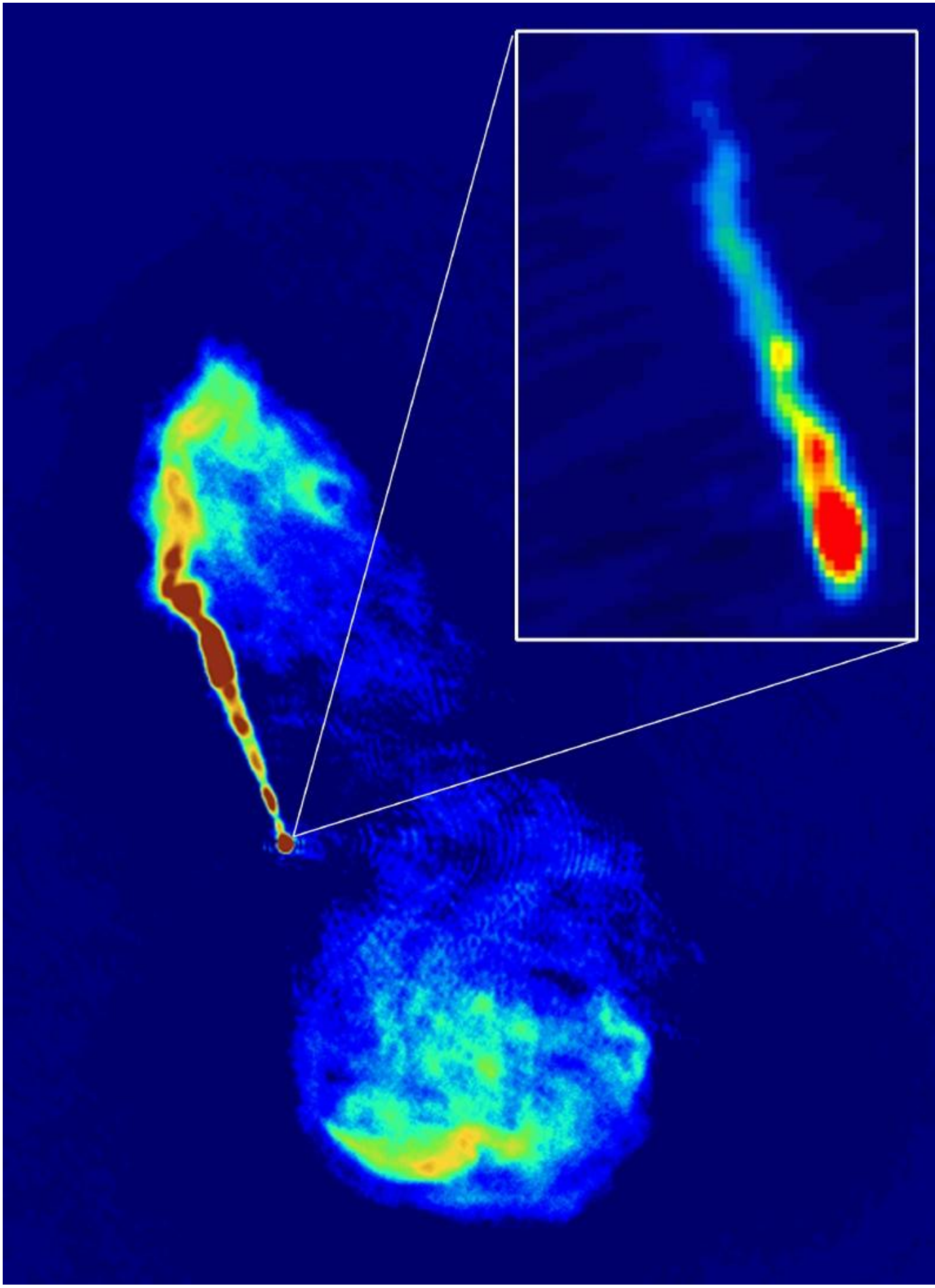

Fig. 0.0.1: (previous page) An image of M87, the central galaxy in the Virgo cluster as observed by the Very Large Array. The smaller image was made by the *Very Long Baseline Array* (VLBA) and the HALCA satellite (*Highly Advanced Laboratory for Communications and Astronomy*) at 1.6 GHz (wavelength 18cm) and shows evidence for a helical jet structure. (courtesy of the *VLBI Space Observation Program*, VSOP)

SUMMARY

The BL Lac object Mkn 501 was in a state of high activity in the X-ray and TeV energy range in 1997. During this time Mkn 501 was observed, amongst other experiments, by all 6 Cherenkov telescopes of the HEGRA collaboration and the ASM on board the RXTE satellite. The analysis of this data represents a rare opportunity to address several fundamental theoretical and technical questions in VHE γ-astronomy. The diffuse extragalactic background radiation density and/or characteristic parameters of the BL Lac object, like magnetic field strength and Doppler factor can be constrained by the observation of high-energy γ-rays above $E_\gamma \gtrsim 10$TeV. The strong γ-ray signal on the other hand, allows one to compare individual detectors or to check observation and/or analysis techniques. Furthermore, the 1997 light curve of Mkn 501 with its long duration and significant flux variations allows extended investigations on the temporal characteristics of the object. Of special interest in this respect are the characteristic timescales of the flux variation, e.g. the mean rise and decay time of the flares, and the search for possible periodic structures in the light curve. The characteristic timescales may provide information on the acceleration mechanisms, the size of the γ-ray emission region and on the magnetic field strength in the emission region. The search for periodic or quasi periodic oscillations allows one to identify and investigate the structure of binary systems.

Here I present the results from the spectral analysis of the HEGRA CT1 data and from the temporal analysis of the HEGRA CT and ASM data. In order to derive the results from the Mkn 501 data sample as precise as possible, several analysis methods have been developed:

♦ A method to estimate the impact parameter and the energy of an observed air shower by means of the derived image parameters (sec. 5.3.1). The obtained energy resolution is $\sim 30\%$ and the impact parameter resolution is $\sim 20\%$ (RMS). The small CT1 camera ($\sim 3^\circ$ diameter) has been found to be a limiting factor in the estimation of both parameters. The method was tested on *Monte Carlo* (MC) simulated air shower events and on coincident events between CT1 and the CT-system from the Mkn 501 data sample (sec. 6.3). The tests confirmed the applicability of the method.

♦ Both the γ-ray signal and the background content below the signal are estimated using a χ^2-fit to the $ALPHA$ image parameter distribution (sec. 5.3.2). Therefore, no additional OFF-observations are necessary to derive the significance of an observed signal. In addition, the errors of the fit parameters are used to estimate the errors on the number of excess and background events.

♦ A program to derive dynamical selection cuts, i.e. cuts which take into account the energy, impact parameter and zenith angle of an observed air shower event (sec. 5.3.3). Dynamical cuts yield better cut sensitivities compared to constant cuts (of the order of 13%), especially for high energies. An improved cut sensitivity results in more accurate energy spectra.

♦ Based on the energy estimation routine, a program to derive differential energy spectra was developed (sec. 5.3.5). It could be shown by means of MC simulations, that power law spectra are well reconstructed by the program. Furthermore, for small zenith angle MC data, it was possible to reconstruct power law spectra with an exponential cutoff and distinguish them

from pure power law spectra. The method was also tested on 16.5h of Crab Nebula data giving a reasonable differential flux of $\mathrm{d}F/\mathrm{d}E = (4.6 \pm 1.9)\,(E/\mathrm{TeV})^{-2.72\pm0.27} \cdot 10^{-11}\,\mathrm{cm}^{-2}\mathrm{s}^{-1}\mathrm{TeV}^{-1}$.

♦ Part of the pre-analysis process, where the recorded raw data events are cleaned and the shower image parameters are calculated, was modified in order to take care of the large variations in the night sky background light during moon observations (sec. 5.1.4). The achieved agreement between moon and no-moon observation results was remarkably good.

♦ The time averaged energy spectrum of Mkn 501 in 1997 (sec. 6.1 and 6.2) was derived for the different CT1 data samples (moon and no-moon observations, different high voltage settings of the photomultipliers). The agreement between the results obtained from moon and no-moon observations is very good, but it was not possible to exclude a pure power law spectrum on the basis of the individual data samples. After the results from all CT1 data samples have been combined, a pure power law spectrum is rejected at the 4.5σ level (given a χ^2-value of the power law fit of $\chi^2\,(6) = 35.29$ the corresponding probability becomes $\mathcal{P} = 3.8 \cdot 10^{-6}$). The power law spectrum with an exponential cutoff, on the other hand, agrees very well with the data ($\chi^2\,(5) = 2.56$ and $\mathcal{P} = 0.23$ or 0.7σ). The time averaged energy spectrum of Mkn 501 is then estimated as (only statistical errors):
$\mathrm{d}F/\mathrm{d}E = (10.1 \pm 1.2) \cdot (E/\mathrm{TeV})^{-2.03\pm0.19} \exp\left[-E/\,(6.12 \pm 1.31)\ \mathrm{TeV}\right] \cdot 10^{-11}\,\mathrm{cm}^{-2}\mathrm{s}^{-1}\mathrm{TeV}^{-1}$.
This agrees very well with the results from the CT-system and other experiments.
From a comparison between MC simulated energy spectra (a power law with cutoff at 6.0 TeV) and the observed Mkn 501 energy spectrum, the maximum energy with a significant γ-ray emission from Mkn 501 was estimated as $E_c = 13.8$ TeV. The Mkn 501 energy spectrum therefore extends well above 10 TeV.

♦ Part of the Cherenkov telescope data were taken during the presence of moonlight, thus allowing for the first time to do extensive investigations on this observation technique.

♦ The temporal characteristics of the γ-ray emission from Mkn 501 was investigated in both the TeV and X-ray region (sec. 7). The close relationship between these two energy regions in *Active Galactic Nuclei* (AGN) also shows up in the data: a Fourier analysis of the TeV and X-ray data samples revealed strong evidence for a 23-day periodicity (sec. 7.2.2). The periods of the two data sample were derived as $p_{X-ray} = 23.0^{+1.8}_{-2.0}$ d and $p_\gamma = 22.5^{+1.8}_{-1.7}$ d. The TeV and X-ray data do not only have the same periodicity but are also in phase.

In order to test, whether this periodicity is due to a genuine property of Mkn 501 or artificially produced by randomly distributed flares, the so-called shot noise model was applied to the data (sec. 7.3). This model was used to derive the probabilities of the peaks in the power spectrum, given the null hypothesis of randomly distributed flares with Gaussian shape and exponential time and amplitude distribution. As will be shown here, the normalization of the Mkn 501 power spectra on the shot noise model leads to white noise residuals (except for the 23-day period), which imply an exponential probability distribution of the normalized Fourier power values. The significance of the 23 day period was calculated from the combined TeV and X-ray results as: $\mathcal{P} = 3.6 \cdot 10^{-4}$ or 3.4σ (sec. 7.5). Due to the very different data spacing of the TeV and X-ray data, the corresponding power spectra are not correlated and the combination of both results is justified.

The mean flare width σ was estimated from the TeV and X-ray power spectra as: $\sigma_\gamma = 0.51 \pm 0.07$ and $\sigma_{X-ray} = 0.96 \pm 0.21$. An explanation for this difference could be the different optical depth for photon-photon absorption in the emitting region for X-rays and TeV γ-rays.

There exist several models to explain periodic γ-ray emission (sec. 7.5) from AGN. The model of a binary black hole system, however, is also able to explain the evidence for a helical jet structure in Mkn 501 found in radio observations.

CONTENTS

List of acronyms and abbreviations

ACT	air Cherenkov telescope
ADC	analog to digital converter
AGN	active galactic nucleus
asl	above sea level
ASM	all sky monitor
BBHS	binary black hole system
BLR	broad line region
BLRG	broad line radio galaxy
CF	conversion factor
COG	center of gravity
CR	cosmic rays
CV	cataclysimic variables
DEBRA	Diffuse Extragalactic Background Radiation
DFT	discrete Fourier transformation
DOF	degrees of freedom
EAS	extended air shower
EGRET	energetic gamma-ray experiment telescope
EIC	external inverse compton
FOV	field of view
FR-I	Fanaroff-Riley class I
FR-II	Fanaroff-Riley class II
FSRQ	flat spectrum radio quasar
FWHM	full width at half maximum
GRB	gamma ray burst
HBL	high energy cutoff BL Lac
HEAO	high energy astronomy observatory
HEGRA	high energy gamma ray astronomy
HEXTE	high energy X-ray timing experiment
HST	Hubble space telescope
HV	high voltage
IR	infrared
IT	imaging technique
LBL	low energy cutoff BL Lac
LINER	low ionization nuclear emission region
LSP	Lomb-Scargle periodogram
MBR	microwave background radiation
MC	Monte Carlo
MJD	modified Julian date
Mkn	Markarian
MLE	maximum likeliehood estimate
MSA	mean squared amplitude
MSE	mean squared error
MWL	multi wavelength
NKG	Nishimura Kamata Greisen
NLR	narrow line region
NLRG	narrow line radio galaxy
NSB	night sky background
OSSE	oriented scintillation spectrometer experiment
OVV	optically violent variable quasar
PCA	proportional counter array
PD	Poisson distribution
PDF	probability density function
Pe	photoelectron
PMT	photomultiplier tube
PSPC	position sensitive proportional counter
quasar	quasi stellar radio source
QE	quantum efficiency
QPO	quasi periodic oscillation
QSO	quasi stellar object
RBL	radio selected BL Lac
RMS	root mean squared
RXTE	Rossi X-ray timing explorer
SED	spectral energy distribution
SN	supernova
SND	standard normal distribution
SNR	supernova remnants
SSC	synchrotron self compton
SSCs	scanning shadow cameras
SSRQ	steep spectrum radio quasar
Sy-I	type I Seyfert galaxy
Sy-II	type II Seyfert galaxy
TA	Utah Telescope Array
UV	ultraviolet
XBL	X-ray selected BL Lac
XRB	X-ray binary
ZA	zenith angle

1. INTRODUCTION

High-energy particle astrophysics is a new, rapidly developing field of research, which amongst others, deals with the investigation of *Cosmic Rays* (CR). Historically, the search for understanding cosmic rays is rather old, but only recently the development of the field is progressing due to improved experimental instruments. The fact that this field, in particular the important sector of high-energy γ-ray astronomy, is in its initial phase and subject to dramatic changes was impressively demonstrated by the observation of intense, long lasting TeV γ-ray emission from the extragalactic source *Markarian 501* (Mkn 501) in 1997:
Mkn 501 is an elliptical galaxy of the BL Lac type at a distance of approximately 450 million lightyears (red shift $z = 0.034$). From February until October 1997 this source showed an unexpected strong emission of TeV γ-ray photons (see fig. 1.0.1) which could be confirmed by several groups ([131] and reference therein). During that time Mkn 501 was the brightest known object in the TeV γ-ray sky. The emission was characterized by dramatic, short term variations in intensity ($\Delta t_{obs} \sim 0.5\,\mathrm{d}$), peak flux values of up to 10 times the Crab Nebula flux (the brightest known steady γ-ray source) and a mean flux of about 3 times the Crab flux. In comparison with the 1996 observations of Mkn 501, the mean flux increased by a factor 10 [2, 23]. The energy spectrum of Mkn 501 followed a power law with exponential cutoff and extended at least up to 16 TeV [4].

This thesis deals with the temporal and spectral analysis of this event, based on the results obtained with the 6 Cherenkov telescopes of the HEGRA collaboration and, in part, on the X-ray data taken with the *All Sky Monitor* (ASM) on board the RXTE satellite. The HEGRA data provides the most complete coverage of Mkn 501 in the TeV range in 1997 and, for the first time, includes extensive observations taken during the presence of moonlight.
The detailed investigation of this Mkn 501 outburst was possible due to improved detectors and analysis methods and can be compared favorably to the unsuccessful search for any cosmic γ-ray source until 1989. Obviously, this observation also showed that many unsolved questions concerning the CR still exist.

The cosmic radiation was discovered by Viktor Hess in balloon experiments in 1912. He could prove, that part of the natural radioactivity at ground originates from cosmic particles, permanently striking the earth's atmosphere. The origin of this radiation is still — after nearly 90 years of research — basically unknown. The spectrum of this radiation extends up to energies of $3 \cdot 10^{20}$ eV, far above the energy scales accessible with present day terrestrial accelerators. The CR mainly consist of high energy nuclear particles (protons, αs as well as heavier atomic nuclei), a small admixture of electrons (roughly 2% above 10^{11} eV) and a still smaller fraction of γ-rays ($< 10^{-4}$). The coarse knowledge of this composition, however, extends only up to energies of 10^{13} eV and the high energy γ-ray flux is completely unknown. The differential flux spectrum of the CR follows a power law according to $\mathrm{d}F/\mathrm{d}E \propto E^{-\alpha}$. The differential spectral index α has values between $\alpha = 2.6$ and $\alpha = 3.1$ depending on the energy region (see fig. 1.0.2). Primary fundamental questions are: what are the sources of the CR and what are the production and acceleration mechanisms.

The keV - GeV energy region of the CR is investigated by means of satellite (up to $E \simeq$

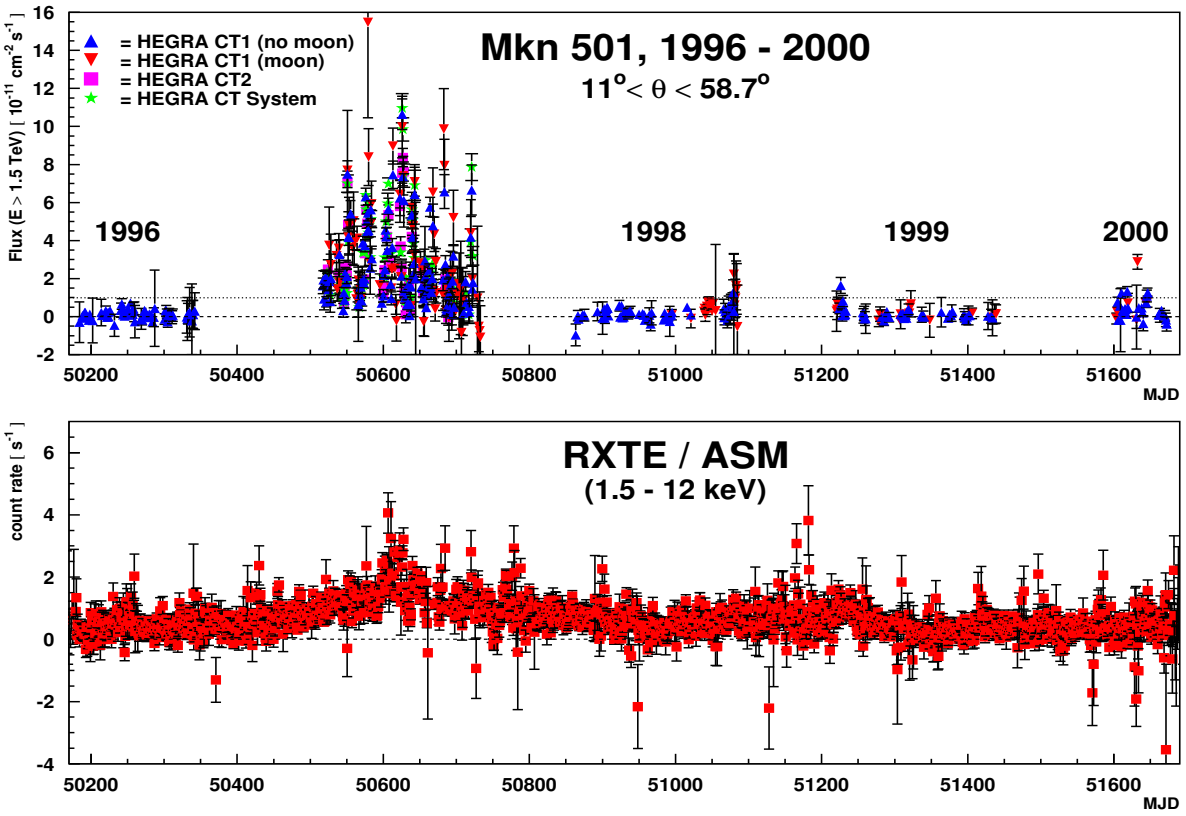

Fig. 1.0.1: The overall Mkn 501 light curve as observed with the HEGRA Cherenkov telescope CT1 (data from CT2 and the CT-system have been added for 1997) and the ASM on board the RXTE satellite. The X-ray data was binned for visual purposes. The *Modified Julian Date* (MJD) gives the number of days since midnight (Greenwich mean time) on November 17, 1858.

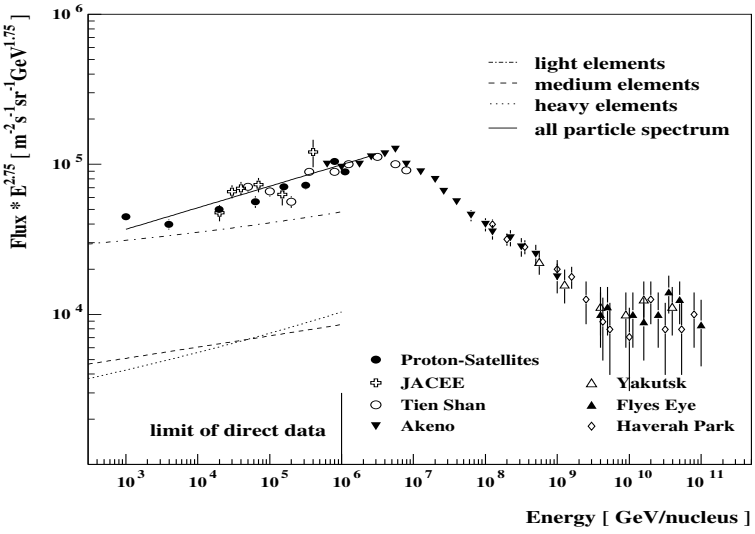

Fig. 1.0.2: The all-particle spectrum of the Cosmic Rays as a function of the particle energy. The spectrum was multiplied by a factor $(E/\mathrm{GeV})^{2.75}$ for visual purposes. (taken from [173])

10^{10} eV) or balloon borne detectors (up to $E \simeq 10^{13}$ eV). For energies above $3 \cdot 10^{11}$ eV it is possible to detect the CR induced atmospheric cascades of secondary particles (so-called *Extended Air Shower*, EAS) with ground-based detectors. The most common methods to observe EAS are the detection of the charged secondary particles and the measurement of the Cherenkov light, produced within an air shower. One big advantage of the Cherenkov light measurement is, that lower energy primaries can be observed even when the secondary particles are not able to reach the ground. The minimum shower energy for Cherenkov detectors is presently $E \gtrsim 3 \cdot 10^{11}$ eV, however, a new generation of large mirror Cherenkov telescopes promises to lower the threshold down to $E \gtrsim 10 \cdot 10^{9}$ eV [7, 95, 100, 115].

Currently, the main targets of investigation concerning CR are:

- Where are the sources and what are the production mechanisms of the Cosmic Rays?
- What is the composition of the Cosmic Rays?
- What is the exact shape of the energy spectrum?

Suitable particles for the search and investigation of CR sources are neutral particles such as photons, neutrons and neutrinos. The charged component of the CR is deflected by the weak galactic or intergalactic magnetic fields and can therefore not be used to trace the particles back to their origin. Due to the neutron mean decay time of 886 s only the highest-energy neutrons can be detected over large distances[1]. Neutrinos are also suitable for the investigation of relativistic (hadronic) processes in the universe. The detection (or non-detection) of neutrinos from active galaxies allows, in principle, to decide between the two major competing classes of γ-production models (see sec. 2.2), therefore neutrino observations are complementary to γ-ray astronomy. Due to the small interaction cross section, however, neutrino observation is very difficult and requires extremely large detectors ($\gtrsim 1\,\mathrm{km}^3$).
At the moment, the γ-ray astronomy is the most efficient method to obtain information on the sources of the CR. In the last years numerous sources in the GeV energy range could be localized with the aid of satellite-borne detectors [56] and several TeV γ-ray emitting objects have been found with ground-based detectors. On the basis of this data it was possible to check the different γ-ray production models. At the present state of knowledge, the most important processes for the production of high-energy γ-radiation are:

- π^0 *-decay*: If high energy protons interact with matter or γ-radiation they produce a variety of hadronic particles. About 30% of these particles are π^0-mesons which decay into γ-rays with a mean lifetime of $\gamma_\pi \cdot 10^{-16}$ s (γ_π is the Lorentz factor of the pion).
- *Inverse Compton scattering*: In this process gamma radiation is produced by the interaction of relativistic electrons (with Lorentz factor γ) and low-energy photons of energy ε. The mean energy of the Compton scattered photon $\langle E_\gamma \rangle$ is given by:

$$\langle E_\gamma \rangle \approx \begin{cases} \frac{4}{3} \langle \varepsilon \rangle \gamma^2 & \text{for } \gamma\varepsilon \ll m_e c^2 \text{ (Thomson limit)} \\ \frac{1}{2} \langle E_e \rangle & \text{for } \gamma\varepsilon \gg m_e c^2 \text{ (Klein} - \text{Nishina limit)} \end{cases} \tag{1.0.1}$$

(E_e denotes the electron energy before interaction) and the corresponding cross sections as [72]:

$$\sigma_c = \begin{cases} \sigma_T \left(1 - \frac{2\gamma\varepsilon}{m_e c^2}\right) & \text{for } \gamma\varepsilon \ll m_e c^2 \\ \frac{3}{8}\sigma_T \left(\frac{m_e c^2}{\gamma\varepsilon}\right) \left[\ln\left(\frac{2\gamma\varepsilon}{m_e c^2}\right) + \frac{1}{2}\right] & \text{for } \gamma\varepsilon \gg m_e c^2 \end{cases} \tag{1.0.2}$$

[1] Neutrons from the center of our galaxy (distance ≈ 8.5 kpc), for example, can only be detected, if $E \gtrsim 10^{18}$ eV.

($\sigma_T = 8\pi r_e^2/3 = 6.65 \cdot 10^{-25}\,\mathrm{cm}^2$ is the Thompson cross section and $r_e = e^2/m_e c^2 = 2.82 \cdot 10^{-13}\,\mathrm{cm}$ the classical electron radius[2]). If the differential energy spectrum of the electrons follows a power law $I_e\left(E_e\right) \propto E_e^{-\Gamma}$ then the same applies to the γ-ray flux f_c [78, 158]:

$$f_c\left(E_\gamma\right) \propto \begin{cases} E_\gamma^{-(\Gamma+1)/2} & \text{for } \gamma\varepsilon \ll m_e c^2 \\ E_\gamma^{-\Gamma} & \text{for } \gamma\varepsilon \gg m_e c^2 \end{cases} \tag{1.0.3}$$

♦ *Bremsstrahlung*: The radiation produced by a charged particle in the Coulomb field of a nucleus or ion. The differential cross section for an electron to radiate a photon with energy between E_γ and $E_\gamma + \mathrm{d}E_\gamma$ is given according to [145] as:

$$\sigma_b\left(E_e, E_\gamma\right)\mathrm{d}E_\gamma = 4\alpha Z^2 r_e^2 \frac{\mathrm{d}E_\gamma}{\mathrm{E}_\gamma} F\left(E_e, \nu = \frac{E_\gamma}{E_e}\right) . \tag{1.0.4}$$

Here E_e denotes the electron energy, r_e the classical electron radius, Z the charge of the nucleus, α the fine structure constant and

$$F\left(E_e, \nu\right) = \left[1 + (1-\nu)^2 - \frac{2}{3}(1-\nu)\right] \cdot \begin{cases} \left[\ln\left(\frac{2E_e}{m_e c^2}\frac{1-\nu}{\nu}\right) - \frac{1}{2}\right] & I \\ \ln\left(183 Z^{-1/3}\right) + \frac{1}{9}(1-\nu) & II \end{cases} \tag{1.0.5}$$

(I applies to the case of no screening, i.e. $E_e \ll 100 m_e c^2 \left[\nu/\left(1-\nu\right)\right] Z^{-1/3}$ and II to the case of complete screening $E_e \gg 100 m_e c^2 \left[\nu/\left(1-\nu\right)\right] Z^{-1/3}$). The spectrum of this radiation is approximately proportional to $1/E_\gamma$ [135], i.e. predominantly photons of low energy are produced.
If the bremsstrahlung is produced by high energy electrons, the γ-ray spectrum has the same shape, i.e. the same spectral index α, as the electron spectrum [158].

♦ *Synchrotron emission*: High-energy charged particles produce this radiation when they are deflected by magnetic fields. In case of an electron (with energy E_e) moving at an angle θ with respect to the field lines of a homogeneous magnetic field (of strength H) the maximum emission of synchrotron radiation occurs at an energy [135]:

$$E_{\gamma,m} = h\nu = 5 \cdot 10^{-9} \frac{H_\perp}{\mathrm{Gauss}} \left(\frac{E_e}{m_e c^2}\right)^2 \mathrm{eV} \tag{1.0.6}$$

(here $H_\perp = H \sin\theta$). The electron lifetime for synchrotron radiation $t_{1/2}$, i.e. the time after which the electron lost half of its energy due to synchrotron emission, is given by:

$$t_{1/2} = 5 \cdot 10^8 \left(\frac{m_e c^2}{E_e}\right)\left(\frac{\mathrm{Gauss}}{H_\perp}\right)^2 \mathrm{s} \tag{1.0.7}$$

As can be seen from eq. 1.0.6, large magnetic field strengths and/or energetic electrons are necessary in order to produce γ-rays by synchrotron emission. Nevertheless, synchrotron emission may provide the seed photon field for the inverse Compton process and therefore plays an important role in the production of high-energy γ-rays. If the electron spectrum follows a power law $I_e\left(E_e\right) \propto E_e^{-\Gamma}$ then the synchrotron photon spectrum will become [135]:

$$f_s\left(E_\gamma\right) \propto E_\gamma^{-(\Gamma+1)/2} \tag{1.0.8}$$

similar to the case of the inverse Compton process (eq. 1.0.3).

[2] Throughout this thesis CGS-units are used.

Source	Type	redshift	Discovery	EGRET
Galactic Sources				
Crab Nebula	Plerion		1989 [172, 71]	yes
PSR 1706-44	Plerion?		1995 [87, 32]	no
Vela	Plerion?		1997 [174]	no
SN1006	Shell		1997 [164]	no
RXJ1713.7-3946	Shell		1999 [117]	no
Cassiopeia A	Shell		1999 [6]	no
Centaurus X-3	Binary		1999 [138, 31]	yes
Extragalactic Sources				
Markarian 421	XBL	0.031	1992 [132, 127]	yes
Markarian 501	XBL	0.034	1995 [133, 23]	yes
1ES2344+514	XBL	0.044	1997 [29]	no
PKS2155-304	XBL	0.116	1999 [33]	yes
1ES1959+650	XBL	0.048	1999 [120]	no
3C66A	RBL	0.44	1998 [118]	yes

Tab. 1.0.1: Source catalog of detected TeV γ-ray sources. XBL and RBL denote X-ray respectively radio selected BL Lac objects (see sec. 2). (adopted from [171])

Since relativistic particles are needed for the production of the γ-radiation in all processes described above, the sources of high-energy γ-radiation might also be responsible for the production of the CR in general.
The following classes of astrophysical objects are assumed to be sources of the CR or have already been detected in the GeV and/or TeV energy range (see tab. 1.0.1):

- *supernova remnants* (SNR)
- *pulsars*
- *Active Galactic Nuclei* (AGN)
- *binary systems*: *Cataclysmic variables* (CV), *X-ray Binaries* (XRB) and microquasars
- *Gamma-ray bursts* (GRB)

In order to fully understand the different production mechanisms, detailed and extensive observation of γ-ray sources are necessary. Thus, constraints on the involved acceleration processes can be derived from the energy spectra, the temporal variations of the photon emission and/or from multi-wavelength observations. An upper limit on the radius R of the emitting volume, for example, can be derived from the variability timescales Δt_{obs} of the observed flux emission: $R < \delta c \Delta t_{obs} \frac{1}{1+z}$ (δ denotes the Doppler factor of the emission region[3], c the speed of light and z the redshift of the object). The correlated emission of TeV γ-ray and X-ray synchrotron radiation suggests the presence of high energy electrons, i.e. such observations are strong evidence that electron acceleration as well as a magnetic field are present. Nevertheless, such an observation is not sufficient to exclude hadronic production mechanism, respectively the absence of X-rays is not a proof of hadron acceleration. A convincing proof for hadron acceleration would be the parallel observation of neutrinos.

[3] For a definition of the Doppler factor δ see eq. 7.5.10 and corresponding text.

photon field	mean energy ε_2	threshold energy ε_t	photon density
2.7 K radiation	$6 \cdot 10^{-4}$ eV	$\approx 4 \cdot 10^{14}$ eV	$\approx 400\,\mathrm{cm}^{-3}$
optical	2 eV	$\approx 10^{11}$ eV	$\approx 5 \cdot 10^{-3}\,\mathrm{cm}^{-3}$

Tab. 1.0.2: Threshold energy ε_t for $\varepsilon^+\varepsilon^-$ pair production by the interaction of high energy γ-rays with photons from the 2.7 K and extragalactic starlight fields. The density of the photon fields and their mean energy ε_2 is given, too. (numbers from [135])

Another important aspect of γ-ray astronomy is the ability to probe the density of the *Diffuse Extragalactic Background Radiation* (DEBRA):
Due to interaction processes, the universe is not completely transparent for high energy γ-rays. A γ-ray of energy ε_1 may interact with another photon of energy ε_2 and create an electron positron pair ($\gamma\gamma \rightarrow e^+e^-$), if the primary energy ε_1 is above the threshold energy [135, p. 20]:

$$\varepsilon_t = \frac{2m_e^2c^4}{\varepsilon_2\,(1-\cos\theta)} \simeq \frac{1}{2}\frac{10^{12}\,\mathrm{eV}}{(\varepsilon_2/\mathrm{eV})\,(1-\cos\theta)} \tag{1.0.9}$$

(θ denotes the angle of incidence, m_e the electron rest mass). For head-on collisions ($\theta = 180°$) the corresponding cross section for pair production in the extreme relativistic region $\omega := \sqrt{\varepsilon_1\varepsilon_2} \gg m_ec^2$ is given as:

$$\sigma_{pp} = \pi r_e^2 \left(\frac{m_ec^2}{\omega}\right)^2 \left[2\ln\left(\frac{2\omega}{m_ec^2}\right) - 1\right] \tag{1.0.10}$$

(here r_e denotes the classical electron radius). The most important background photon fields are the 2.7 K *Microwave Background Radiation* (MBR) field, a remnant from the big bang, and the extragalactic *Infrared* (IR, from dust emission) to *Ultraviolet* (UV) starlight photon field produced in the phase of early galaxy formation. Given a threshold energy for head-on collisions as $\varepsilon_t \simeq 0.25 \cdot 10^{12}/\varepsilon$ eV, the threshold energy for these photon fields can easily be calculated and is given in tab. 1.0.2. From eq. 1.0.10 and the photon densities given in tab. 1.0.2 it is possible to derive rough estimates for the interaction length of γ-rays in these photon fields. The results of a more complete treatment, including the geometry of the collisions and the energy distribution of the target photons is shown in fig. 1.0.3. Since the observed high energy γ-ray spectra are expected to be substantially modified by the IR-UV photon field [43, 159, 160] (fig. 1.0.3) the observation of extragalactic objects like Mkn 501 in the TeV energy region gives very useful constraints on the photon field density. In case the intrinsic TeV source spectrum is known (from the observed X-ray synchrotron emission and other observations), it is possible to estimate the DEBRA density in the relatively unconstrained 0.5 μm to 50 μm wavelength region [92]. Photons within this (infrared) energy region are expected to be a remnant from the time of early galaxy formation. Thus, constraints on the density of this photon field have a large impact on the galaxy formation models and the dark matter problem.

The main experimental problem of γ-ray astronomy is the very small fraction of γ-ray photons within the CR ($< 10^{-4}$). In satellite-borne detectors it is possible to achieve a high γ-hadron separation by means of anti-coincidence counters. However, due to the steeply falling energy spectrum of the γ-radiation (e.g. $F_{crab}\,(E > 1\,\mathrm{TeV}) \approx F_0 \cdot (E/\mathrm{TeV})^{-2.6}$) and the small effective collection area in present day satellite-borne detectors, observable γ-ray energies are limited to $E_\gamma \lesssim 10\,\mathrm{GeV}$.

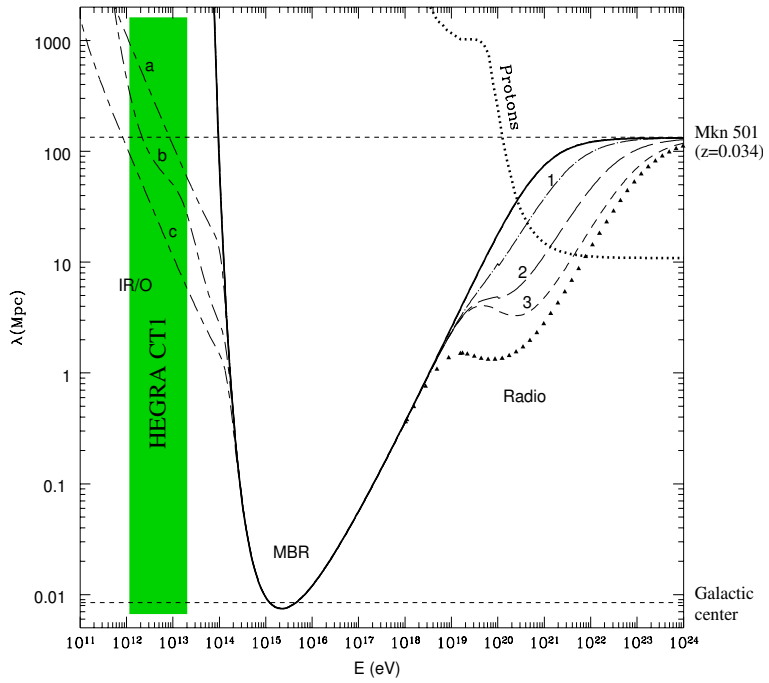

Fig. 1.0.3: Mean free path λ for pair production as a function of the photon energy E (no cosmological effects included). The curves a, b, and c correspond to different models on the IR/Optical background and 1, 2 and 3 to different extragalactic radio background models. The triangles denote the lower limit on λ by assuming that the total observed radio background is extragalactic. The heavy dotted line denotes the energy-loss mean free path for protons (taken from [37]).
The distance to Mkn 501 and the galactic center (a Hubble constant of $H_0 = 75\,\mathrm{km\,s^{-1}\,Mpc^{-1}}$ was used) as well as the energy region covered by the HEGRA telescope CT1 is shown in addition.

Energy range	classification	technique	experiment
$0.51 - 10$ MeV	low energy	NAI-spectroscopy	BATSE, OSSE
$10 - 30$ MeV	medium energy	Compton-telescope	COMPTEL
30 MeV $-$ 10 GeV	high energy (HE)	spark chamber	SAS-2, COS-B, EGRET
10 GeV $-$ 100 TeV	very high energy (VHE)	atmospheric Cherenkov technique	Whipple, HEGRA, CANGAROO
100 TeV $-$ 100 PeV	ultra high energy (UHE)	air shower detectors	CASA, CYGNUS, Tibet AS, HEGRA
100 PeV $-$ 100 EeV	extremely high energy (EHE)	air shower detectors	Akeno, Haverah Park, Fly's Eye

Tab. 1.0.3: Classification of the distinct energy regions in high-energy γ-ray astronomy. (taken from [170])

At the present time, the only possibility to measure γ-radiation within or above the VHE-region ($\sim$ 10 GeV $-$ 100 TeV, see tab. 1.0.3) is to observe the γ-ray induced extended air showers by ground-based detectors. In that case, the atmosphere serves as active absorber material and effective collection areas of about 10^5 m^2 can be obtained. The main drawback of this method, however, is that the shower composition and development differs only slightly for γ- and hadron-induced air showers. These differences need to be resolved in order to carry out an efficient γ-hadron separation.

If a particle of the CR hits the atmosphere, the first interaction with the nucleus of an air molecule takes place at a height of about 20 km. As a result, several secondary particles are produced, which themselves give rise to new particles in consecutive interactions. The particle numbers thus dramatically increase till the maximum of $\sim \mathcal{O}(10^5)$, depending on the energy of the primary particle, is reached. The mean energy per particle decreases as the number of particles increases and, at some point, is not sufficient to create new secondary particles. Energy losses through ionization of air molecules then becomes dominant. This causes a deceleration of the shower particles without the production of new secondary particles. As a result, the shower dies out slowly.

Due to the high energy of the primary particle all shower particles are strongly collimated along the direction of the incident primary. The mean transverse momentum in hadronic interactions and multiple scattering in electromagnetic showers leads to an expanding lateral distribution with progressing shower development. In addition, the earth magnetic field widens the showers a bit, too. Yet, the majority of secondary particles is still within $\sim$ 150 m distance to the shower axis (see fig. 1.0.4).

In contrast to γ-induced air showers, which mainly contain secondary electrons and photons (electromagnetic showers), hadron-induced air showers contain a hadronic component. The hadronic component essentially consists of protons, neutrons and mesons and a small admixture of muons and neutrinos mainly from meson decays. The electromagnetic component of hadron showers mainly originates from neutral pion decays $\pi^0 \to \gamma\gamma$. Since π^0-mesons are produced within almost every hadronic interaction, the major part of the energy of hadron showers is gradually transferred into the electromagnetic component. The photoproduction process on the other hand, in which energy is transferred from the electromagnetic to the hadronic component has a very small cross section and can be ignored.

At the moment, several methods to observe extended air showers exist:

- A small fraction of the primary energy ($\sim 10^{-5}$) is isotropically emitted as fluorescence

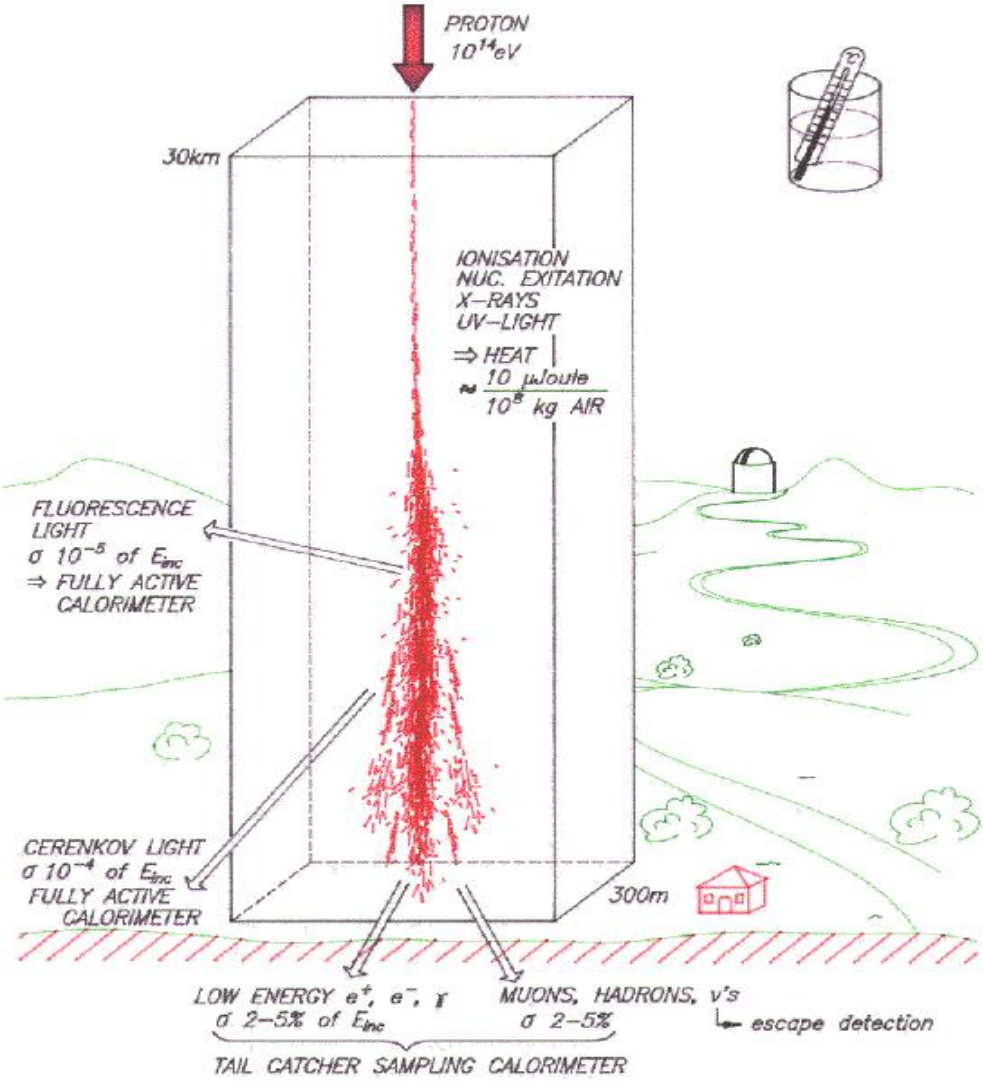

Fig. 1.0.4: Schematic picture of a 10^{14} eV proton shower.

light by excited nitrogen molecules and can be detected with photon detectors of large collection area. Due to the isotropic light distribution the EAS can be observed under large viewing angles (with respect to the shower axis), the energy threshold, however, is very high ($E \geq 10^{16}$ eV).

- For shower energies above $\sim 10^{13}$ eV more and more secondary particles are able to reach the ground. The number of charged particles can then be measured by suitable detectors like scintillator counters. Due to the high number of secondary interactions, basically all information of the initial CR is lost. Such detectors therefore have a very poor γ-hadron separation except when additional muon detectors are added.

- The charged relativistic particles of the air shower produce Cherenkov light on their way through the atmosphere (the total energy fraction amounts to about 10^{-4}). Due to the small refractive index of air, the Cherenkov light is strongly collimated and can only be measured up to about a distance of 150 m from the shower axis. An advantage of the Cherenkov light detection is that even showers whose hadronic secondaries, as well as electrons and positrons are not able to reach the ground can be observed. The energy threshold is therefore lower compared to the detection of the charged shower component. Furthermore, only a small fraction of the produced Cherenkov light is necessary in order to detect an EAS. Another advantage compared to the detection of charged particles is that the observed Cherenkov light comes from nearly all regions of the air shower, whereas the measured charged particles originate from the shower tail. Systematic differences in the shower development of γ- and hadron-induced air showers therefore allow an improved γ-hadron separation. A drawback of the Cherenkov light measurement is that observations are restricted to clear and (almost) moonless nights.

Due to the large hadron background, the crucial point in all γ-ray astronomy observations is an effective γ-hadron separation. Thus it took about 75 years, despite intensive search, until in 1989 the Crab nebula was detected as the first γ-ray source within the VHE region [172]. The used detector was a so-called *Air Cherenkov Telescope* (ACT).
A Cherenkov telescope is a simple reflecting telescope with a (usually) spherical mirror and a camera build up from a large number ($\mathcal{O}(100)$) of *Photomultiplier Tubes* (PMTs), located in the focal plane. The field of view of an ACT is typically $3^\circ - 5^\circ$, the main limitation coming from the size of the camera. As a result, only individual source candidates can be observed. The basic detection principle of ACTs is as follows:
Part of the Cherenkov light produced within an EAS is collected by the mirror, reflected onto the PMT-camera and recorded by a fast electronic readout. As photons are generated by different particles at different atmospheric heights, the light hitting the mirror carries some angular information. Thus a specific "image" of the shower is produced in the focal plane (this image is not a complete projection of the shower). Based on the recorded shower images, an analysis method proposed by Hillas [75] is used to effectively separate the γ-ray induced air showers from the hadronic background:
A set of parameters which describe the shape and orientation of the shower image in the camera is calculated for each event. Due to the differences in the shower development of γ- and hadron-induced air showers the distributions of the image parameters of both shower types show small but systematic differences. As a result, it is possible to separate between γ- and hadron showers by using selection cuts on the derived image parameters. Presently, this method represents the most efficient way to enhance the signal to noise ratio. It contributed considerably to the success of ACTs.

Outline of this thesis

The main goal of this thesis is the spectral and temporal analysis of the Mkn 501 outburst in 1997.

Chapter 2 is dedicated to the AGN class of objects, Mkn 501 belongs to. The history of AGN, the different incarnations and a classification scheme is briefly described. Some of the various theoretical models to explain the production of high-energy γ-ray emission are presented. In the last section of this chapter, more detailed information on Mkn 501 is summarized.

The data used for this analysis have been recorded with the 6 Cherenkov telescopes of the HEGRA detector. The HEGRA detector (*High Energy Gamma Ray Astronomy*) is located on the Roque de Los Muchachos at about 2200 m *above sea level* (asl) on the Canary Island La Palma. In part data from the ASM on board the *Rossi X-Ray Timing Explorer* (RXTE) has been used. The ASM measures X-ray emission in the $2-12\,\mathrm{keV}$ energy band. The properties of both detectors are presented in chapter 3.

Chapter 4 starts with a description of EAS. Production mechanisms, shower development and the radiation of Cherenkov light are presented, the different possible methods for shower detection are discussed. The differences between γ- and hadron-induced air showers are emphasized. The remaining part of the chapter is dedicated to the analysis and γ- hadron separation of EAS, based on the shape and orientation of the recorded shower images.

The standard pre-analysis of the CT1 raw data is briefly summarized in sec. 5.1. Main topics are the calibration of the camera, preselection of the shower events, calculation of the image parameters and the special treatment of data observed during the presence of moonlight. Apart from sec. 5.3.4, all sections within chapter 5.3 describe analysis methods newly developed in context of this thesis for the investigation of the Mkn 501 data samples:

- A method to estimate the impact parameter and the energy of EAS by means of the image parameters. The obtained energy resolution is $\sim 30\%$ *Root Mean Squared* (RMS) and the impact parameter resolution is $\sim 20\%$ (RMS).

- The background content in a given data sample is estimated using a χ^2-fit to the $ALPHA$ image parameter distribution. Therefore, no additional OFF-observations are necessary to derive the significance of an observed signal.

- A program to derive dynamical, i.e. energy and zenith angle dependent selection cuts. Dynamical cuts yield better cut sensitivities compared to constant cuts, especially at large zenith angles and shower energies.

- A program to derive differential energy spectra. MC simulations have been used to show the reliability of the obtained results.

The results from the spectral analysis of Mkn 501, i.e. energy spectra and flux light curves are shown in chapter 6. Special emphasis is given to the results obtained from observations in the presence of moonlight (so-called moon observations). Coincident events between CT1 and the CT-system are used to compare the different energy estimation methods.

Chapter 7 deals with the temporal analysis of the Mkn 501 HEGRA CT and RXTE ASM data. The first part describes the Lomb-Scargle periodogram, a method used to derive Fourier power spectra from unevenly sampled data. Properties of the method are discussed. In the case of objects with flaring activity, the standard Fourier analysis is not appropriate in deriving the significance of a prominent frequency component. This problem is addressed by means

of the shot noise model. The model and its implications on the significance calculation are discussed in sec. 7.3. The results of the timing analysis are presented and discussed in the last section of this chapter.

2. ACTIVE GALACTIC NUCLEI

In general the term *Active Galactic Nuclei* (AGN) refers to the central region of a galaxy where high-energetic processes take place which cannot be attributed to normal (thermal, nuclear) processes in stars. The first AGN class, the Seyfert galaxies, were discovered by Seyfert in the 1940s. They appeared to be spiral galaxies, but with a star-like nucleus showing broad and strong emission lines, different compared to normal galaxies. Quasars, a very high luminosity subclass of AGN, were discovered in the early 1960s in radio surveys. The optical counterparts of some of the observed bright radio sources were star-like, but turned out to be amongst the most distant objects known at that time. The first quasar, 3 C 273, was detected by Maarten Schmidt in 1962 and is more than 1000 times more luminous compared to a galaxy like our own.
A lot of AGN have been found in all wavebands, from radio to γ-rays since then. Depending on the observed features, AGN have been classified into Seyfert galaxies, radio galaxies, quasars, QSOs, OVVs, LINERs, blazars and others. The connection between these subclasses has been thoroughly investigated, but not completely solved yet.
With regard to high energy γ-ray astronomy, the blazars represent the most important AGN subclass. About 60% of the identified EGRET AGN sources above 100 MeV seem to be blazars [69][1] and all of the presently known AGN with TeV γ-ray emission belong to this class.

In the next section, a short summary of the properties and classification of AGN is presented. Section 2.2 deals with a simple model of an AGN, its connection to the AGN classification and the theoretical models to explain high energy γ-radiation. The last section covers some details of the AGN Mkn 501.

2.1 Properties and classification of Active Galactic Nuclei

This section gives a brief description of the different subclasses of AGN. The classification is based on observational results like the presence or absence of emission lines, variability, emission in certain energy bands etc.. Due to the lack of complete understanding of AGN there is no definite division into physically distinct classes possible yet, and as may be seen from this list, the various classifications are not mutually exclusive. For a complete treatment of AGN and their classification schemes, the reader is referred to the books from Kembhavi & Narlikar [84] and Peterson [125], the articles from Antonucci [11], Dopita [50] and Urry & Padovani [167] and the Web page of Bill Keel at `http://www.astr.ua.edu/keel/galaxies/index.html`.

♦ **Seyfert Galaxies**: Seyfert galaxies are low luminosity AGN with a (bolometric) magnitude $M_B > -21.5 + 5 \log h_0$ (h_0 is the Hubble constant in units of $100\,\mathrm{km\,s^{-1}\,Mpc^{-1}}$). They have bright, star-like nuclei, but the host galaxy is clearly detectable. Most if not all Seyferts appear to have the morphology of spiral galaxies. Depending on the properties of the optical spectrum, Seyfert galaxies are subdivided into two categories:

[1] From the 271 detected γ-ray sources in the 3rd EGRET catalog, 170 sources have not been identified yet. The remaining 101 sources contain 66 'high confidence' and 27 'lower confidence' blazars.

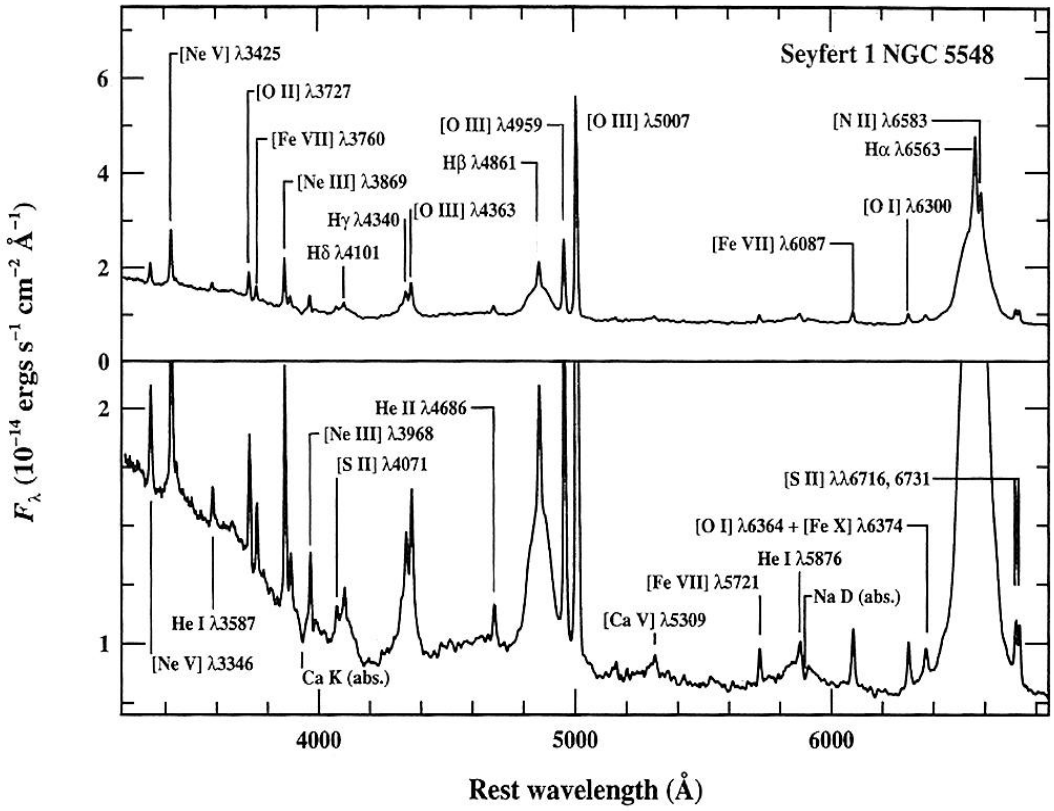

Fig. 2.1.1: The optical spectrum of the Seyfert 1 galaxy NGC 5548. The prominent broad and narrow emission lines are labeled, as are strong absorption features of the host galaxy spectrum. The vertical scale is expanded in the lower panel to show the weaker features. (figure and caption taken from [125])

Seyfert type I (Sy I): This type emits strong continuum radiation from the IR to the X-ray band. Furthermore, type I Seyfert galaxies also show broad and narrow emission lines, superimposed on the continuum spectrum (see fig. 2.1.1). The narrow lines are characteristic for a low-density ionized gas with an electron density n_e of typically $n_e \approx 10^3 - 10^6\,\mathrm{cm}^{-3}$ [125, p. 21] and the line widths correspond to velocities of about $\mathcal{O}\,(100\,\mathrm{km\,s}^{-1})$[2]. The broad lines, on the other hand, have widths of up to $10^4\,\mathrm{km\,s}^{-1}$ and are related to a high density gas of $n_e \approx 10^9\,\mathrm{cm}^{-3}$.
Seyfert type II (Sy II): This type emits a weak continuum emission and only narrow lines are present in the spectrum.
Both types show weak absorption lines due to stars in the host galaxy.

♦ **Quasars** and **Quasi Stellar Objects** (QSOs): Quasars represent the most luminous and most distant subclass of the AGN. The (bolometric) magnitude is $M_B < -21.5 + 5\log h_0$ and the redshift extends up to $z \lesssim 5$. A small percentage ($\sim 5\% - 10\%$) are strong radio sources and a few quasars have jets (e.g. 3C273). Quasars are distinguished from Seyferts in

[2] It is assumed, that the emission lines in AGN spectra are Doppler-broadened, so line widths are generally measured in velocity units.

that they are spatially unresolved in the Palomar Sky Survey photograph, their diameter $\varnothing$ thus being limited to $\varnothing \lesssim 7''$. No host galaxy of a quasar has been found yet, although some quasars are surrounded by a halo (so-called quasar fuzz) which appears to be starlight from the host galaxy. The optical spectra of quasars and Seyfert galaxies are quite similar. The quasar spectrum, however, has only weak or no absorption lines and the broad emission lines are generally more pronounced compared to the narrow lines than in Seyfert galaxies.
Based on the (differential) spectral index α_r measured at a few GHz, the radio loud quasars are further subdivided into *Flat Spectrum Radio Quasars* (FSRQ, $\alpha_r \leq 0.5$) and *Steep Spectrum Radio Quasars* (SSRQ, $\alpha_r > 0.5$). Note that historically the term quasar was used to denote the strong radio sources amongst the quasar subclass, while the term QSO was used for the radio quiet population thereof.

♦ **Radio Galaxies**: Radio galaxies are the optical counterparts of strong radio sources with extended radio lobes and radio luminosities of at least 10^{42} erg/s. Most of them appear to be elliptical galaxies, but some have also been associated with quasars. Some of the radio galaxies have an optically bright nucleus, emitting strong continuum radiation combined with broad and/or narrow emission lines. Similar to the case of Seyfert galaxies, this sample of radio galaxies is further subdivided into *Broad Line Radio Galaxies* (BLRGs) and *Narrow Line Radio Galaxies* (NLRGs). Most of the radio galaxies have jets connecting the extended radio lobes to the central component of the AGN. Based on the properties of the radio lobes, radio galaxies are further classified into:
Fanaroff Riley type I (FR I): These are weak radio sources which are (radio) brightest close to center. Jets have been observed in 80% of these objects.
Fanaroff Riley type II (FR II): In contrast to FR I galaxies this subclass is limb brightened and, in general, more luminous. FR II galaxies often have regions of enhanced emission within or at the edge of the extended radio lobes (hot spots). Less than 10% of the FR II galaxies, but nearly all quasars within this subclass have jets.

♦ **Low Ionization Nuclear Emission Line Region** (LINER)**:** LINERs have a low nuclear luminosity. Their optical spectrum resembles that of Sy II galaxies, but with relatively strong low ionization lines. The relationship between LINERs and AGN is still not completely understood. Some, but not all, seem to be low luminosity Seyfert galaxies. LINERs are extremely common in nearby galaxies.

♦ **Optically Violent Variable quasars** (OVVs) and **BL Lac Objects:** These objects have a strong non-thermal continuum emission that shows rapid variability. They tend to have highly polarized emission (up to a few % compared to $\lesssim 1\%$ for most AGN) varying in both magnitude and position angle. BL Lacs and OVVs have always been found to be strong radio sources. The distinction between both subclasses is again determined by the spectral properties: In contrast to OVVs, BL Lac objects have only weak or no emission and absorption lines. Sometimes, like in the case of Mkn 501, BL Lacs are found in elliptical galaxies.
It is assumed that both objects have a strong, relativistically beamed component close to the line of sight. OVVs, BL Lacs and FSRQs are often grouped together and referred to as blazars. Blazars are strong γ-ray sources and some BL Lac objects have even been detected at TeV energies[3].
Another classification scheme, based on the X-ray to radio luminosity, has been proposed for

[3] Due to the large distance of OVVs and FSRQs ($z > 0.1$), TeV γ-rays from these objects are almost completely absorbed by the intergalactic infrared background.

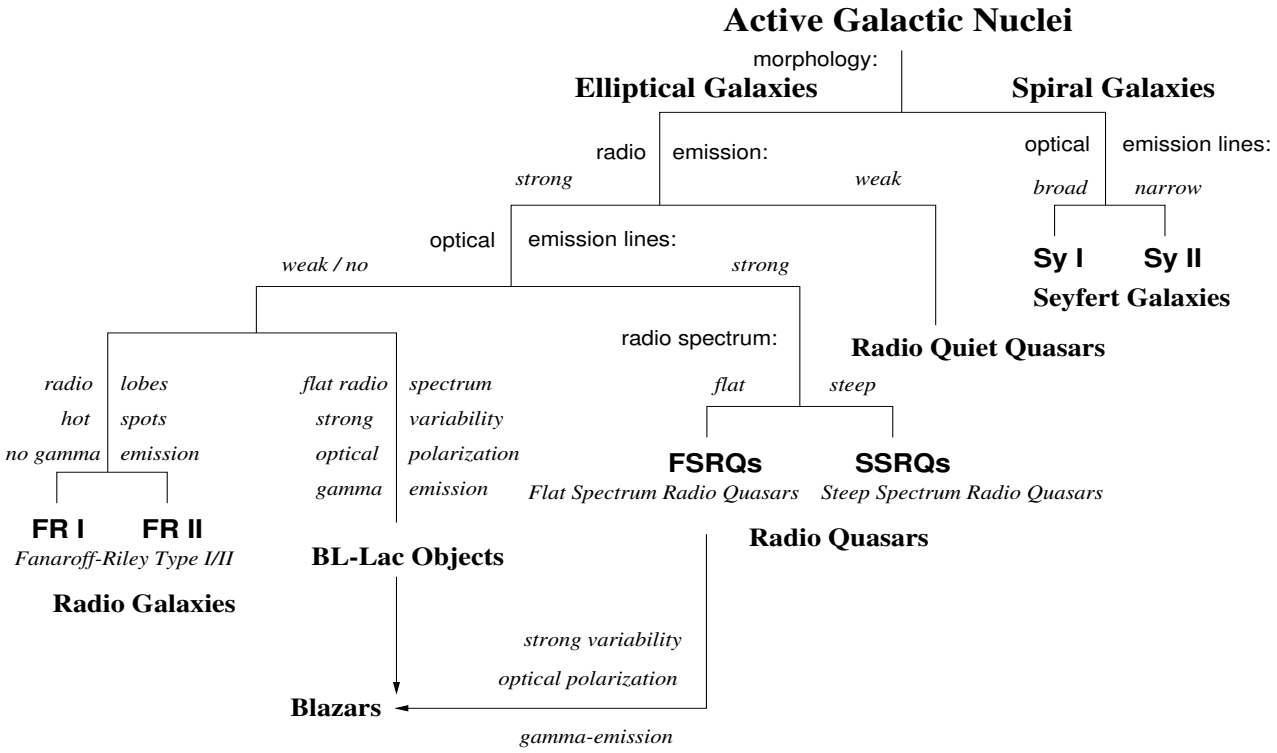

Fig. 2.1.2: Classification of Active Galactic Nuclei (taken from [22])

BL Lac objects [122, 147, 161]. Given the X-ray and radio fluxes F_X and F_r respectively, a BL Lac object is considered a *Radio Selected BL Lac* (RBL also denoted as *Low Energy Cutoff BL Lac*, LBL), if $\log(F_X/F_r) < -5.5$, whereas it is classified as a *X-ray Selected BL Lac* (XBL or *High Energy Cutoff BL Lac*, HBL) otherwise. Up to now, only XBLs like Mkn 501 and Mkn 421 have been detected at TeV energies.

Note that a further classification of AGN is given by means of their radio luminosity as radio quiet objects (Seyferts, QSOs) and radio loud objects (FR I, FR II, quasars, BL Lacs, FSRQs and SSRQs). Radio loud AGN, which make up $15\% - 20\%$ of the AGN, have a radio (5 GHz) to optical (B-band) flux ratio of about $F_{5\,\mathrm{GHz}}/F_B \gtrsim 10$. An overview of the described AGN classes and their interconnections is shown in fig. 2.1.2. In the next section an AGN model and a unification scheme for the different AGN classes is presented.

2.2 Model of Active Galactic Nuclei

The results presented in the previous section roughly resemble the situation in particle physics before the Standard Model was developed: the AGN sample consists of a large number of different subclasses and the classification depends on spectral and variability characteristics, on certain detection criteria and others. An attempt to put the different subclasses in perspective has therefore been made [11, 50, 167]. The basic idea of this unification model is to relate the wide variety of AGN phenomena to observer- or aspect-dependent variables, like the orientation of the AGN with respect to the observer, and to real differences in a few characteristic parameters, like accretion rate, galaxy morphology and the evolutionary status of the central black hole. In order to explain the unification model, we must first start with the current picture of an AGN (see. fig. 2.2.1):

A supermassive black hole of about $10^6 - 10^9$ solar masses $M_\odot$ is accreting surrounding material, thus forming a large accretion disk. Due to friction and turbulent processes in the accretion disk, gravitational potential energy is transferred into thermal radiation, mainly emitted in the UV region. This radiation may then excite and/or ionize atoms in the rapidly moving gas clouds close to the central black hole (broad line region in fig. 2.2.1). These atoms then produce the observed Doppler broadened strong optical and UV emission lines. The broad-line region is still within a large torus of gas and dust wrapped around the accretion disk. Gas clouds which are further away from the black hole and the torus also produce emission lines, but, due to the small velocity of these clouds, the emission lines are much narrower (narrow line region in fig. 2.2.1). In some cases outflow of strongly collimated, highly relativistic plasma, i.e. a plasma jet, perpendicular to the accretion disk occurs. When the jet interacts with surrounding material, the plasma gets de-accelerated and forms extended radio lobes. The radio emission is due to synchrotron emission from electrons moving within the magnetic fields of the jet.
The acceleration mechanism, leading to the relativistic jet outflow is still unknown. Some models include charged, rotating black holes which act as a giant dynamo ([86] and reference therein). The magnetic fields, essential for the emission of synchrotron radiation and necessary to keep the jet collimated over long distances, naturally appear in such a scenario.
High-energy γ-radiation is expected to be created within the jet. In lepton-based models the γ-rays are produced by means of inverse Compton scattering of high-energy electrons. The (optical to X-ray) seed photons in this process may be either synchrotron photons, originating from the electrons themselves (so-called *Synchrotron Self Compton* (SSC) model [20, 106, 107]) or thermal radiation from the accretion disk (*External Inverse Compton* (EIC) model [47, 48]). The thermal photons could also be scattered by the surrounding gas- and dust clouds beforehand [155]. It is assumed, that the high-energy electrons are produced via shock acceleration in the jet [19, 73].
In hadronic models [103, 102], the γ-rays are produced from high energy protons. The protons of the jet plasma are subject to the same shock acceleration mechanism as the electrons. Due to a larger gyro radius, however, the acceleration of protons is more efficient. Through interaction with ambient soft photons, the high-energy protons produce (amongst others) π^0 mesons, which then decay into $\gamma\gamma$. Thus, the π^0 mesons give rise to electromagnetic cascades with high-energetic electrons, necessary to produce the observed synchrotron radiation. The observation of a correlated neutrino emission would be the 'smoking gun' signal for proton acceleration.

According to [167] possible scales for a $10^8\ M_\odot$ mass black hole are:

- black hole radius: $\sim 3 \cdot 10^{13}$ cm
- radius of the emitting accretion disk: $\sim (1 - 30) \cdot 10^{14}$ cm
- distance of the broad-line clouds: $\sim (2 - 20) \cdot 10^{16}$ cm
- inner radius of the dust torus: $\sim 10^{17}$ cm
- the narrow-line region extends from $\sim 10^{18} - 10^{20}$ cm
- jet scales from $\sim 10^{17} - 10^{24}$ cm

Observational results in favor of mass accretion disks and supermassive black holes are as follows: The width of a certain emission line is mainly determined by the radial velocity

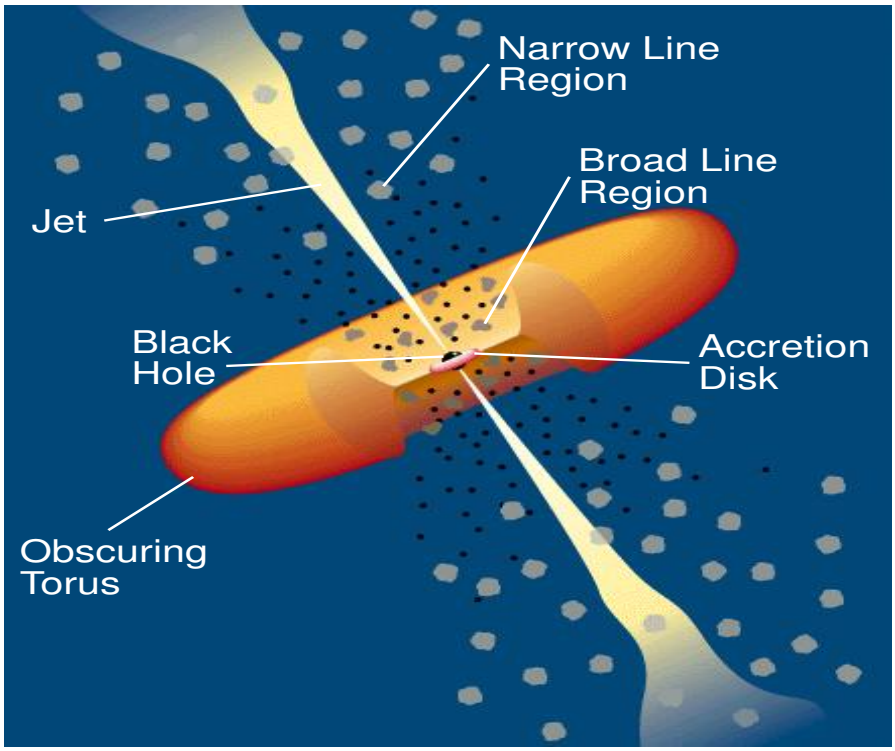

Fig. 2.2.1: Simple model of a radio loud AGN (not to scale). (taken from [167])

of the emitting gas (Doppler broadened emission lines) and the line of sight of the observer. It is therefore possible to derive the radial velocity of the emitting gas as a function of the distance from the central object by means of the observed narrow line widths (so-called spatially resolved kinematics). In the case of the radio galaxy NGC 4261, the obtained velocity profiles could be attributed to the Keplerian motion of ionized gas which, confined in a disk, orbits around a central object of $(4.9 \pm 1.0) \cdot 10^8 M_\odot$ [55]. Furthermore, the *Hubble Space Telescope* (HST) images, published in [55], clearly show a flat dust and gas disk of about 230 pc ($= 7 \cdot 10^{20}$ cm) diameter. In a similar analysis of the LINER NGC 4203 [154] evidence for an accretion disk could be found too. The mass of the central object was constrained to $M \leq 6 \cdot 10^6 \, M_\odot$.

In reverberation mapping [61, 125], another technique, the time delay Δt between brightness variations in the continuum and the broad emission lines is used to estimate the distance r of the line emitting region to the central object ($r \approx c\Delta t$). In combination with the velocity v from the broad emission line widths, the mass of the central object is given as: $M \approx v^2 r/G$ (G is the Gravitational constant). An important advantage of this technique is that it can be applied to far distant AGN, where the limited resolution of the HST prevents spatially resolved kinematics.

Another possibility to infer the mass of the central object is by means of gravitationally redshifted X-ray emission lines (the redshift becomes $z = GM/rc^2$) like in MCG-6-30-15 [163].

Evidence for the supermassive black hole theory is then derived from the small spatial extension of the massive objects, like in the case of the above mentioned NGC 4261. Furthermore, the collimated jets observed in several AGN can only be assigned to an individual object (i.e. no starburst region) and, since the jet orientation does not change over large distances, these objects must be very good gyroscopes.

Unification schemes:

According to Dopita [50], the large variety of AGN can be assigned to 3 parameters: aspect, accretion rate and evolutionary status of the central black hole. These are briefly discussed in the remaining part of the section.

Aspect: In case the line of sight of the observer is close to the torus plane, the *Broad Line Region* (BLR) is obscured by the torus material (fig. 2.2.1). As a result, only the narrow lines of the *Narrow Line Region* (NLR) are visible and the AGN show the characteristics of Sy II galaxies. If the line of sight is closer to the torus axis, the BLR becomes un-obscured and the typical Sy I spectra emerge. This model is further supported by polarization spectra from Sy II galaxies: A small fraction of the observed photon flux comes from broad line emission which is back-scattered from the NLR. This fraction is not visible in the optical spectrum, but it can be detected in the polarization spectrum since the scattered light is polarized. The polarization spectra of Sy II galaxies therefore reveal typical Sy I characteristics.
In the case of a head-on observation of the jet, no emission and/or absorption lines are visible and the observed photon energies, the intensity and the variability time-scales are Doppler boosted due to the beamed emission. The AGN then show the typical blazar features. Observational evidence for the beamed emission is given by the detection of superluminal motion in AGN (e.g. the quasar 3C273 [124]).

Accretion: A possible explanation of the radio-loud, radio-quiet dichotomy can be given by the mass accretion rate onto the central black hole. If the accretion rate into the BLR is highly super-Eddington[4], the supply of gas into the central region might be enough to suppress high-luminosity radio jets. The AGN are then radio-quiet. At sub-Eddington accretion rates, the relativistic jets may escape the nuclear region and the AGN become radio-loud.

Evolution: This parameter is strongly correlated to the accretion rate since super Eddington accretion rates cannot be sustained over long time periods. As a result, the AGN might be radio-quiet in the early phase of the accretion process, but will, as the nuclear accretion rate falls, later become radio-loud. In case some of the AGN are the result of a merger of gas-rich systems, the evolutionary status also affects the shape of the host galaxy. The younger, far distant galaxies may not have had enough time to form spiral galaxies and therefore have elliptical shape.

2.3 The BL Lac object Markarian 501

The elliptical galaxy Mkn 501 (see fig. 2.3.1) appeared at first in a catalog of 1515 strong UV sources, mostly Seyfert or starburst galaxies, put together by the Armenian astronomer B.E. Markarian. The radio counterpart of Mkn 501 was found in 1972 as the radio source B2 1652+39 [35]. In 1975, Mkn 501 was identified as a BL Lac object and the redshift was derived as $z = 0.034$ [166], i.e. the distance to Mkn 501 is roughly 450 million lightyears. Mkn 501 is therefore the 2nd closest known BL Lac object after Mkn 421 ($z = 0.031$). Based on observations with the *High Energy Astronomy Observatory* (HEAO) satellite in the $2 - 6$ keV X-ray band in 1978 [152], Mkn 501 could be identified with the X-ray source 4U 1651+39. In 1984, the results from a *Multi Wavelength* (MWL) campaign, covering radio, optical, UV and X-ray wavebands up to 20 keV already showed that the X-ray emission of Mkn 501 is due to synchrotron, rather than self Compton emission [116]. Using present day naming conventions, this observation classified Mkn 501 as a BL Lac object of the HBL type. The first detection

[4] At the Eddington limit, the radiation pressure on the in-falling matter balances the gravitational force [52].

of Mkn 501 in the few 100 GeV region was announced by the Whipple collaboration in 1995 [133]. One year later, this detection could be confirmed by the HEGRA data in the TeV range [23], based on 147 h of observations. The first report of the detection in the 200 keV to 30 GeV window of EGRET during a MWL campaign in 1996 was given in 1999 [83].

In 1997, Mkn 501 showed an unexpected strong emission of TeV γ-rays lasting from February until October. During that time Mkn 501 was the brightest known TeV γ-ray source and was observed by several groups [2, 3, 10, 49, 70, 134]. The emission was highly variable on short time scales of $\Delta t_{obs} \sim 0.5$ d and also showed evidence for a quasi periodic structure of about 20 day cycle duration. The peak flux was up to 10 times the Crab Nebula flux and the mean flux increased by a factor 10 compared to the 1996 observation of Mkn 501. The energy spectrum of Mkn 501 extended at least up to 16 TeV [4] and, as several groups also found, followed a power law with evidence for an exponential cutoff.
Increased emission from Mkn 501 was also detected by several satellite-borne experiments, e.g. BeppoSAX at $0.2-200$ keV [128], the *Oriented Scintillation Spectrometer Experiment* (OSSE) at $0.05-10$ MeV [30] and the All Sky Monitor (ASM) at $2-10$ keV [30]. The synchrotron peak of Mkn 501 was found at ~ 100 keV, thus being shifted up by ~ 2 orders of magnitude compared to 1996 (see fig. 2.3.2).
Significant correlation between the X-ray and γ-ray emission has been found on short timescales of $\mathcal{O}$ (1 d) [30, 62] and long timescales of $\mathcal{O}$ (100 d) [2, 3, 128].

In the following years, Mkn 501 was again in a quiescent state of about 1/3 the Crab Nebula flux ([1], see also fig. 1.0.1) while showing some sporadic flares.

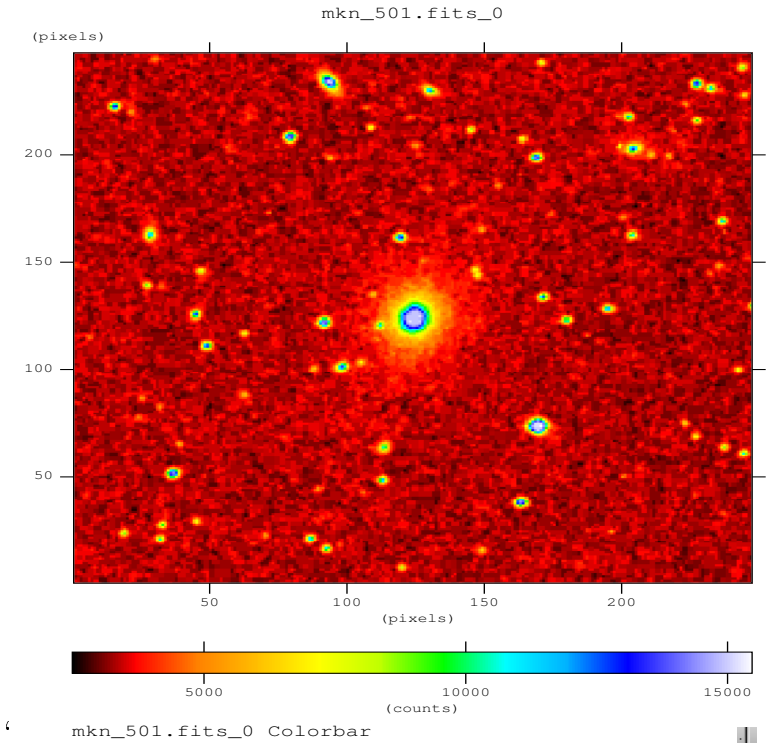

Fig. 2.3.1: Image of Mkn 501 taken with the Palomar 48-inch Schmidt telescope. The covered sky region is about $7.2'$x$7.2'$ (Based on photographic data of the National Geographic Society – Palomar Observatory Sky Survey (NGS-POSS) obtained using the Oschin Telescope on Palomar Mountain. The NGS-POSS was funded by a grant from the National Geographic Society to the California Institute of Technology. The plates were processed into the present compressed digital form with their permission. The Digitized Sky Survey was produced at the Space Telescope Science Institute under US Government grant NAG W-2166. Copyright (c) 1994, Association of Universities for Research in Astronomy, Inc. All rights reserved).

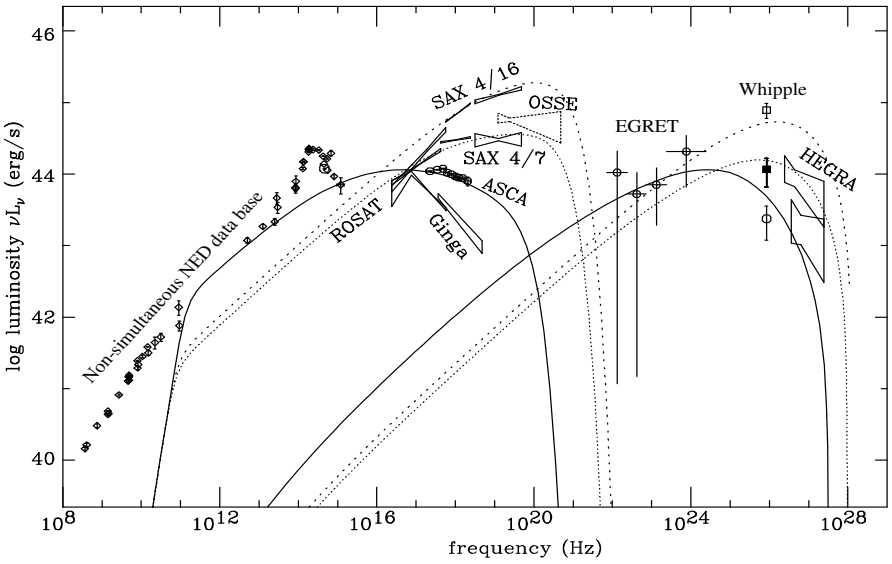

Fig. 2.3.2: Spectral energy distribution of Mkn 501 as obtained with several instruments during 1996 and 1997. The solid line denotes a SSC model fit to the spectrum in March 1996, the dotted line to April 7 and the dashed line to the spectrum on 16 April 1997. (taken from [83])

3. DESCRIPTION OF THE HEGRA DETECTOR AND THE RXTE SATELLITE

3.1 The HEGRA detector

Originally, the experiment was proposed by the Institut für Kernphysik of the University of Kiel and built as a small scintillator array in 1988 on the Canary Island La Palma (28.75° N, 17.89°W). Gradually more institutes joined and the detector enlarged. At present the HEGRA collaboration consists of seven Institutes: University of Hamburg, Max-Planck-Institut für Kernphysik in Heidelberg, University of Kiel, University of Madrid, Max-Planck-Institut für Physik in Munich, University of Wuppertal and the Yerevan Physics Institute. The HEGRA experiment is located at the site of the Observatorio del Roque de los Muchachos at about 2200 m above sea level. In its 1997 setup, the experiment consisted of 17 Geiger counters, 244 scintillator counters, 77 wide angle Cherenkov counters and 6 Cherenkov telescopes (see fig. 3.1.1). Only observations with the Cherenkov telescopes have been used for this thesis.

The first Cherenkov telescope of the HEGRA collaboration, CT1 (see fig. 3.1.2), was installed in 1992. It comprised an equatorial mount, a 5 m^2 segmented mirror and a fast imaging 37 pixel[1] camera with $\sim 3°$ *Field Of View* (FOV) [112]. The camera was replaced by a high resolution 127 pixel camera ($\sim 3°$ FOV) in December 1994 [139]. CT1 was operated in this configuration until November 1997, when it was upgraded to $\sim 10\,m^2$ all-aluminum mirrors. This represents the present set-up. In 1997, the threshold energy of CT1 was ~ 1.2 TeV. CT1 is operated as a stand-alone telescope.
The second HEGRA Cherenkov telescope, CT2, was installed in 1993. In contrast to CT1, CT2 has an alt-azimuth mount and is equipped with a 8.5 m^2 segmented mirror. Originally, the CT2 camera comprised 61 pixels with $\sim 3.7°$ FOV, but was replaced by a high resolution 271 pixel camera ($\sim 4.9°$ FOV) in 1998. CT2 was operated as a stand alone telescope until 1998, when it was included into the CT-system. In 1997, the threshold energy of CT2 was ~ 1.0 TeV.
The Cherenkov telescope system (CT-system) denotes the set of 4 (5 after the incorporation of CT2) identical telescopes which are operated in the so-called stereoscopic mode. Here, all telescopes are pointed towards the same object and thus several images of an EAS are observed simultaneously. This leads to an improved γ- hadron separation, a more precise reconstruction of the shower direction and position, and an improved energy reconstruction. The first telescope of the CT-system, CT3, was installed in October 1995. CT4, CT5 and CT6 were successively installed until the end of 1996. All telescopes of the CT-system have an alt-azimuth mount, a 8.5 m^2 segmented mirror and a high resolution 271 pixel camera ($\sim 4.9°$ FOV). The threshold energy of the CT-system is ~ 500 GeV.

Only the 1997 Mkn 501 data taken with CT1 have been reanalyzed for this thesis. The results from the other Cherenkov telescopes, i.e. CT2 and the CT-system were taken as published in [3] and [2]. These detectors are therefore not described any further and the

[1] A pixel consists of a light concentrator, PMT and preamplifier.

reader is referred to [126] and [41] instead.

The Cherenkov telescope CT1

CT1 is sometimes referred to as 'prototype telescope', since it was also used to gain experience for the design of the 2nd generation HEGRA Cherenkov telescopes (CT2-CT6). In contrast to most other Cherenkov telescopes it is equipped with an equatorial mount, i.e. one axis points towards the celestial pole and the other axis is perpendicular to the first axis, i.e. lies within a plane parallel to the earth equator. Advantages of the equatorial mount are:

- Simplified steering: in principle only one axis has to be rotated with constant speed during tracking, thus avoiding the problems with mechanical resonances (this is not an issue with present day motor drives anymore). Small corrections of the polar axis are necessary if the axis is not perfectly aligned with the celestial pole.

- No FOV rotation: the camera does not rotate with respect to the sky during observations. Bright stars therefore always stay in the same pixel or group of pixels.

A drawback of this type of mount is that heavy counterweights are needed to balance the mirror dish and that it has restrictions in the accessible angular range. This requires a very stable and therefore expensive construction. All new generation Cherenkov telescopes are designed with alt-azimuth mounts.
In its 1997 set-up, CT1 was equipped with a 5 m^2 reflector consisting of 18 circular mirrors with 60 cm diameter each. An individual mirror consisted of a borosilicate glass disc of 2 cm thickness coated with a 0.4 μm aluminum layer. A second layer of about 1 μm of SiO_2 served as weather protection [112]. The focal length of the individual spherical mirrors is $\approx$ 490 cm (6 central mirrors), $\approx$ 492 cm (6 adjacent mirrors) and $\approx$ 494 cm for the 6 mirrors at the edges of the mirror dish. This configuration was chosen in order to approach the optimum shape for the reflector [111].

The camera of CT1 consists of 127 10-stage EMI-9083A PMTs equipped with so-called Winston cones, which serve as light concentrators and, furthermore, protect the camera PMTs from large angle stray light. The PMTs are operated at medium gain with 8 stages and are coupled to fast preamplifiers (10 fold amplification) to compensate for the reduced gain. Thus, large and damaging anode currents in the PMTs (e.g. due to bright stars) can be avoided. This set-up is essential for the extended observations during moonshine, carried out with CT1 in 1997 (see sec. 5.1.4). The signal from the preamplifiers is fed into RG 58 cables and transferred to the readout electronics. In order to separate the intense, short light flash of an air shower from the Poisson distributed noise of the *Night Sky Light Background* (NSB), an event trigger is then applied. The trigger condition requires that within 13 ns any 2 out of 127 pixels must show a signal above 50 mV (this corresponds to about 13 photoelectrons). In that case, the digitized signals of all PMTs[2], the precise orientation of the telescope and the time information, supplied by a rubidium clock, are recorded. The trigger rate also depends on the high voltage of the PMTs, the NSB, the atmospheric conditions, the zenith angle of the observation and on telescope parameters like the mirror area and the FOV of the camera. The trigger rate for CT1 is about 1.7 Hz at 0° zenith angle. The CT1 camera and the readout electronics is described in detail in [139].
The main parameters of CT1 in its 1997 configuration are summarized in table 3.1.1.

[2] Le Croy #2249A *Analog to Digital Converters* (ADCs) are used to produce the digitized signals.

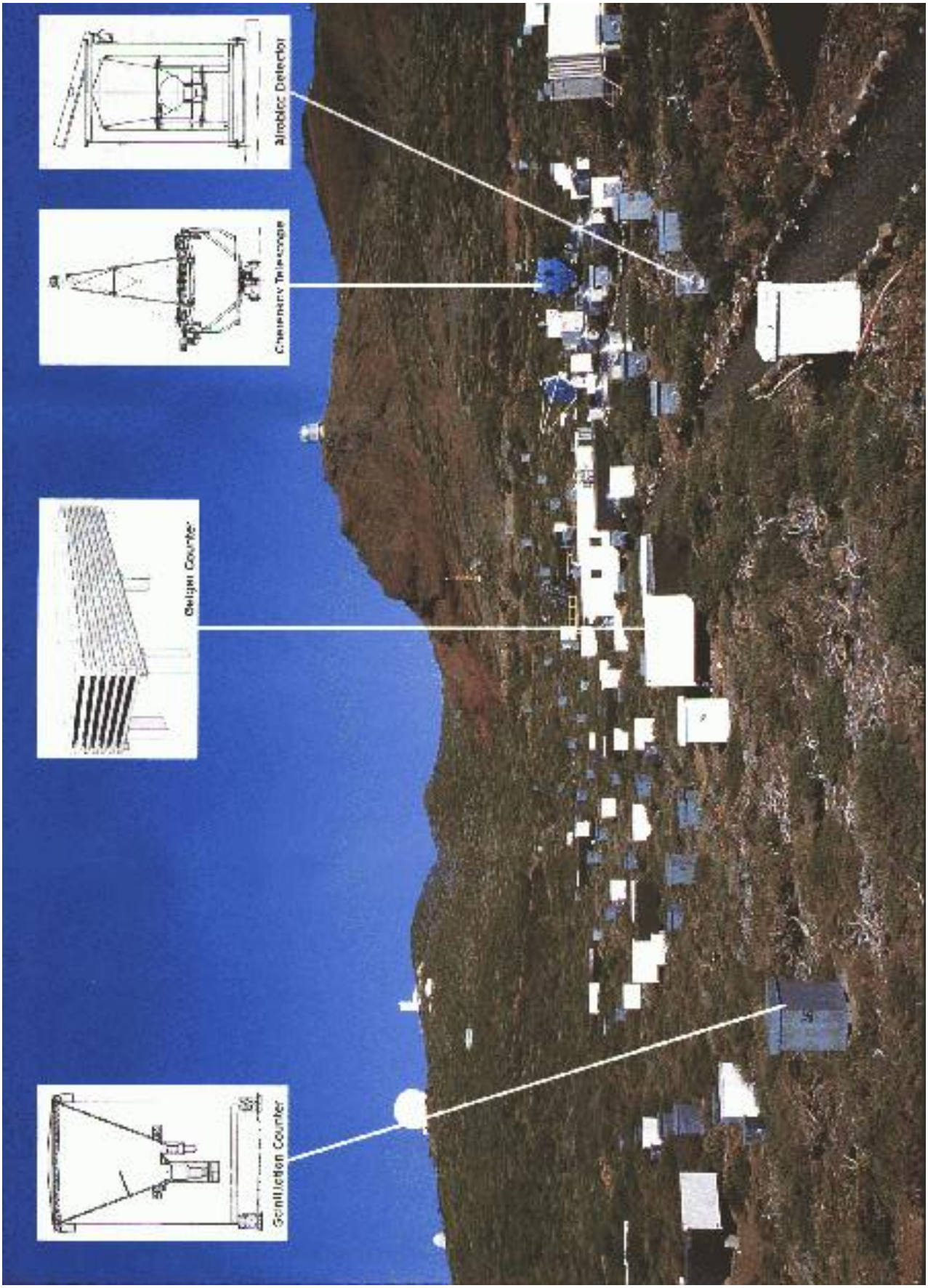

Fig. 3.1.1: The HEGRA experiment on the Canary Island La Palma.

Fig. 3.1.2: Image of the first HEGRA Cherenkov telescope CT1.

energy threshold	~ 1.2 TeV
trigger rate ($\theta = 0°$)	1.7 Hz
effective collection area	$\approx 10^4$ m^2 at $E = 1.2$ TeV
f/d	1.7
mount	
type	equatorial
tracking error	0.03°
pointing error	$< 0.13°$
mirror	
shape	spherical
material	aluminized glas, SiO_2 coating
diameter	60 cm
number of mirror segments	18
mirror area	5 m^2
focal length	492 ± 4 cm
angular resolution	$20 - 40$ arcsec
reflectivity	$\geq 84\%$ ($300\,\text{nm} \leq \lambda \leq 600\,\text{nm}$)
camera	
field of view	3.0°
number of pixels	127
PMT type	EMI-9083A (10-stage)
quantum efficiency	26% (375 nm)
light cone	hollow Winston cones
pixel diameter	0.25° ($\widehat{=}$21 mm)
calibration	337 nm N_2-laser (3 ns pulse width) + optical fibre +NE-111 szintillator
trigger	
trigger condition	$2/127 \geq 50$ mV in 13 ns
ADC-gate width	30 ns
dead time	2.5 ms

Tab. 3.1.1: The main parameters of the HEGRA Cherenkov telescope CT1 (1997 set-up).

	Detector	collecton area (cm^2)	energy range (keV)	FOV (FWHM)	Time resolution	Sensitivity (mCrab)
PCA	5 Xenon Prop. counters	6250	$2-60$	1°x1°	$\sim 1\,\mu$s	0.1 (10 min)
HEXTE	4 NaI/CsI (2 clusters)	1600	$15-250$	1°x1°	$8\,\mu$s	1 (10^5 s)
ASM	PSPC+Mask	90	$2-12$	3′x15′	1.5 h	30 (1.5 h)

Tab. 3.2.1: Technical characteristics of the experiments on board the RXTE satellite.

3.2 The RXTE satellite

The RXTE satellite [24], launched on December 30 in 1995, was designed to probe cosmic X-ray sources on variability time scales in the range of milliseconds to years. There are three distinct experiments on board the RXTE satellite (fig. 3.2.1), covering an energy range from $2-250$ keV:

- *Proportional Counter Array* (PCA): The PCA consists of five xenon gas proportional counters with a large collecting area of about 6200 cm^2. It is sensitive to X-rays in the energy range from $2-60$ keV and measures short-term variability down to the microsecond level.

- *High-Energy X-ray Timing Experiment* (HEXTE): The HEXTE consists of two independent clusters of 4 NaI/CsI phoswich scintillation detectors. The covered energy range is $15-250$ keV and the time resolution is again at the microsecond level.

- *All Sky Monitor* (ASM): The ASM consists of three *Scanning Shadow Cameras* (SSCs) and covers the energy range from $2-12$ keV. Each SSC is equipped with a one dimensional slit mask and *Position Sensitive Proportional Counters* (PSPC), filled with xenon (see fig. 3.2.2 a). Each X-ray source within the FOV produces a characteristic profile in the PSPC (fig. 3.2.2 b), which can be used to infer the direction and intensity of the source. In practice, the measured PSPC signal is a superposition of X-ray profiles from several X-ray sources. The contribution (i.e. intensity) of known X-ray sources to the PSPC signal is then inferred from a master catalog containing the shadow patterns of these sources. The residuals are examined for additional sources [96]. The ASM scans $\sim 80\%$ of the sky every 1.5 h and is used to measures long-term variability (hours to months) of bright X-ray sources.
  Only the data from the ASM has been used for this thesis.

Technical characteristics of the three experiments are summarized in tab. 3.2.1. For a complete description of HEXTE and ASM see [68] and [96].

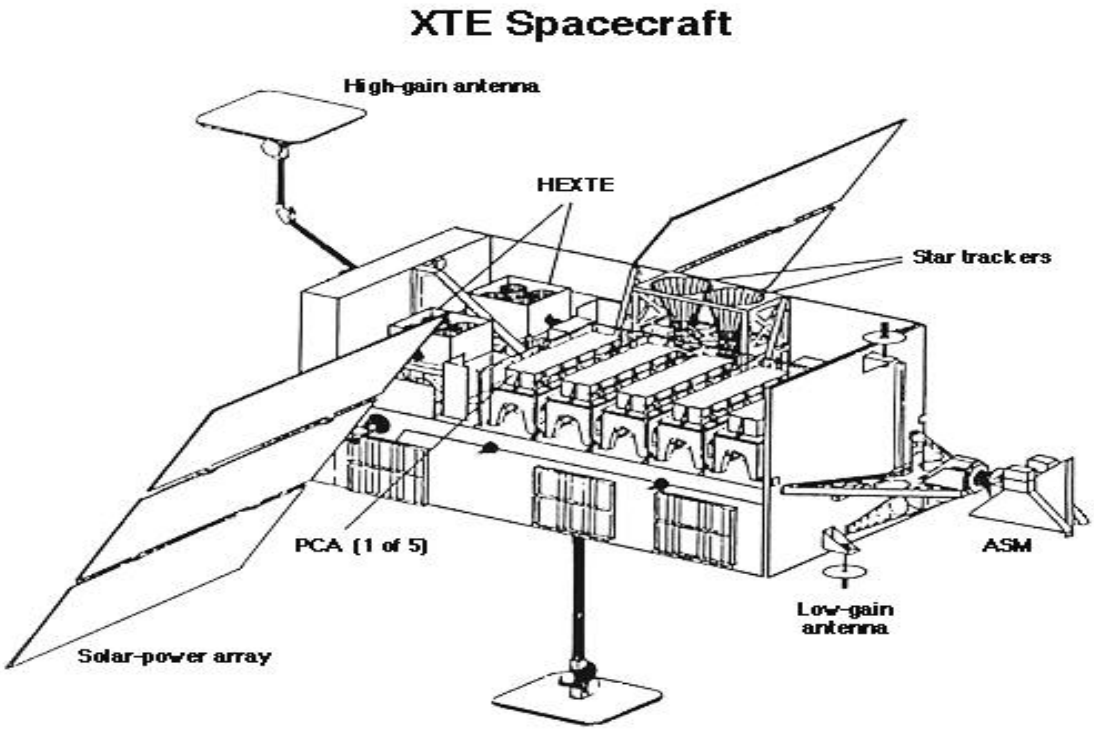

Fig. 3.2.1: The RXTE spacecraft.

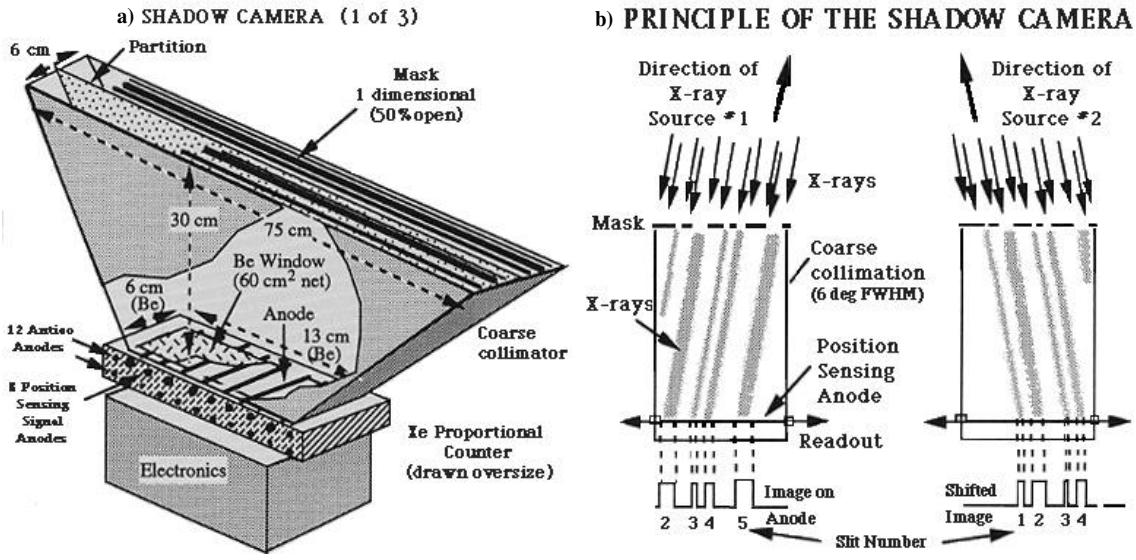

Fig. 3.2.2: a) Schematic diagram of a shadow camera. The major components are shown. b) The basic principle of the shadow camera.

4. THE IMAGING TECHNIQUE

One of the main problems in γ-ray astronomy is the small proportion of γ-rays to charged CR. Since less than 0.01% of the energetic CR are γ-rays, an efficient γ-hadron separation becomes a crucial point. Satellite-borne detectors achieve an efficient γ-hadron separation by using anti-coincidence counters, but these detectors are restricted to low energies (≤ 20 GeV) and high γ-fluxes due to the limited detection area[1]. At present, the only method to investigate the energy range above 20 GeV is by means of earth-bound detectors which observe γ-ray induced EAS. The effective collection area for these detectors is $\mathcal{O}(10^4)$ m^2, but since all particles of the CR produce EAS, the γ-hadron separation has to be carried out by detecting specific EAS structures. So far, the most efficient method to discriminate between γ- and hadron-induced EAS is the so called *Imaging Technique* (IT). In this technique, the short flash of Cherenkov light produced by an EAS is recorded with an ACT. Since differences in the shower development of γ- and hadron-induced EAS show up in the recorded images, it is possible to discriminate up to a certain level between γs and the charged (hadronic) CR.

At first, an efficient γ-hadron separation on the basis of the image analysis is absolutely crucial for ground based γ-astronomy. Therefore the basic principles and some improvement ideas will be discussed here. The first section describes the basic processes involved in EAS and Cherenkov light production and the main differences between γ- and hadron-induced EAS are discussed. The second part describes the procedure to record the Cherenkov light flashes from EAS, the parameters used to characterize the recorded images and the selection criteria based on these image parameters.

4.1 Characteristics of the atmosphere for Extended Air Shower production

If a particle of the CR approaches the earth, it interacts with the nuclei of the atmosphere molecules between typically 20-25 km height. As a result, several secondary particles are produced, which again interact with the atmosphere. That way, the number of secondary particles grows rapidly and an EAS evolves. Since the energy of the primary particle is distributed over all secondary particles, at some stage the energy of the secondary particles is too small to produce further particles. Energy losses due to ionization processes then become dominant and the shower dies out.
This evolution is described in detail here. Special attention is put on the production of Cherenkov light during the shower development and the differences between γ- and hadron-induced EAS.

4.1.1 The basic processes in the shower development

a) γ-induced air showers:

There are three main processes in the development of γ-ray showers:

[1] Typical integral fluxes in the TeV-range are of the order 10^{-11} cm^{-2}s^{-1}.With an effective detector area of 10^3 cm^2 (EGRET) it would therefore take $\sim$ 1200 days to observe one TeV-photon at this flux level.

- **pair production:** $\gamma \rightarrow e^+ + e^-$: The photon is transformed into an electron-positron pair[2] in the strong Coulomb field of a nucleus. The **interaction length** or **mean free path** for pair production in air is $X_p = 47.2\ \mathrm{g/cm^2}$.

- **Bremsstrahlung:** The radiation produced by a charged particle in the Coulomb field of a nucleus or ion.

- **photoproduction**: γ+nucle*us* $\rightarrow$ hadrons: Hadronic states, mostly pions, are produced here.

The cross section for photoproduction increases with increasing photon energy, but is only $1-2\,\mathrm{mb}$ for $0.1-20\,\mathrm{TeV}$ photons [94]. This is about 300 times smaller than the cross section for pair production ($\sigma^{air}_{\gamma\rightarrow e^+e^-} = 520\,\mathrm{mb}$). If the first interaction of the incident photon is due to the photoproduction process, the resulting shower cannot be distinguished from a hadron-induced air shower. Throughout this thesis the term "γ-induced air shower" is used only for EAS formed by an initial pair production process.
The electrons and positrons from the pair production process further interact with the air molecules by emitting Bremsstrahlung. The **radiation length** of air, i.e. the path length after which the electron energy decreased by a factor e due to Bremsstrahlung is $X_0 = \frac{7}{9}X_p = 36.7\,\mathrm{g/cm^2}$ [165]. The Bremsstrahlung photons again produce electron-positron pairs and thus an avalanche of charged particles, i.e. an EAS evolves. The mean electron[3] and photon energy decreases as the shower development proceeds (and the number of particles increases). Below the *critical energy* E_c ($E_c \approx 83\,\mathrm{MeV}$ for e^- in air [58, p. 55]) ionization of the air molecules becomes the dominant process for electrons to loose their energy. Below a few MeV, Compton scattering becomes dominant for photons. As a result, less particles are produced and the shower dies out.

A γ-induced air shower therefore consists of a cascade of high energy electrons, positrons and secondary γ-rays, eventually with a small admixture of hadrons (and their decay products) created in photoproduction processes of secondary photons. All particles are strongly collimated along the incident direction due to their relativistic energies. The main process that broadens the shower transversely is multiple scattering and, in second order, the deflection by the earth magnetic field. Most electrons and positrons have velocities close to the speed of light, thus giving rise to Cherenkov light emission (see sec. 4.1.2). The total fraction of the primary energy, converted into Cherenkov light is $\sim 10^{-4}$.

The longitudinal and lateral[4] electron distribution for γ-ray showers can be described by theoretical models. The number of electrons N_e above the critical Energy E_c as a function of the slant depth X[5] and the primary energy was calculated by Greisen [64]:

$$N_e\left(t, E\right) = \frac{0.31}{\sqrt{\ln\left(E/E_c\right)}} \exp\left[t\left(1 - 1.5\ln s\right)\right] \tag{4.1.1}$$

[2] Production of muon-antimuon pairs can be ignored due to the high muon mass of 106 MeV ($\sigma^{air}_{\gamma\rightarrow\mu^+\mu^-} = 12\,\mu\mathrm{b}$).

[3] The term 'electron' is used synonymously for electrons and positrons.

[4] With respect to the shower axis which is defined by the direction of the primary particle.

[5] The slant depth X determines the thickness of the atmosphere along the shower axis. For vertical showers we have $X = X_v$ (with the atmospheric depth $X_v = \int_h^\infty \rho_{air}\left(h\right)\mathrm{d}h$, $[\mathrm{g/cm^2}]$).

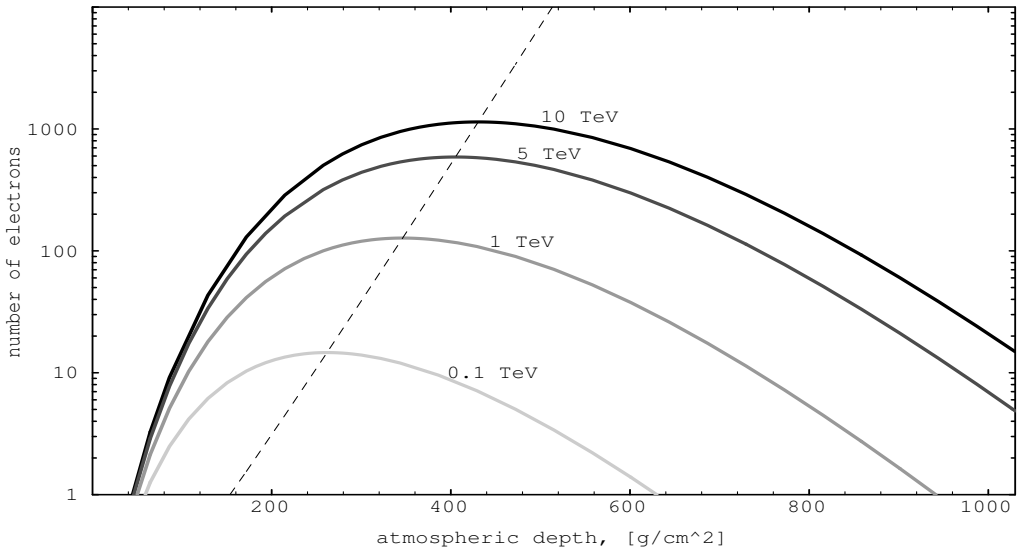

Fig. 4.1.1: The number of electrons above the critical energy E_c as a function of the atmospheric depth for vertical γ-ray showers of different energy. The dashed line marks the position of the shower maxima ($s = 1$).

E : energy of the primary photon
t : slant depth in units of X_0; ($t = X/X_0$)
E_c : critical energy
s : shower age, defined by $s\,(t, E) = 3t/\,(t + 2\ln\,(E/E_c))$, dimensionless

The meaning of the shower age s is explained by the derivative:

$$\frac{\mathrm{d}N_e\,(t, E)}{\mathrm{d}s} = N_e\,(t, E) \cdot \frac{3\ln\,(E/E_c)\,(s - 3\ln s - 1)}{(3 - s)^2} \tag{4.1.2}$$

For $0 < s < 1$ the electron number N_e increases with s ($\mathrm{d}N_e/\mathrm{d}s > 0$) and the shower evolves. At $s = 1$, the number of electrons reaches its maximum ($\mathrm{d}N_e/\mathrm{d}s = 0$) and then decreases with increasing s ($\mathrm{d}N_e/\mathrm{d}s < 0$). According to the definition of the shower age s, the depth of the shower maximum only depends on the primary energy: $t_{max} = \ln\,(E/E_c)$. Figure 4.1.1 shows the longitudinal electron distribution (according to eq. 4.1.1) for vertical γ-ray showers of different primary energy. The shower maximum lies deeper in the atmosphere when the shower energy increases, but even for a 10 TeV shower the maximum is still at ≈ 6.8km height. The number of electrons reaching the detector level ($\sim 780\,\mathrm{g/cm^2}$ for La Palma) is therefore much less than the number of electrons at the shower maximum.
The lateral distribution of electrons can be modeled by the NKG-formula which was derived by **N**ishimura and **K**amata [119] and modified by **G**reisen [65]. The NKG-formula describes the electron density as a function of the distance r from the shower axis. It is strictly valid for a shower age $1 \leq s \leq 1.4$ and is defined as:

$$\rho_e\,(r, t, E) = \frac{\Gamma\,(4.5 - s)}{2\pi\Gamma\,(s)\,\Gamma\,(4.5 - 2s)} \frac{N_e\,(t, E)}{r_0^2} \left(\frac{r}{r_0}\right)^{s-2} \left(1 + \frac{r}{r_0}\right)^{s-4.5} \tag{4.1.3}$$

r_0 : Moliére radius ($r_0 = 79$ m at sea level)
s : shower age
N_e : electron number (see equ. 4.1.1)
Γ : Gamma function

In order to put eq. 4.1.3 in agreement with Monte Carlo simulations, the Moliere radius r_0 has to be reduced by a factor 2 [54].

b) hadron-induced air showers:

When a high energy proton (or heavier nucleus) interacts with the nucleus of an air molecule, it creates a large number of secondary particles[6]. About 90% of these particles are pions, 10% kaons and antiprotons. The mean transverse momentum of the secondary particles is of the order $0.3\,\mathrm{GeV}/c$ [58, p. 396] and in first order independent of the proton energy.
The secondary hadrons again interact with the atmosphere, thus giving rise to a particle cascade, or, in case of mesons, they can decay (mainly into μs). At particle energies below $\sim 1\,\mathrm{GeV}$ ($\approx$the threshold for pion production), ionization processes become dominant and the hadronic particles are brought eventually to rest. The mean interaction length for hadrons in air is [60]:

$$\begin{aligned} \lambda_p^{air}\,(1\,\mathrm{TeV}) &= 83\,\mathrm{g/cm^2} \\ \lambda_\pi^{air}\,(1\,\mathrm{TeV}) &= 107\,\mathrm{g/cm^2} \\ \lambda_K^{air}\,(0.1\,\mathrm{TeV}) &= 138\,\mathrm{g/cm^2} \end{aligned}$$

and the average *Center Of Mass* (CM) lifetime [58, p. 585ff]:

hadron	average CM lifetime	decay channel	branching ratio
π^+	$2.6 \cdot 10^{-8}\,\mathrm{s}$	$\pi^+ \to \mu^+ + \nu_\mu$	100%
π^0	$0.83 \cdot 10^{-16}\,\mathrm{s}$	$\pi^0 \to \gamma + \gamma$	98.9%
K^+	$1.24 \cdot 10^{-8}\,\mathrm{s}$	$K^+ \to \mu^+ + \nu_\mu$	63.5%
		$K^+ \to \pi^+ + \pi^0$	21.2%

Depending on the γ-factor of the particle the decay time in the laboratory frame is much larger than the CM decay time, but even for π^0-energies of $E \sim 100\,\mathrm{GeV}$ it is still only $\tau \sim 0.6 \cdot 10^{-13}$s (corresponding to a flight path of $2 \cdot 10^{-3}$ cm). Therefore all π^0-mesons decay immediately into photons before any hadronic interaction can take place. The energetic photons then create electromagnetic sub-showers. Since π^0-mesons carry about 30% of the energy from each hadronic interaction, this process transfers energy from the hadronic to the electromagnetic part of the shower. In a cascade of multiple hadronic interactions eventually a large fraction of the primary energy is transformed into the electromagnetic shower component[7].
In the beginning of the shower evolution the charged pions and kaons have a high enough Lorentz factor, such that interactions are more likely than decays. With increased shower age more and more secondary mesons decay into muons and neutrinos[8]. Due to their long lifetime ($\tau \approx 2.2 \cdot 10^{-6}$s) and the small interaction cross section, most of the muons are able to reach the ground. Together with the neutrinos these muons remove part of the shower energy from the atmosphere. Low energy muons may decay into electrons ($\mu^+ \to e^+ \overline{\nu}_\mu \nu_e$) thus also releasing a fraction of their energy into electromagnetic sub-showers.

A proton-induced air shower therefore consists of three components: A hadronic core built up from high energy nucleons and mesons, a set of electromagnetic sub-showers mainly

[6] The mean multiplicity of charged secondary particles is: $\langle n_{ch} \rangle \approx 1.97 \cdot (E_{lab}/\mathrm{GeV})^{0.25}$ [28]. For a 1 TeV proton therefore $\langle n_{ch} \rangle \approx 11$.

[7] According to Monte Carlo simulations [74] $\sim 60\%$ of the total shower energy (for 1 TeV proton showers) is transfered into the electromagnetic component.

[8] The decay channels $\pi^+ \to e^+ + \nu_e$ and $K^+ \to e^+ + \nu_e$ are strongly suppressed due to helicity conservation [129, 151, p. 25ff].

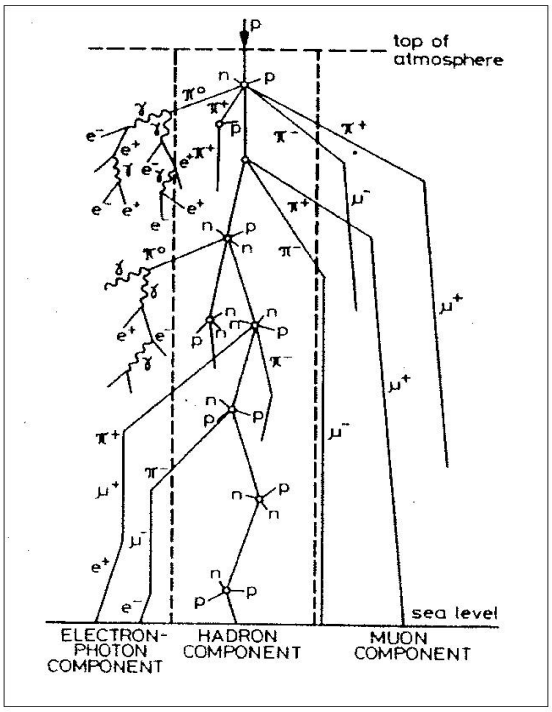

Fig. 4.1.2: Scheme of interaction processes taking place in the development of EAS (taken from [9]).

originating from the π^0-decays, and a fraction of basically noninteracting muons and neutrinos (see Fig. 4.1.2). Due to the significant transverse momentum transfer in hadronic interactions, the hadronic showers are substantially broader than pure electromagnetic showers.

4.1.2 Origin of Cherenkov-light in the atmosphere

A charged particle passing through matter loses energy due to Coulomb interaction with the electrons of the matter. In general this energy is absorbed in the vicinity of the particle track, but if the particle velocity is high enough, part of the energy is emitted as radiation and, in case of materials of high optical transmissivity, might escape from the matter. This radiation is called Cherenkov light (or Cherenkov radiation) and was discovered by P.A. Cherenkov in 1934 [34]. The theoretical explanation was given by Frank and Tamm in 1937 [57].
The minimum velocity required for emission of Cherenkov light with angular frequency ω depends on the refractive index of the material for the frequency ω. It can be calculated according to [80, p. 764]:

$$v > \frac{c}{\sqrt{\varepsilon\,(\omega)}} = \frac{c}{n\,(\omega)} \;(\text{for } \mu = 1) \tag{4.1.4}$$

v : particle velocity
c : velocity of light in vacuum
ε : dielectric constant
ω : angular frequency of emitted radiation
μ : magnetic permeability ($\mu_{air} \approx 1$)
n : refractive index ($n = \sqrt{\varepsilon\mu}$)

Other characteristics of the Cherenkov light are its linear polarization and the angle θ_c between

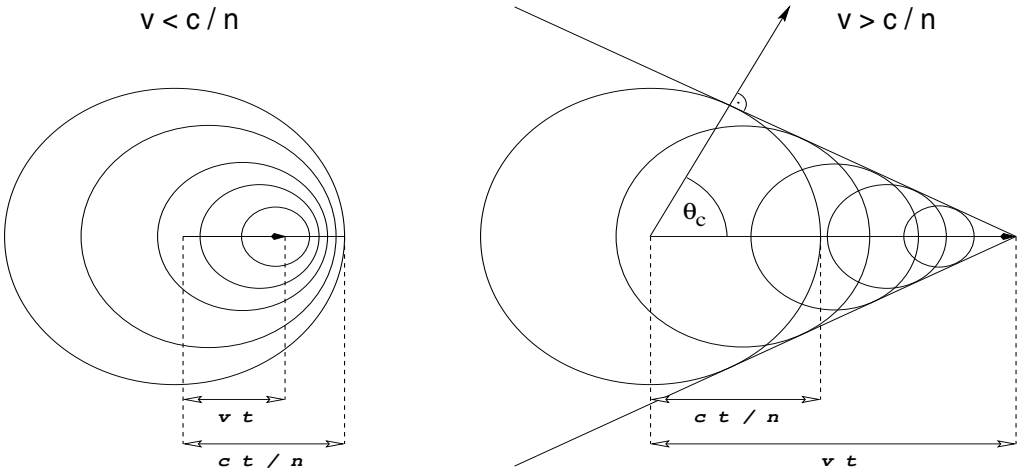

Fig. 4.1.3: Propagation of Cherenkov light derived from Huygens' principle. Constructive interference of the spherical waves is achieved if the particle velocity $v > c/n$. The resulting cone-shaped wavefront propagates at an angle $\cos\theta_c = 1/(\beta n)$ relative to the particle track. (adapted from [80, p. 766])

the particle velocity vector and the emission direction. The **Cherenkov angle** θ_c is defined by the equation (see also fig. 4.1.3):

$$\cos\theta_c = \frac{1}{\beta\sqrt{\varepsilon\,(\omega)}} = \frac{1}{\beta \cdot n}, \quad \text{with } \beta = v/c \tag{4.1.5}$$

Qualitatively, the emission of Cherenkov light can be described by the superposition of spherical waves using Huygen's principle. Under the assumption that spherical waves emerge from each point of the particle track, constructive interference only takes place if $v > c/n$ (see fig. 4.1.3). The resulting cone-shaped wavefront is similar to the shock wave produced by a jet flying at supersonic speed. Equation 4.1.5 also restricts the frequency range where Cherenkov light is emitted. For particle velocities $\beta \simeq 1$ this frequency range is determined by $n\,(\omega) > 1$. The energy $\mathrm{d}E$ radiated by a particle with charge e per track length $\mathrm{d}h$ can be calculated according to [81][9]:

$$\frac{\mathrm{d}E}{\mathrm{d}h} = \frac{e^2}{c^2}\int_{\beta n>1}\left(1 - \frac{1}{\beta^2 n^2}\right)\omega \mathrm{d}\omega \tag{4.1.6}$$

The integrand defines the differential frequency spectrum for Cherenkov light emission[10].

Some important features of Cherenkov light emission in EAS can be derived from eq. 4.1.4 to 4.1.6:

a) The threshold energy for a charged particle of rest mass m_0 to emit Cherenkov light is:

$$E_{th} = \frac{m_0 c^2}{\sqrt{1 - 1/n^2}} \tag{4.1.7}$$

Using an approximation for the refractive index as a function of the atmospheric depth [137][11]

[9] Equation 4.1.6 and all equations deduced thereof are given in CGS units.

[10] Note that the observed Cherenkov photon spectrum differs considerably from the produced spectrum due to the transmission characteristics of the atmosphere (e.g. Ozone absorption, see sec. 4.1.4).

[11] The frequency dependence (dispersion) of the refraction index in air is small for wavelengths between 300 nm - 600 nm. The variations for $1 - n$ are 5% there (U.S. standard atmosphere at 1013.25 hPa, 15° C, [39]).

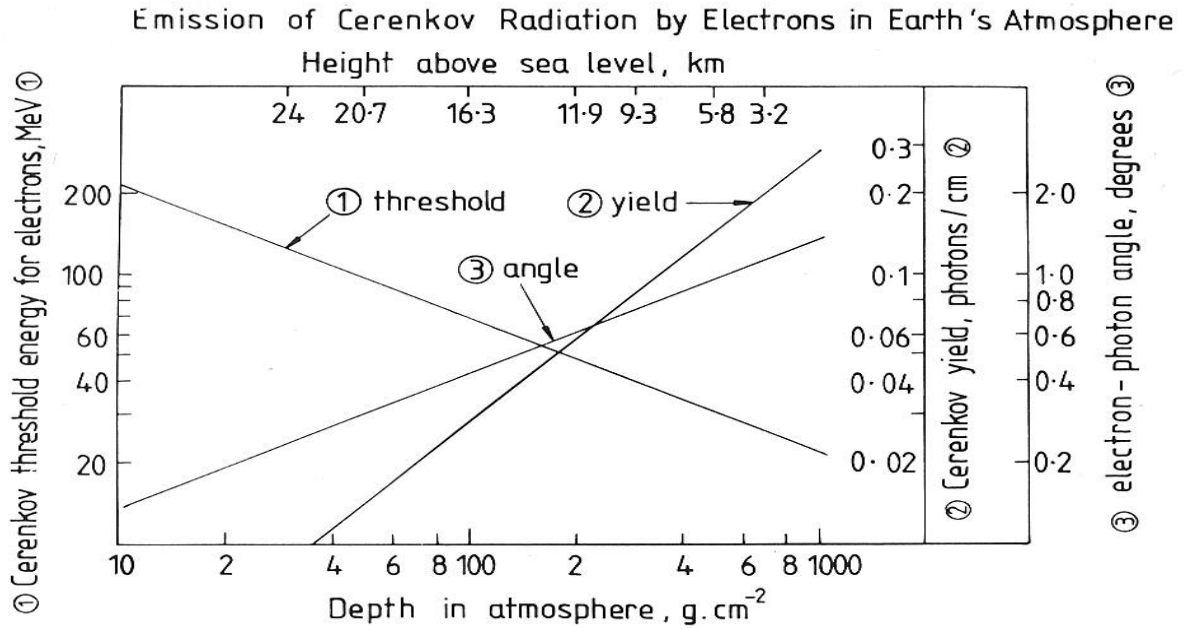

Fig. 4.1.4: Dependence of some properties of Cherenkov radiation on the atmospheric depth. (1) is the threshold energy for electrons to emit Cherenkov light, (2) is the intensity of Cherenkov radiation and (3) is the Cherenkov angle θ_c (taken from [135, p. 176]).

$$n\left(X_v\right) = 1 + \eta := 1 + \frac{0.0002926 X_\nu}{1030\,\mathrm{g/cm^2}} \cdot \frac{273.2\,\mathrm{K}}{T\left(\mathrm{X}_v\right)} \tag{4.1.8}$$

$X_v = \int_h^\infty \rho\left(h\right) \mathrm{d}h\,\mathrm{g/cm^2}$: atmospheric depth for height h and air density ρ
$T = \left(204 + 0.091 \cdot \frac{X_v}{\mathrm{g/cm^2}}\right)\,\mathrm{K}$: air temperature at depth X_v

the threshold energy for Cherenkov light emission can be written as $E_{th} \approx m_0 c^2/\sqrt{2\eta}$. At sea level the threshold energy becomes $E_{th} = 4.6\,\mathrm{GeV}$ for muons, $E_{th} = 40\,\mathrm{GeV}$ for protons and $E_{th} = 22\,\mathrm{MeV}$ for electrons. The main fraction of Cherenkov light produced within EAS therefore originates from electrons. The threshold energy for electrons as a function of the atmospheric depth is shown in fig. 4.1.4. Due to the decreasing refractive index with height, the energy threshold becomes rather high in the upper atmosphere. The higher threshold at high altitudes does practically not affect the fraction of Cherenkov light emitting electrons since in the early phase of the shower development the mean momentum of the electrons is significantly higher than in the tail. The small number of electrons at large heights, however, only produce a small amount of Cherenkov light. The most relevant region for Cherenkov light production is therefore the atmospheric depth range between $100\,\mathrm{g/cm^2}$ and $400\,\mathrm{g/cm^2}$, i.e. where the shower maxima lie.

b) Dependence of the Cherenkov angle on the atmospheric depth:

Since the refractive index of air is close to 1, eq. 4.1.4 implies that all Cherenkov light emitting electrons must have β close to 1. The Cherenkov angle for $\beta = 1$ becomes (eq. 4.1.5):

$$\theta_c = \arccos\left(1/n\right) \approx \sqrt{2\eta} \tag{4.1.9}$$

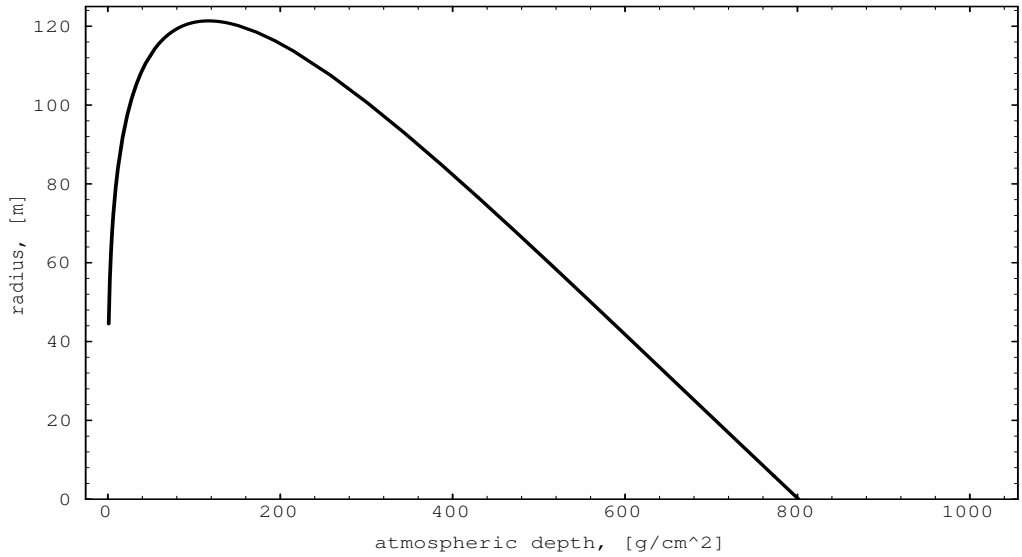

Fig. 4.1.5: Radius of the Cherenkov light cone at 2200 m asl. as a function of the atmospheric depth of the Cherenkov light emission.

As a consequence of the height dependence of the refractive index, θ_c increases with decreasing height. Since the mean scattering angle of the electrons (mostly determined from Coulomb scattering) also increases with the shower age, both effects add up leading to a somewhat increased (with shower age) mean angle between the Cherenkov light emission and the shower axis (see fig. 4.1.4 and 4.1.6).

c) The radius of the Cherenkov light cone at 2200 m asl. as a function of the emission height:

As can be seen from fig. 4.1.5, a large fraction of the Cherenkov light is deposited at radial distances between 60 m and 120 m from the particle trajectory and only light which is produced at small or very large heights gets closer. The Cherenkov light distribution of an EAS on the ground is then given by the superposition of the Cherenkov light cones from all individual shower electrons. However, the inclination angle of the electrons with respect to the shower axis has to be taken into account. The inclination angle is mainly due to multiple electron scattering and is small at large heights, but of the order of the Cherenkov angle close to the ground. From the point of view of a photon detector, the following picture then emerges (see fig. 4.1.6):

For radial distances between 60 m and 120 m the detector receives Cherenkov light from all stages of the shower development thus getting a complete 'picture' of the shower. Below $\sim$ 60m most of the detected light stems from the lower part of the EAS showing large fluctuations due to multiple scattering. Above $\sim$ 130 m the light density and therefore the number of detectable EAS drops very rapidly. A quantitative determination of the photon distribution at ground, taking into account the electron scattering and the atmospheric absorption, requires extensive Monte Carlo simulations (e.g. [137], see also fig. 5.3.1).

d) Estimation of the number of produced Cherenkov photons and their energy contribution:

For simplification $\beta = 1$ and $n = 1 + \eta$ being independent of the frequency (see footnote, eq. 4.1.8) is used. With $1 - 1/n^2 \approx 2\eta$ and $\mathrm{d}X_v = -\rho\,\mathrm{d}h$ (appendix to eq. 4.1.8) eq. 4.1.6 can be written as:

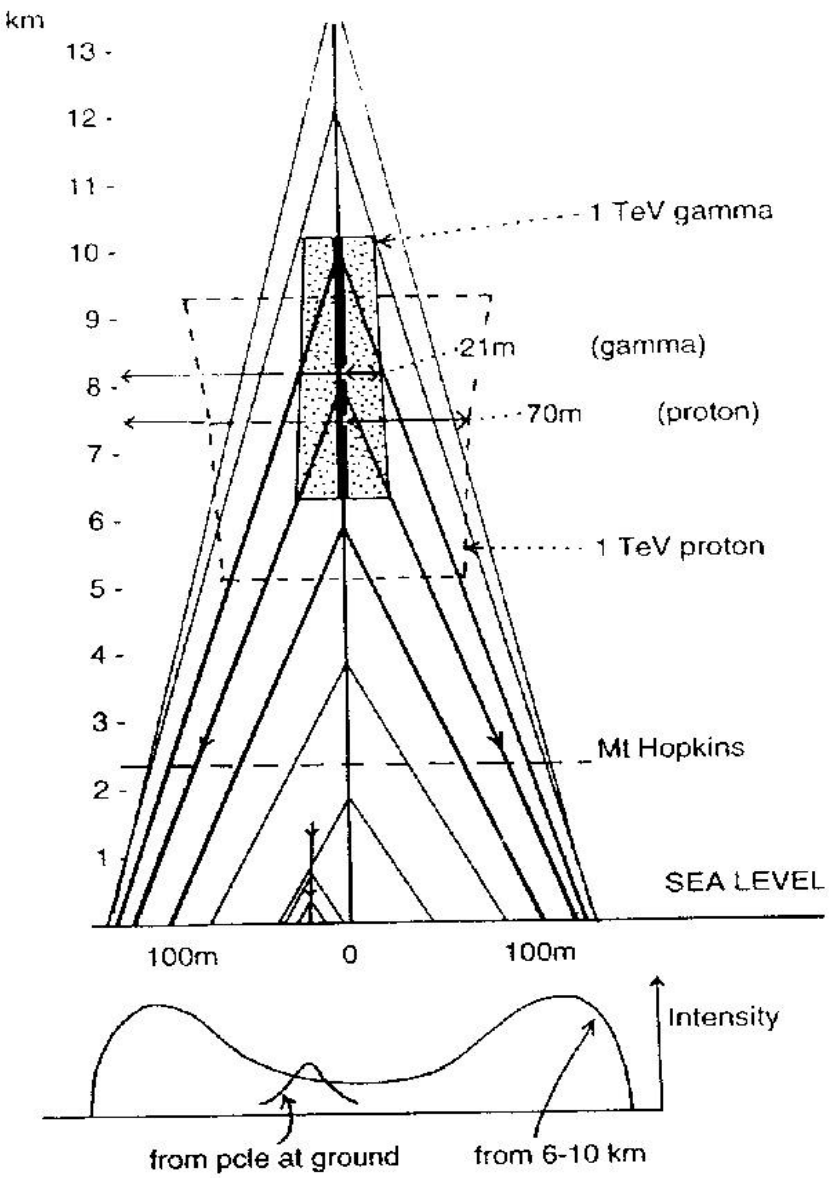

Fig. 4.1.6: Distribution of Cherenkov light in EAS. The dotted area marks the region of maximum light emission for γ-ray showers: 25% of the total Cherenkov light is emitted in the region above and below this area. The height of this area is 8.1 km asl. (for 1 TeV). At this height, 50% of the Cherenkov light is emitted at radial distances within this area. The dashed line marks the equivalent area for proton-showers of the same energy. Note the small secondary air shower. (taken from [76])

$$\frac{\mathrm{d}E}{\mathrm{d}X_v} = \frac{\mathrm{d}E}{\mathrm{d}h}\frac{\mathrm{d}h}{dX_v} = 8\pi^2 e^2 \frac{\eta}{\rho}\int_{\lambda_1}^{\lambda_2}\frac{1}{\lambda^3}\mathrm{d}\lambda = 4\pi^2 e^2 \frac{\eta}{\rho}\left(\frac{1}{\lambda_1^2}-\frac{1}{\lambda_2^2}\right) \tag{4.1.10}$$

The largest amount of energy is therefore emitted at short wavelengths λ, i.e. in the UV and blue waveband. No Cherenkov light is produced below $\lambda \lesssim 180\,\mathrm{nm}$, since eq. 4.1.4 is not fulfilled there ($\varepsilon(\lambda) < 1$ due to anomalous dispersion). Since η is proportional to the air density ρ, the amount of energy emitted per radiation length is constant. The energy can be estimated from eq. 4.1.10 using $h_0 = 2\,\mathrm{km} \mathrel{\widehat{=}} 780\,\mathrm{g/cm^2}$, $\rho(h_0) = 1.0 \cdot 10^{-3}\,\mathrm{g/cm^3}$, $\eta(h_0) = 2.2 \cdot 10^{-4}$, $\lambda_1 = 300\,\mathrm{nm}$ (Ozone cutoff) and $\lambda_2 = 600\,\mathrm{nm}$ (sensitivity limit of PMTs) and becomes: $\mathrm{d}E/\mathrm{d}X_v = 1.0\,\mathrm{keV}\,(\mathrm{g/cm^2})^{-1}$.
This can be compared to the energy loss rate due to ionization losses (so-called stopping power) which is $\mathrm{d}E_{ion.}/\mathrm{d}X_v \gtrsim 2.0\,\mathrm{MeV}\,(\mathrm{g/cm^2})^{-1}$ [99, p. 52]. Energy losses due to Cherenkov radiation in air are therefore very small (about 10^{-4} of the primary electron energy). From eq. 4.1.10 the number of produced Cherenkov photons per atmospheric depth $\mathrm{d}X_v$ can be estimated as:

$$\frac{\mathrm{d}N_{ph}}{\mathrm{dX}_\nu} = \int_{\lambda_1}^{\lambda_2}\frac{1}{\hbar\omega}\frac{\mathrm{d}^2E}{\mathrm{dX}_v\mathrm{d}\lambda}\mathrm{d}\lambda = 4\pi\alpha\frac{\eta}{\rho}\left(\frac{1}{\lambda_1}-\frac{1}{\lambda_2}\right) \tag{4.1.11}$$

(here $\alpha = e^2/\hbar c = 1/137$ is the fine structure constant). Using the same numbers as above we have: $\mathrm{d}N_{ph}/\mathrm{dX}_v = 336\,(\mathrm{g/cm^2})^{-1}$. Each electron therefore emits $\sim 10^4$ Cherenkov photons per radiation length.

e) The atmosphere as calorimeter:

According to Longair [99, p. 51] the stopping power $\mathrm{d}E_{ion.}/\mathrm{dX}_v$ is independent of the atmospheric depth. Therefore a linear (in first order) correspondence between the energy emitted as Cherenkov light and the energy losses through ionization processes exists. As the main part of the shower energy is lost through ionization, a measurement of the integral Cherenkov photon content reveals a method to estimate the shower energy (see fig. 4.1.7).

4.1.3 Detection of extended air showers

The experimental observation of EAS and, in turn, the determination of the parameters of the primary particle, such as direction, energy and chemical nature, make use of the above described features of EAS.

- At shower energies $E_{th} \geq 10^{13}\,\mathrm{eV}$ more and more particles are able to reach the ground. These particles can be measured by suitable detectors (e.g. by arrays of scintillation counters or tracking detectors). The observation time is not restricted to night but angular resolution is poor ($\mathcal{O}(0.5^\circ - 5^\circ)$) and only modest γ-hadron separation is possible. The detectors are 'tail catching' calorimeters of modest energy resolution. The initial direction is determined from time of flight measurements across the shower front.

- A small fraction of the primary energy is emitted as fluorescent light from excited nitrogen molecules. The fluorescent light is isotropically distributed and can therefore be detected from all directions. Observation can only be carried out during dark nights (no moon) and the energy threshold is rather high ($E_{th} \geq 10^{16}\,\mathrm{eV}$). The light yield for fluorescent light is $\simeq 10^{-5}$ of the total energy.

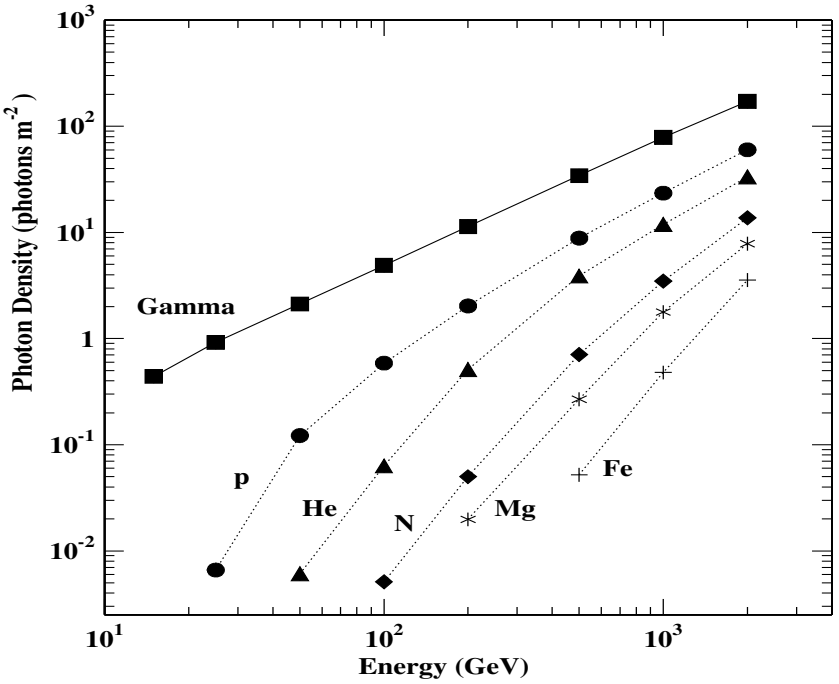

Fig. 4.1.7: Cherenkov photon density (300-600 nm) at 2000 m asl. as a function of the type and energy of the primary particle. The photon density is averaged over an area of 50 000 m^2. (taken from [121])

- Detection of neutrinos: due to the extreme weak interaction with matter, there exist no suitable detectors with high efficiency yet. There exist plans to build km^3 size detectors in sea water or ice. Neutrinos would be the unambiguous proof of cosmic hadron acceleration.

- Another possibility is to measure the Cherenkov light produced by EAS. Common instruments are Air Cherenkov Telescopes (ACTs, see sec. 4.2). The energy threshold of ACTs depends mainly on the mirror size and the quantum efficiency of the PMTs and is, for present day ACTs, $E_T \geq 3 \cdot 10^{11}$ eV. The detectors operate only during dark nights, but successful observations under the presence of moonlight have already been carried out (see sec. 5.1.4). Since the light flashes from Cherenkov light are rather short (2-10 ns FWHM) advanced electronics are needed in order to detect the signals against the ubiquitous night sky light background.

The advantages of Cherenkov light detection are manifold:

- In contrast to the isotropically emitted fluorescent light, the Cherenkov light is strongly peaked forward, its intensity is about a factor 10 higher and the signal duration is very short. This results in a typical reduction in threshold by a factor 10.

- The energy threshold is significantly lower compared to scintillator array detectors, because the shower tail does not have to reach the ground.

- The Cherenkov light pool on ground is large and rather uniformly illuminated. Thus a single telescope is sufficient to detect light from showers up to ~ 140 m impact distance.

- Detected Cherenkov light stems from all parts of the shower development and therefore contains more information compared to data extracted from the shower tail particles. This allows an improved γ- hadron separation.

- The number of Cherenkov photons is about 4 orders of magnitude larger compared to the number of secondary particles in the entire shower. Depending on the energy this difference increases dramatically if one compares the light flux with only the particles reaching ground. Thus photon detectors do have an increased sensitivity for EAS. Another advantage of large photon numbers coming from all parts of the shower is the reduced fluctuation of individual showers compared to shower tail calorimetry.

- The time spread of arrival times is smaller for Cherenkov photons than for secondary particles (2 - 10 ns compared to 5 - 100 ns FWHM). This results in a clearer signal for shower detection and identification.

- γ-induced air showers produce more light compared to equal energy hadrons (see fig. 4.1.7). Thus a small γ-hadron enhancement occurs already at the trigger level.

Disadvantages are:

- The restricted observation time as stated above.

- Scattering and absorption processes in the atmosphere change the intensity and spectral shape of the Cherenkov light. These processes depend strongly on the height and the atmospheric conditions (see sec. 4.1.4).

- Due to the very small field of view of Cherenkov telescopes (typically $3° - 4°$) one can only observe preselected objects. Therefore observation guidance is needed. The objects of interest might belong to a certain class of already detected sources (plerion type SNRs like the Crab and Vela pulsar) or might be established sources in other wavebands (keV-GeV) which are considered to produce also TeV photons (e.g. AGN, X-ray binaries, micro quasars etc.).

4.1.4 Attenuation of Cherenkov light in the atmosphere

On their way through the atmosphere, some Cherenkov photons interact with air molecules, the dominant processes being Ozone absorption, Rayleigh scattering and Mie scattering. The efficiency of each process depends strongly on the atmospheric height of interaction and on the wavelength of the photons. Since the scattering angles of Mie- and Rayleigh scattering are generally large compared to the Cherenkov angle ($\sim 1°$) all photons subject to these processes (including absorption) are lost for an ACT. Thus, the atmospheric conditions affect the amount of photons collected from a given EAS, which, on the other hand, also affects the threshold energy of the ACTs and the estimation of shower energies (sec. 5.3.1). The basic properties of the interaction processes are as follows:

Rayleigh scattering describes the process of light scattering on polarizable particles with sizes small compared to the photon wavelengths. The reduction $\mathrm{d}I$ of the photon intensity I per path length $\mathrm{d}x$ can be derived from the Rayleigh scattering equation and is approximately ([80, p. 499], using $k = \omega/cn = 2\pi/\lambda n \simeq 2\pi/\lambda$)

$$\mathrm{d}I/\mathrm{d}x = -I \cdot \frac{32\pi^3}{3N\lambda^4} (n-1)^2 \tag{4.1.12}$$

N : density of scattering particles
n : refractive index
λ : photon wavelength

Integration from 0 to x and ignoring any possible x-dependence of the refractive index n gives:

$$I(x) = I_0 \cdot \exp(-\alpha x) \quad \text{with } \alpha = \frac{32\pi^3}{3N\lambda^4}(n-1)^2 \tag{4.1.13}$$

Since the extinction coefficient α depends on the refractive index n, it also depends on the atmospheric height. The strong dependence of Rayleigh scattering on the photon wavelength (λ^{-4}) mainly affects the short wavelength region of the Cherenkov photon spectrum. For atmospheric heights between 3-15 km (and perfect weather conditions) Rayleigh scattering is the dominant process for Cherenkov light attenuation [93, p. 70].

Mie scattering describes light scattering on polarizable particles with sizes comparable or larger than the photon wavelength. The relative contribution to the light attenuation above 2000 m atmospheric height is small, but poor atmospheric conditions (high humidity, clouds, dust etc.) can make Mie scattering the dominant process. The spectral dependence of the cross section (and therefore extinction coefficient) is $\sigma_{mie} \propto \lambda^{-a}$ with $1 \lesssim a \lesssim 1.5$ [144].

Ozone absorption ($O_3 + \gamma \rightarrow O_2 + O$) only affects the UV range of the Cherenkov photon spectrum below 300 nm. Due to the high Ozone concentration at large heights ($> 10\,\text{km}$), this process plays an important role there. Cherenkov light in the UV range below 300 nm can therefore only be detected from particles at short distances. Other absorption processes (O_2, N_2) are negligible.

4.1.5 Distinction between γ- and hadron-induced air showers

Section 4.1.1 described the basic properties of γ- and proton induced air showers. Due to the different processes involved, the geometry of both types of air showers is somewhat different and it is then possible to distinguish between them (see fig. 4.1.8 and 4.2.2):

- The interaction length of protons and mesons in air is about 3 times larger compared to photons. Proton showers are therefore more extended than γ-ray showers.
- The secondary particles, which are produced in hadronic interactions, have a mean transverse momentum of about $0.3\,\text{GeV}/c$. Thus, decaying neutral pions might initiate electromagnetic sub-showers at larger transverse distances and angles from the shower axis. The lateral distribution of proton showers is therefore broader.
- Proton showers are subject to larger fluctuations in the shower development (fig. 4.1.9), both between individual air showers and within a given air shower. The fluctuations are caused by:
  - the large interaction length of the hadronic particles
  - the large transverse momentum of the secondary particles
  - the variety and number of secondary particles
- The electromagnetic component of proton-induced air showers contains only a fraction of the primary energy. The overall amount of Cherenkov light produced within proton showers is therefore generally smaller compared to γ-induced air showers of the same

energy. As a consequence photon detectors do have an increased energy threshold for proton showers. In the case of CT1, the trigger probability at the threshold (i.e. $\sim 1\,\mathrm{TeV}$) is reduced by a factor 3-6 for proton showers compared to γ-ray showers [93].

- For point-like sources all γs reaching the earth have the same incident direction. This property is also inherent in the produced air showers. The protons of the CR in contrast, are isotropically distributed because they are randomly deflected by the galactic magnetic fields. It is therefore possible to reduce a large fraction of background by measuring the incident angle of the primary particles. A good angular resolution is therefore also of key importance.

- A possibility to distinguish between γ- and proton induced air showers is to measure the muon component of the shower. The muons originate from decaying mesons and their rate is at least an order of magnitude lower in γ-ray showers. This method is limited by the small number of muons at shower energies below, say, $\sim 10\,\mathrm{TeV}$ and by the increased occurrence of photoproduction processes in very-high-energy γ-ray showers ($E \geq 1\,\mathrm{PeV}$, [94]).

High-energy protons are only one part of the CR ($\sim 54\%$ above 100 GeV). The CR also contain heavier nuclei (mainly He with $\sim 23\%$) up to iron and electrons ($\sim 0.2\%$). In a simplified picture, EAS produced by heavy nuclei can be regarded as a superposition of several (according to the number of nucleons A) proton showers of reduced energy E/A [82, p. 15]. As a consequence, these showers develop earlier in the atmosphere, produce somewhat less Cherenkov light (Rayleigh and Mie scattering losses are larger) and show less fluctuations. The dominant part of the hadronic background therefore consists of proton showers (see fig. 4.1.7).
Electron induced air showers are indistinguishable from γ-ray showers. But similar to the hadronic part of the CR, the electrons are isotropically distributed and only add to the isotropic background. Due to the very steep electron spectrum (spectral index $\alpha = 3.3$, [173]) electron showers above 500 GeV can be ignored.

Nearly all methods for γ-hadron separation (except muon detection) described here are accessible for ACTs through the Imaging Technique. This explains why this technique is such a powerful method for γ-hadron separation. The next section describes the Imaging Technique in detail.

4.2 Detection of Extended Air Showers with Air Cherenkov Telescopes

Due to the large hadronic background, an effective γ-hadron separation is crucial in the search for TeV γ-ray sources. It took over 20 years of intense experimental efforts to discover the first γ-ray source with high significance: In 1989 the Whipple collaboration reported the observation of TeV γs from the Crab nebula [172]. The detector was an Air Cherenkov Telescope with a 37 pixel PMT camera. This observation was only possible due to the improved γ-hadron separation capabilities of the Imaging Technique.
In the following, a brief introduction to the Imaging Technique will be given. The first part describes the basic principles of detecting EAS and reviews problems that are encountered. The then following section deals with the so called HILLAS image parameters, which are used to describe the light content, shape and orientation of the recorded shower images in the

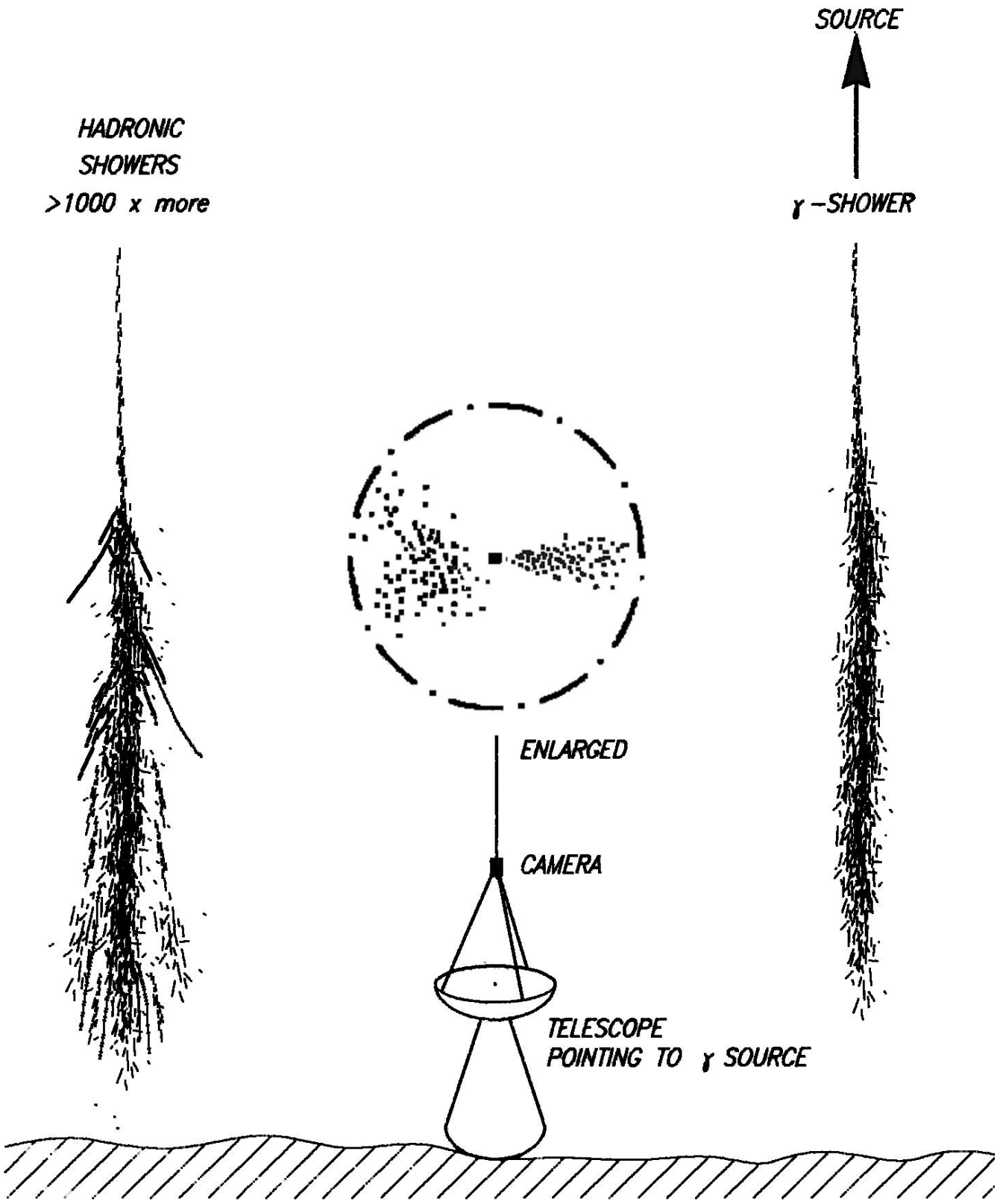

Fig. 4.1.8: Comparison of photon and hadron induced air showers (sketch). The camera picture is rotated by 180 degrees and shows the image of the hadronic shower on the left and the photon shower on the right.

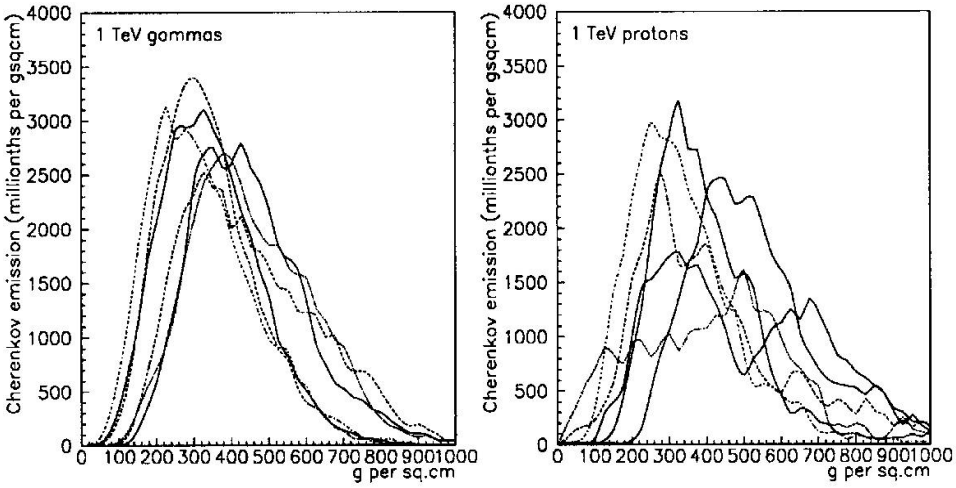

Fig. 4.1.9: Example of the longitudinal development of 6 individual γ-ray showers (left hand side) and proton showers (right hand side) of 1 TeV energy. The fluctuations within and between individual showers are larger for proton induced air showers. (taken from [76])

camera. The different processes involved in the shower development of γ- and hadron induced air showers lead to differences in the HILLAS parameters. The γ- hadron separation is then obtained by applying selection cuts on the HILLAS parameters of the data. This is described in sec. 4.2.3.

4.2.1 Basic principle

When a high-energy particle interacts with the molecules of the atmosphere it creates an EAS. The electrons and positrons produced within the EAS emit Cherenkov light on their way through the atmosphere. The Cherenkov light can be detected by an ACT located within the light pool on the ground. The mirror of the ACT collects a certain amount of the Cherenkov light and reflects it onto the PMT camera located in the focal plane of the mirror (see fig. 4.2.1). Since the incident angle of the Cherenkov light depends on the height of the emission region, there is in first order (if position and direction of the shower axis are kept fixed) a one-to-one correspondence between the height of this region and the position of the corresponding light distribution in the camera plane. For EAS parallel to the optical axis of the telescope, light from the upper part of the shower is therefore reflected close to the camera center while the light from the lower parts of the shower is reflected further away from the camera center. It is therefore possible to take space (and time) resolved 'pictures' of EAS. This information can then be used to discriminate between γ- and hadron induced EAS. One effect of the directed Cherenkov light emission is that the photons of some shower regions are not able to reach the mirror. These shower regions are therefore not contained in the shower image.

The Imaging Technique has to address several topics:

1. Small photon numbers:

On the one hand, the number of Cherenkov photons produced within EAS exceeds the number of produced particles. On the other hand, these photons are distributed over a large area on the ground. The amount of light reaching an ACT is therefore limited. Because of the general observation, that the fluxes of nearly all sources follow a power law with a sizable negative coefficient one expects most of the events closely above the threshold where the yield

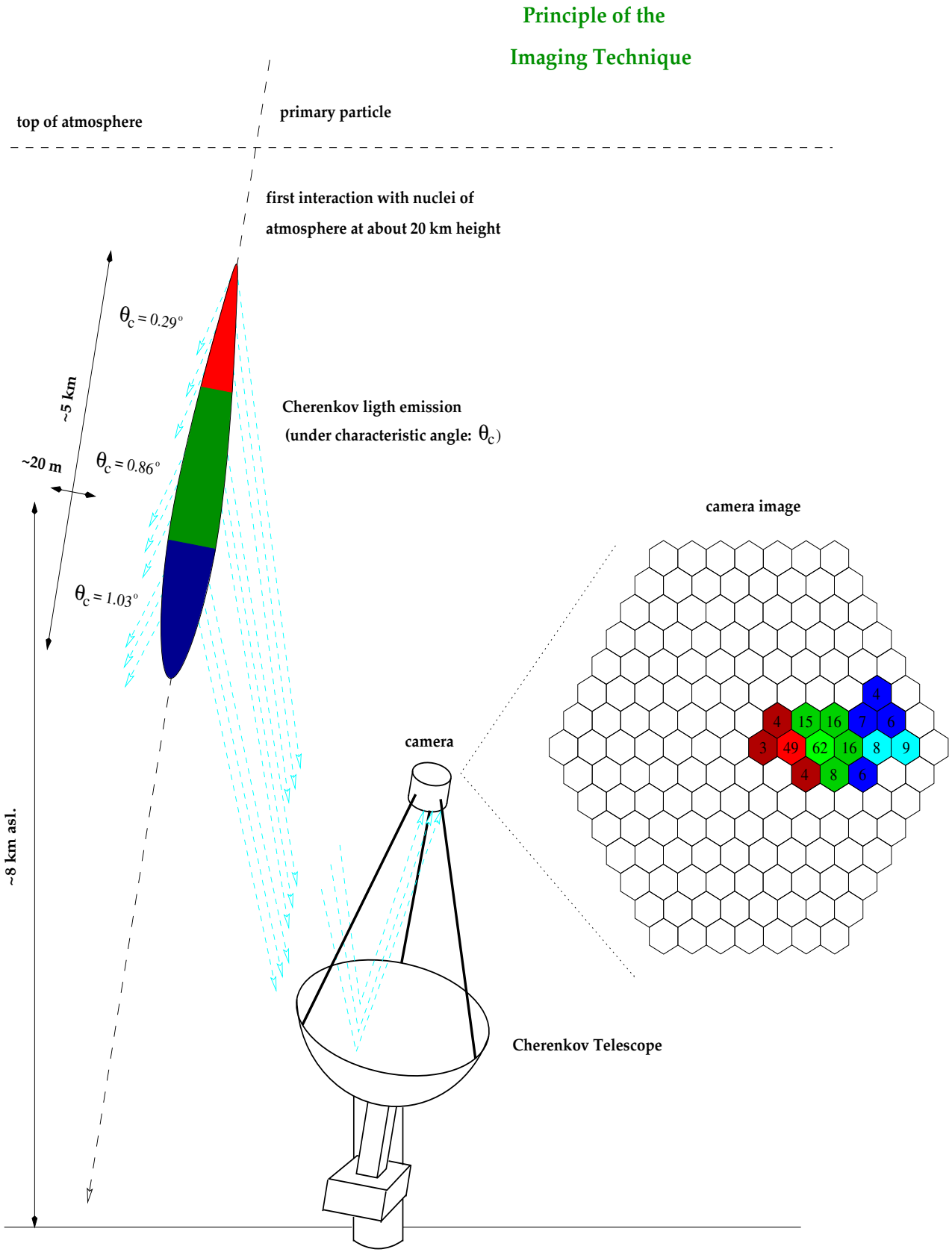

Fig. 4.2.1: Basic principle of the Imaging Technique (see text). The stated dimensions are typical for vertical γ-ray showers of 1 TeV primary energy. The camera image shows a typical γ-ray shower image (the stated numbers denote the PMT signal in photoelectrons). (adopted from [126])

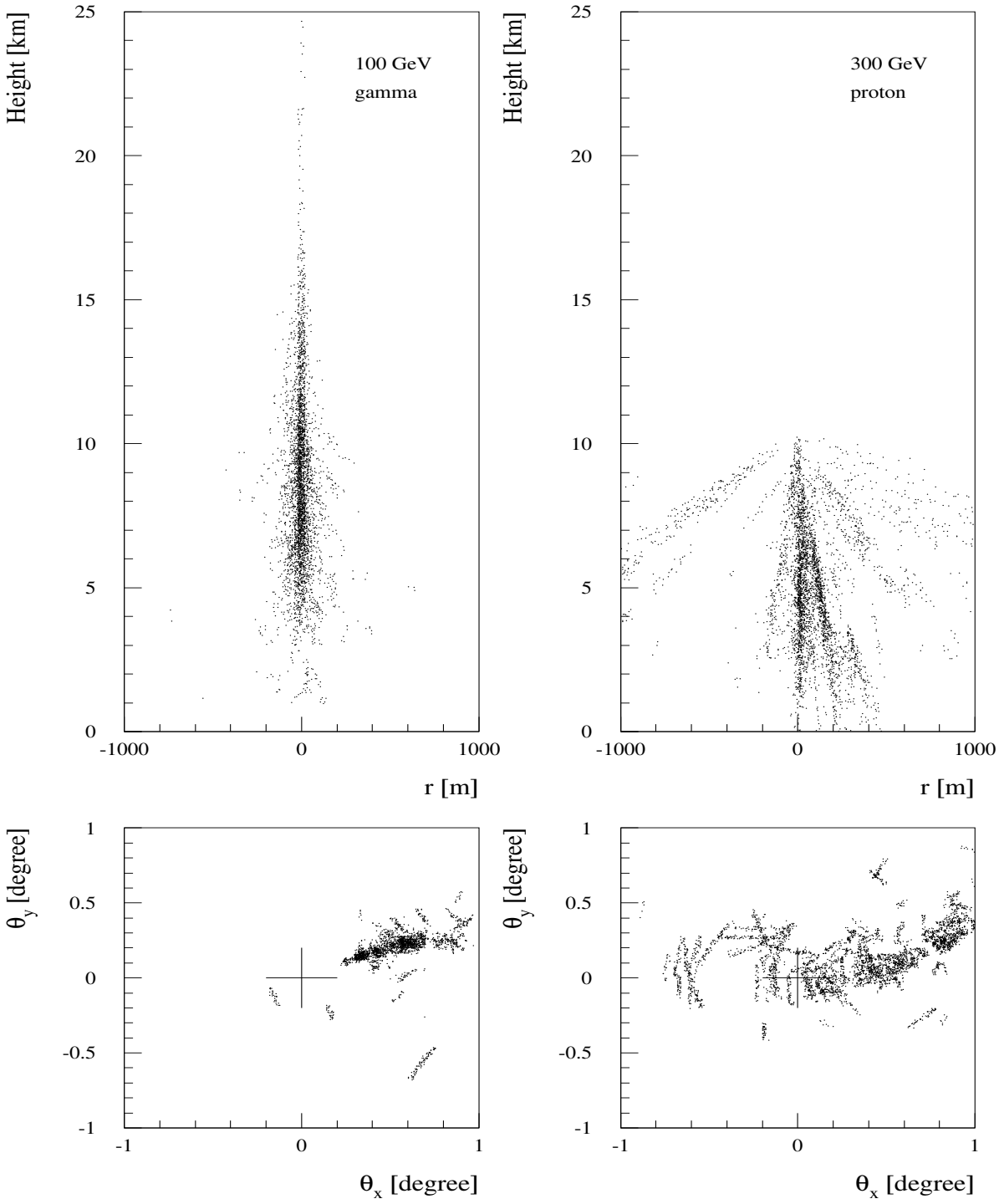

Fig. 4.2.2: Comparison between a γ- and proton induced air shower. The upper part of the picture shows the shower development, the lower part shows the corresponding light distribution in the camera. (taken from [8])

of Cherenkov photons is lowest.

2. The effect of the NSB:

The NSB is built up from several components such as star light, fluorescent light from the ionosphere, moon light, airglow light and light from terrestrial sources. According to Mirzoyan [113] the average photon flux of the NSB at La Palma for the wavelength band $\lambda = 300$ - 600 nm is: $\Phi_{NSB} = (2.30 \pm 0.15) \cdot 10^{12}$ photons/ $(\mathrm{m}^2\,\mathrm{sr}\,\mathrm{s})$. The photon flux includes the diffuse component of light scattered at the earth's surface, but does not contain the moonlight and light from bright stars. The light from the NSB can cause several problems [13, p. 181]:

- Statistical fluctuations in the NSB can generate artificial triggers. The resulting signal pattern can in general be easily distinguished from real EAS images, but the increased trigger rate must be handled by the data acquisition system.

- The NSB light adds to the EAS images and can significantly change their shape and light yield[12]. This effect worsens the energy reconstruction and the γ-hadron separation capability.

- Some low-energy showers may be raised above the telescope trigger by the NSB light. This reduces the energy threshold of the telescope. Since the energy threshold now depends on the amount of NSB light it worsens the investigation of EAS at low energies.

- In order to reduce the influence of the NSB on the recorded EAS images one needs high sensitivity photon detectors of very fast time response, i.e. PMTs. Due to the high sensitivity of the PMTs the observation time is restricted to night (not during full moon).

- A peculiarity of PMTs is that photoelectrons can liberate ions absorbed at the first dynode. These ions are accelerated towards the cathode and can in turn liberate a large number of electrons, thus generating large afterpulses that can mimic EAS signals. The rate is in first order proportional to the NSB. A partial cure is to set discriminators to typically 15 photoelectrons.

The effect of the NSB can be minimized by using narrow trigger coincidence- and ADC gate widths (typically $\mathcal{O}(10\,\mathrm{ns})$). This also requires a fast pulse-height recording system (see sec. 3.1).

3. An effective method for γ-hadron separation and energy estimation:

Since ACTs produce space and time resolved images of EAS, these images also show differences in the shower development as described in sec. 4.1.5. The larger longitudinal and lateral distribution of a proton shower is therefore also visible in the resulting shower image (see fig. 4.2.2). Using advanced selection criteria on these images it is possible to reduce the hadronic background by a large factor while keeping most of the γ-ray showers (efficiency example for CT1: $\varepsilon_h \simeq 0.03$, $\varepsilon_\gamma \simeq 0.7$, see sec. 4.2.3). To make use of the timing information it is necessary to have appropriate electronics like F-ADCs (not available for CT1 but for the CT-system).

A method for estimating the energy of γ-ray showers with single ACTs is described in sec. 5.3.1. The energy resolution achieved by this method is $\sim 25\%$ RMS. In the next chapters, the essential parameters for γ-hadron separation will be described.

[12] Bright stars may add up to 50% of the overall amount of light of an image.

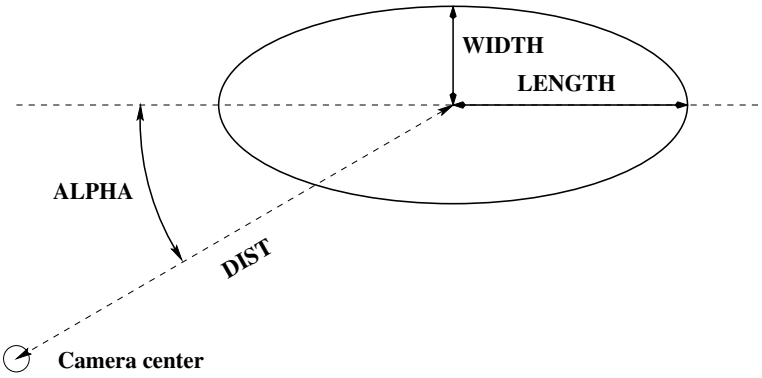

Fig. 4.2.3: Definition of the HILLAS parameters $LENGTH$, $WIDTH$, $DIST$ and $ALPHA$.

4.2.2 Definition of the so-called HILLAS image parameters

The quality of the camera images of EAS plays a dominant role in maximizing the γ-hadron selection capabilities. Up to now nearly all methods for γ-hadron separation within the IT are based on the so-called HILLAS parameters [75, 172]. These image parameters describe the light content, shape and orientation of the shower images in the camera. The γ-hadron separation is then achieved by applying selection cuts on the HILLAS parameters.
The *HILLAS Parameters* (HP) are derived from the light distribution in the camera and are defined as follows (see fig. 4.2.3):

$LENGTH$	a measure of the length of an EAS. It corresponds to the RMS value of the light distribution along the main axis of the shower image
$WIDTH$	a measure of the width of an EAS. It corresponds to the RMS value of the light distribution along the minor axis of the shower image
$ALPHA$	the angle between the main axis of the shower image and the connecting line from the camera center to the *Center Of Gravity* (COG) of the image
$CONC$	ratio between the light content in the 2 pixels with the highest light yield and the overall light content of the image
$DIST$	distance between the camera center and the COG of the image
$SIZE$	overall light content of the image

In general the HP are not calculated from the raw events (as observed), but some image cleaning procedures are applied beforehand. These procedures, as well as the exact formulas for deriving the HP are presented in sec. 5.1.2 and 5.1.3.

The image parameters $LENGTH$, $WIDTH$, $CONC$ and $SIZE$[13] describe the shape and light content of the shower image, whereas $ALPHA$ and $DIST$ characterize the orientation and position of the image in the camera. The image parameter $ALPHA$ depends on the relative orientation of the (optical) telescope axis and the shower axis (see fig. 4.2.4)[14]. If

[13] The total quantity of light, as well as the signal in individual pixels, is usually given in units of number of photoelectrons (Pe). From the experiment the conversion factor between an electron released at the photocathode of the PMT and the signal of the ADC is well-known [110]. The number of released Pe, however is proportional to the light intensity and therfore a measure of it. The conversion factor, and concomitantly the $SIZE$, depends on the QE of the PMT and the applied high voltage.

[14] In the standard approach only moments up to 2nd order are taken into account. The range of the $ALPHA$ parameter is then $-90 \leq ALPHA \leq 90$ (since the $ALPHA$ parameter distribution is symmetric it is common to show only its absolute value). The full angular range can be obtained by including 3rd order moments. This allows for an improved γ-hadron separation.

the shower axis of an EAS and the telescope axis lie within one plane the $ALPHA$ parameter becomes very small ($ALPHA \approx 0°$). The uncertainty of the $ALPHA$ parameter is mainly determined by the pixel size of the camera, typically with a σ_{ALPHA} of 6-8°. This is particularly the case for all showers parallel to the telescope axis (where the direction of the primary particle coincides with the direction of observation). Inclined showers lying in this plane also possess a small $ALPHA$ value, but they can be distinguished to some extent from parallel showers by means of their $WIDTH/LENGTH$ ratio (a purely geometrical effect). Nevertheless, to unambiguously determine the orientation of the shower axis at least 2 (and in some cases 3) ACTs are needed. The image parameter $ALPHA$ becomes large if the shower axis and the telescope axis do not lie within one plane.

The $CONC$ parameter describes the compactness of the shower maximum region. For γ-induced air showers this region is very compact and the $CONC$ parameter therefore large. Hadron showers, on the other hand, are more extended and have small $CONC$ values.

The value of the $DIST$ parameter corresponds roughly to the angle to the telescope axis, under which the shower maximum is seen. For parallel air showers of the same energy, the $DIST$ parameter is a measure of the impact distance between shower axis and telescope axis. Showers with small $DIST$ values ($\leq 0.5°$) develop close to the telescope axis. This means that for parallel showers with small $DIST$ values only (almost) the isotropic Cherenkov light from the strongly scattered electrons of the shower tail region can be measured (see fig. 4.1.6). For large $DIST$ parameters ($\geq 1.2°$), the telescope can only detect Cherenkov light from shower halo particles. In the first case large fluctuations in the images of similar (similar energy and identical primary particle) air showers occur while in the second case only a low intensity light flash is observed, thus only (primary) particles of higher energy are detected. In both cases the images are unsuitable for the distinction between gamma and hadron showers. Typical shower images and the distribution of their HILLAS parameters are shown in fig. 4.2.6 and fig. 4.2.5.

In the remaining chapters the HILLAS parameters $WIDTH$, $LENGTH$, $DIST$ and $ALPHA$ are always given in units of degree and the $SIZE$ is always given in units of number of photoelectrons. These units are therefore not always explicitely stated.

4.2.3 γ-hadron separation based on HILLAS parameter cuts

Most of the properties of γ- and hadron induced EAS mentioned in sec. 4.1.5 are reflected in the HP of the corresponding images. The larger longitudinal and lateral extension of hadron showers results in larger $WIDTH$ and $LENGTH$ values. The $ALPHA$ distribution of hadron showers is (in principle) flat, i.e. all $ALPHA$ values have equal probability. Deviations from the flat distribution might occur if the camera is too small (as for CT1). In that case, some shower images, especially those with large $DIST$ values, are cut by the camera edge and the corresponding $ALPHA$ parameters are shifted to large values [89, p. 48]. For point-like gamma sources the $ALPHA$ distribution consists of a narrow peak (about $\sigma_{ALPHA} \approx 6°$ for CT1, slightly energy dependent). The $ALPHA$ distribution peaks at 0°, if the direction of the γ-ray source coincides with the direction of observation. Otherwise the peak is extended and shifted towards larger $ALPHA$ values. For extended gamma sources the width of the $ALPHA$ distribution is getting broader and the difference between the $ALPHA$ distribution of γ- and hadron induced EAS is therefore less pronounced.

The distribution of the $DIST$ parameter is similar for γ- and hadron showers. Differences show up at small and large $DIST$ values. A reason for this behavior is that at large or small $DIST$ values some of the inclined hadronic showers are more likely to trigger the telescope

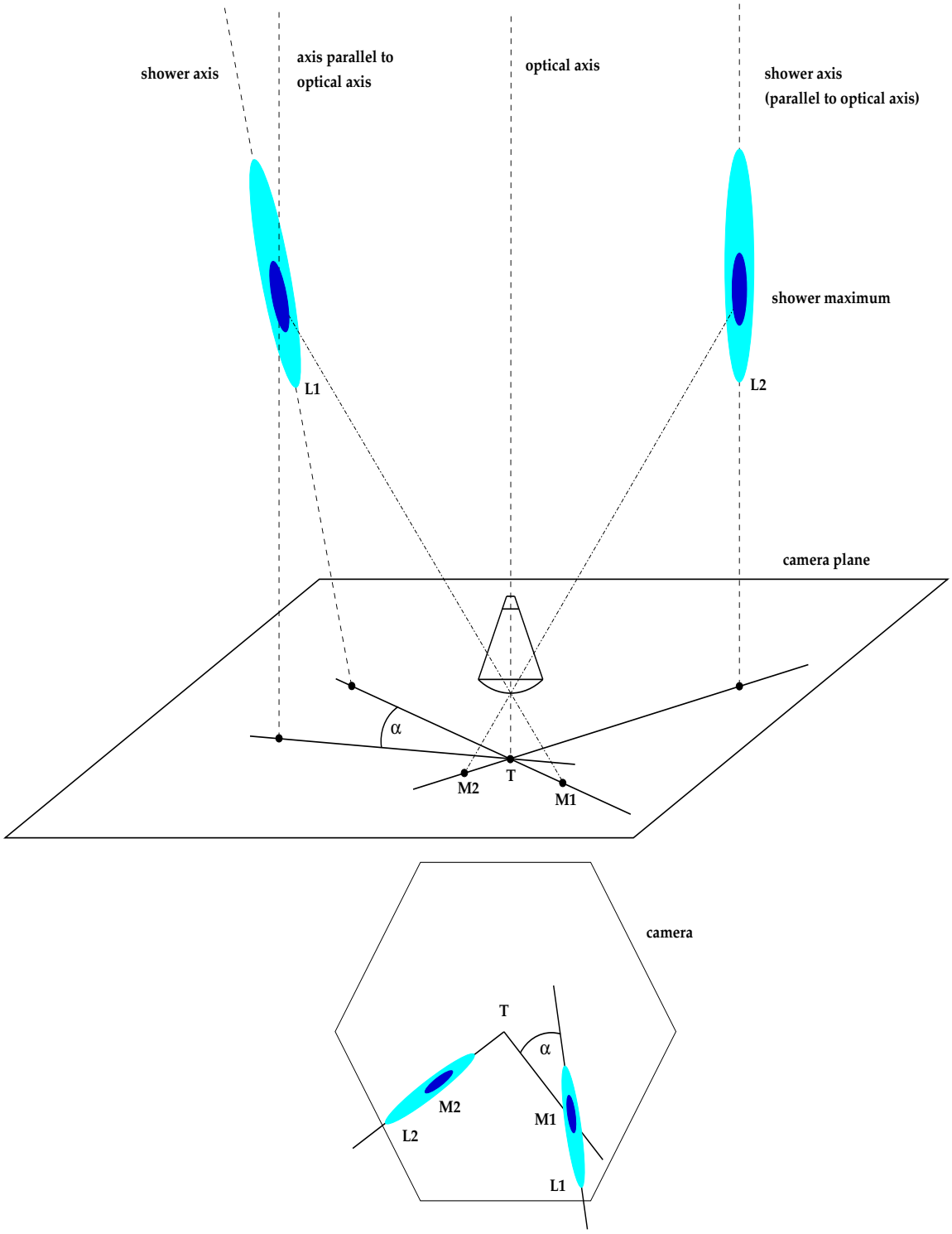

Fig. 4.2.4: Connection between shower axis orientation and the image parameter $ALPHA$. (adopted from [44])

than the parallel γ-ray showers[15]. Thus a cut on the $DIST$ parameter rejects some additional hadronic showers.

A comparison of a γ- and a hadron-like air shower image and the corresponding HILLAS parameters are shown in fig. 4.2.5. For a comparable $SIZE$, the γ-like image has in general a smaller $WIDTH$, $LENGTH$ and $ALPHA$ value. The above mentioned properties are also clearly visible in fig. 4.2.6. The dashed region shows the distribution of some image parameters for MC generated γ-ray air showers (0°zenith angle and spectral index $\alpha = 2.7$). The solid lines represent MC generated proton showers and the dashed lines real hadronic showers (below 5° zenith angle). The differences between the proton and hadron distributions can be assigned to the presence of air showers from heavier nuclei in the hadronic case.

As can be clearly seen from the image parameter distributions in fig. 4.2.6, there are big differences between γ- and hadron induced air showers. It is therefore possible to achieve an efficient γ- hadron separation by limiting the admissible image parameter range. If, for example, only $WIDTH$ parameter values between $0.07 < WIDTH < 0.15$ are accepted, 86% of all hadron showers, but only 21% of the γ-ray showers are rejected.

With the specification of an optimized γ-hadron separation, the WHIPPLE collaboration derived a set of constant cuts for the image parameters $DIST$, $WIDTH$, $LENGTH$ and $ALPHA$ from MC data [141]. This set of cuts was called 'supercuts'. For CT1 the following, with respect to the supercuts slightly modified and expanded by a $CONC$-cut [127], *Supercuts* (SCUTs) were used:

$$\begin{array}{rcl} 0.51 < & DIST & < 1.1 \\ 0.07 < & WIDTH & < 0.15 \\ 0.16 < & LENGTH & < 0.3 \\ 0.4 < & CONC & \\ & ALPHA & < 10 \end{array}$$

Due to the steep power spectrum of all presently known γ-ray sources, the constant SCUTs were optimized mainly on the most frequent showers, i.e. on showers of small energy and small zenith angle. As a consequence, the cut efficiency worsens at large energies and/or large zenith angles. One solution for this problem is to derive energy, distance and zenith angle dependent cuts as discussed in sec. 5.3.3.

The γ-hadron separation power, possible with the IT, is shown in fig. 4.2.7. The plot shows the $ALPHA$ distribution for a subset of the overall Mkn 501 data taken with CT1 in 1997. The left part shows the $ALPHA$ distribution after the so-called filter cuts (used to preselect the raw data, see sec. 5.1.2). Also shown are the results after all image cuts (on an expanded scale to the right). The cut efficiency for this set of cuts is roughly: $\varepsilon_h \simeq 0.03$ and $\varepsilon_\gamma \simeq 0.7$.

[15] The inclination angle adds to or compensates the Cherenkov angle such that the Cherenkov light can be detected by the telescope.

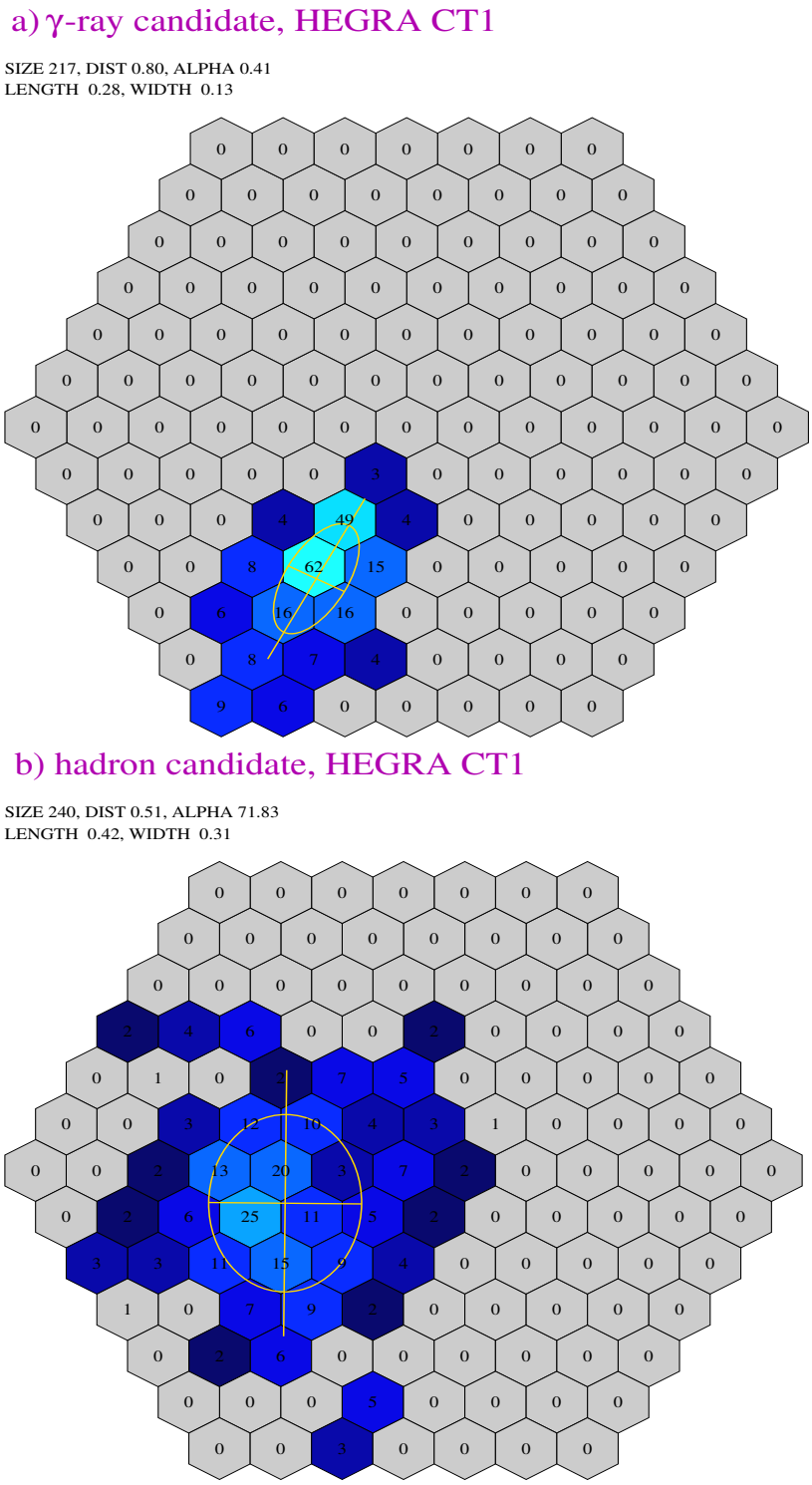

Fig. 4.2.5: Comparison between a γ- (a) and a hadron-like (b) air shower image and their HILLAS parameters. The γ-like image has smaller $WIDTH$, $LENGTH$ and $ALPHA$ values. The numbers in the individual pixels represent the signal in photoelectrons. Signals below the tailcut condition are set to zero (see sec. 5.1.2). The images were taken with the 127 pixel camera of CT1.

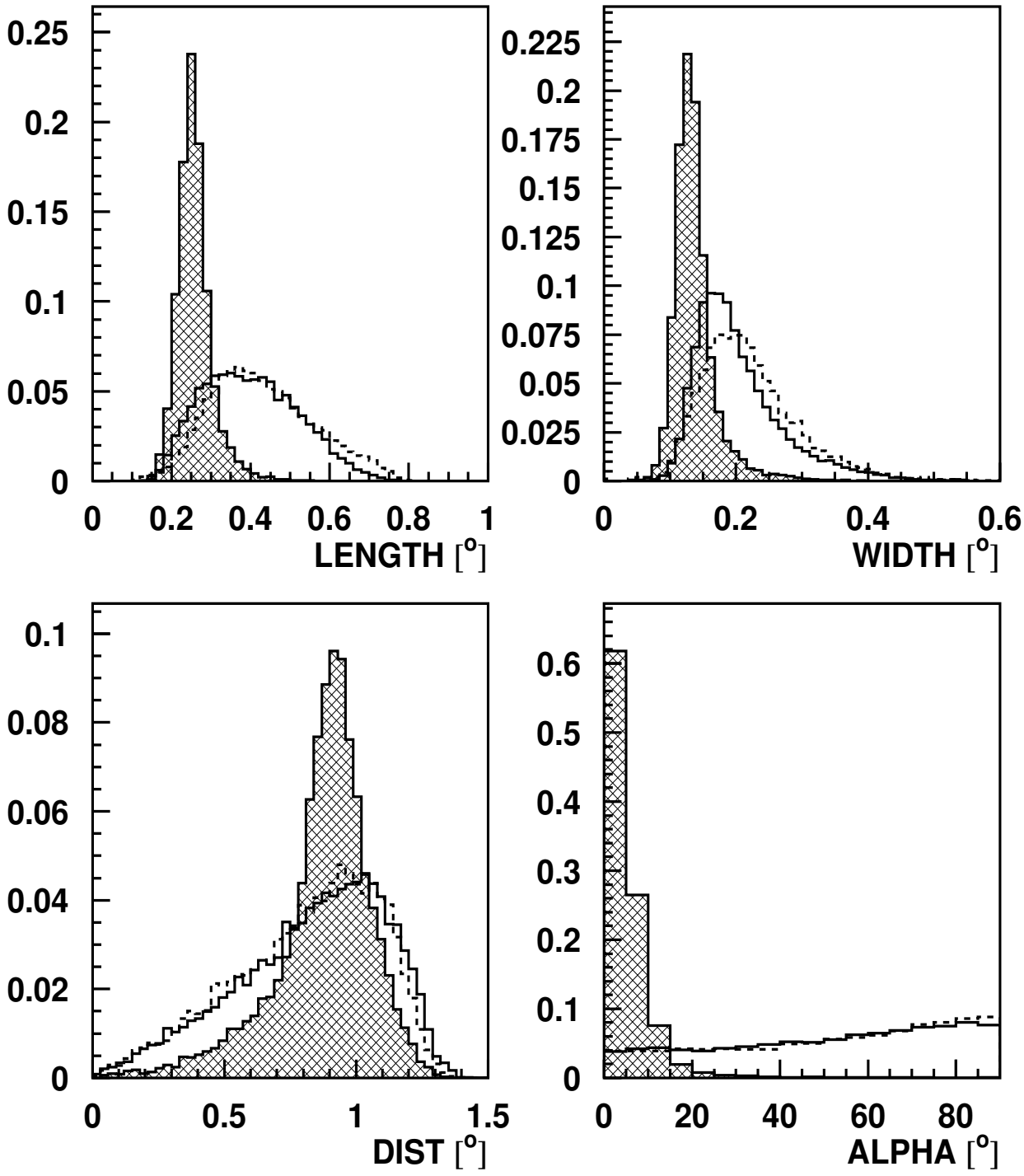

Fig. 4.2.6: Comparison between the distribution of image parameters of simulated γ-ray showers (dashed region), simulated proton showers (solid line) and real hadronic showers (dashed line) from CT1. The MC showers were generated for 0°zenith angle and spectral index $\alpha = 2.7$, the hadronic showers were taken from observations below 5° zenith angle. All distributions are normalized to unit area.

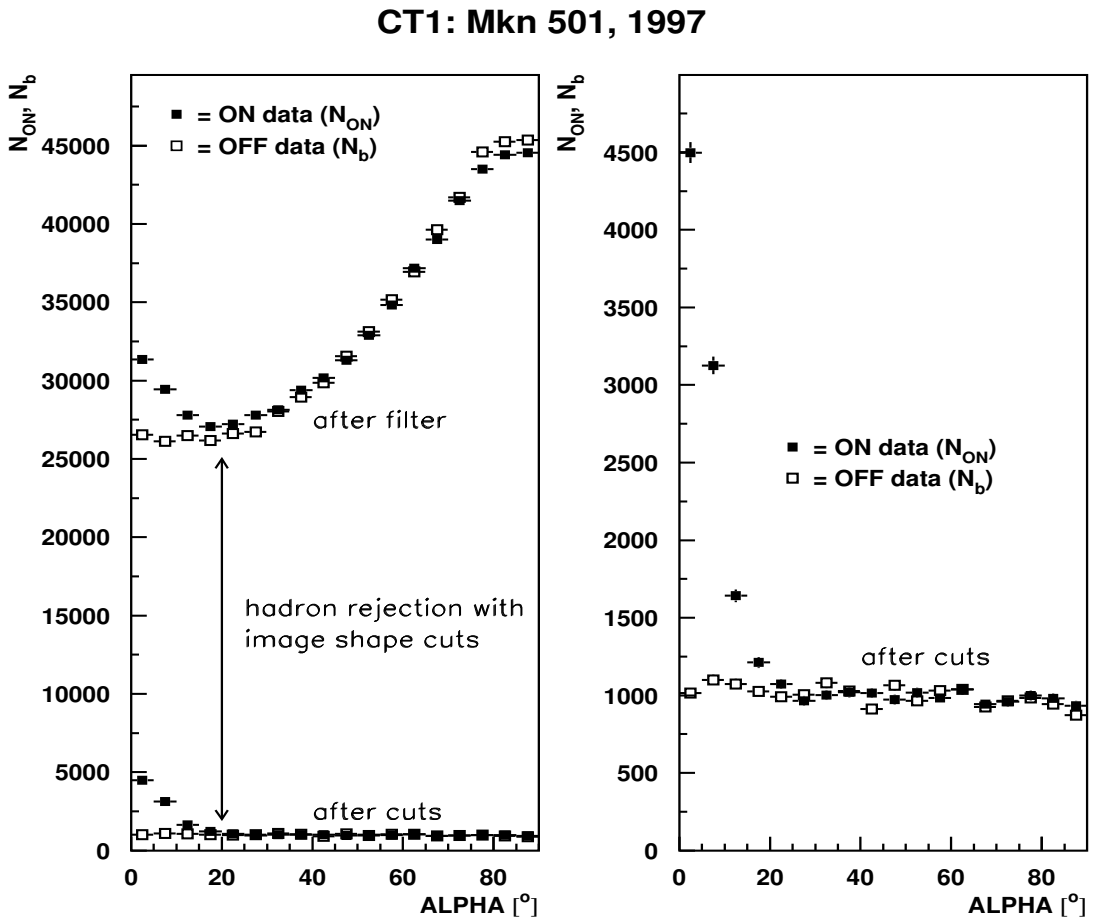

Fig. 4.2.7: Example of the γ-hadron separation capabilities using the imaging technique. The figure on the left shows the $ALPHA$ distribution for ON- and OFF data after filter cuts (upper points) and after all image cuts (lower points). The figure on the right shows the $ALPHA$ distribution after all image cuts on an expanded scale. The total observation time was 194 h.

5. ANALYSIS OF THE CHERENKOV TELESCOPE DATA

In this chapter the individual steps in analyzing the CT1 raw data are described. Analysis methods, which have been developed for this thesis and which were used on CT1 data for the first time, are presented in detail, while the standard methods are only briefly summarized. The CT2 and CT-system data analysis procedure is not discussed here and the reader is referred to [126] and [41] (and reference therein) instead.

5.1 Preprocessing of the data

The first step in analyzing the CT1 raw data is to convert the recorded ADC channels into the number of photoelectrons, which are a direct measure of the observed Cherenkov photons (sec. 5.1.1). In the subsequent process, the shower images are cleaned and unusable events are removed from the data sample (sec. 5.1.2). Finally, the HILLAS image parameters are calculated (sec. 5.1.3). In order to properly analyze the data taken during the presence of moonlight, some modifications to the standard raw data analysis procedure were necessary. These are described in sec. 5.1.4.

5.1.1 Calibration

a) relative calibration:

A pre-condition for the investigation of EAS images is that the same amount of Cherenkov light should give the same signal output in the different channels[1]. This is achieved by means of the so-called flat fielding, where all the individual channels are calibrated against each other. In this procedure, the short light pulses of a nitrogen laser are transmitted by an optical fiber onto a piece of NE-111-scintillator, which transforms the single line emission laser spectrum into a broader spectrum of isotropic scintillation light (emission maximum at 370 nm). The scintillator is positioned at the center of the reflector and thus homogeneously illuminates the CT1 camera with short light pulses. The light pulses then give a trigger and thus the signals from all PMTs get recorded.

In a so-called laser run, 100 laser induced trigger events are recorded. The mean and relative laser gain of the ith PMT is then derived as:

$$L_i = \sum_{j=1}^{100} (L_{ij} - P_i)/100 \tag{5.1.1}$$

and

$$l_i = \frac{L_i}{\sum_{j=1}^{127} L_j/127} \tag{5.1.2}$$

[1] A channel denotes a unit of pixel, cable and amplifier.

respectively (here, L_{ij} is the signal of the ith PMT for the jth laser event, P_i is the pedestal[2] of the ith PMT and 127 is the number of PMTs in the CT1 camera; both L_{ij} and P_i are given in units of ADC counts; l_i is the relative gain of a PMT against the mean of the camera).

b) absolute calibration:

The ADC signal of a given PMT depends on the light intensity, the *Quantum Efficiency* QE[3] and on the PMT gain, mainly determined by the used HV setting. Since the gain of a PMT under load decreases with time (so-called fatigue), the ADC signal is not a time independent measure of the PMT light yield. Instead the signal of a PMT is expressed in *Photoelectrons* (Pe), i.e. the number of photoelectrons on the first dynode. The relation between the two quantities is given by the *single photoelectron to ADC-counts Conversion Factor* (CF), which is gain-dependent and therefore has to be measured on a regular basis. A method to directly measure the CF is described in [110] and the average CF for the CT1 PMTs in 1995 was derived as: $\chi = 0.72 \pm 0.07\,\mathrm{Pe/ADC\,counts}$.

In 1997 several HV settings were used in order to cope with the different NSB brightness during moon observations. Furthermore the nominal HV setting for dark night observations was also increased by 6% in the beginning of 1997. Since the direct measurement of the CF is very time consuming, two alternative methods were used to estimate the CFs for the different HV settings. Both methods depend on the known CF for a comparable data sample (same mirror area, PMT type, etc.) and are described in the following:

1. Comparing the observed CR event rate: Here we assume, that the CR trigger rate r_{tr} is proportional to the integral CR flux (spectral index $a \simeq 1.7$) above the threshold energy E_{th} and that the threshold energy is proportional to the PMT gain and therefore to the CF. Thus

$$\frac{r_{tr,1}}{r_{tr,2}} = \left(\frac{E_{th,1}}{E_{th,2}}\right)^{-1.7} = \left(\frac{\chi_1}{\chi_2}\right)^{-1.7} \tag{5.1.3}$$

and the unknown CF χ_1 can be calculated according to:

$$\chi_1 = \chi_2 \left(\frac{r_{tr,2}}{r_{tr,1}}\right)^{1/1.7} \tag{5.1.4}$$

Using $\chi_2 = \chi = 0.72\,\mathrm{Pe/ADC\,counts}$ and $r_{tr,2} = 0.90\,\mathrm{Hz}$ from the 1995/96 Crab observation, the CFs derived for the 1997 data sets are summarized in tab. 5.1.1 (column 2 and 3). The stated errors are purely statistical. Note that the CR trigger rate is calculated after removing the NSB triggered events (i.e. after applying the filter cuts; sec. 5.1.2).

2. Estimation of the CF from fluctuations of laser signals: The fluctuations of the strong signals from normalized laser trigger events (see below) can also be used to derive the CF. If the individual laser events are of similar strength, the CF can be estimated as [114]:

$$\chi = \frac{m}{\langle Q \rangle} = \frac{F^2 \cdot \langle Q \rangle}{\sigma^2\,(Q)} \tag{5.1.5}$$

[2] The pedestal values are derived from a so-called pedestal run, where the ADC signals of all PMTs are recorded from 500 artificial triggers. After excluding possible outliers, the pedestal P_i for a certain PMT is given by the mean while the pedestal noise ΔP_i is given by the RMS of the pedestal distribution.

[3] The QE denotes the ratio between the number of photoelectrons emitted from the photocathode and the number of incident photons. In case of the EMI 9083A PMTs, used for all CTs of the HEGRA experiment, the QE is $\sim 26\%$ at 375 nm.

HV setting	CR trigger rate [Hz]	χ [Pe/ADC] (CR trigger rate)	χ [Pe/ADC] (F-factor)	trigger threshold [Pe]	threshold energy [TeV]
NOM00	1.07 ± 0.07	0.65 ± 0.03	0.60 ± 0.06	13	1.2
NOM06	0.65 ± 0.03	0.87 ± 0.03	0.92 ± 0.09	19	1.8
HV00	1.17 ± 0.24	0.62 ± 0.09	0.60 ± 0.06	13	1.2
HV06	0.56 ± 0.03	0.95 ± 0.03	0.95 ± 0.10	20	1.8
HV10	0.37 ± 0.03	1.21 ± 0.06	1.20 ± 0.12	25	2.4
HV14	0.21 ± 0.02	1.69 ± 0.09	1.70 ± 0.17	35	3.4
HV16	0.18 ± 0.01	1.86 ± 0.06	1.95 ± 0.20	41	3.9

Tab. 5.1.1: Conversion factor χ for the 1997 data sets, as derived with two different methods (see text). The trigger threshold and the corresponding threshold energy are also given. The terms $NOMxx$ and $HVxx$ denote observations taken during dark nights and during the presence of moonlight respectively and the value of xx denotes the relative HV reduction.

Here, m denotes the number of Pe of the signal Q, $\langle Q \rangle$ the mean and $\sigma^2(Q)$ the variance of the signal distribution[4]. The *specific excess noise Factor* F characterizes the quality of a PMT (the smaller the better) and has values of typically $F \simeq 1.15$. The F-factor does not change with time and once it is known, allows the calculation of the CF from the values of $\langle Q \rangle$ and $\sigma^2(Q)$ for any given data sample. From the 1995/96 Crab data (with known CF) the F-factor was calculated by means of eq. 5.1.5 as: $F = 1.09 \pm 0.05$. Table 5.1.1 (column 4) summarizes the CFs and the combined systematical and statistical errors for the different 1997 data sets. The corresponding trigger and energy thresholds are given too.

As can be seen from tab. 5.1.1, the agreement between the two different methods is quite good. In the following, the CFs obtained with the F-factor method have been used for the data analysis. The reason is, that the F-factor method is more direct and therefore less prone to systematic errors. The same CF was used for all pixels.

The derived CF and relative laser gain values are then used to calibrate the PMT signals S_i recorded during observations. The calibrated signal s_i (in units of Pe) for the ith PMT is calculated according to:

$$s_i = \frac{1}{l_i} (S_i - P_i) \cdot \chi \tag{5.1.6}$$

(here, S_i is the PMT signal in units of ADC counts).

The results from the laser runs are also used to identify 'hot' or broken pixels, which are then excluded from the data analysis. Separately, the trigger pattern for each data sample is investigated in order to find temporarily 'hot' or broken pixels and to search for crosstalk between individual pixels (see [85] for details).

5.1.2 Pre-analysis

Once, the calibrated signals have been derived, the next steps in the analysis chain are the image cleaning and the so-called filter cuts. The goal of the first is to reduce the contribution of the NSB on the observed shower images while the second is used to remove unusable events from the data sample. The unusable events are either shower events, which are too small for a reasonable image parameter calculation, or NSB triggered events. This section summarizes the relevant parts from [126, sec. 3.2].

[4] Since the signals Q are derived according to eq. 5.1.6, the CF has to be derived in an iterative process using a reasonable start value.

The necessity for the image cleaning stems from the fact that in the calculation of the image parameters (sec. 5.1.3), only the calibrated PMT signals, but not their errors are used. As a result, NSB induced fluctuations in the PMT signals may strongly affect the derived image parameters and therefore spoil the γ-hadron separation. A solution to this problem is to exclude all pixels from the image parameter calculation whose signals are very likely due to NSB noise (i.e. set these signals to zero). This is done in the so-called topological tailcut, which consists of 4 different steps:

- Estimation of the NSB noise contribution from the RMS of the pedestal distribution, ΔP_i. In concordance with eq. 5.1.6, the calibrated noise Δp_i of the ith PMT is calculated as:
$$\Delta p_i = \frac{1}{l_i} \cdot \Delta P_i \cdot \chi \tag{5.1.7}$$

- A pixel is considered to be part of the shower image core if its signal is larger than three times its calibrated noise, $s_i \geq 3.0 \cdot \Delta p_i$, and if there is a neighboring pixel with the same property.

- A pixel is considered to be part of the shower image boundary if its signal is larger than 2.5 times its calibrated noise, $s_i \geq 2.5 \cdot \Delta p_i$, and if it has a neighboring core pixel.

- The signals of all pixels, which are neither core nor boundary pixels are set to zero.

After the image events have been cleaned, the filter cut is applied to the data. It consists of several independent selection criteria:

- An additional software trigger: at least 2 out of the inner 91 pixels are required to have a calibrated signal s_i above the trigger threshold (i.e. 13 Pe for NOM00). From MC simulations there are no γ-ray events expected to trigger in the outer most ring of the CT1 camera.

- Shower events with more than 92 core pixels nearly cover the whole camera. Since the image parameters for these events are poorly determined, they are removed from the data sample.

- Shower events with less than 4 core pixels or $SIZE$ values below 60 Pe have not enough structure for γ-hadron separation or might be caused by NSB noise (e.g. bright stars) and therefore give systematic differences compared to the MC simulations. These events are also rejected.

- Shower events with a pointing error (i.e. the angular distance between the telescope and the target direction) larger than 0.1° are rejected (telescope tracking error).

- Data taken during exceptional high or low trigger rates (6σ above or 8σ below the mean trigger rate) are removed and the observation time (i.e. the run duration) is re-adjusted accordingly. The high trigger rates are mainly due to artificial light sources (e.g. car light) and low rates may be due to a temporarily closed camera, dew deposition on the mirrors or a fog/cloud layer.

In order to select data taken under reasonable atmospheric conditions, several additional steps are performed. First, the ACT operator run-books are searched for notes on bad weather conditions and the corresponding data are removed. In addition, the atmospheric extinction measurements from the Carlsberg Automatic Meridian Circle are used whenever available. The extinction coefficient in the Johnson V-band is required to be below 0.25. Finally, the mean trigger rate after filter[5] is investigated. Taking into account the zenith angle of the observation, all runs with a mean trigger rate of more than 2σ away from the sample mean are removed. Care must be taken, since a small trigger rate might also be due to a different HV setting. These runs have to be analyzed separately.

5.1.3 Determination of the HILLAS parameters

This section summarizes the formulas, used to calculate the HILLAS image parameters from the calibrated PMT signals [172]. In the following, x_i and y_i denote the pixel coordinates (in degrees; the origin being the center of the camera) and s_i denotes the calibrated signal in the ith PMT.

The different moments of the signal distribution in the camera are then given by:

$$\begin{aligned}
\langle x \rangle = \sum_i s_i x_i / \sum_i s_i \quad &, \quad \langle y \rangle = \sum_i s_i y_i / \sum_i s_i \\
\left\langle x^2 \right\rangle = \sum_i s_i x_i^2 / \sum_i s_i \quad &, \quad \left\langle y^2 \right\rangle = \sum_i s_i y_i^2 / \sum_i s_i \\
\langle xy \rangle \quad &= \quad \sum_i s_i x_i y_i / \sum_i s_i \\
\sigma_x^2 = \left\langle x^2 \right\rangle - \langle x \rangle^2 \quad &, \quad \sigma_y^2 = \left\langle y^2 \right\rangle - \langle y \rangle^2 \\
\sigma_{xy} \quad &= \quad \langle xy \rangle - \langle x \rangle \langle y \rangle
\end{aligned} \tag{5.1.8}$$

If the orientation of the shower image in the camera is expressed by $y = ax + b$, we have (with $d := \sigma_y^2 - \sigma_x^2$):

$$\begin{aligned}
a \quad &= \quad \frac{d + \sqrt{d^2 + 4\sigma_{xy}^2}}{2\sigma_{xy}} \\
b \quad &= \quad \langle y \rangle - a \langle x \rangle
\end{aligned} \tag{5.1.9}$$

and the Hillas image parameters are calculated as:

$$\begin{aligned}
CONC \quad &= \quad \frac{s^{max} + s^{2nd\,max}}{\sum_i s_i} \\
WIDTH \quad &= \quad \sqrt{\frac{\sigma_y^2 + a^2\sigma_x^2 - 2a\sigma_{xy}}{1 + a^2}} \\
LENGTH \quad &= \quad \sqrt{\frac{a^2\sigma_y^2 + \sigma_x^2 + 2a\sigma_{xy}}{1 + a^2}} \\
DIST \quad &= \quad \sqrt{\langle x \rangle^2 + \langle y \rangle^2} \quad \text{and} \\
ALPHA \quad &= \quad \arcsin\left(\frac{|b|}{DIST \cdot \sqrt{1 + a^2}}\right)
\end{aligned} \tag{5.1.10}$$

[5] The trigger rate before filter cuts strongly depends on the NSB and is therefore unsuitable here.

(here, s^{max} denotes the maximum and $s^{2nd\,max}$ the 2nd largest pixel signal in the shower image).

In principle there is considerable potential for improvement (e.g. including the signal errors), but this work is still under development and beyond the scope of this thesis.

5.1.4 Moon observations

Until 1997, only observations during dark nights had been performed with the HEGRA CTs. The above mentioned tailcut procedure was introduced to analyze these data and the results were accurate and reliable. In 1997, when extended observations during the presence of moonlight were performed, the same tailcut procedure was used to analyze the data. Later it turned out, that a modified tailcut procedure was necessary to circumvent a deficiency in this technique.

The reason for the deficiency can be seen in fig. 5.1.1 a), showing the calibrated pedestal noise as a function of the run number for four consecutive observation days within the Mkn 501 HV06 data sample. The two prominent features can both be attributed to the increased NSB noise due to the moonlight. The decreasing (from day to day) pedestal noise values are a consequence of the changing moon phase and the increase of the pedestal noise after the beginning of an observation at a given day is due to the rising moon. Since the tailcut depends linearly on the pedestal noise, the changes in the pedestal noise strongly affect the obtained image parameters (e.g. the $WIDTH$, fig. 5.1.1 b). As a result, the cut-efficiency (sec. 5.3.3) and therefore the calculated flux values depend on the NSB noise during the observation.

The following modifications on the tailcut are based on the argument, that since the intrinsic Cherenkov light distribution of an EAS is independent of the NSB noise, the obtained shower images should also be made basically independent of the NSB[6]. The minimum signal of a pixel to become a core or boundary pixel was then re-defined according to: $s_i \geq 3.0 \cdot f(\Delta p_i)$ and $s_i \geq 2.5 \cdot f(\Delta p_i)$ respectively. The function $f(\Delta p_i)$ was empirically derived from the moon observation data and was chosen such, that the image parameter distributions for a given HV setting do not change with the pedestal noise. Depending on the HV setting of the observation, this function is given as (fig. 5.1.1 c):

$$f(\Delta p_i) = \begin{cases} 0.9 + 0.1 \log(\Delta p_i + 0.1) & \text{for } \Delta p_i > 0.9 \\ \Delta p_i & \text{for } \Delta p_i \leq 0.9 \end{cases} \tag{5.1.11}$$

(for HV00 data),

$$f(\Delta p_i) = \begin{cases} 1.9 + \log(\Delta p_i - 0.9) & \text{for } \Delta p_i > 1.9 \\ \Delta p_i & \text{for } \Delta p_i \leq 1.9 \end{cases} \tag{5.1.12}$$

(for HV06 data), and

$$f(\Delta p_i) = \begin{cases} 1.5 + 2.1 \log(\Delta p_i) & \text{for } \Delta p_i > 2.2 \\ \Delta p_i & \text{for } \Delta p_i \leq 2.2 \end{cases} \tag{5.1.13}$$

(for HV10, HV14 and HV16 data). As can be seen from fig. 5.1.1 d), the agreement of the $WIDTH$ distributions for the different data sets has improved significantly (the shown data has not been used to determine the function $f(\Delta p_i)$). For a discussion of the results obtained from the moon observations see sec. 6.2.

[6] Alternatively one could use for each set of NSB a separate MC simulation and cut optimization. Given the large number of different NSB sets, this approach is hardly practicable.

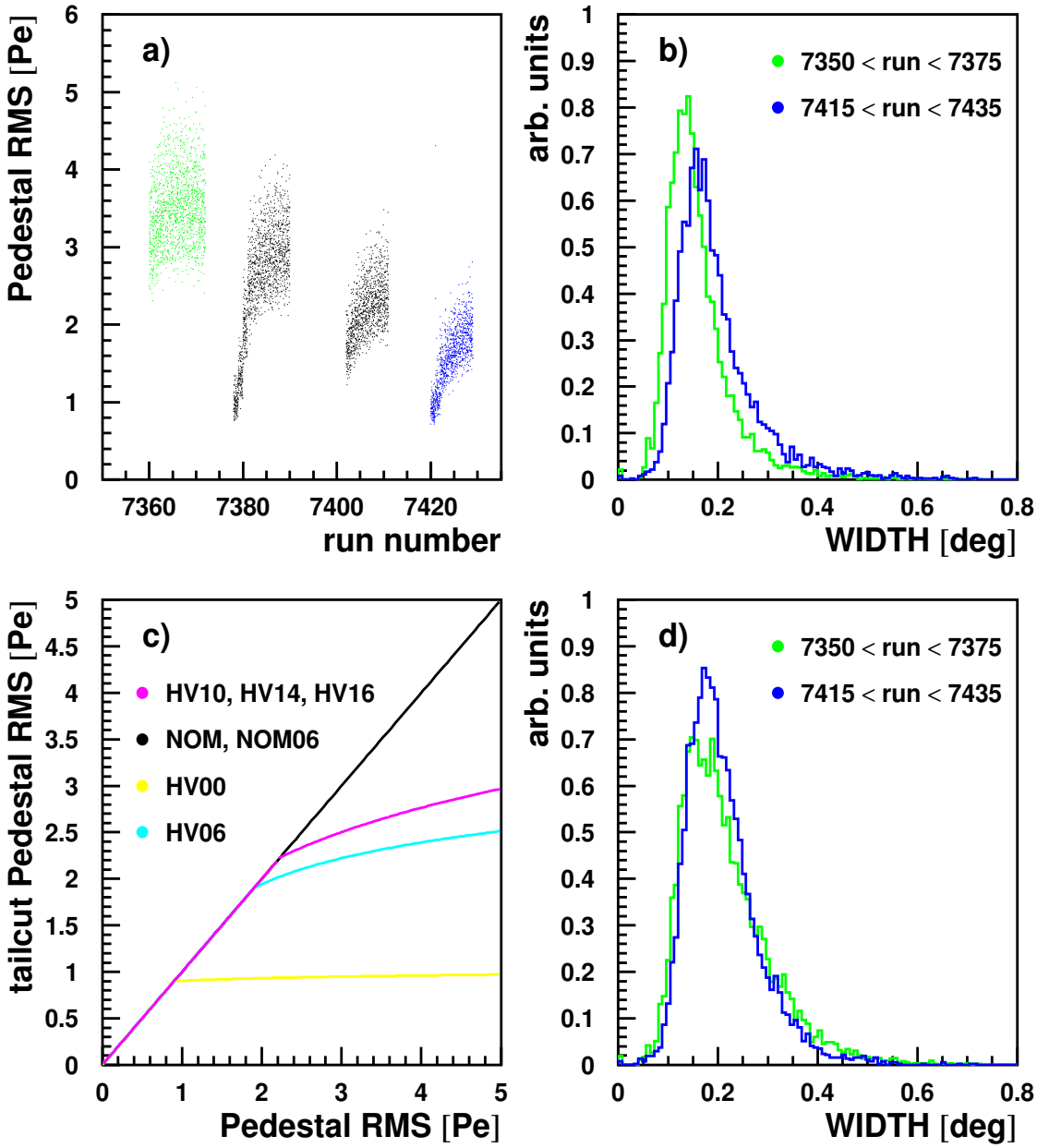

Fig. 5.1.1: a) Pedestal RMS values as a function of the run number for a Mkn 501 HV06 data sample. Each group of points belongs to one day. b) Distribution of the image parameter $WIDTH$ for the two marked data sets of fig. a) using the standard tailcut procedure. c) Shape of the modified tailcut pedestal RMS as a function of the measured pedestal RMS for the different HV settings in use. d) Distributions of the $WIDTH$ image parameter using the modified tailcut procedure.

particle type	zenith angle [degree]	radial distance [m]	energy region [TeV]	number of simulated showers
γ	0°	$0 - 250$	$0.05 - 30$	26000
γ	30°	$0 - 250$	$0.05 - 30$	10267
γ	45°	$0 - 250$	$0.05 - 30$	9200
proton	0°	$0 - 250$	$0.05 - 30$	228961

Tab. 5.2.1: Overview of the used Monte Carlo data base.

In conclusion it can be said, that despite the rather coarse implementation, the presented method already yields improved results. Nevertheless, further refinement is needed. A better solution would probably be to omit the tailcut and include the signal errors into the image parameter calculations instead.

5.2 Description of the Monte Carlo data

The *Monte Carlo* (MC) data used within this thesis has been produced by A. Konopelko and is described in [71]. The MC data sample (see tab. 5.2.1) consists of γ-ray showers at a 0°, 30° and 45° zenith angle. The proton showers were simulated at a 0° zenith angle with isotropically distributed inclination angles up to 3°.
In order to simulate the optical imperfections of the telescope, the light distribution within each pixel is folded with a two dimensional Gaussian distribution [126, p. 143] and partly distributed onto the neighboring pixels (5.7% in case of the 1997 data).

The simulation of the NSB is adopted to each observation data sample, i.e. the NSB is simulated according to a Poisson distribution with mean (and therefore variance) $\mu = (\Delta p_i)^2$. Since the pedestal noise values Δp_i are taken from the real observations, the NSB noise simulation is adapted to the individual observation conditions (moon observation, reduced HV, etc.).

5.3 Analysis methods

5.3.1 Estimation of energy and impact parameter from EAS

Once a source of high energy photons is found, further investigations are carried out. Besides the flux one of the most important issues is to determine the shape of the energy spectrum. Does the observed energy spectrum follow a strict power law or does it show a cut off? What are the highest energies observed? Does the energy spectrum change with time or with the intensity of the emission? The answers to these questions are needed for a better understanding of the physical processes taking place in the object or might give constraints on the density of the diffuse infrared background radiation, through which the high energy γs have to pass on their way to earth. In order to address these questions, the energy spectra must be determined as precise as possible. This requires a set of efficient γ-hadron separation cuts and, on the other hand, an efficient method to determine the energy of the primary particle. This chapter describes the method used to estimate shower energies for the CT1 data.

In order to highlight the difficulties of energy measurements we briefly recapitulate the situation in the HE (30 MeV to 10 GeV) domain. HE γs are observed by satellite borne detectors comprising a scintillator veto for rejecting the charged CR, a stack of thin converters and trackers for directional analysis and an electromagnetic calorimeter which absorbs the

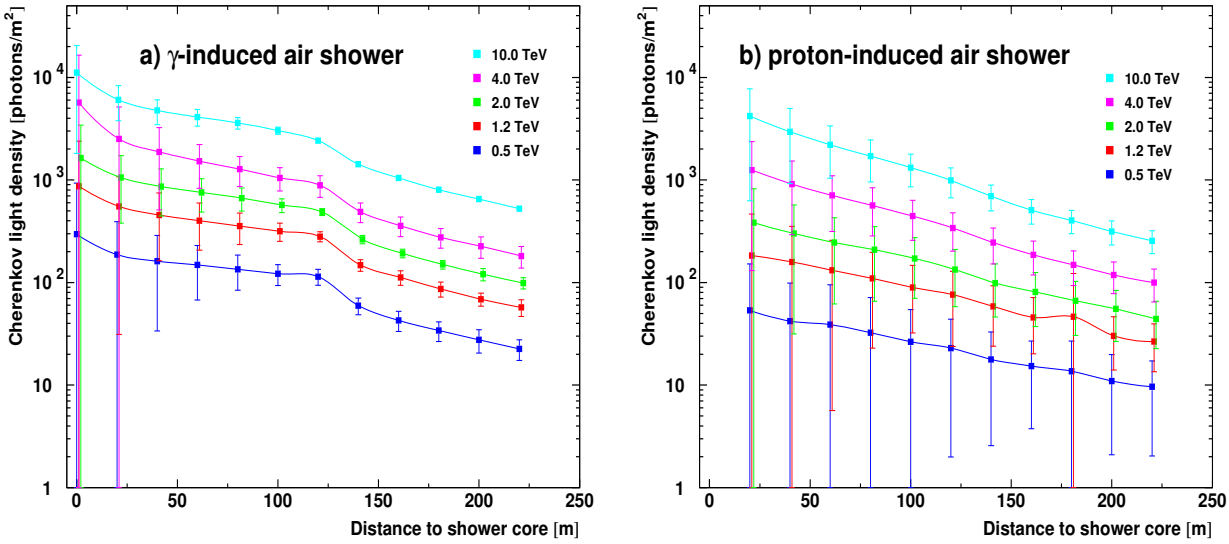

Fig. 5.3.1: Cherenkov photon density at 2200 m asl. for several primary energies as a function of the distance to the shower core (a - γ-induced air showers, b - proton induced air showers). The errors denote the inter-shower fluctuations. The lines are simple spline interpolations between the individual data points.

full energy. This calorimetric device has a rather good energy resolution (e.g. $(\sigma/E)_{fluct} \approx 0.01/\sqrt{E/\mathrm{GeV}}$ for homogeneous, fully active shower counters [21]). The situation is similar for ACTs, but now the calorimeter material is given by the atmosphere itself. The resulting signal, i.e. the total amount of Cherenkov light produced within an EAS, is in first order directly proportional to the shower energy and therefore to the energy of the primary particle (see end of sec. 4.1.2). In contrast to the satellite borne detector however, only a small fraction of the calorimeter signal is detected, i.e. the Cherenkov light collected by the ACT. Furthermore, second order corrections arise from the fact, that the Cherenkov light distribution on the ground depends on the distance to the shower core (see fig. 5.3.1). Other processes such as atmospheric transmission changes (sec. 4.1.4) and the height of the shower maximum[7] also influence the amount of observed Cherenkov-light. In summary, there are several additional factors which have to be taken into account when estimating the energy of individual air showers.

The basic idea of the energy estimation method is to use certain image parameters ($SIZE$, $WIDTH$, $LENGTH$ and the zenith angle ϑ) to determine the energy of the primary particle. Here, the image parameter $SIZE$ denotes the observed light yield and is in first order proportional to the primary energy. The other parameters are used to characterize some of the 2nd order corrections mentioned above. The functional relationship between the image parameters and the primary energy is determined from a sample of MC simulated air showers. Note, that for the time being the atmospheric transmission changes are ignored, since only mean values are yet included in the MC simulations. In order to compensate this deficiency, only observation data from clear nights are used. One specific complication for CT1 arises from the fact that the camera diameter is too small for high energy showers, i.e. the images are often truncated and the obtained $SIZE$ is too small.

[7] Due to the statistical processes involved in the evolution of an EAS, the position of the shower maximum of particles with the same energy is not a fixed value, but can fluctuate by up to a few interaction lengths (see fig. 4.1.9). The largest fluctuations occur in proton induced showers.

The estimation of shower energies is done in two steps (the index r stands for reconstructed):

- Estimation of the impact parameter I (see fig. 5.3.2) from the observed shower thus fixing the position of the ACT in the Cherenkov light pool on the ground. This is a relatively easy task for a system of Cherenkov telescopes [41] but much more complicated for a single telescope like CT1. The used functional Ansatz was: $I_r = I_r\,(DIST, WIDTH, \vartheta)$.
- Estimation of the shower energy by means of the reconstructed impact parameter I_r, the zenith angle ϑ, the $SIZE$, $WIDTH$ and the $LENGTH$ parameter: $E_r = E_r\,(SIZE, WIDTH, LENGTH, I_r, \vartheta)$.

In the following, both steps are described in detail.

The impact parameter I of a parallel (with respect to the telescope axis) EAS is given by the $DIST$ image parameter and the distance d between the ACT and the center of gravity of the EAS (see fig. 5.3.2). Since the distance d can be quantified by means of the image parameter $WIDTH$, the impact parameter becomes a function of $DIST$ and $WIDTH$: $I \propto f\,(DIST, WIDTH)$[8]. One point not taken into account so far, is the *Zenith Angle* (ZA) of the observation. For large ZAs the thickness of the atmosphere increases and the shower is further away from the telescope. The distance d to an EAS located at height d_0 and observed under a ZA ϑ is (fig. 5.3.2): $d \simeq \widetilde{d} = d_0/\cos\vartheta$ (since $\widetilde{d} \gg I$). Ignoring atmospheric absorption, the observed WIDTH is given in the first order as: $WIDTH \simeq \tan(WIDTH) = w/d = \cos(\vartheta)\cdot w/d_0$ (w denotes the absolute lateral width of the shower). Since the $DIST$ parameter is also proportional to $1/d$ ($DIST \simeq \sin(DIST) = I/d$) it has the same ZA dependence as the $WIDTH$ parameter. A simple Ansatz for the reconstructed impact parameter I_r is then (the index i stands for impact):

$$\begin{aligned} I_r &= f\,(DIST, WIDTH)\cdot g\,(\vartheta) \\ &= (a_i + b_i\cdot DIST + c_i\cdot WIDTH)\cdot \frac{(\cos^{-1}(\vartheta) + d_i\cdot\cos^{-2}(\vartheta))}{1+d_i} \end{aligned} \qquad (5.3.1)$$

Here, the function $f\,(DIST, WIDTH)$ is approximated by a Taylor series expansion using terms up to the first order. The term $g\,(\vartheta)$ denoting the ZA dependence also contains a 2nd order correction (the denominator is used to normalize this term to unity at $\vartheta = 0°$). The function parameters a_i-d_i are derived from MC generated air showers (see below).

The strategy to estimate the shower energy is similar to that of the impact parameter. The estimated energy is again considered a product of two independent functions $E_r = f'\,(DENS, LENGTH, I_r)\cdot g'\,(\vartheta)$, one to estimate the energy for events observed under 0° ZA and another one to take the zenith angle dependence into account. The first function depends on the light density ($DENS := SIZE/(WIDTH\cdot LENGTH)$, see fig. 5.3.3 c) the reconstructed impact parameter I_r and the $LENGTH$ parameter. The reason for using the light density instead of the $SIZE$ is as follows: For large energy and/or large distance parameters, the present camera of CT1 is too small to contain the entire shower image. If part of the shower image leaks out of the camera, the measured $SIZE$, as well as the $LENGTH$ and/or the $WIDTH$ values are underestimated. Using the ratio $SIZE/(WIDTH\cdot LENGTH)$ instead of the $SIZE$ therefore reduces the leakage effects on the energy estimation. The $LENGTH$ is used, since it also depends on the energy and provides additional information

[8] Another possible approach could be $I \propto f\,(WIDTH)\cdot\sin(DIST) \simeq f\,(WIDTH)\cdot DIST$, but the results are quite similar.

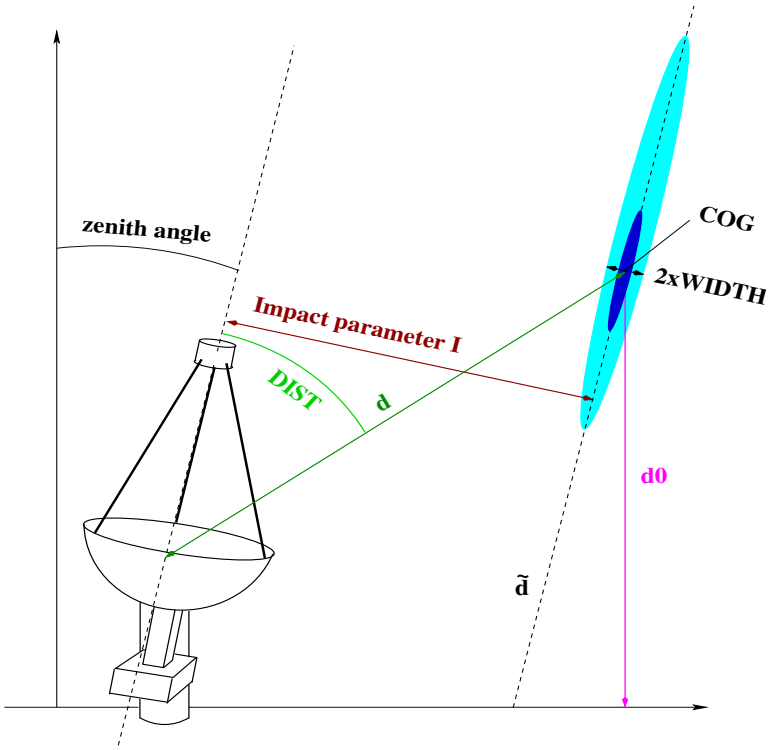

Fig. 5.3.2: Basic principle in estimating the impact parameter of an EAS (see text).

of the event. The function is again approximated by a Taylor series, but in contrast to the Taylor series expansion of the impact parameter Ansatz, second order terms are included (giving a small, but significant improvement). The Ansatz for the 2nd order terms was found empirically.

The function $g'(\vartheta)$ is similar to $g(\vartheta)$ from eq. 5.3.1, but now 2nd and 4th order terms are used. The reason is that the $SIZE$ and as a consequence thereof the $DENS$ parameter depends quadratically on $\cos(\vartheta)$[9]. In summary, the Ansatz to estimate the energy of an EAS is given by (the index e stands for energy):

$$\begin{aligned} E_r &= f'(DENS, LENGTH, I_r) \cdot g'(\vartheta) \\ &= (a_e + b_e \cdot DENS + c_e \cdot I_r + d_e \cdot LENGTH + e_e \cdot DENS \cdot LENGTH \\ &\quad + f_e \cdot I_r \cdot LENGTH) \cdot \frac{(\cos^{-2}(\vartheta) + g_e \cdot \cos^{-4}(\vartheta))}{1 + g_e} \end{aligned} \tag{5.3.2}$$

(the function parameters a_e-g_e are again derived from MC simulations).

In order to derive the parameters a_i-d_i and a_e-g_e, MC-generated γ-ray showers have been used (the simulations cover 0°, 30° and 45° ZA, see sec. 5.2). Since the energy of the primary particle and the impact parameter of a shower are known for the MC data (index MC), the quality of the energy- and impact parameter estimation for an individual shower can be quantified by:

[9] Since the radius of the Cherenkov light pool is proportional to the distance of the EAS, the area of the Cherenkov light pool (perpendicular to the shower axis) approximately scales with $1/\cos^2(\vartheta)$ and the energy density with $\cos^2(\vartheta)$. The $SIZE$, proportional to the number of measured Cherenkov photons, therefore scales with $\cos^2(\vartheta)$. In the case of the density, the '$WIDTH \cdot LENGTH$'-term is used to correct the leakage effects, so its zenith angle dependence does not cancel against that of the $SIZE$ (for small ZAs large leakage effects, for large ZAs with smaller $WIDTH$ and $LENGTH$ values small leakage effects).

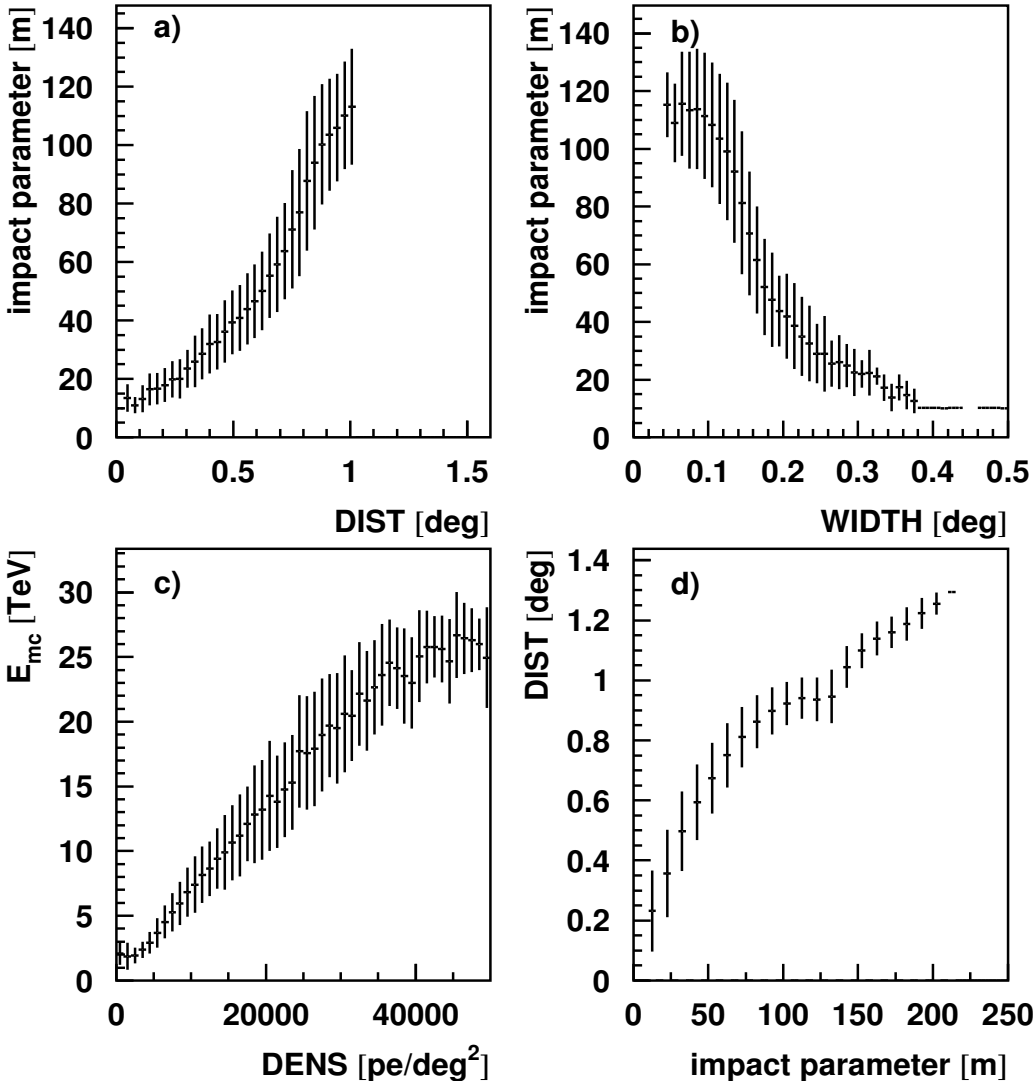

Fig. 5.3.3: Dependence between the image parameters $WIDTH$ and $DIST$ and the impact parameter (a and b) and between the density $DENS$ and the MC energy (c). The $WIDTH$, $DIST$ and density are the dominant parameters in estimating the impact parameter and energy. The last plot shows the result of camera leakage effects, which is explained as follows: Up to 130 m, where the hump is located (see fig. 5.3.1), a large amount of Cherenkov light is collected from each EAS. As the impact parameter exceeds 100 m and the $DIST$ parameter reaches 1°, an increased fraction of each shower light 'leaks' out of the camera and the $DIST$ parameter does not change significantly with the impact parameter. Beyond 140 m impact distance the amount of light collected from an EAS drops dramatically. Some of these showers still trigger the telescope, but the corresponding shower images are small and thus fit into the camera. For these showers, the correlation between $DIST$ and the impact parameter is restored. All results were obtained with MC data at 0° ZA and $DIST$ values below 1.0° (except fig. d).

$$\Delta I := (I_{MC} - I_r)/I_{MC} \quad (5.3.3)$$
$$\Delta E := (E_{MC} - E_r)/E_{MC} \quad (5.3.4)$$

The overall energy and impact parameter resolution is then given by the RMS of the ΔE and ΔI distribution (one entry for each MC event) and the bias of the energy and impact parameter estimation is given by the mean of the ΔE and ΔI distribution. In order to minimize the resolution, as well as the bias, a common minimization routine (MINOS, part of the MINUIT package [67]) was used. The goal was to find the set of parameters a_i-d_i and a_e-g_e such that the *Mean Squared Error* (MSE - sum of the variance and the bias squared) of the ΔE and ΔI distribution becomes a minimum:

$$MSE(\Delta I) := \sigma^2(\Delta I) + bias^2(\Delta I) = \left\langle (\Delta I)^2 \right\rangle \quad (5.3.5)$$
$$MSE(\Delta E) := \sigma^2(\Delta E) + bias^2(\Delta E) = \left\langle (\Delta E)^2 \right\rangle \quad (5.3.6)$$

Since, in both cases, the bias is equal to the mean value, the MSE of ΔI and ΔE is given by the 2nd algebraic moment of the ΔI and ΔE distribution, respectively.

The results obtained with this method are shown in fig. 5.3.4 and tab. 5.3.1. The overall energy and impact parameter resolution is 26% and 20% RMS, respectively and the mean bias is close to zero. The situation is changed when smaller (MC) energy regions are selected (see fig 5.3.5 a and b). The bias is changing with energy, having a minimum at -29% (ΔE) and -35%(ΔI) (first points, not within the scale of the plot) and a maximum at 18% (ΔE) and 10% (ΔI). The reason for this bias is explained as follows: At shower energies close to the threshold energy of the telescope, only showers from which an increased amount of Cherenkov photons is detected give a trigger. These are showers, which due to fluctuations in the shower development, evolve deeper in the atmosphere. The $DENS$ and $DIST$ values of these showers are therefore larger than the typical $DENS$ and $DIST$ values in that energy range. This deviation from the $DENS$ - energy and $DIST$ - impact parameter relationship cannot be compensated by the energy and impact parameter estimation functions. As a result, the energy and impact parameters are overestimated and the bias $\langle \Delta E \rangle$ and $\langle \Delta I \rangle$ becomes negative.

Leakage effects become more and more important at large energies, since the shower images also become larger with energy. As a result, the $DENS$ and $DIST$ values do not change with increasing energy and the energy and impact parameters are thus underestimated.
The bias cannot be corrected, since it does not show up when the reconstructed energy regions are considered (see fig. 5.3.5 c and d). Since there are events with underestimated energy (impact parameter) as well as overestimated energy (impact parameter) in each single reconstructed energy region, the bias values of all events just cancel out and the combined bias is (close to) zero.

Another important result of fig. 5.3.5 is the rather flat (within the whole energy range) energy and impact parameter resolution. The improved performance at high energies is due to the larger photon statistics of the shower images. The obtained resolution for the highest energy bin (fig. 5.3.5 c and d) is too small, since there were no events simulated at larger energies and therefore no events could spill down into this bin. The large error in fig. 5.3.5 d) is due to an outlier with 2 TeV MC energy and a density of $2.0 \cdot 10^4$ Pe/deg^2 which was mistakenly estimated as a 12 TeV event (but which is reasonable according to fig 5.3.3 c).

Remarks:

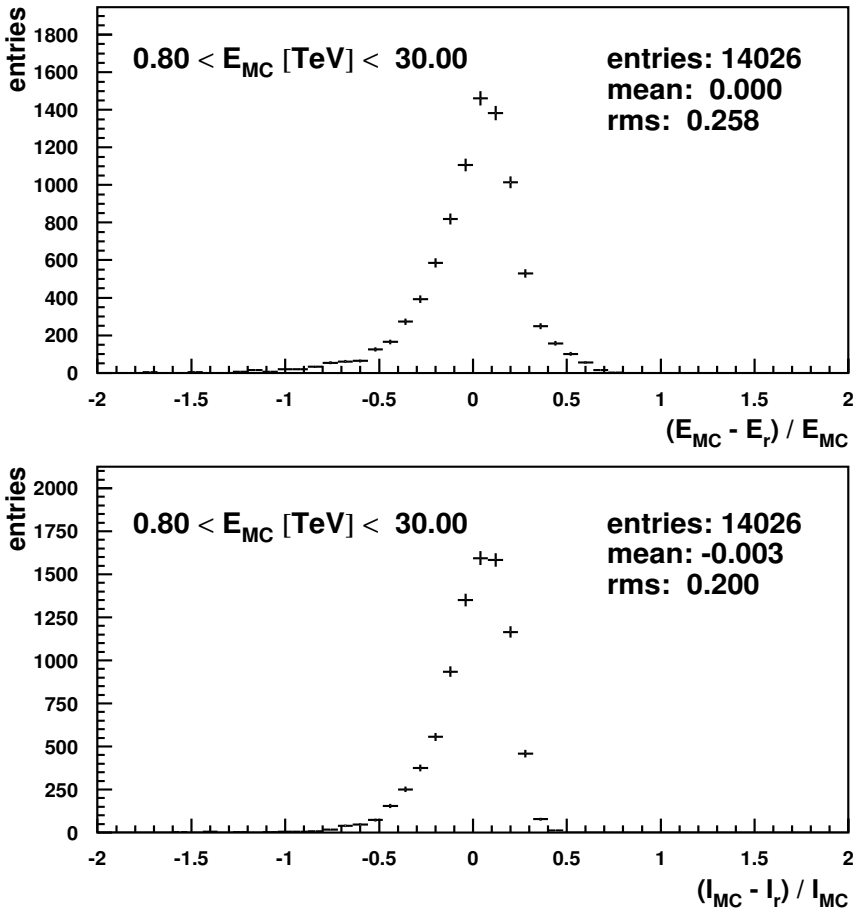

Fig. 5.3.4: Energy (top) and impact parameter resolution (bottom) as obtained with the presented method. The energy range of the MC data was 0.8 TeV $< E_{MC} <$ 30 TeV, the ZA values were 0° , 30° and 45°. The derived RMS values are 26% and 20% respectively. These numbers are larger than the corresponding standard deviations from a Gaussian fit (20% energy resolution with $\chi^2_{red} = 11.5$ and 14% impact parameter resolution with $\chi^2_{red} = 26.8$), since the (non Gaussian) tails get a higher weight in the RMS calculation. γ-hadron selection cuts and an additional $DIST < 1.0$ cut have been applied beforehand. The MC data was weighted according to a power law with differential spectral index $\alpha = 2.7$.

impact	value	energy	value
a_i :	(36.507 ± 9.3188) m	a_e :	(3.1156 ± 1.0532) TeV
b_i :	(140.85 ± 8.1527) m	b_e :	$(2.3867 \pm 1.2410) \cdot 10^{-4}$ TeV
c_i :	(-532.96 ± 43.504) m	c_e :	$(-0.033417 \pm 9.5428 \cdot 10^{-3})$ TeV m^{-1}
d_i :	0.45328 ± 0.27363	d_e :	(-11.578 ± 4.1143) TeV
		e_e :	$(1.3899 \cdot 10^{-3} \pm 4.8315 \cdot 10^{-4})$ TeV
		f_e :	(0.12764 ± 0.037741) TeV m^{-1}
		g_e :	0.24409 ± 0.10399

Tab. 5.3.1: Results for the function parameters of eq. 5.3.1 and 5.3.2 obtained after minimizing the MSE of the ΔE and ΔI distribution. ΔE denotes the energy resolution and ΔI the impact parameter resolution for an individual shower (see text and eq. 5.3.3 and 5.3.4).

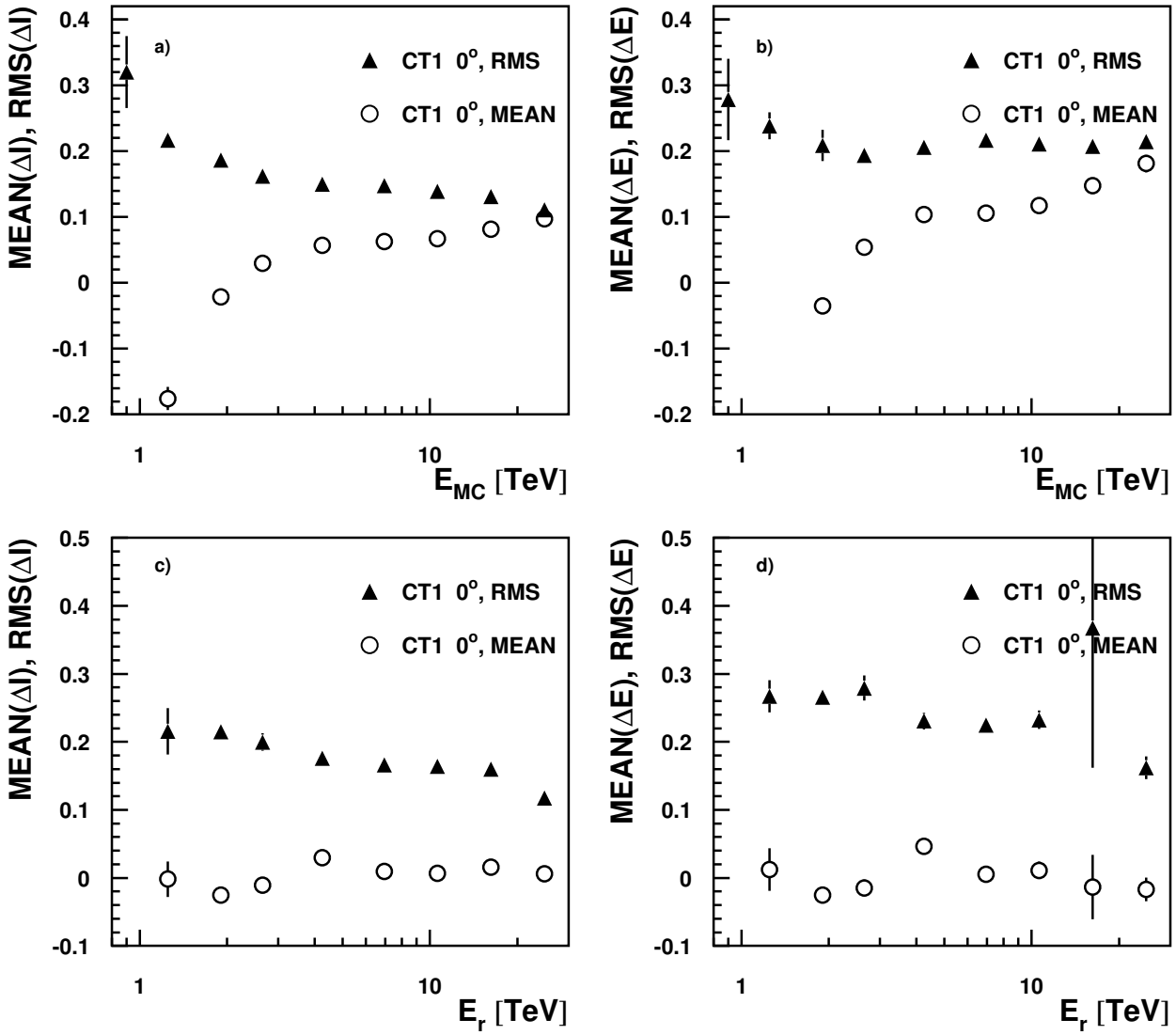

Fig. 5.3.5: Energy $(RMS\,(\Delta E = (E_{MC} - E_r)\,/E_{MC}))$ and impact parameter resolution $(RMS\,(\Delta I = (I_{MC} - I_r)\,/I_{MC}))$ as a function of the MC energy (a and b) and the reconstructed energy (c and d). Also shown is the mean $(MEAN\,(\Delta E))$ and $(MEAN\,(\Delta I))$ as a function of the reconstructed energy and impact parameter, respectively (points beyond the scale of the y-axis are omitted). γ-hadron selection cuts (ds97) and an additional $DIST < 1.0$ cut have been applied beforehand. The MC data was weighted according to a power law with differential spectral index $\alpha = 2.7$.

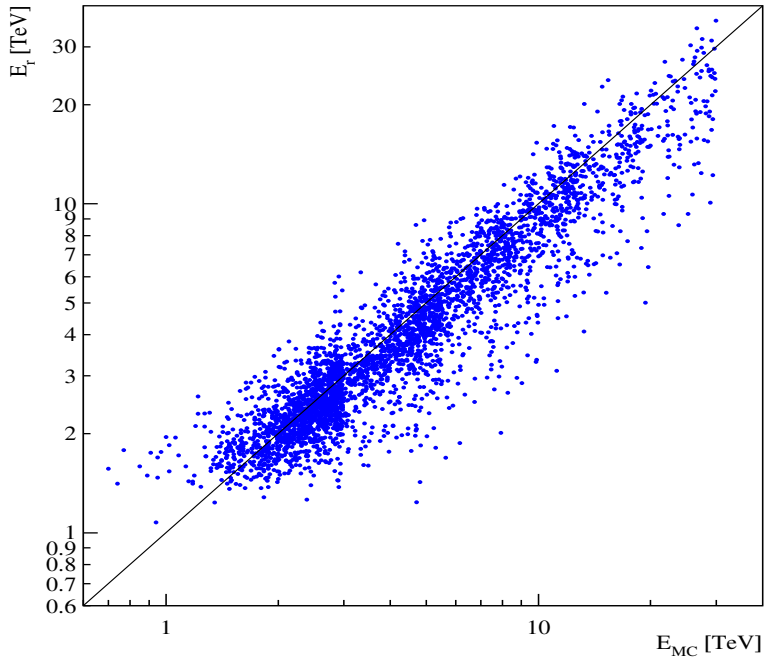

Fig. 5.3.6: Comparison of the reconstructed energy E_r with the simulated shower energy E_{MC} for the complete MC data sample (0°, 30° and 45° ZA). A γ-hadron selection cut (ds97) and an additional $DIST < 1.0$ cut was applied beforehand.

- In order to avoid the effect of the 'discontinuity' in fig. 5.3.3 d), a cut $DIST < 1.0$ was used for all the MC data. Omitting this cut gives an RMS energy resolution of 29% and an impact parameter resolution of 20%.

- Since the calculated image parameters are (nearly) independent of the HV setting of the PMTs and, with certain modifications, independent of the NSB (see sec. 5.1.4), one energy and impact parameter estimation function can in principle be applied to all moon- and no-moon data.

- The obtained results depend weakly on the used set of γ-hadron separation cuts. Differences are in the order of a few percent. Without any preselection (except the above noted $DIST < 1.0$ cut) the energy and impact parameter resolution is still 27% and 25% RMS, respectively. In order to obtain the best results, the energy and impact parameter estimation functions have been recalculated for each individual γ-hadron separation cut.

- A harder γ-spectrum (spectral index $\alpha = 2.0$) gives a somewhat better energy and impact parameter resolution of 24% and 18% while a softer γ-spectrum (spectral index $\alpha = 3.4$) gives worse results (28% and 22%). The reason is the improved reconstruction of E_r and I_r at higher energies (see fig. 5.3.5 a and b).

- The image parameters used in eq. 5.3.1 and 5.3.2 do not depend on the orientation of the shower image in the camera. The presented method should therefore also work for extended sources or off-axis observations. MC studies have not been carried out yet to confirm this conclusion.

resolution	impact parameter			energy		
spectral index α:	2.0	2.7	3.4	2.0	2.7	3.4
no preselection	25%	25%	27%	33%	34%	35%
$DIST < 1.0$	25%	25%	26%	25%	27%	30%
ds97 cuts	18%	20%	22%	28%	29%	31%
ds97 cuts + $DIST < 1.0$	18%	20%	22%	24%	26%	28%

Tab. 5.3.2: Energy and impact parameter resolution (RMS) for certain spectral indices and image selection cuts (see sec. 5.3.3).

- The quality of the presented method was checked by comparing the reconstructed energy and impact parameter of observed EASs to the results obtained with the CT-system (see sec. 6.3). A comparison of the real (E_{MC}) and reconstructed energy (E_r) for MC simulated EASs is shown in fig. 5.3.6.

- Using the MC impact parameter instead of the estimated one in eq. 5.3.2 results in an energy resolution of 20% RMS. Since the estimation of the impact parameter is also affected by leakage effects, better results should be obtained for a larger camera.

- The effect of variable atmospheric conditions (and therefore transmission) has not been taken into account and might slightly worsen the obtained results.

In summary the presented method provides a useful procedure to estimate the energy and impact parameter of individual EAS for a stand alone Cherenkov telescope. The impact and energy estimation functions can easily be recalculated for modified or new detectors, provided corresponding MC data is available. The obtained energy resolution is 24%-35% RMS and the impact parameter resolution is 18%-27% RMS (see tab. 5.3.2) depending on the used spectrum and γ-hadron selection cuts. Since a larger γ-statistics is more important than a slightly better energy resolution, the $DIST < 1.0$ cut is not used for any further analysis. The energy resolution throughout this thesis is therefore about 30%.

5.3.2 Determination of the significance of a signal

In γ-ray astronomy the calculation of significances is an important topic. Since the detector sensitivity and the signal to noise ratio is limited, the significance of a signal, i.e. the probability that the observed signal is due to a genuine source and not produced by background fluctuations, must be carefully derived. The next two sections describe the methods used for the CT1 data analysis.

a) Estimation of the background content in the signal region:

The first step in calculating the significance of a signal is to estimate the background content in the signal region[10]. Since a certain amount of events[11] in the signal region is due to γ-like

[10] For most ACTs (including CT1) the signal region denotes the region of small ALPHA values (see sec. 4.2.3) where, in the case of on-axis observations, nearly all γ-induced air showers show up. Another possibility is to estimate the incident angle of the primary particle with respect to the source location. The signal region then consists of all events with a small inclination angle. This approach is used for the CT-system.

[11] The term *event* is used for an observed shower event that satisfies a certain set of selection criteria (see sec. 4 and 5.3.3).

hadronic showers and not part of the source signal it is necessary to estimate this amount of hadronic events. Several methods exist to achieve this goal:

- The most common procedure requires consecutive On-Off observations. After an object has been observed for a certain amount of time ($\sim$ 20 min for CT1) the telescope is pointed back to its initial position and the same zenith angle range is scanned for background (Off) measurements[12]. The number of expected background events $\widehat{N_b}$ (in the following, $\widehat{N}_x$ denotes a random variable and N_x a sample thereof) is then calculated as:

$$\widehat{N}_b = r \cdot N_{off} \tag{5.3.7}$$

  N_{off} is the number of events in the signal region of the camera for the Off observation and r is the ratio of the On to Off observation time.

- A similar method [127] uses a set of independently taken Off data to estimate $\widehat{N}_b$. Advantages of this method are having a free choice when the Off observations are carried out and the possibility to accumulate a large sample of Off data thus reducing the error on $\widehat{N}_b$[13]. A disadvantage is that the ZA distributions of On and Off data sample can be different and must be properly taken into account. Also data of similar optical transmission conditions of the atmosphere must be used. Another problem is that the ratio r is calculated as the ratio of the number of events in the normalization region[14] for the two data samples (On, Off)[15]. In the case of small Off statistics the error on r becomes quite large and strongly affects the significance calculation.

- Other techniques use modified observation procedures. One of them, the so called 'Wobble Mode' [5], is used for the CT-system. In this technique, an object is observed off-axis with an offset of $\pm 0.5°$ (the change in sign meaning that frequent repositioning of the telescope with respect to the source is necessary to avoid systematic effects). If the object is observed at an offset of, say, $0.5°$, all events in the signal region have inclination angles within $0.5° \pm \Delta\xi$ (with $\Delta\xi \sim 0.3°$). The background content in the signal region is then given by the number of observed events at a $-0.5° \pm \Delta\xi$ inclination angle. No Off observations are needed here, but a sufficiently large ($\sim 4°$) camera is needed to reduce camera edge effects (see sec. 5.3.1). This method is therefore not suitable for CT1 and is not further taken into account.

- The method used for CT1 does not rely on any Off observations except for the confirmation of the method and routine stability monitoring.
  The idea is to use the ALPHA distribution in the normalization region ($20 < ALPHA < 80$, described by the first two terms in eq. 5.3.8)**, where no signal events are expected, and a smooth continuation Ansatz to estimate the background in the signal region and thus deduce $\widehat{N}_b$ in the signal region.**

[12] It is important to cover the same ZA range since all image parameters and the detector sensitivity depend on it (see sec. 5.3.3). Furthermore the order of the On-Off observations should be changed (Off-On observations) to avoid systematic effects.

[13] Estimating the error on $\widehat{N}_b$ as $\sigma(\widehat{N}_b) = r \cdot \sqrt{N_{off}}$ it is possible to reduce the error by a factor $\sqrt{2}$ when doubling the observation time ($r \to r/2, N_{off} \to 2 \cdot N_{off}$).

[14] In the case of On-axis observations, the normalization region for CT1 is defined as the range $20 < ALPHA < 80$. According to MC simulations less than 1% of the γ-showers lie within this region.

[15] Since the raw data contain lots of NSB induced, noisy events, the number of raw events strongly depends on the observed sky region. It is therefore necessary to apply the selection cuts beforehand.

Possible systematic differences between the On and Off data sample can be avoided here. Since a larger data sample is used to estimate $\widehat{N}_b$ (the number of events in the normalization region is typically four times larger than in the signal region) the statistical error on $\widehat{N}_b$ is smaller compared to data from consecutive On-Off observations. This method is explained in detail in the remaining paragraph.

The distribution of the image-parameter ALPHA is, as fig. 4.2.7 shows, quite simple. After applying the image shape cuts (sec. 5.3.3), the Off-data can be described sufficiently well by a polynomial of 2nd order. The linear term can be ignored since the $ALPHA$ distribution of hadron showers is flat (sec. 4.2.3). Since eq. 5.3.8 is also used in the cut optimization process (sec. 5.3.3) this property of the $ALPHA$ distribution is not destroyed by the derived selection cuts. In the case of the On-data, the normalization region solely contains background showers and should therefore follow the Off-data distribution. The main difference compared to Off-data is an additional peak (the γ-events) at small ALPHA values. A Gaussian distribution was chosen to describe the signal peak since a χ^2-fit to the data yielded sufficiently good results. The final function to describe the ALPHA distribution of a given On-data sample therefore consist of a Gaussian (excess source signal) on top of a polynomial (describing the background):

$$f_{On}\left(ALPHA\right) = a + b \cdot ALPHA^2 + \frac{c}{\sigma_p} \cdot \exp\left(-\frac{ALPHA^2}{2\sigma_p^2}\right) \tag{5.3.8}$$

The parameters of this function (a, b, c and σ_p) are derived from a χ^2-fit to the data. The number of expected background events $\widehat{N_b}$ is then given by the integral over the polynomial in the signal region, and the number of excess (or signal) events by the integral over the Gaussian in the signal region.

The results after applying this method to some data samples are shown in fig. 5.3.7 (the Off data are shown for comparison). As can be seen, the $ALPHA$ distributions are described very accurately by the fit. In the case of strong signals (fig: 5.3.7 a) the Gaussian solely describes the signal events, but for weak signals the Gaussian also contains part of the background distribution (fig. 5.3.7 c) and might therefore also affect the estimation of $\widehat{N_b}$. To circumvent this problem, the standard deviation σ_p can be determined once from a data sample with a prominent signal (i.e. Crab, Mkn 501) and then be used for all other (point-like) sources. This procedure is justified since the value of σ_p mainly depends on the pixel size of the camera for point-like sources. For the different data sets of Mkn 501 in 1997 the value of σ_p varies between $\sim 6^\circ - 7^\circ$; therefore a fixed value of $\sigma_p = 6.5^\circ$ was used. The results with this σ_p are shown in fig. 5.3.7 b and d. In the case of the strong signal the differences are marginal and the derived χ^2 is only slightly worse (12 and 13 degrees of freedom, respectively). For the weak signal however a fixed σ_p gives more reasonable results. All data presented in this thesis have therefore been analyzed with fixed $\sigma_p = 6.5^\circ$.

Remarks:

- The number of signal events can be derived in two ways, either by subtracting the estimated background $\widehat{N_b}$ from the number of events in the signal region, or by using the Gaussian part of eq. 5.3.8. The latter was used for all data presented here.
- The errors of the fit parameters can be used to estimate the errors on the number of excess and background events (see sec. 5.3.4).

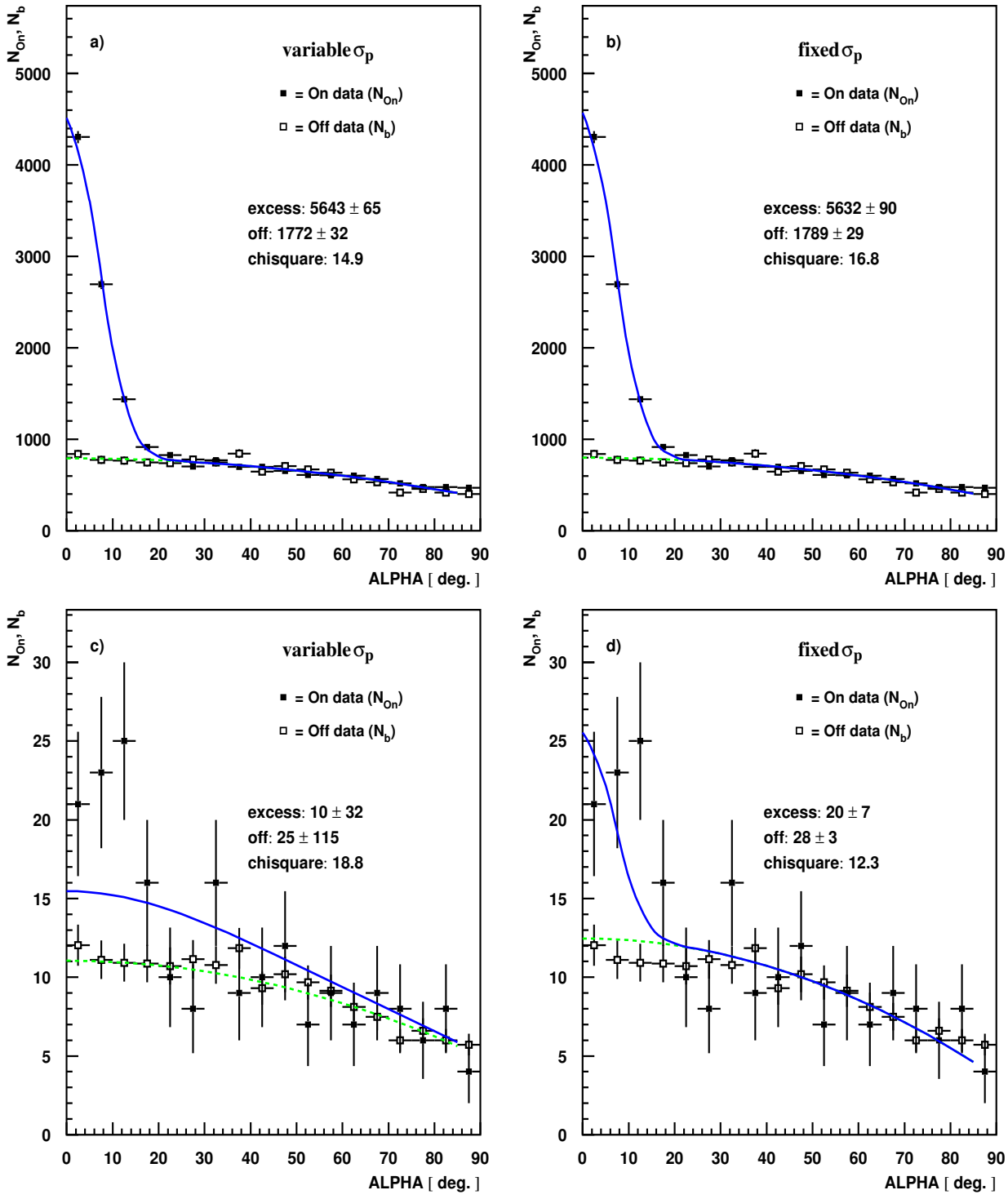

Fig. 5.3.7: Results for fitting eq. 5.3.8 (blue line) with variable σ_p (fig. a and c) and fixed $\sigma_p = 6.5°$ (fig. b and d) to the data (1st row: Mkn 501, 1997, no moon observation; 2nd row Mkn 501, 1997, moon observation, HV reduced by 14%). The green line denotes the polynomial part of the function and is used to estimate the background content in the signal region ($ALPHA < 11.2°$). The difference between the blue and the green line is due to the contribution of the Gaussian part of the function. The Gaussian part is therefore used to estimate the number of excess (or signal) events. The distribution of a properly normalized Off data sample (open squares) is shown for comparison. The errors on the number of excess and background events are derived from the fit parameter errors.

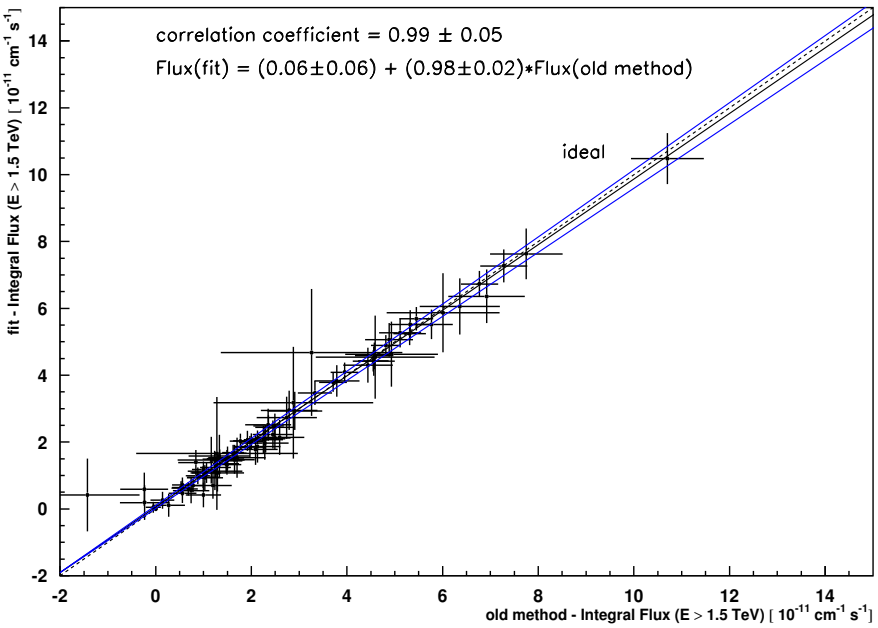

Fig. 5.3.8: Comparison of the Mkn 501 fluxes (proportional to the number of signal events) obtained from the old analysis method (x-axis) and the fluxes derived from the fit function (y-axis). The black line is a linear fit to the data and the blue lines mark the 1σ errors from the fit. The dashed line indicates a perfect correlation. Note the zero offset of both axis.

- Since the ALPHA distribution for Off data is rather flat for small ALPHA values, the linear term of the polynomial is set to zero (this is also expected theoretically for a rotational symmetric camera acceptance).

- It is assumed in eq. 5.3.8 that the signal peak is located at $ALPHA = 0$ (i.e. on-axis observations). In the case of off-axis observations, the signal peak is located at larger $ALPHA$ values and, in addition, the signal peak is not symmetric around its maximum. In principle eq. 5.3.8 can be generalized accordingly, but this has not been done yet.

- The last two bins of the ALPHA distribution are not included in the χ^2-fit since they might contain misinterpreted events (fluctuations might interchange the WIDTH and LENGTH of a shower image close to the camera edge).

In order to test the new method, the results have been compared to those obtained with the old analysis method (based on On-Off observations, see [127]). Figure 5.3.8 compares the derived fluxes for a Mkn 501 data sample, using the old (x-axis) and the new method (y-axis). The agreement is very good for both weak and strong signals and the new method is therefore justified. The correlation coefficient is consistent with unity (indicated by the dashed line). The black line is from a linear fit to the data and the blue lines are derived from the 1σ-errors of the fit parameters.

In summary, the presented method is very effective and only requires a minimum of Off data for consistency checks. The derived results are consistent with other methods, independently of the strength of the signal. This method can be adopted easily to parameters other than ALPHA (used to represent a source signal), as long as the background follows a smooth distribution which can be safely extrapolated into the signal region.

b) Calculation of the significance:

(this section is a short summary of the relevant parts from [175])
In ACT observations, the signal, i.e. the excess seen for a given object is calculated as [97]:

$$N_s = N_{on} - \widehat{N}_b \tag{5.3.9}$$

N_{on} is the number of events in the signal region,
$\widehat{N}_b$ is the number of expected background events in the signal region. $\widehat{N}_b$ cannot be measured directly but, as discussed above, there exist several possibilities to estimate its value.
Once $\widehat{N}_b$ is derived, the problem of calculating the significance for the observed excess (eq. 5.3.9) is solved by testing the null hypothesis

$$H_0 : \mu\left(\widehat{N}_s\right) = N_{on} - rN_{off} = 0 \tag{5.3.10}$$

(the observed excess is produced by a background fluctuation, i.e. the expectation value $\mu\left(\widehat{N}_s\right)$ of the excess is zero) against the alternative hypothesis

$$H_1 : \mu\left(\widehat{N}_s\right) > 0 \tag{5.3.11}$$

(a real signal is present in the data). If $\widehat{N}_{on}$ and $\widehat{N}_{off}$ follow a *Poisson Distribution* (PD)[16] this is equivalent to testing

$$H_0 : \mu_{on} = r \cdot \mu_{off} \tag{5.3.12}$$

against

$$H_1 : \mu_{on} > r \cdot \mu_{off} \tag{5.3.13}$$

According to [175] the best method for significance calculations is based on Fishers Exact Test [26]. Assuming that $\widehat{N}_{on}$ and $\widehat{N}_{off}$ follow a PD, the probability that a background fluctuation generates an excess equal or larger than the observed excess can be calculated. A comparison with the *Standard Normal Distribution* (SND) then yields the significance of the observed excess. Under the hypothesis that $\left\langle \widehat{N}_{on} \right\rangle = \mu_{on}$ and $\left\langle \widehat{N}_{off} \right\rangle = \mu_{off}$, the probability to have more or equal than N_{on} On-events for given $N_{on} + N_{off}$ is:

$$P_{fin} = \sum_{n=N_{on}}^{N_{on}+N_{off}} \left(\begin{array}{c} N_{on}+N_{off} \\ n \end{array} \right) p^n \cdot (1-p)^{N_{on}+N_{off}-n} \quad \text{with } p = \frac{\mu_{on}}{\mu_{on}+\mu_{off}} \tag{5.3.14}$$

The sum in eq. 5.3.14 is the *cumulative binomial probability* and can be estimated using the *incomplete beta function* $I_p(a,b)$ [130, p. 229].
Under the null hypothesis $H_0 : \mu_{on} = r \cdot \mu_{off}$ (i.e., the assumption that the excess N_s is caused by a background fluctuation) we have $p = \frac{r}{r+1}$ and $P_{fin} = I_p(N_{on,} N_{off} + 1)$. The significance of the signal is then derived from the SND as quantile[17] for the probability P_{fin}.

[16] N_{on} and N_{off} are derived from a χ^2-fit (see above) and do not strictly follow a PD. Nevertheless, since the estimated N_{on} and N_{off} agree with the data (following a PD, see fig. 5.3.8) the deviations can be ignored.
[17] The quantile x_q for a given probability q and probability density function f is defined by the equation $\int_{-\infty}^{x_q} f(x)\,\mathrm{d}x = q$ [25, p. 23].

5.3.3 Cut optimization

The efficiency of an ACT depends on several factors. On the one hand there are the contributions from the hardware such as PMT gain, QE of the PMTs, mirror area and reflectivity etc.. Improving the hardware set-up is expensive and time consuming. On the other hand there are the data analysis methods which strongly affect the γ-hadron separation capability and therefore also influence the efficiency of the ACT. In contrast to the hardware set-up, the analysis methods can be easily changed and thus play an important role in improving the efficiency of an ACT. This section describes a method to derive selection cuts with an improved γ-hadron separation compared to the constant cuts of sec. 4.2.3.

The so-called standard supercuts used to distinguish between γ- and hadron induced air showers are constant cuts (as described in sec. 4.2.3) and are applied to the entire data set, irrespective of changes in image parameters due to external parameters. These cuts imply that the image parameters of **all** good shower events must lie within a constant range (e.g. $0.16 < LENGTH < 0.3$). In general, these cuts are optimized on the largest class of showers, namely showers of small energy and at small zenith angles. High-energy showers, or showers observed under large zenith angles are basically ignored by this method due to their lower statistics and different image parameter distributions. Thus, an idea to improve the γ-hadron separation was to derive **dynamical cuts**, i.e. cuts which take the **dependence of the image parameters on the zenith angle, the impact parameter and the energy of the shower** into account. The advantage of the dynamical cuts is that they are nearly independent of the source spectrum. The first version of the dynamical cuts is described in [89], so the basic principles are only briefly mentioned here. The algorithm to optimize the dynamical cuts has been completely changed within this thesis and is therefore presented in detail.
There exist 5 main parameters which determine the image parameters of an air shower:

- the type of the primary particle
- the energy of the primary particle
- the zenith angle of observation
- the impact parameter and
- the orientation of the telescope axis with respect to the shower axis.

For a point-like source, all γ-ray showers are expected to have the same direction. The shower orientation, as well as the type of the primary particle, are therefore taken implicitly into account when training/optimizing the cuts on a data sample (containing also hadron showers). Thus, there are basically three independent main shower parameters: the energy, the impact parameter and the zenith angle ϑ. Only the zenith angle is measured directly with high precision, while the energy and impact parameter have to be replaced by measured quantities. According to sec. 5.3.1, the energy of an EAS is in first order proportional to the image parameter $SIZE$ and the impact parameter is proportional to the $DIST$ parameter. The three shower parameters can therefore be represented by the parameters ϑ, $SIZE$ and $DIST$.

The primary energy effects the image parameters $WIDTH$ and $LENGTH$[18]. High-energy showers are more extended and their images will thus have larger $WIDTH$ and $LENGTH$

[18] In contrast to the first version of the dynamical cuts, the $CONC$ cut is not used anymore. It proved to be superfluous in the case of dynamical $WIDTH$ and $LENGTH$ cuts.

values. EASs with larger impact parameter are located further away from the telescope. Their $WIDTH$ is therefore smaller compared to near showers. The $LENGTH$ value also decreases, since the 'directed' Cherenkov light from the lower parts of the air shower cannot reach the telescope anymore. EASs observed under large zenith angle develop further away from the telescope and less Cherenkov light can be detected partly due to the light spread over a larger area on the ground[19] and partly due to increased absorption losses. Therefore both, $WIDTH$ and $LENGTH$ decrease as a function of the ZA (see fig. 5.3.9). The $DIST$ parameter itself depends also slightly on the zenith angle and the shower energy. Showers with a small energy or large zenith angle develop further away from the telescope reducing the angle under which the shower is observed ($DIST$). Therefore the $DIST$ cut has also been made dynamical. In contrast to the constant supercuts the so-called dynamical cuts are now functions of the 3 main shower parameters (ϑ, $SIZE$ and $DIST$), i.e.:

$$\begin{array}{rcl} D_{low}\,(SIZE,\vartheta) < & DIST & < D_{up}\,(SIZE,\vartheta) \\ W_{low}\,(SIZE,DIST,\vartheta) < & WIDTH & < W_{up}\,(SIZE,DIST,\vartheta) \\ L_{low}\,(SIZE,DIST,\vartheta) < & LENGTH & < L_{up}\,(SIZE,DIST,\vartheta) \\ & ALPHA & < A_{up} = \text{const.} \end{array}$$

Since large shower images allow a more precise calculation of the $ALPHA$ parameter, the $ALPHA$-cut should in principle be $SIZE$ dependent too. In the case of CT1, however, there exists a fundamental problem: due to the small camera most of the images from high energy showers or showers with large impact parameter are truncated. Since the $ALPHA$ parameter of most of these showers is unprecisely calculated, there is virtually no $SIZE$ dependence of the $ALPHA$-distribution for CT1 data. The $ALPHA$-cut is therefore kept constant.

a) Determination of the dynamical cuts:

Each of the individual cuts (D_{low}, W_{low}, etc.) is described as a Taylor series. The variables of the Taylor series were chosen to be $\ln(SIZE)$, $DIST^2$ and $\cos(\vartheta)$ instead of $SIZE$, $DIST$ and ϑ itself. The (natural) logarithm of the $SIZE$ is more sensitive in the important low energy range whereas purely geometrical considerations lead to the linear dependence on $\cos(\vartheta)$ (see sec 5.3.1). $DIST^2$ was chosen to take care of the rapid changes at large $DIST$ values ($DIST > 1$). The dependence of the image parameters $LENGTH$ and $WIDTH$ as a function of the variables $\ln SIZE$, $\cos\vartheta$ and $DIST^2$ are shown in fig. 5.3.9 (these dependencies are basically the same for γ-ray and hadronic shower events).
The final Ansatz for each cut is then:

$$\begin{aligned} Cut_{low,up}\,() \;=\; & a + b\cdot DIST^2 + c\cdot[\cos(\vartheta) - 1] \\ & + [\ln(SIZE) - 4.1]\cdot\left[d + e\cdot DIST^2 + f\cdot[\cos(\vartheta) - 1]\right] \\ & + [\ln(SIZE) - 4.1]^2\cdot\left[g + h\cdot DIST^2\right] \end{aligned} \qquad (5.3.15)$$

(all cuts $Cut_{low,up}\,()$ and the $DIST$ parameter are in units of degrees, the $SIZE$ is in units of Pe)

Here, the *cut parameters* a-h[20] determine the shape (and therefore efficiency) of each

[19] Since these showers develop in a volume of the atmosphere where the refractive index is lower, the Cherenkov angle is somewhat smaller. As a result, some of the geometrical widening is compensated.

[20] In the case of the DIST cut, the parameters c, f and h are fixed to 0. For the ALPHA cut all parameters except a are fixed to 0.

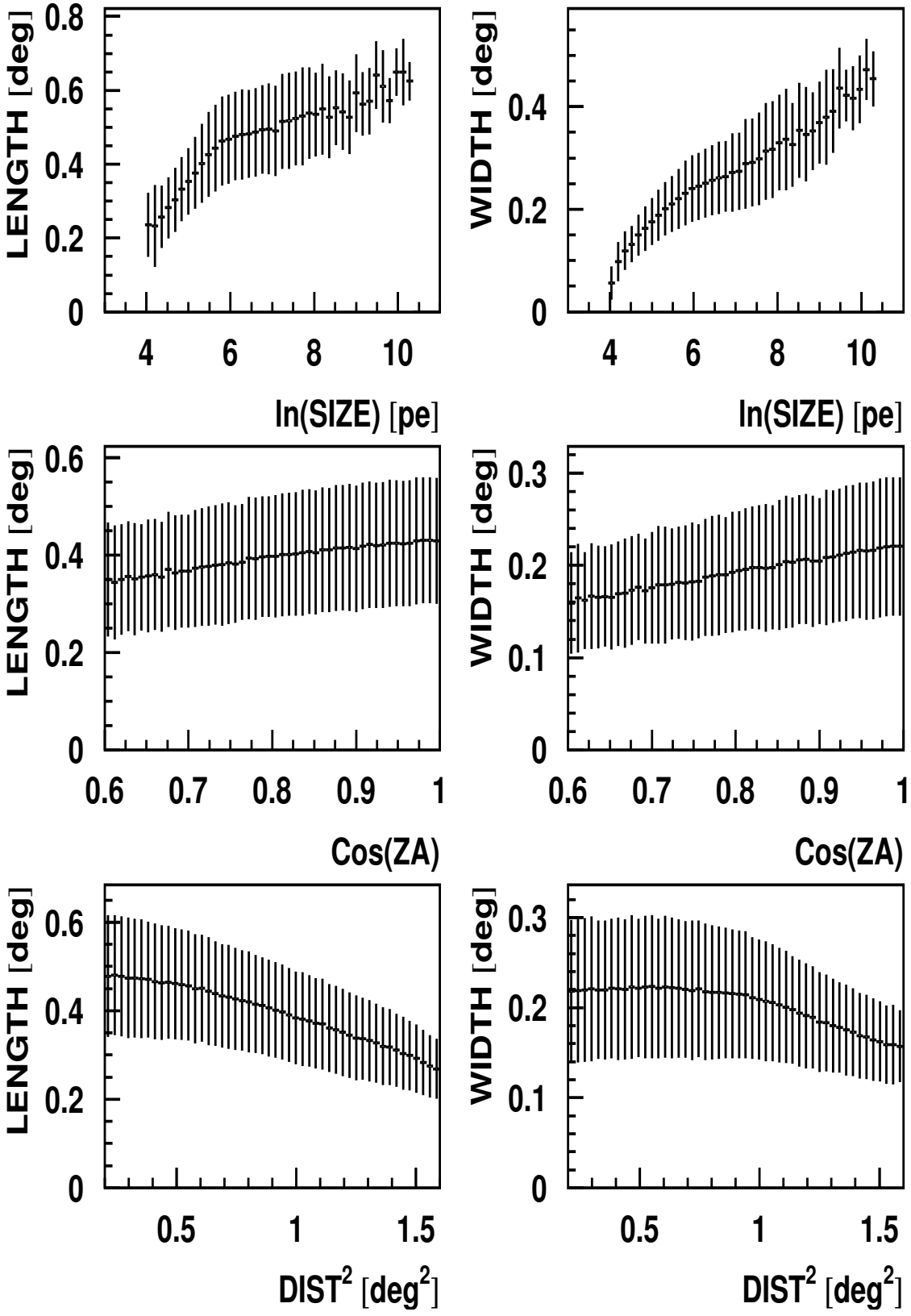

Fig. 5.3.9: Dependence of the image parameters $WIDTH$ and $LENGTH$ on the $SIZE$, zenith angle (ZA) and $DIST$ of the showers. The used data were derived from Off observations with a restricted ZA (except for the ZA plots) of ZA $< 10°$ and $ALPHA < 10°$. The RMS of the individual distributions is shown as error bars.

cut. The optimal set of cut parameters for a given data sample[21] is derived with a common minimization routine (the SIMPLEX method[22] of the MINUIT package [67]). The procedure is as follows:

1. Determination of the start parameters for the cuts. As start parameters the standard SCUTS were used.

2. Calculation of the significance for the resulting signal (excess) according to sec. 5.3.2.

3. Modification of all cut parameters until the signal has maximum significance.

Since the MC data for CT1 was generated for 3 discrete zenith angles (0° , 30° and 45°), the data is not too well suited for optimizing the zenith angle depending cuts. Therefore real observation data is used for this procedure.

Remarks:

- MC simulations do not perfectly describe the real data in general[23]. Taking real data should therefore give better results provided a data sample with a significant content of γ-ray events is used.

- Physics results must not be derived from the data sample used for the cut optimization since the derived signal is artificially enhanced. Tests with a Mkn 501 data sample divided into two equal sized subsamples showed that this artificial enhancement is in the order of $\sim 5\%$.

- For data samples without or with a small γ-admixture one can produce fake signals[24] by optimizing on small statistical fluctuations.

- In principle, the $ALPHA$-cut should also be $SIZE$ dependent, since large $SIZE$ values enable a better calculation of the $ALPHA$ parameter. Due to the small CT1 camera this is not reflected in the data and a constant $ALPHA$-cut was used instead.

- The calculated significance is not a smooth function of the cut parameters, but behaves like a step function (the number of events varies as the cuts change). It was therefore not possible to use the MINOS routine of the MINUIT package, which relies on function derivatives. The SIMPLEX method was used instead.

- In eq. 5.3.15 the companion terms of $\ln(SIZE)$ and $\cos(\vartheta)$ (i.e. 4.1 and 1) were chosen in order to give small factors for small $SIZE$ and ZA values.

In order to cope with the different data samples of the Mkn 501 observation in 1997 (see sec. 6), two different sets of cuts have been calculated, one to analyze the moon and no-moon data observed with the standard HV setting of the PMTs and another cut set to analyze the data observed with reduced HV (see tab. 5.3.3):

[21] Either a MC data set containing a mixture of background and γ-ray events or real data of a strong source.

[22] The *simplex* method is a multidimensional minimization algorithm due to Nelder and Mead (see [130] and reference therein).

[23] This is due to the complexity of the shower development and the detector. In the MC simulations some simplifications have to be made to cut computing time.

[24] It was possible to produce a fake 6σ signal for a given Off data sample. Applying the cuts to a different Off data sample however resulted in a 0.2σ signal.

- the cuts ds96 and ds97hv00 – calculated from the no-moon data, observed with the standard HV setting. This cut-set is applied to the no-moon data with reduced HV (by 6%) or to moon data with standard HV setting. In the first case, the cut-set is denoted ds96[25], in the second case ds97hv00 (the term hvxx is solely used for moon data; with xx describing the percentage of the HV reduction).

- the cuts ds97, ds97hv06 and ds97hv10 – calculated from the no-moon data, observed with reduced HV, this cut-set is applied to the no-moon data with standard HV or to moon data with reduced HV. The cuts are labeled as described above.
  This cut-set is also applied to the moon data samples with 14% and 16% reduced HV. However, these data samples are rather small and are therefore ignored in the remaining discussion.

A third static cut-set, scuts96, was calculated in order to compare the results obtained with the dynamical cuts. The same algorithm (program) was used, but all cut parameters except a (eq. 5.3.15) were fixed at zero. The static cuts were also derived from the no-moon data with standard HV setting.

The quality of a given image selection cut depends on several factors. A high sensitivity is needed in order to detect weak sources. Once a source is found, the energy spectrum is of primary interest and the γ-efficiency[26] and effective collection area (for a definition see sec. 5.3.4) of the cut is then important (both affect the statistical error of the spectrum and the alteration of the initial source spectrum due to the cut procedure). These topics are discussed in the rest of this section.

b) Effective collection areas:

The effective collection area (for the definition see eq. 5.3.17) for the different cuts, HV settings and zenith angles as a function of the energy of the primary γ-ray photon is shown in fig. 5.3.10 for MC data. The maximum effective collection area is about $4 \cdot 10^4 - 7 \cdot 10^4$ m^2 for ds97, ds97hv06 and ds97hv10 and about $5 \cdot 10^4 - 8 \cdot 10^4$ m^2 for the ds96 and ds97hv00 cuts. There is no significant zenith angle dependence of the dynamical cuts, unless caused by the different threshold energies. Only the ds96 and ds97hv00 cuts show a (slightly) increasing effective collection area up to the highest energies. The data sample used to calculate the other cuts (all but ds96 and ds97hv00) contains no clear photon signal at the highest energies. This energy region is therefore suppressed in the optimization process and the effective collection area decreases there. In the case of the static cuts (fig. 5.3.10 f), the collection area strongly depends on both the zenith angle and the energy of the primary γ-ray.

The differential excess rate after cuts is obtained from MC data by folding the effective collection area with a certain 'source' spectrum (see fig. 5.3.11 and eq. 5.3.16). As can be seen, the threshold energy of the cuts (defined as the maximum of each individual distribution) and the differential rate values, mainly depend on the zenith angle and HV setting of the observation, but only marginally on the NSB noise (no-moon vs. moon observations). In the case of the dynamical cuts, the differential event rate shows no zenith angle dependence unless caused by the different threshold energies (as expected from the shape of the effective collection area). The slope of the trigger rate is in good agreement with the simulated source

[25] The name is explained by the fact, that the reduced HV was the standard setting until April, 29th 1997. This cut is therefore also used for the analysis of 1996 data.

[26] Here, the γ-efficiency of a certain cut is defined as the ratio of the number of γs surviving the cut and the number of γs before the cut (i.e. after filter, see sec. 5.1.2).

cut:	ds96, ds97hv00							
parameter	a	b	c	d	e	f	g	h
$LENGTH_{up}$	0.310	0.0229	0.196	$3.32 \cdot 10^{-3}$	$6.65 \cdot 10^{-3}$	0.0446	$1.31 \cdot 10^{-3}$	$7.61 \cdot 10^{-4}$
$LENGTH_{low}$	0.193	$5.58 \cdot 10^{-3}$	0.0938	-0.0358	0.0217	0.0135	-0.0112	$6.26 \cdot 10^{-3}$
$WIDTH_{up}$	0.164	-0.0354	0.0769	0.0211	-0.0164	$6.03 \cdot 10^{-3}$	$3.60 \cdot 10^{-3}$	$-3.62 \cdot 10^{-4}$
$WIDTH_{low}$	0.0907	-0.0473	1.220	0.0134	-0.0493	0.0258	$4.19 \cdot 10^{-4}$	$-7.90 \cdot 10^{-3}$
$DIST_{up}$	1.261	—	1.064	0.0878	—	0.103	0.0174	—
$DIST_{low}$	0.601	—	0.363	-0.0522	—	0.123	-0.0102	—
$ALPHA_{up}$	12.02	—	—	—	—	—	—	—
cut:	ds97, ds97hv06, ds97hv10							
parameter	a	b	c	d	e	f	g	h
$LENGTH_{up}$	0.330	$3.54 \cdot 10^{-3}$	0.152	$5.62 \cdot 10^{-3}$	$-1.75 \cdot 10^{-3}$	0.0649	$6.14 \cdot 10^{-4}$	$-9.82 \cdot 10^{-4}$
$LENGTH_{low}$	0.188	$-3.47 \cdot 10^{-3}$	0.0317	0.0124	-0.0151	0.0123	$8.37 \cdot 10^{-4}$	$-4.01 \cdot 10^{-3}$
$WIDTH_{up}$	0.156	$-8.99 \cdot 10^{-3}$	0.0819	$3.30 \cdot 10^{-3}$	$1.69 \cdot 10^{-3}$	0.0256	$8.31 \cdot 10^{-4}$	$1.90 \cdot 10^{-5}$
$WIDTH_{low}$	0.0497	-0.0313	0.0140	-0.0194	-0.0157	$3.79 \cdot 10^{-3}$	$-3.45 \cdot 10^{-4}$	$3.71 \cdot 10^{-3}$
$DIST_{up}$	1.109	—	0.195	-0.0204	—	0.0816	$-5.09 \cdot 10^{-3}$	—
$DIST_{low}$	0.617	—	0.236	0.0181	—	0.0980	$3.13 \cdot 10^{-3}$	—
$ALPHA_{up}$	11.24	—	—	—	—	—	—	—
cut:	scuts96							
$LENGTH_{up}$	0.308	—	—	—	—	—	—	—
$LENGTH_{low}$	0.180	—	—	—	—	—	—	—
$WIDTH_{up}$	0.134	—	—	—	—	—	—	—
$WIDTH_{low}$	0.058	—	—	—	—	—	—	—
$DIST_{up}$	1.039	—	—	—	—	—	—	—
$DIST_{low}$	0.519	—	—	—	—	—	—	—
$ALPHA_{up}$	11.73	—	—	—	—	—	—	—

Tab. 5.3.3: Cut parameters, as derived from the Mkn 501 data samples. The names of the cut-sets (e.g. ds96) were chosen to reflect the data they are used for (see text).

	scuts96			ds96			signal
	signal	excess	background	signal	excess	background	gain
training sample	$44.4\,\sigma$	2913 ± 64	869 ± 21	$48.9\,\sigma$	3459 ± 70	979 ± 23	1.10
test sample	$42.2\,\sigma$	2752 ± 63	902 ± 21	$47.6\,\sigma$	3336 ± 69	981 ± 23	1.13
test sample $SIZE > 500$	$4.3\,\sigma$	21 ± 6	3 ± 3	$6.8\,\sigma$	81 ± 11	34 ± 4	1.58
test sample $\vartheta > 40°$	$10.6\,\sigma$	294 ± 25	253 ± 11	$12.0\,\sigma$	244 ± 19	97 ± 7	1.13
Mkn 501 reduced HV	$22.3\,\sigma$	816 ± 35	304 ± 12	$26.1\,\sigma$	1040 ± 39	331 ± 13	1.17
Mkn 501 moon, HV00	$19.2\,\sigma$	542 ± 28	158 ± 9	$20.7\,\sigma$	688 ± 32	243 ± 11	1.08
Crab, 95-96	$8.5\,\sigma$	263 ± 27	352 ± 13	$9.9\,\sigma$	343 ± 31	439 ± 15	1.16

Tab. 5.3.4: Results of the static scuts96 and dynamical ds96 cuts when applied to several data samples. The training sample consists of half of the Mkn 501 data (randomly chosen), observed during dark nights with the standard HV setting. The test sample contains the other half of the data. In order to test the cut efficiency at high energies a $SIZE > 500$ cut was used, which mainly selects shower events above 7 TeV. All but the Crab data were taken in 1997. The observation time for Crab was 36.3 h, the zenith angle range 6.6 - 55.1 degrees.

spectrum (black straight line), i.e. the initial spectrum is not changed much by the dynamical cuts. Again, the ds96 and ds97hv00 cuts show the best results. The static cuts (fig. 5.3.11 f) again show a strong zenith angle dependence and the agreement with the initial spectrum slope is worse compared to the ds96 cuts.
The threshold energy of the cuts must not be mixed up with the threshold energy of the telescope, which is determined by the maximum of the differential trigger rate without cuts.

The energy dependent γ-efficiency is shown in fig. 5.3.12 for MC data. The individual values mainly depend on the cut-set, but only slightly on the HV setting. Taking into account the zenith angle dependence of the cut thresholds, the γ-efficiency does not change very much with the zenith angle. As in the case of the effective collection area, the γ-efficiency is rather stable for the ds96 and ds97hv00 cuts. At γ-ray energies close to the threshold, the γ-efficiency drops rapidly. Comparing the results of the static cuts (scuts96, fig. 5.3.12 f), with those of the dynamical cuts (ds96, fig. 5.3.12 a) shows the improvement of the dynamical approach[27]. The energy and zenith angle dependence of the γ-efficiency is much weaker for the dynamical cuts than for the static cuts. As a result, the modifications of the observed energy spectra are less severe in the case of dynamical cuts and the errors for the derived spectra therefore smaller. The differences between dynamical and static cuts are smaller for the other cuts (ds97, ds97hv06 and ds97hv10), but as said before, this problem is related to the used training sample. Nevertheless, the zenith angle dependence of the γ-efficiency is superior for the dynamical cuts.

Besides the aim for a flat γ-efficiency, the main goal in deriving dynamical cuts is to maximize the sensitivity. While the first is obtained through the energy and zenith angle dependent cut-ansatz, the latter is a result of the cut optimization procedure. Table 5.3.4

[27] This procedure is justified, since both cut-sets were optimized on the same data sample.

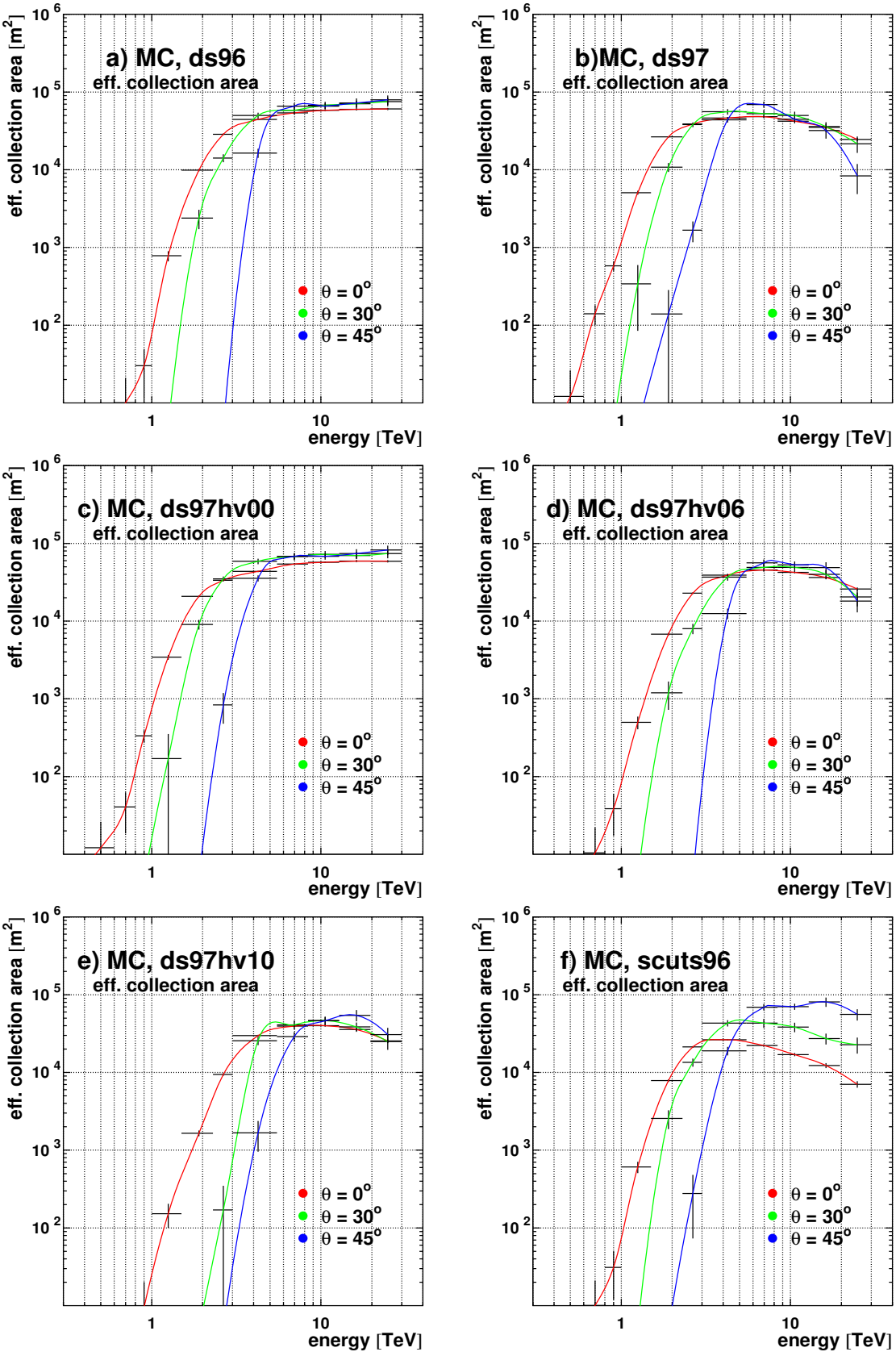

Fig. 5.3.10: The effective collection area for MC data as a function of the primary γ-ray energy, shown for several zenith angles, cut-sets and HV settings. The lines are a simple connection of the individual data points.

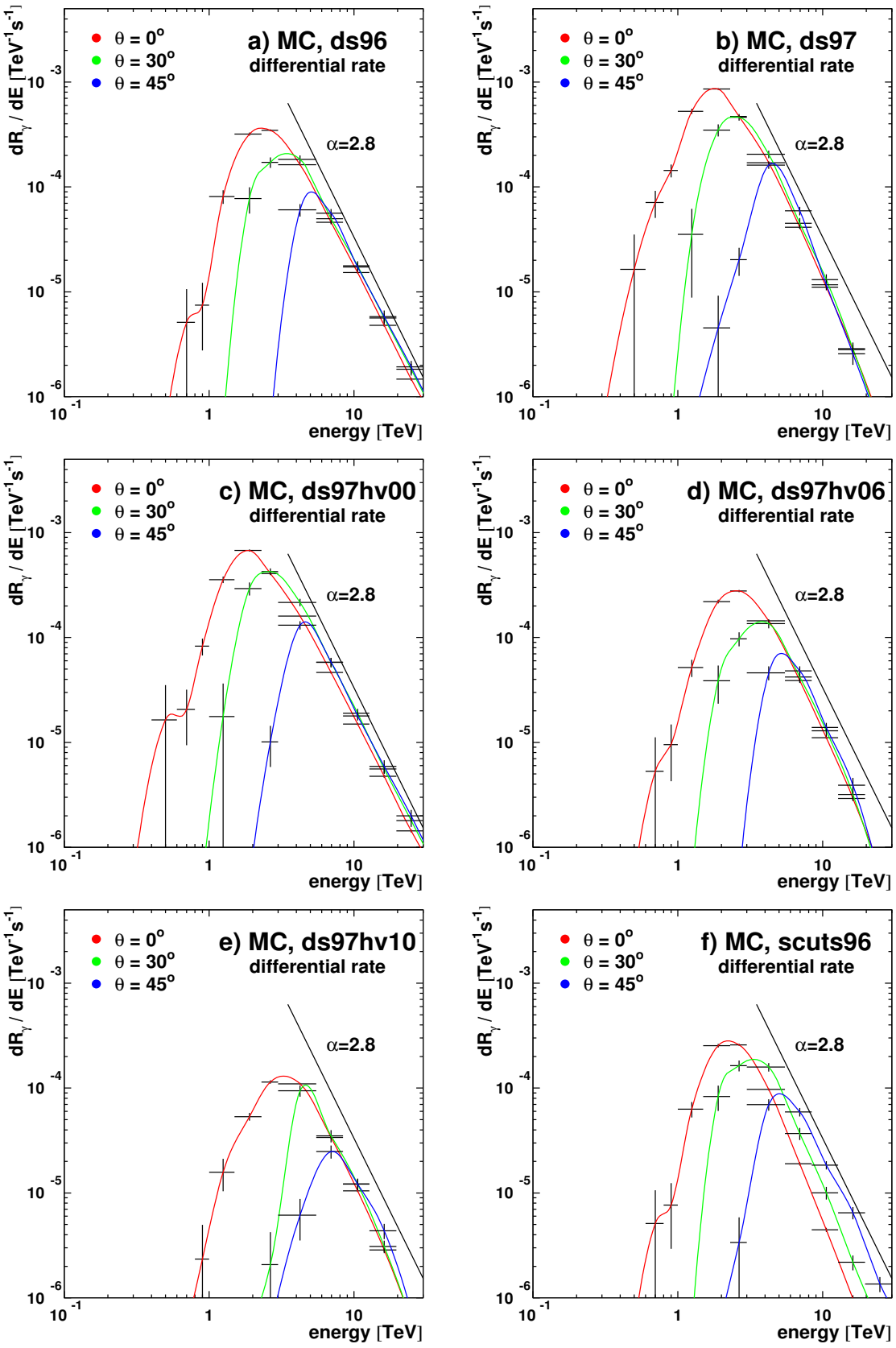

Fig. 5.3.11: Differential excess rate after cuts as a function of the primary γ-ray energy for several cut-sets, zenith angles and HV settings. All values correspond to a power law spectrum with integral flux above 1.0 TeV of $10^{-11}\,\mathrm{cm}^{-2}\mathrm{s}^{-1}$ and differential spectral index $\alpha = 2.8$. The colored lines are a simple connection of the individual data points, the straight line denotes the slope of the initial differential spectrum.

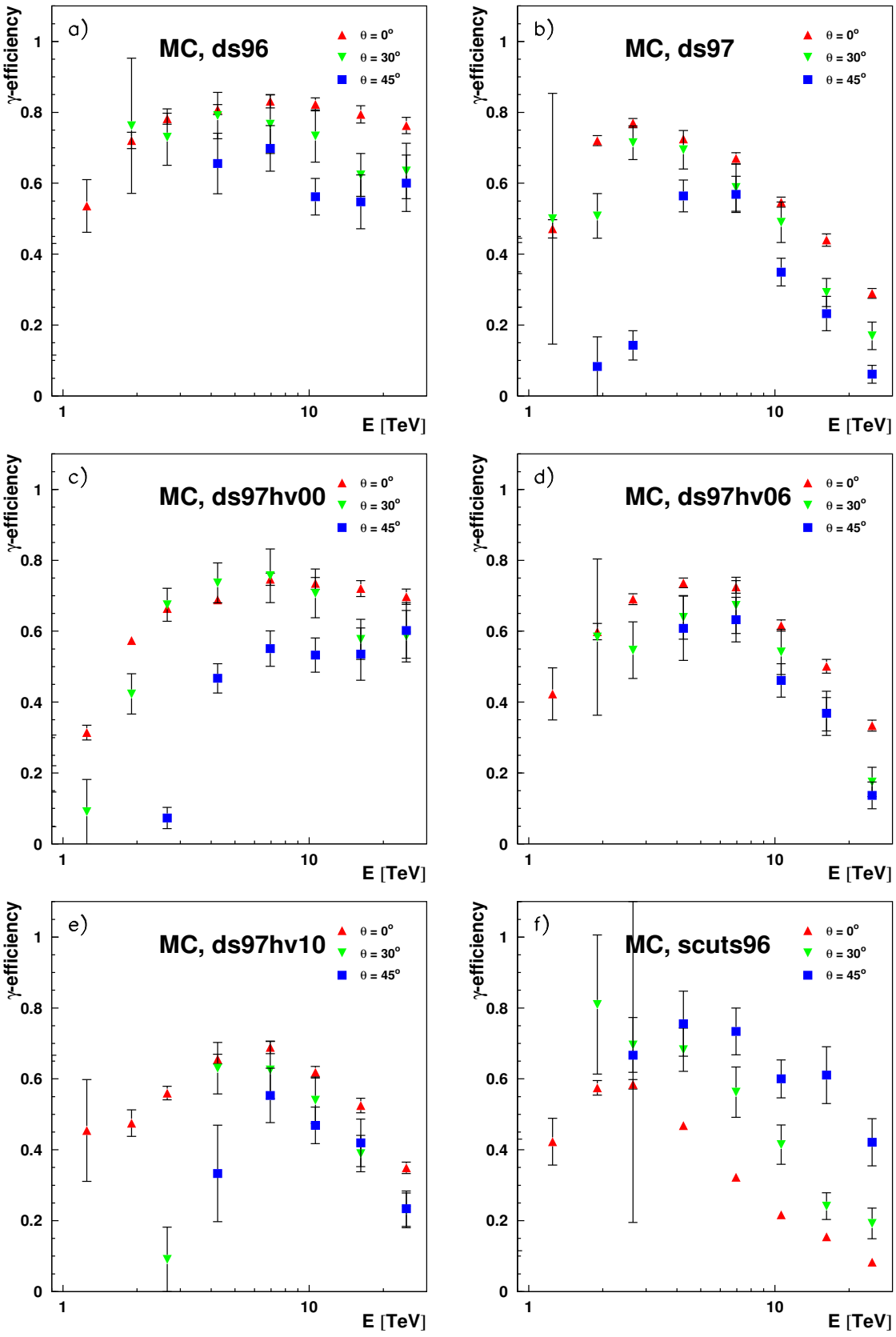

Fig. 5.3.12: γ-efficiency as a function of the energy for several zenith angles, cut-sets and HV settings. As in the case of the effective collection area, the reduced γ-efficiency at large energies for the ds97, ds97hv06 and ds97hv10 cut-sets is due to the lack of a large γ-ray signal in this energy region in the training sample.

shows the comparative results, as obtained with the scuts96 and ds96 cuts for several data samples. As can be seen, the dynamical cuts give about 13% improvement in significances for the total data samples. The improvement is much larger (58%), if only high-energy events are considered. The larger γ-efficiency of the ds96 cuts is reflected by the larger excess numbers, which is also important in reducing the statistical errors on the derived spectra.

In summary, the dynamical cuts give a clear improvement compared to static cuts, especially at high energies. The obtained significances are about 13% larger and the energy and zenith angle dependence of the γ-efficiency is much weaker. MC simulations at continuous zenith angles are under way and the problem of inappropriate data samples for the cut optimization will be solved in the future. At the present stage, moon observations are not treated in the optimal way. Improvements are expected with new dynamical cuts optimized on large statistics moon or MC data and with analysis methods adapted to the special conditions of moon observations (see sec. 5.1.4).

5.3.4 Calculation of flux values

This section describes the method used to derive (integral) flux values from CT1 data. The technique was introduced by D. Petry [126, p. 91ff] and is briefly summarized here.
The most important parameter in deriving flux values is the **effective collection area** A_{eff}. It connects the differential γ-ray flux $\mathrm{d}F(E)/\mathrm{d}E$ with the differential excess rate $\mathrm{d}R(E,\vartheta)/\mathrm{d}E$ through the equation:

$$\frac{\mathrm{d}F(E)}{\mathrm{d}E} = \frac{\mathrm{d}R(E,\vartheta)/\mathrm{d}E}{A_{\mathrm{eff}}(E,\vartheta)} \tag{5.3.16}$$

The effective collection area depends on the zenith angle ϑ, the shower energy E, the applied γ-selection cuts and on 'environment' variables like the conversion factor or the NSB contribution, which might change from observation to observation. The effective collection area is calculated from MC data according to:

$$A_{eff}(E,\vartheta) = 2\pi \int_0^\infty \mathcal{P}_\gamma(E,r,\vartheta)\, r\mathrm{d}r \tag{5.3.17}$$

Here $\mathcal{P}_\gamma(E,r,\vartheta)$ denotes the probability that a γ-ray shower with given energy E, zenith angle ϑ and radial distance r triggers the telescope and fulfills the γ-hadron selection criteria. It is assumed that the probability $\mathcal{P}_\gamma$ depends on the impact parameter of a shower but not on its azimuth angle. For binned data, eq. 5.3.17 translates into (assuming $\mathcal{P}_\gamma(E,r,\vartheta) = const.$ for each bin):

$$A_{eff}(E_i,\vartheta) = \sum_j \mathcal{P}_\gamma(E_i,r_j,\vartheta)\,\pi\left(r_{j,up}^2 - r_{j,lo}^2\right) \tag{5.3.18}$$

with

$$\mathcal{P}_\gamma(E_i,r_j,\vartheta) := \frac{N_{pass}(E_i,r_j,\vartheta)}{N_{sim}(E_i,r_j,\vartheta)} \tag{5.3.19}$$

being the ratio of the number of events passing all γ-hadron selection cuts and the number of simulated events for a given energy, distance and zenith angle bin[28]. The summation runs over all simulated impact parameter bins where the upper/lower boundary of the individual bins is given by $r_{j,up}$ and $r_{j,lo}$ respectively. In general the zenith angle is simulated for certain

[28] The zenith angle indices are omitted, since they are not used here.

discrete values (0°, 30° and 45° for CT1) such that the effective collection area for different ZA values must be interpolated.

Once the effective collection area is known, the (integral) excess rate R above a certain threshold energy E_{th}[29] can be estimated from eq. 5.3.16 according to:

$$R(\vartheta) \equiv R(E_{th}, \vartheta) = \int_{E_{th}}^{\infty} A_{eff}(E, \vartheta) \frac{\mathrm{d}F(E)}{\mathrm{d}E} \mathrm{d}E \tag{5.3.20}$$

In the case of binned data, this becomes

$$R(\vartheta) = \sum_i A_{eff}(E_i, \vartheta) \int_{E_{i,lo}}^{E_{i,up}} \frac{\mathrm{d}F(E)}{\mathrm{d}E} \mathrm{d}E \,. \tag{5.3.21}$$

Here $E_{i,up}$ and $E_{i,lo}$ denote the upper and lower bin boundary of the ith energy bin. In case, the spectral shape (but not the amplitude) of a given source is known, eq. 5.3.21 can be integrated. A comparison between the estimated excess rate $R(\vartheta)$ and the observed excess rate then gives an estimator for the amplitude (or integral flux) of the source.

In case $F(E) = F_{th} f(E) = F_{th} (E/E_{th})^{-(\alpha-1)}$ describes the integral source spectrum with known differential spectral index α[30], eq. 5.3.21 becomes:

$$\begin{aligned} R(\vartheta) &= \sum_i A_{eff}(E_i, \vartheta) \left[F(E_{i,lo}) - F(E_{i,up})\right] \\ &= F_{th} \cdot \sum_i \frac{1}{E_{th}^{-(\alpha-1)}} A_{eff}(E_i, \vartheta) \left[E_{i,lo}^{-(\alpha-1)} - E_{i,up}^{-(\alpha-1)}\right] \\ &= F_{th} \mathcal{R}(E_{th}, \alpha, \vartheta) \end{aligned} \tag{5.3.22}$$

($\mathcal{R}(E_{th}, \alpha, \vartheta)$ is defined by the second line of eq. 5.3.22). The estimated excess rate $R(\vartheta)$ and the observed excess rate $R_{ex}(\vartheta)$ agree, if the assumed spectrum and the MC simulation is correct. The integral flux above E_{th} is then:

$$F(E_{th}) = F_{th} = \frac{R_{ex}(\vartheta)}{\mathcal{R}(E_{th}, \alpha, \vartheta)} \tag{5.3.23}$$

In the case of different spectral shapes (different $f(E)$ functions) the defining equation for $\mathcal{R}(E_{th}, \alpha, \vartheta)$ changes, but eq. 5.3.23 still holds.

The statistical error of F_{th} is calculated from the error of R_{ex} (estimated from the errors on the *ALPHA*-fit, see sec. 5.3.2) and on $\mathcal{P}_\gamma$ (contributing to A_{eff}; it is assumed that $\Delta N_{pass} = \sqrt{N_{pass}}$ and $\Delta N_{sim} = 0$). The systematic error of F_{th} is mainly due to the uncertainties of the differential spectral index α and the conversion factor χ (see sec. 5.1.1). It can be estimated by calculating the integral flux with modified values $\alpha \pm \Delta\alpha$ and $\chi \pm \Delta\chi$.

5.3.5 Calculation of energy spectra

With the results of sec. 5.3.1 and 5.3.4, energy spectra can be derived in a straight forward manner. At first, the energy of each individual shower is estimated and the (reconstructed) differential excess rate $\mathrm{d}R(E_i^r, \vartheta) / \mathrm{d}E_i^r$ for each energy bin is calculated. MC data is

[29] This energy must not be confused with the energy threshold of the ACT. In principle E_{th} can have any value. If E_{th} is below the energy threshold, however, the excess rate has to be extrapolated from the covered energy region and therefore has large uncertainties.

[30] The shape of $F(E)$ is chosen such that the integral flux above a given energy E_{th} is simply $F(E_{th}) = F_{th}$.

energy range	$\kappa_i = \varepsilon_i^r / \varepsilon_i$
1.0 - 1.5	2.61 ± 0.58
1.5 - 2.3	0.72 ± 0.04
2.3 - 3.0	0.90 ± 0.05
3.0 - 5.5	1.16 ± 0.07
5.5 - 8.4	1.21 ± 0.10
8.4 - 12.8	1.34 ± 0.12
12.8 - 19.6	1.38 ± 0.18
19.6 - 30.0	1.93 ± 0.33

Tab. 5.3.5: Proportionality constants κ_i as derived for the ds97 cuts and MC simulations adjusted to the Mkn 501 data (for $\alpha = 2.7$).

used in a second step to derive the proportionality constants κ_i between $\mathrm{d}R\left(E_i, \vartheta\right)/\mathrm{d}E_i$ and $\mathrm{d}R\left(E_i^r, \vartheta\right)/\mathrm{d}E_i^r$. Equation 5.3.16 then becomes:

$$\frac{\mathrm{d}F\left(E_i\right)}{\mathrm{d}E_i} = \frac{\mathrm{d}R\left(E_i, \vartheta\right)/\mathrm{d}E_i}{A_{\mathrm{eff}}\left(E_i, \vartheta\right)} = \frac{\kappa_i}{A_{\mathrm{eff}}\left(E_i, \vartheta\right)} \frac{\mathrm{d}R\left(E_i^r, \vartheta\right)}{\mathrm{d}E_i^r} \tag{5.3.24}$$

Note: E_i denotes a MC energy bin, i.e. $1.5\ \mathrm{TeV} < E_{MC} < 2.3\ \mathrm{TeV}$ and E_i^r denotes the corresponding reconstructed energy bin $1.5\ \mathrm{TeV} < E^r < 2.3\ \mathrm{TeV}$.
The proportionality constant κ_i is a ratio of two factors. The first is the percentage ε_i^r of events with the correct energy in a given reconstructed energy bin E_i^r. The second is the percentage ε_i of events of the MC energy bin E_i, which have been reconstructed with the correct energy:

$$\kappa_i = \varepsilon_i^r \cdot \frac{1}{\varepsilon_i} = \frac{N\left(E_i^r \mid E_i\right)}{N\left(E_i^r\right)} \cdot \frac{N\left(E_i\right)}{N\left(E_i^r \mid E_i\right)} = \frac{N\left(E_i\right)}{N\left(E_i^r\right)} \tag{5.3.25}$$

$N\left(E_i^r \mid E_i\right)$: is the number of events in bin E_i^r, reconstructed with the correct energy
$N\left(E_i^r\right)$: is the number of events in bin E_i^r
$N\left(E_i\right)$: is the number of events in bin E_i

The parameters ε_i, ε_i^r and κ_i slightly depend on the shape of the energy spectrum (for $\alpha = 2.0$ and $\alpha = 2.7$ the difference of the κ_i-values is about 5-15%). They are therefore recursively calculated when deriving the energy spectra (see below). As an example, tab. 5.3.5 summarizes the κ_i values as obtained with the ds97 cuts. The MC simulations were adjusted to the Mkn 501 data sample with a spectral index of $\alpha = 2.7$.

The next step in deriving the energy spectrum is the calculation of the mean energy values $\overline{E_i}$ for each bin (i.e. the energy value assigned to each individual bin). For a known differential flux $f\left(E\right)$, the mean energy is calculated according to:

$$\overline{E_i} = \frac{\int_{E_{i,lo}}^{E_{i,up}} E \cdot f\left(E\right) \mathrm{d}E}{\int_{E_{i,lo}}^{E_{i,up}} f\left(E\right) \mathrm{d}E} \tag{5.3.26}$$

Since the differential flux $f\left(E\right)$ is not know in advance, the mean energy bin values $\overline{E_i}$ have to be calculated recursively, too. The main algorithm to estimate the spectrum is then as follows:
A power law spectrum with spectral index $\alpha = 2.7$ is used to get a first estimate of the mean

energy values $\overline{E_i}$ and the constants κ_i[31]. The energy spectrum itself is derived from a χ^2-fit of a model function (e.g. power law: $f(E) = f_0 \cdot E^{-\alpha}$ or a power law modified by a cutoff parameter[32]: $f(E) = f_0 \cdot E^{-\alpha} \cdot e^{-E/E_0}$) to the data pairs $(\mathrm{d}F(E_i)/\mathrm{d}E_i, \overline{E_i})$. Again *MINOS* from the MINUIT [67] package was used for this purpose. Once the spectral shape is known, $\overline{E_i}$, κ_i and the spectrum are recalculated. This continues until the relative difference of the fit parameters is below 1%[33].

A series of simulations have been carried out in order to test this method (see fig. 5.3.13 and tab. 5.3.6). First, a data sample of MC γ-ray events was used to generate randomly compound subsamples which follow an energy spectrum with spectral index α (power law spectrum) or spectral index α and cutoff energy E_0 (so called cutoff spectrum)[34]. The spectrum was then estimated for each subsample in the above mentioned way. The mean and RMS of the individual spectrum parameters α, f_0 and, if used, the cutoff energy E_0 were then calculated. From the results, presented in tab. 5.3.6 several conclusions can be drawn:

- cutoff spectra:
  - Fitting a power law Ansatz to the simulated cutoff spectra yielded an unacceptable χ^2 in most cases for small zenith angles. Due to the reduced energy range at larger zenith angles, no distinction is possible.
  - For small zenith angles, the simulated cutoff spectra are correctly reconstructed by the cutoff Ansatz. The derived spectral index as well as the cutoff energy are consistent with the initial numbers. At larger zenith angles, the covered energy range and/or the MC statistics are again too small to give clear results.
  - Cutoff spectra are only justified when the fit yields an error for the cutoff parameter E_0 that is considerably smaller than E_0.
- power law spectra:
  - The different spectral indices are well reconstructed by the power law fit. Due to the small MC statistics at larger zenith angles, the fit parameters have larger errors there.
  - Applying a cutoff fit to the power law spectrum also gives consistent results. Most of the derived spectral indices agree within their error with the simulated spectral index. The cutoff energy shows large fluctuations and uncertainties. For a 0° zenith angle, even the minimum cutoff energy $E_0^{min} = (11.8 \pm 12.6)$ TeV is still consistent with having no cutoff energy in the CT1 energy range. One can therefore conclude that a pure power law spectrum is unlikely to be interpreted as a cutoff spectrum. Due to the reduced number of data pairs for large zenith angles, it does not make sense to apply a cutoff fit. Nevertheless, the agreement with the spectral indices is good. Some fits give small cutoff energies, always coinciding with a small spectral index (e.g. $E_0 = 1.7$TeV and $\alpha = 0.7$), but as the power law fit with less parameters gives comparable χ^2-values, there is no justification for a cutoff spectrum.

[31] The κ_i-values for $\alpha = 2.0$, $\alpha = 2.7$ and $\alpha = 3.4$ were calculated from MC data. All other κ_i-values are obtained through linear interpolation.

[32] The exponential cutoff model is physically motivated due to absorption losses in the DEBRA.

[33] Since the estimated cutoff energy E_0 might undergo large fluctuations if there is no cutoff present in the data, the relative difference of E_0 is only considered for $E_0 < 15$ TeV.

[34] Since the subsamples were generated from one data base, they are not completely independent.

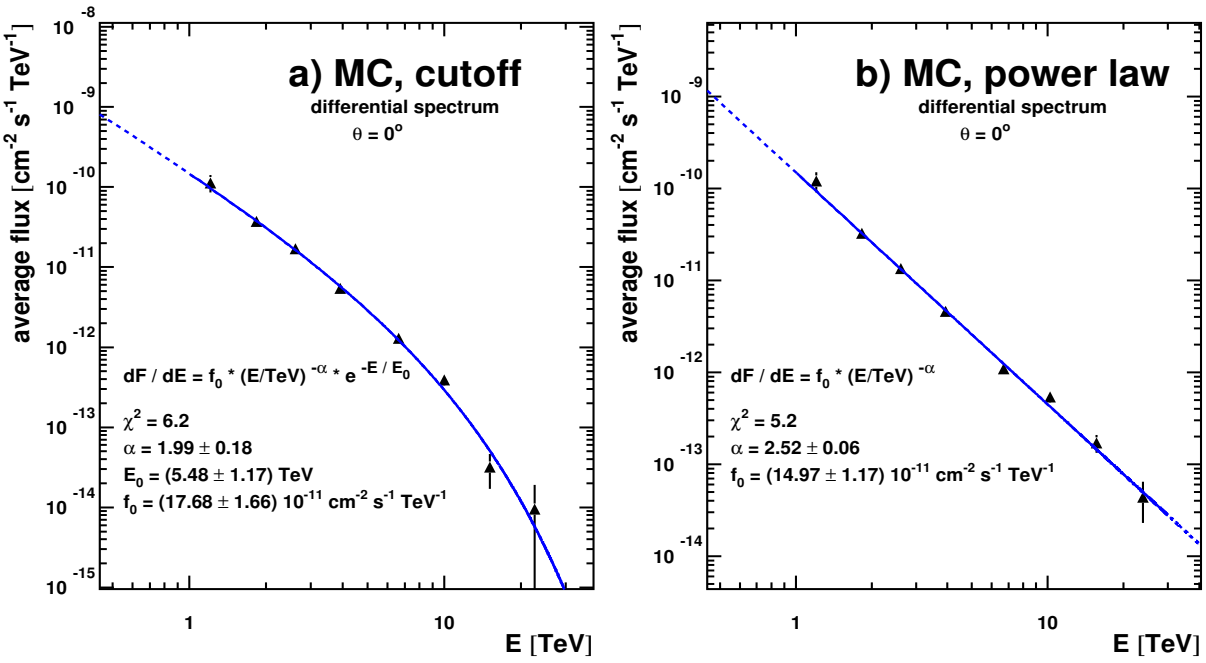

Fig. 5.3.13: Tests of the spectrum estimation algorithm when applied to different MC generated source spectra. In fig. a) a cutoff spectrum with spectral index $\alpha = 2.0$ and cutoff energy $E_0 = 6.0\,\mathrm{TeV}$ was simulated, in fig b) a power law spectrum with spectral index $\alpha = 2.5$. The solid line denotes the energy region used for the spectrum fit. All input parameters are accurately reconstructed.

- The same MC data sample was used for the calculation of the energy estimation functions, the calculation of the κ_i-values and the generation of the subsamples. The results might therefore be somewhat too optimistic. This seems to be also reflected by the small χ^2-values of nearly all fits.

- In some cases of cutoff fits at large zenith angles the spectrum calculation routine did not converge. These were not taken into account here.

The determination of the Crab spectrum is an important test of the presented method. Since the Crab is a strong and steady γ-ray emitter with a power law spectrum extending well above 20 TeV, it is often used as a standard candle of TeV astronomy. Figure 5.3.14 a) shows the results for the spectrum analysis of the 1995-96 Crab data. Due to the small data sample, the errors are somewhat large, but nevertheless, the agreement with other results (e.g. [5]: $\mathrm{d}F/\mathrm{d}E = (2.79 \pm 0.02 \pm 0.5)\,(\mathrm{E/TeV})^{-2.59\pm0.03\pm0.05} \cdot 10^{-11}\ \mathrm{cm^{-2}s^{-1}TeV^{-1}}$) is very good. In addition, there is also a good agreement of the fluxes at different zenith angle regions. The first data points at the telescope threshold (open markers; they depend on the HV setting and the zenith angle region) do not fit well into the power law spectrum. The flux values are too small by about a factor of 3. The reason for this discrepancy is due to some simplifications in the MC simulations where the telescope trigger performance is not taken into account in the correct way[35]. As a result, the number of trigger events and therefore the effective collection area are overestimated. In addition the calculation of the proportionality constants κ_i (eq. 5.3.25) is also effected. Recent simulations [156] showed that the problem is mainly related

[35] The arrival time distribution of the individual photo-electrons, the slight mismatch of the signal cable lengths and the fluctuations in the QE and electron collection efficiency of the PMTs were not considered properly.

ZA 0°	cutoff fit (4 DOF)	power law fit, (5 DOF)
cutoff spectrum ($\alpha = 2.0$, $E_0 = 6.0$)	$\overline{\alpha} = 2.198 \pm 0.16$, $\overline{E_0} = 7.8 \pm 2.6$ $\overline{f_0} = 18.6 \pm 0.8$, $\overline{\chi^2} = 2.2 \pm 1.4$	$\overline{\alpha} = 2.80 \pm 0.08$ $\overline{f_0} = 22.7 \pm 1.6$, $\overline{\chi^2} = 15.8 \pm 10.3$
power law spectrum ($\alpha = 2.2$)	$\overline{\alpha} = 2.09 \pm 0.06$, $\overline{E_0} = 63.2 \pm 75.8$ $E_0^{min} = 19.6 \pm 7.5$, $\overline{f_0} = 14.4 \pm 0.7$, $\overline{\chi^2} = 5.2 \pm 2.9$	$\overline{\alpha} = 2.20 \pm 0.03$ $\overline{f_0} = 14.8 \pm 0.5$, $\overline{\chi^2} = 2.8 \pm 1.9$
power law spectrum ($\alpha = 2.7$)	$\overline{\alpha} = 2.72 \pm 0.07$, $\overline{E_0} = 2.6 \cdot 10^6 \pm 4.8 \cdot 10^6$ $E_0^{min} = 16.7 \pm 11.5$, $\overline{f_0} = 15.3 \pm 0.8$, $\overline{\chi^2} = 3.8 \pm 2.5$	$\overline{\alpha} = 2.74 \pm 0.06$ $\overline{f_0} = 15.5 \pm 1.0$, $\overline{\chi^2} = 3.6 \pm 1.4$
power law spectrum ($\alpha = 3.2$)	$\overline{\alpha} = 3.30 \pm 0.11$, $\overline{E_0} = 1.9 \cdot 10^6 \pm 2.8 \cdot 10^6$ $E_0^{min} = 11.8 \pm 12.6$, $\overline{f_0} = 16.9 \pm 1.3$, $\overline{\chi^2} = 4.1 \pm 2.5$	$\overline{\alpha} = 3.31 \pm 0.08$ $\overline{f_0} = 16.7 \pm 1.2$, $\overline{\chi^2} = 4.7 \pm 2.8$
ZA 30°	cutoff fit (3 DOF)	power law fit (4 DOF)
cutoff spectrum ($\alpha = 2.0$, $E_0 = 6.0$)	$\overline{\alpha} = 2.18 \pm 0.59$, $\overline{E_0} = 9.5 \cdot 10^4 \pm 3.3 \cdot 10^5$ $\overline{f_0} = 82.6 \pm 19.4$, $\overline{\chi^2} = 0.7 \pm 0.7$	$\overline{\alpha} = 3.06 \pm 0.19$ $\overline{f_0} = 92.8 \pm 22.3$, $\overline{\chi^2} = 0.9 \pm 0.7$
power law spectrum ($\alpha = 2.2$)	$\overline{\alpha} = 2.27 \pm 0.14$, $\overline{E_0} = 2.5 \cdot 10^5 \pm 3.7 \cdot 10^5$ $E_0^{min} = 11.3 \pm 18.0$, $\overline{f_0} = 56.3 \pm 6.3$, $\overline{\chi^2} = 0.8 \pm 0.5$	$\overline{\alpha} = 2.35 \pm 0.14$ $\overline{f_0} = 49.8 \pm 8.4$, $\overline{\chi^2} = 0.8 \pm 0.5$
power law spectrum ($\alpha = 2.7$)	$\overline{\alpha} = 2.71 \pm 0.18$, $\overline{E_0} = 8.7 \cdot 10^5 \pm 1.7 \cdot 10^6$ $E_0^{min} = 7.4 \pm 8.7$, $\overline{f_0} = 97.9 \pm 14.8$, $\overline{\chi^2} = 0.7 \pm 0.5$	$\overline{\alpha} = 2.92 \pm 0.18$ $\overline{f_0} = 67.1 \pm 12.6$, $\overline{\chi^2} = 1.3 \pm 0.9$
power law spectrum ($\alpha = 3.2$)	$\overline{\alpha} = 2.93 \pm 0.78$, $\overline{E_0} = 2.6 \cdot 10^6 \pm 5.8 \cdot 10^6$ $E_0^{min} = 1.7 \pm 1.6$, $\overline{f_0} = 163.5 \pm 55.9$, $\overline{\chi^2} = 1.4 \pm 1.2$	$\overline{\alpha} = 3.70 \pm 0.39$ $\overline{f_0} = 122.9 \pm 53.0$, $\overline{\chi^2} = 1.3 \pm 0.8$
ZA 45°	cutoff fit (2 DOF)	power law fit (3 DOF)
cutoff spectrum ($\alpha = 2.0$, $E_0 = 6.0$)	$\overline{\alpha} = 2.99 \pm 0.45$, $\overline{E_0} = 4.3 \cdot 10^7 \pm 1.1 \cdot 10^8$ $\overline{f_0} = 217.8 \pm 81.8$, $\overline{\chi^2} = 0.8 \pm 0.5$	$\overline{\alpha} = 3.10 \pm 0.29$ $\overline{f_0} = 245.8 \pm 123.2$, $\overline{\chi^2} = 1.1 \pm 0.7$
power law spectrum ($\alpha = 2.2$)	$\overline{\alpha} = 1.88 \pm 0.62$, $\overline{E_0} = 1.9 \cdot 10^6 \pm 4.3 \cdot 10^6$ $E_0^{min} = 2.8 \pm 2.3$, $\overline{f_0} = 60.1 \pm 25.4$, $\overline{\chi^2} = 1.2 \pm 0.3$	$\overline{\alpha} = 2.23 \pm 0.19$ $\overline{f_0} = 80.5 \pm 29.7$, $\overline{\chi^2} = 1.3 \pm 0.5$
power law spectrum ($\alpha = 2.7$)	$\overline{\alpha} = 2.60 \pm 0.35$, $\overline{E_0} = 8.3 \cdot 10^7 \pm 3.9 \cdot 10^8$ $E_0^{min} = 6.7 \pm 14.1$, $\overline{f_0} = 125.3 \pm 52.6$, $\overline{\chi^2} = 1.1 \pm 0.5$	$\overline{\alpha} = 2.77 \pm 0.22$ $\overline{f_0} = 149.0 \pm 48.8$, $\overline{\chi^2} = 1.2 \pm 0.6$
power law spectrum ($\alpha = 3.2$)	$\overline{\alpha} = 3.24 \pm 0.37$, $\overline{E_0} = 7.0 \cdot 10^9 \pm 2.9 \cdot 10^9$ $E_0^{min} = 3.9 \pm 8.9$, $\overline{f_0} = 266.1 \pm 176.3$, $\overline{\chi^2} = 0.9 \pm 0.4$	$\overline{\alpha} = 3.19 \pm 0.31$ $\overline{f_0} = 230.8 \pm 89.1$, $\overline{\chi^2} = 1.0 \pm 0.5$

Tab. 5.3.6: Results of the spectrum estimation algorithm when applied to different MC generated source spectra. The results of a cutoff fit are presented in the 2nd, the results of a pure power law fit in the 3rd column. The numbers represent the mean and RMS value for 30 individually generated source spectra. α denotes the spectral index, E_0 the cutoff energy in TeV and f_0 the absolute flux in units of 10^{-11} cm^{-2}s^{-1}TeV^{-1}. The latter cannot be directly compared for different rows or columns. The number of degrees of freedom (DOF) is given for each individual section.

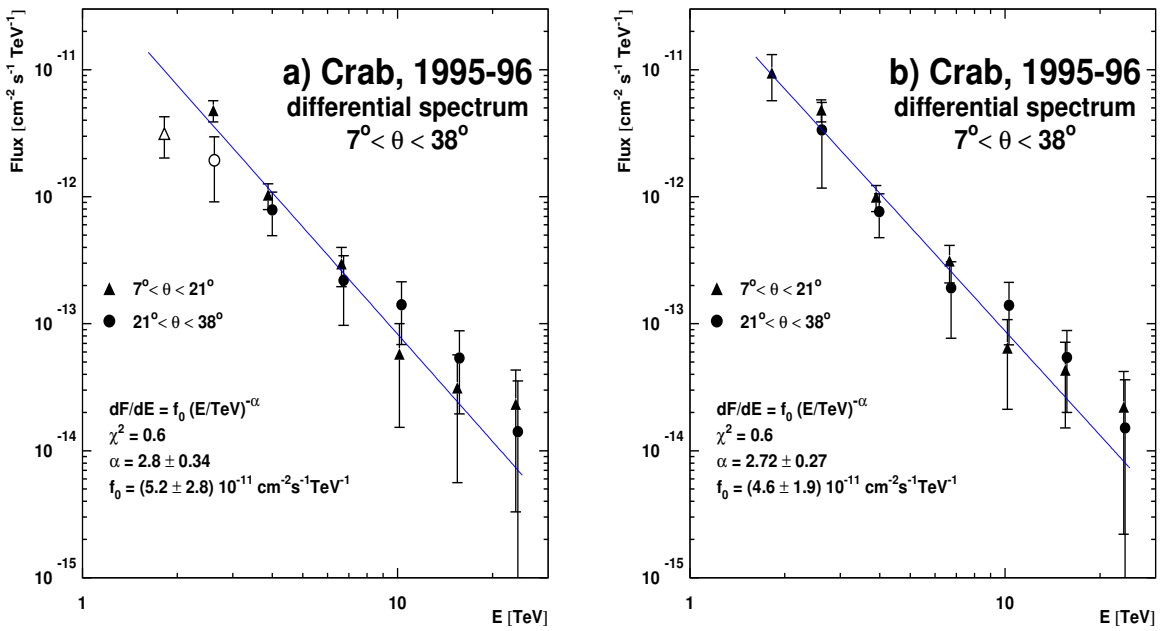

Fig. 5.3.14: a) The energy spectrum of the Crab Nebula as derived for two different zenith angle regions. Only the data points, represented by solid markers, have been used for the power law fit. In figure b) the data points at the threshold have been rescaled according to the new MC simulations (see text). No normalization of the individual data samples was applied. The overall observation time was 16.5 h for $6.6° < \theta < 21°$ and 10.9 h for $21° < \theta < 38°$ zenith angle. All errors are purely statistical.

to the ignored arrival time distribution. In order not to lose the important data points at the threshold, the corresponding flux values are rescaled according to the new simulations in all subsequent energy spectra (see sec. 6.1). The resulting Crab spectrum is shown in fig. 5.3.14 b).

In summary, the presented method works fairly well. At small zenith angles, it is possible to distinguish between power law and cutoff spectra. Spillover effects of the energy binning are therefore treated in the correct way. At larger zenith angles, the MC statistics is too small to give a conclusive answer, but it seems that due to the reduced energy range, cutoff spectra cannot be resolved here anyhow. The discrepancy at the threshold energy is solved by the latest MC simulations.

6. RESULTS FROM THE ANALYSIS OF THE CHERENKOV TELESCOPE DATA

The Mkn 501 outburst in 1997 represents a rare opportunity to address several fundamental theoretical and technical questions in VHE γ-astronomy. The observation of high-energy γ-rays with $E_\gamma \gtrsim 10\,\mathrm{TeV}$ for example, puts constraints on the *Diffuse Extragalactic Background Radiation* (DEBRA) density and/or some characteristic parameters of the BL Lac object, like magnetic field strength and Doppler factor. The strong γ-ray signal on the other hand, allows to compare individual detectors or to check new and/or existing observation techniques. This section covers some of the investigations, carried out with the $\sim 400\,\mathrm{h}$ of observational data from CT1. For further investigations, including the results from different detectors and experiments the reader is referred to e.g. [2, 3, 4, 10, 49, 70, 92, 134].

The overall Mkn 501 light curve in 1997, including the data from CT2 and the CT-system is presented in sec. 6.1. Furthermore, the differential energy spectra as obtained from the individual CT1 data samples (NOM00, HV06, etc.) are shown. The following section, sec. 6.2, briefly summarizes the basics of the moon observation technique. A comparison of the flux values and energy spectra derived from moon and no-moon observations is also presented. The analysis of coincident events between CT1 and the CT-system is described in sec. 6.3. The reconstructed energy and impact parameter of individual shower events are compared. All results are briefly discussed in the last section of this chapter.

6.1 Lightcurve and energy spectra

The 1997 CT1 data from Mkn 501 consist of several different data samples which have been taken with different PMT HV settings and/or have been taken during the presence of moonlight. Each data sample was separately analyzed and appropriate MC simulations were used to derive the individual flux values and energy spectra. In the following, the raw data analysis procedure is briefly summarized.
At first, the raw data are pre-processed, i.e. the PMT pedestals are determined, the flat-fielding and tailcut procedure are applied and the HILLAS image parameters are calculated (see sec. 5.1). Data runs, which were taken under poor atmospheric conditions or runs, where detector problems showed up, are removed from the data sample. Depending on the specific data sample, one of the derived cut-sets (see sec. 5.3.3) is then applied to the data and the significance, flux values and energy spectra are calculated as described in sec. 5.3. The characteristic parameters (i.e. γ-efficiency, effective collection area, etc.) of a given cut-set, which are essential for the calculation of fluxes and energy spectra, strongly depend on the HV setting and NSB noise of the data. The MC simulations, used to estimate these parameters, therefore have to be properly adjusted to the individual data samples. This was done by means of the photoelectron to ADC counts conversion factor (sec. 5.1.1), the modified tailcut procedure (sec. 5.1.4) and by adopting the MC NSB noise simulation to the observed data (sec. 5.2).

The obtained integral flux values (above 1.5 TeV) together with the results from CT2 and the CT-system (as published in [2, 3]) are shown in fig. 6.1.1. The CT1 fluxes were calculated

as described in sec. 5.3.4 using a differential spectral index of $\alpha = 2.8$ [2]. In case moon observations with different HV settings were carried out at a given day, the obtained flux values were combined (as weighted mean). The individual flux values of all CT1 data samples are listed in Appendix B. Some statistics of the different CT1 data samples are summarized in tab. 6.1.1 and the individual $ALPHA$-distributions are shown in fig. 6.1.2. As already said, the label $NOMxx$ denotes no-moon, while $HVxx$ denotes moon observation data; the value of xx refers to the HV reduction of the PMTs.
The strong and short term variations in the γ-ray emission of Mkn 501 are clearly visible in fig. 6.1.1. The observed peak flux values are $(15.48 \pm 5.02) \cdot 10^{-11}\,\mathrm{cm}^{-2}\mathrm{s}^{-1}$ for the moon data and $(10.64 \pm 0.80) \cdot 10^{-11}\,\mathrm{cm}^{-2}\mathrm{s}^{-1}$ for the no-moon data. The average γ-ray flux in 1997 (March 10. - October 12.), calculated from all CT1 data samples, is determined as:

$$F\,(E > 1.5\ \mathrm{TeV}) = (1.88 \pm 0.04_{stat}) \cdot 10^{-11}\,\mathrm{cm}^{-2}\mathrm{s}^{-1}\,. \tag{6.1.1}$$

This value can be compared to the integral Crab flux which was derived as:

$$F_{Crab}\,(E > 1.5\ \mathrm{TeV}) = (0.82 \pm 0.1_{stat}) \cdot 10^{-11}\,\mathrm{cm}^{-2}\mathrm{s}^{-1} \tag{6.1.2}$$

[126, p. 181]. Therefore the average Mkn 501 flux in 1997 was ~ 2.3 times larger as compared to the Crab Nebula flux.

The calculation of the energy spectra for the Mkn 501 data samples followed the procedure described in sec. 5.3.5. However, as pointed out at the end of this section, some adjustments had to be made in order to circumvent the trigger related deficiencies of the MC simulations. The basic problem was that the arrival time distribution of the Cherenkov photons is ignored in the trigger simulation, leading to an overestimation of the effective collection area. As a result, the derived flux values at the telescope threshold are systematically underestimated.
A solution to this problem was obtained by means of recent MC simulations [156] which performed the correct trigger simulation. These simulations could not be directly used for the energy spectrum calculations, since the simulated mirror reflectivity was slightly different compared to the 1997 CT1 set-up. Instead, the new simulations were used to derive scaling factors for correcting the results from the old MC simulations:

The main equation of sec. 5.3.5 (eq. 5.3.24) can be written as

$$\frac{\mathrm{d}F\,(E_i)}{\mathrm{d}E_i} = \frac{1}{A_{\mathrm{eff}}\,(E_i, \vartheta)} \frac{\mathrm{d}R\,(E_i, \vartheta)}{\mathrm{d}E_i} = \beta_i \cdot \frac{\mathrm{d}R\,(E_i^r, \vartheta)}{\mathrm{d}E_i^r} \tag{6.1.3}$$

where $\beta_i := \kappa_i / A_{\mathrm{eff}}\,(E_i, \vartheta)$ is determined from the MC simulations (i denotes a MC energy bin, $\mathrm{d}E_i^r$ a bin of the reconstructed energy, ϑ the zenith angle and $\mathrm{d}R/\mathrm{d}E_{\mathrm{i}}^{\mathrm{r}}$ the differential excess rate). In the case of the inadequate trigger simulation, the β_i terms at the telescope threshold and therefore the differential flux values $\mathrm{d}F/\mathrm{d}E_{\mathrm{i}}$ are underestimated. In order to correct this effect, the new MC simulations have been used, to estimate the relative change in the β_i terms due to the different trigger simulations. These scaling factors sf_i are estimated according to:

$$sf_i\,(E_i, \vartheta) := \frac{\beta_i^{newMC,ct}}{\beta_i^{newMC,wt}} \tag{6.1.4}$$

(ct stands for correct trigger and wt for "wrong" or inadequate trigger) and eq. 6.1.3 then becomes:

$$\frac{\mathrm{d}F\,(E_i)}{\mathrm{d}E_i} = sf_i \cdot \beta_i^{oldMC,wt} \frac{\mathrm{d}R\,(E_i^r, \vartheta)}{\mathrm{d}E_i^r}\,. \tag{6.1.5}$$

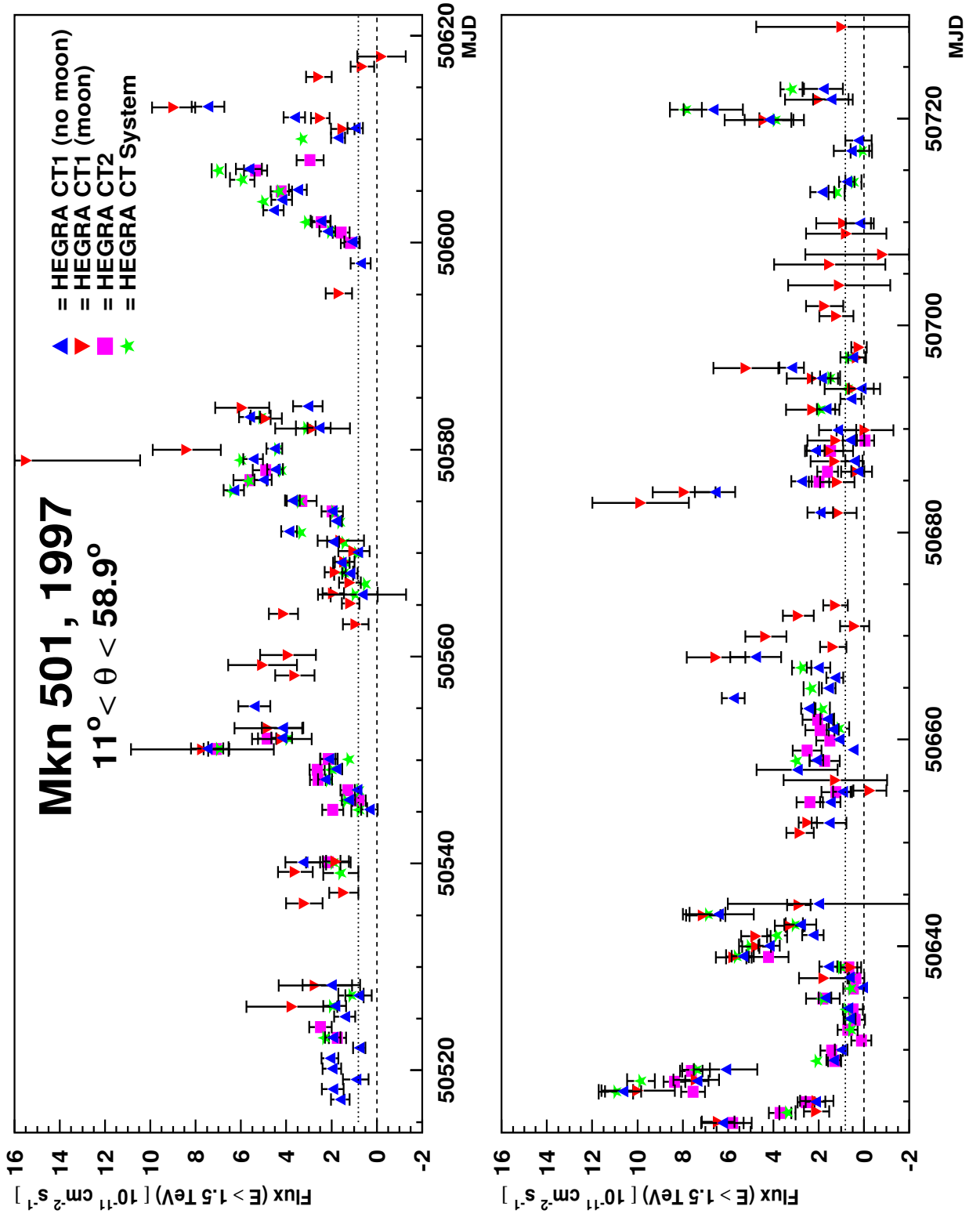

Fig. 6.1.1: The Mkn 501 lightcurve in 1997 as obtained with the Cherenkov telescopes of the HEGRA collaboration. The flux values are given as integral flux above 1.5 TeV (only statistical errors). The dotted line denotes the crab flux (from [126]). Please note that data from different instruments do not exactly overlap in time.

	NOM00	NOM06	HV00	HV06	HV10	HV14	HV16
threshold energy [TeV]	1.2	1.8	1.2	1.8	2.4	3.4	3.6
effective on-time [h]	196.9	61.0	20.2	77.3	22.4	13.5	6.0
zenith angle [deg.]	$11.0^\circ - 58.7^\circ$	$11.0^\circ - 58.2^\circ$	$11.0^\circ - 48.4^\circ$	$11.0^\circ - 58.9^\circ$	$11.0^\circ - 44.2^\circ$	$11.0^\circ - 42.3^\circ$	$11.0^\circ - 31.3^\circ$
background events	2074 ± 31	331 ± 13	243 ± 11	866 ± 20	183 ± 9	29 ± 4	10 ± 3
background rate $[\mathrm{h}^{-1}]$	10.53 ± 0.16	5.43 ± 0.22	12.03 ± 0.55	11.20 ± 0.26	8.17 ± 0.41	2.15 ± 0.30	1.67 ± 0.5
excess events	6335 ± 96	1040 ± 39	688 ± 32	1307 ± 50	247 ± 22	18 ± 7	17 ± 6
excess rate $[\mathrm{h}^{-1}]$	32.17 ± 0.49	17.05 ± 0.64	34.06 ± 1.59	16.91 ± 0.65	11.03 ± 0.99	1.33 ± 0.52	2.83 ± 1.0
average flux above 1.5 TeV $[10^{-11}\ \mathrm{cm}^{-2}\mathrm{s}^{-1}]$	1.86 ± 0.04	1.71 ± 0.08	1.87 ± 0.13	2.33 ± 0.11	2.74 ± 0.27	0.67 ± 0.41	1.57 ± 0.80
significance $[\sigma]$	64.1 ± 0.7	26.1 ± 0.7	20.7 ± 0.7	24.1 ± 0.7	10.1 ± 0.8	2.2 ± 0.6	2.8 ± 0.8
sensitivity $[\sigma/\sqrt{h}]$	4.57 ± 0.05	3.34 ± 0.09	4.61 ± 0.16	2.74 ± 0.08	2.13 ± 0.17	0.60 ± 0.17	1.14 ± 0.33

Tab. 6.1.1: Statistical data and results for the different data samples for Mkn 501 taken with CT1. The error on the significance was estimated from the error on the excess events.

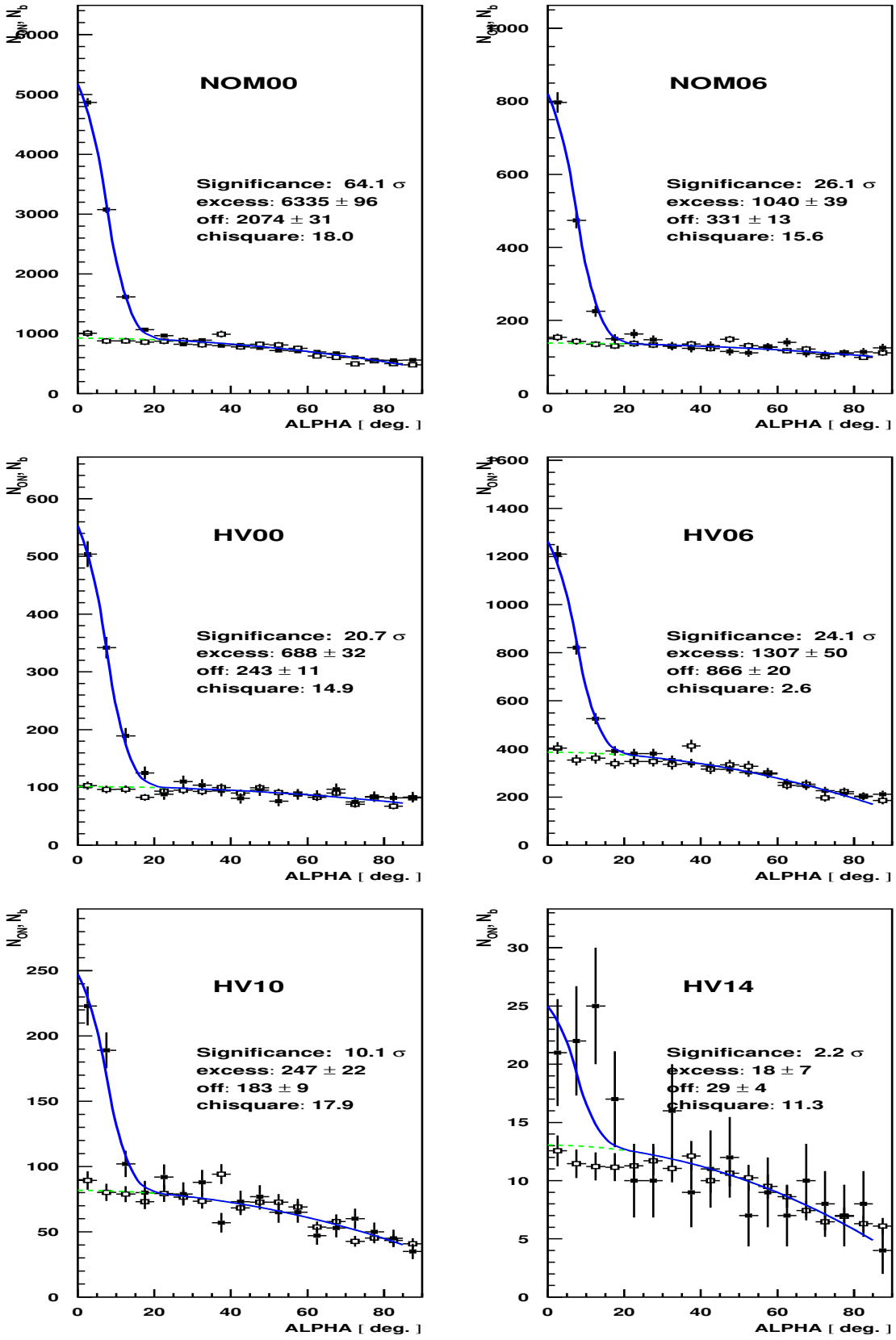

Fig. 6.1.2: ALPHA-distributions for the different CT1 moon and no-moon data samples.

data sample (corresponding cut)	0° zenith angle energy range [TeV]	scaling factor	30° zenith angle energy range [TeV]	scaling factor	45° zenith angle energy range [TeV]	scaling factor
NOM00	1.0 – 1.5	3.4	1.5 – 2.3	2.0	2.3 – 3.0	2.0
(ds97)	1.5 – 2.3	1.5	2.3 – 3.0	1.3	3.0 – 5.5	1.3
NOM06	1.5 – 2.3	3.7	2.3 – 3.0	2.8	3.0 – 5.5	1.6
(ds96)	2.3 – 3.0	2.1	3.0 – 5.5	1.8	5.5 – 8.4	1.4
HV00	1.0 – 1.5	2.1	1.5 – 2.3	1.8	2.3 – 3.0	1.3
(ds97hv00)	1.5 – 2.3	1.4	2.3 – 3.0	1.3	3.0 – 5.5	1.3
HV06	1.5 – 2.3	18.0	2.3 – 3.0	3.4	3.0 – 5.5	2.9
(ds97hv06)	2.3 – 3.0	2.7	3.0 – 5.5	1.7	5.5 – 8.4	1.6
HV10	2.3 – 3.0	18.0	3.0 – 5.5	3.4	5.5 – 8.4	2.9
(ds97hv10)	3.0 – 5.5	2.7	5.5 – 8.4	1.7	8.4 – 12.4	1.6

Tab. 6.1.2: The flux scaling factors as used for the different CT1 data samples energy bins and zenith angles.

Table 6.1.2 summarizes the scaling factors which result in significant changes above the 10% level. All other scaling factors were set to unity. As can be seen, the corrections to the old MC simulations are quite substantial, but only the energy region close to the telescope threshold is affected. In the case of the HV10 data sample, the effect of the trigger problem has not been investigated in new MC simulations yet. In a coarse approach, the scaling factors from the HV06 data sample were used for the corresponding threshold energy bins.

The differential energy spectra for the CT1 data samples and the two zenith angle regions ($11° < \theta < 21°$ and $21° < \theta < 38°$) are shown in fig. 6.1.3. Given the variable γ-ray emission of Mkn 501 in 1997, the different energy spectra had to be normalized beforehand. The energy spectra were not normalized on a single energy bin, but on the two energy bins between 5.5 TeV and 12.4 TeV, covered by each data sample. The differential flux values $f_i := \mathrm{d}F\left(E_i\right)/\mathrm{d}E_i$ were normalized according to:

$$f_i' = \frac{f_5^{nom00} \cdot E_5^{2.8} + f_6^{nom00} \cdot E_6^{2.8}}{f_5 \cdot E_5^{2.8} + f_6 \cdot E_6^{2.8}} \cdot f_i \,. \tag{6.1.6}$$

Here, f_5 and f_6 denote the differential flux in the 5th and 6th energy bin, while E_5 and E_6 denote the mean energy of these bins. A differential spectral index $\alpha = 2.8$ was used to give the flux values f_5 and f_6 equal weights. All energy spectra were normalized onto the spectrum from the $NOM00$ data sample.

As can be seen from fig. 6.1.3, the individual energy spectra agree very well. The only outlier, the ~ 4 TeV data point from the $HV10$ data sample is attributed to the uncertainty in the scaling factors for this data (as mentioned above). Both, the fit of a pure power law (fig. 6.1.3 a and b) and the fit of a power law with exponential cutoff (fig. 6.1.3 c and d) give reasonable χ^2_{red}-values. A pure power law spectrum is therefore not ruled out here. Note, that in the case of a power law with exponential cutoff the two fit variables α (the differential spectral index) and E_0 (the cutoff energy) are strongly correlated. If the spectral index for the $21° < \theta < 38°$ zenith angle data (fig. 6.1.3 d) is fixed to $\alpha = 2.11$, the other fit variables become: $E_0 = (6.58 \pm 0.82)$ TeV and $f_0 = (9.7 \pm 1.3) \cdot 10^{-11}\,\mathrm{cm^{-2}s^{-1}TeV^{-1}}$ with a slightly larger χ^2_{red}-value of 0.5. These results are in good agreement with the results from the $11° < \theta < 21°$ zenith angle data (fig. 6.1.3 c).

The energy spectrum of the combined CT1 data is shown in fig. 6.1.4 a) and b) and in

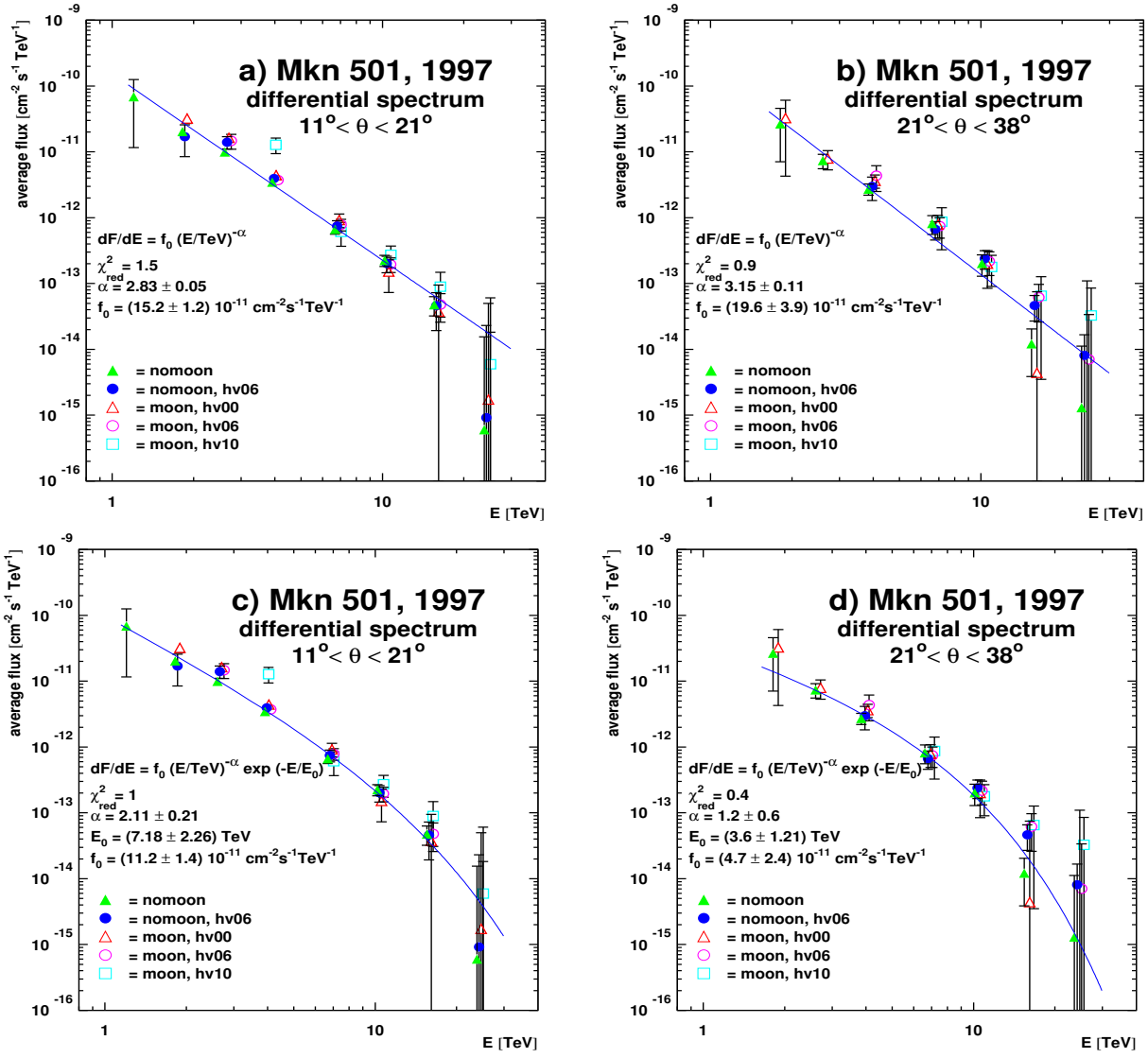

Fig. 6.1.3: Differential energy spectra as derived for the different CT1 data samples and zenith angle regions. The results from a power law fit to the data are shown in fig. a) and b) whereas in fig. c) and d) a power law with exponential cutoff was fitted to the same data points. Spectra for different observation conditions were normalized to the weighted mean of the 5th and 6th energy bin (see text).

energy [TeV]	$\mathrm{d}F/\mathrm{d}E$ $[\mathrm{cm}^{-2}\mathrm{s}^{-1}\mathrm{TeV}^{-1}]$	$\sigma_{stat}\,(\mathrm{d}F/\mathrm{d}E)$ $[\mathrm{cm}^{-2}\mathrm{s}^{-1}\mathrm{TeV}^{-1}]$
1.2	$6.86 \cdot 10^{-11}$	$5.70 \cdot 10^{-11}$
1.82	$2.11 \cdot 10^{-11}$	$1.96 \cdot 10^{-12}$
2.61	$1.01 \cdot 10^{-11}$	$7.12 \cdot 10^{-13}$
3.88	$3.36 \cdot 10^{-12}$	$1.84 \cdot 10^{-13}$
6.65	$6.91 \cdot 10^{-13}$	$5.85 \cdot 10^{-14}$
10.14	$1.91 \cdot 10^{-13}$	$2.08 \cdot 10^{-14}$
15.49	$2.85 \cdot 10^{-14}$	$6.21 \cdot 10^{-15}$
23.71	$3.85 \cdot 10^{-15}$	$5.42 \cdot 10^{-15}$

Tab. 6.1.3: The time averaged differential spectrum of Mkn 501.

tab. 6.1.3. The individual data points denote the weighted mean, which was derived from the $NOM00$, $NOM06$, $HV00$ and $HV06$ flux values (the $HV10$ data was ignored due to the above mentioned restrictions). In this case, a pure power law spectrum is clearly ruled out. Given a χ^2-value of $\chi^2\,(6) = 35.29$ the corresponding significance level is $\mathcal{P} = 3.8 \cdot 10^{-6}$ or 4.5σ. The cutoff fit, on the other hand agrees very well with the data ($\chi^2\,(5) = 2.56$ and $\mathcal{P} = 0.23$ or 0.7σ). The time averaged energy spectrum of Mkn 501 in 1997 is therefore estimated as (only statistical errors):

$$\frac{\mathrm{d}F}{\mathrm{d}E} = (10.1 \pm 1.2) \cdot \left(\frac{E}{\mathrm{TeV}}\right)^{-2.03 \pm 0.19} \exp\left[-\frac{E}{(6.12 \pm 1.31)\ \mathrm{TeV}}\right] \cdot 10^{-11}\mathrm{cm}^{-2}\mathrm{s}^{-1}\mathrm{TeV}^{-1}. \quad (6.1.7)$$

This result can be compared to the CT-system spectrum, which was derived according to [4] $\mathrm{d}F/\mathrm{d}E = f_0\,(E/\mathrm{TeV})^{-\alpha} \cdot \exp\,(-E/E_0)$ with $f_0 = (10.8 \pm 0.2_{stat} \pm 2.1_{sys}) \cdot 10^{-11}\mathrm{cm}^{-2}\mathrm{s}^{-1}\mathrm{TeV}^{-1}$, $\alpha = 1.92 \pm 0.03_{stat} \pm 0.20_{sys}$ and $E_0 = \left(6.2 \pm 0.4_{stat}\,(-1.5 + 2.9)_{sys}\right)$ TeV. The reason for the smaller errors of the CT-system results has its origin in the much lower energy threshold thus constraining the fit over a wider energy range. Equation 6.1.7 is also in good agreement with the published CT1 result [2] where $\alpha = 2.09 \pm 0.09$ and $E_0 = (7.16 \pm 1.04)$ TeV was found.
In case all the rescaled flux values (eq. 6.1.5) are omitted in the energy spectrum calculation the results (fig. 6.1.5 a and b) are in good agreement with eq. 6.1.7. Again, the pure power law model is ruled out at a significance level of $\mathcal{P} = 4.9 \cdot 10^{-4}$ or 3.3σ, while the cutoff fit agrees with the data ($\mathcal{P} = 0.38$ or 0.3σ).

The highest observed γ-ray energies are of special interest in deriving limits on the DEBRA density and/or acceleration models. It is therefore essential to properly investigate the main source of errors for the high-energy region of the spectrum, i.e. the misinterpretation of low-energy showers as high-energy events (so called spillover events). This analysis is described in the remaining section.
The highest energy bin with a significant flux value in the Mkn 501 energy spectrum corresponds to the $E = 15.5$ TeV data point (see tab. 6.1.3). In order to test, whether such a flux level can be solely produced by low-energy events, MC simulated energy spectra (see sec. 5.3.5) with a sharp cutoff (no events with energies above E_c) have been used. For a given value of E_c (varied in steps of 0.1 TeV between 12.0 TeV and 15.9 TeV) a set of 200 individual energy spectra with a power law shape ($\alpha = 2.7$) or a power law with a cutoff ($\alpha = 2.0$ and $E_0 = 6.0$ TeV) were generated. Each individual energy spectrum was then analyzed and a power law cutoff fit was tried. In case one of the MC simulated energy spectra resulted in a flux ratio $fr := \frac{f_7}{f_2} > 1.35 \cdot 10^{-3}$ (f_2 and f_7 denote the differential flux in the 2nd and 7th

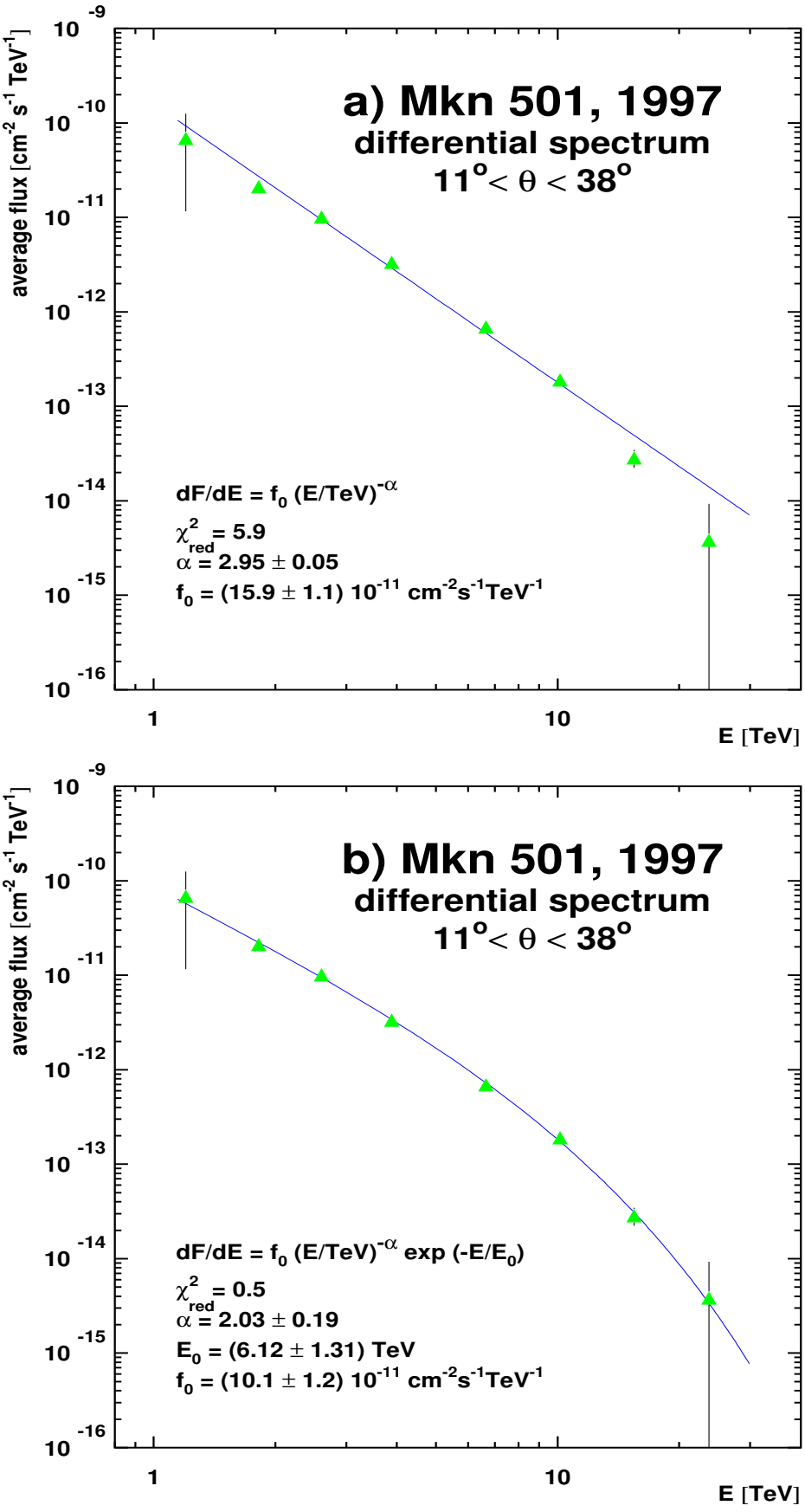

Fig. 6.1.4: Averaged Mkn 501 energy spectrum from the complete CT1 data (values are given in tab. 6.1.3). Figure a) shows the results from the fit of a pure power law while the results from a cutoff fit to the same data points are shown in fig. b).

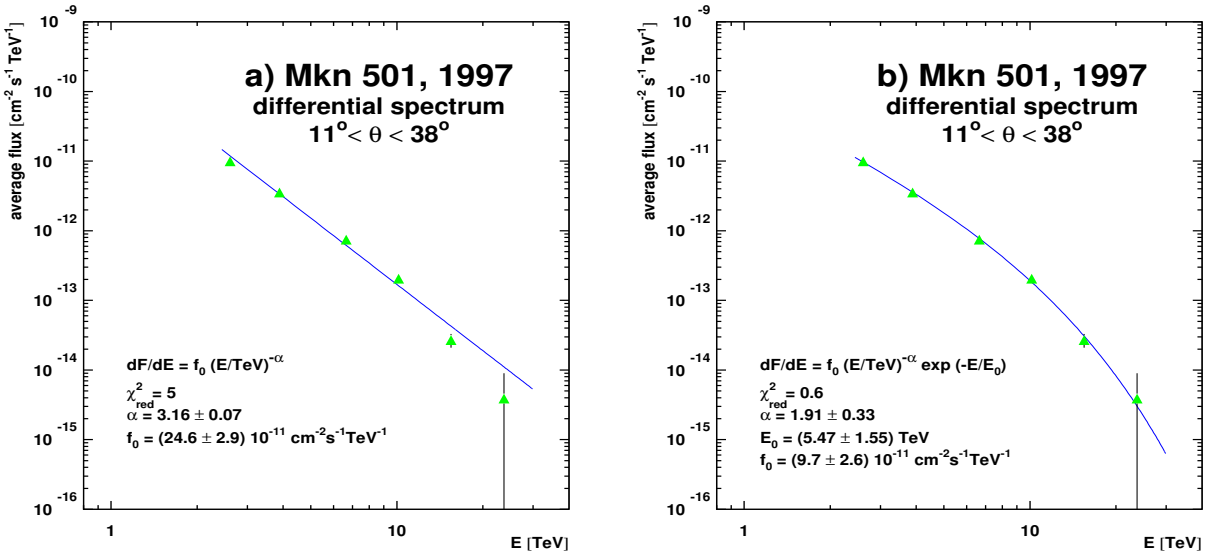

Fig. 6.1.5: Averaged Mkn 501 energy spectrum from the complete CT1 data. Only data which is not affected by the inadequate MC trigger simulation is used.

energy bin, $1.35 \cdot 10^{-3}$ denotes the corresponding flux ratio from tab. 6.1.3) it was considered a fake high energy spectrum. The highest observed energy was then defined as the maximum energy E_c with less than 5% (corresponding to 2σ) fake high energy spectra. In addition, a reasonable $\chi^2 = 19.8$ was demanded (corresponding to 3σ). Note, that the MC statistics in the $E = 15.5$ TeV bin was about a factor 10 smaller compared to the real data sample. The error on the 15.5 TeV MC flux value is therefore larger compared to real data and the probability for fake high energy spectra is overestimated.
The maximum energy with a significant γ-ray emission was derived as $E_c = 12.6$ TeV (pure power law) and $E_c = 13.8$ TeV (power law with cutoff at 6.0 TeV).

6.2 Observations in the presence of moonlight

The main goal of moon observations (i.e. the observation in the presence of moonlight) is to increase the duty cycle of an ACT. In case observations are performed until 85% moon illumination, the duty cycle of an ACT (at 40° latitude) can be increased from 18% up to 27% [42]. Advantages of moon observations are:

- The possibility to accumulate a larger amount of data from a source candidate, which might result in the detection of the object.
- A more complete time coverage of variable objects, like AGN.

The first point is not a compelling argument for moon observations, since it can be compensated by extending the dark night observations for the object of interest (however, at the expense of observations of other objects). In the case of variable sources, however, the dark night data cannot be used to substitute the moon data and the moon observations are of great importance then. The greatest obstacle in performing moon observations is given by the NSB noise, which can increase by up to a factor $\sim 30 - 50$ during full moon [42] compared to no-moon conditions.
In the past, two approaches to perform moon observations have been successfully tested

[123, 149]. However, both methods require hardware modifications (solar blind PMTs [123] or UV sensitive filters [149]) and are therefore time consuming (when switching from no-moon to moon observations) and expensive. Therefore, another approach was investigated with CT1 in 1997 (see [91] for details). Due to the low gain operation of the PMTs (see sec. 3.1) it was possible to compensate the increased NSB noise during moon observations with a moderate reduction of the PMT HV setting. Depending on the NSB noise, the PMTs were operated at nominal HV ($\lesssim$ 20% moon illumination), 6% HV reduction ($\lesssim$ 70% illumination), 10% HV reduction ($\lesssim$ 90% illumination), 14% HV reduction ($\lesssim$ 95% illumination) and 16% HV reduction ($\lesssim$ 97% illumination). The HV setting of the PMTs was reduced whenever the average PMT current reached 12 μA[1]. The increase in the energy threshold of the telescope was $\lesssim$ 50% for most of the data (see tab. 6.1.1) and was about a factor of 3 for the data with 16% reduced HV. The main advantages of this technique are:

- It is possible to adapt the detector to the individual NSB noise conditions. The energy thresholds are only moderately affected by HV reduction (see tab. 6.1.1 and fig. 5.3.11).
- No additional costs for hardware modifications emerge. However, the PMTs show some increased fatigue due to the increased currents.
- The standard analysis methods are still applicable. Only slight modifications to the tailcut procedure were necessary (see sec. 5.1.4).
- In the case of moon observations with $\lesssim$ 70% moon illumination (i.e. HV00 and HV06), which make up $\sim$ 70% of the overall moon observation data, the obtained sensitivities are comparable or only slightly worse compared to no-moon observations with similar HV setting (tab. 6.1.1) .
- The HV reduction can be done very quickly (within seconds).

Note that this method is not applicable for PMTs operated at high gain, i.e. without the additional pre-amplifiers. In that case the HV has to be drastically reduced in order to cope with the increased NSB noise. As a result, the PMTs are operated in the non-linear domain and the resulting strong signal fluctuations spoil the image analysis.

The first important result concerning the CT1 moon observations was already shown in fig. 6.1.2. It proved the possibility to observe and detect γ-ray sources with the presented moon-observation technique. The next step in the verification of this technique is to compare the derived moon and no-moon flux values. The 1997 Mkn 501 data with its strong variations and high γ-ray rate is fairly well suited to check the derived flux values over a large flux range. A comparison of the Mkn 501 flux values as derived from moon and no-moon observations taken during the same night is shown in fig. 6.2.1. Due to the strong variability of the source, individual data points have a somewhat larger deviation from a one-to-one correspondence (depending on the phase of the moon, the moon observations were performed either before or after the no-moon observations). This is also reflected by the fact, that the correlation coefficient (0.84 ± 0.08) is 2σ away from unity. Considering the mean flux, however, this effect should level out and this is also shown by the result from a straight line fit:

$$\frac{flux_{moon}}{10^{-11}\,\mathrm{cm^{-2}s^{-1}}} = (0.23 \pm 0.17) + (0.98 \pm 0.06) \cdot \frac{flux_{no-moon}}{10^{-11}\,\mathrm{cm^{-2}s^{-1}}}\,. \qquad (6.2.1)$$

[1] This current was used as a limit. However, according to the data sheets the PMTs could be operated up to 25 μA.

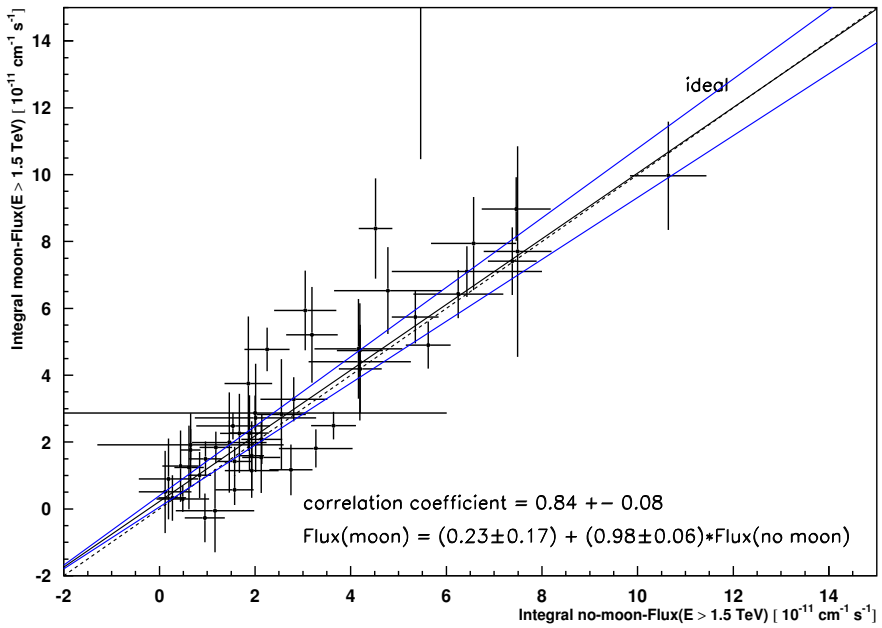

Fig. 6.2.1: Comparison of the Mkn 501 flux from moon and no-moon observations taken during the same night. The black line is a linear fit to the data and the blue lines mark the 1σ errors from the fit. The dashed line indicates a perfect correlation.

data sample	cutoff fit			
	f_0 $[10^{-11}\,\mathrm{cm}^{-2}\mathrm{s}^{-1}\mathrm{TeV}^{-1}]$	α	E_0 [TeV]	χ^2_{red}
NOM00	8.1 ± 1.3	1.74 ± 0.26	4.95 ± 1.18	0.9
NOM06	10.6 ± 3.7	2.22 ± 0.42	9.13 ± 7.06	0.4
HV00	11.0 ± 2.6	1.93 ± 0.52	4.44 ± 3.08	0.2
HV06	24.3 ± 7.2	2.97 ± 0.15	56.91 ± 133.66	0.1
HV06 (fixed α)	10.7 ± 2.0	2.03	6.87 ± 1.33	0.3

Tab. 6.2.1: Differential energy spectra as derived for the different CT1 data samples (all zenith angles included). The results from a power law fit with exponential cutoff are shown.

Note, that the results from a similar analysis presented in [91, fig 5] showed somewhat larger deviations from the (mean) one-to-one flux correspondence ($flux_{moon} = (0.04 \pm 0.09) + (0.80 \pm 0.03) \cdot flux_{no-moon}$, with $flux_{moon}$ and $flux_{no-moon}$ in units of $10^{-11}\,\mathrm{cm}^{-2}\mathrm{s}^{-1}$). This effect is attributed to the modified tailcut procedure (sec. 5.1.4) which was not applied in [91] and results in somewhat different flux estimates.

Another consistency test of the moon observation technique can be made by comparing the energy spectra. As before, the variability of Mkn 501 is not a problem, since all data samples cover a large time range and possible variations in the spectral shape of Mkn 501 should therefore level out. The results of a cutoff fit to the differential energy spectra as derived from the CT1 moon and no-moon data samples (including all zenith angles) are shown in tab. 6.2.1. As can be seen, the obtained fit parameters are in good agreement. In the case of the HV06 data, a pure power law was favored by the data (E_0 well above the maximum observed energies), however, keeping α fixed at the value derived in eq. 6.1.7 shows that the data is still in good agreement with the other CT1 data samples. The good agreement between the CT1 moon and no-moon energy spectra is also visible in fig. 6.1.3.

In summary, the CT1 moon observations have proven to yield reliable results for both integral flux values and energy spectra. Due to the easy applicability (no hardware modifications and only slight changes in the analysis procedure are necessary) this observation technique is very valuable in extending the time coverage of TeV sources. The increased time coverage is of main importance in the case of variable sources, like Mkn 501 (see sec. 7). It should be noted, that this is the first time, that TeV energy spectra have been derived from moon observational data.

6.3 Comparison of coincident events from CT1 and the CT-System

The Mkn 501 flare of 1997 was the first time where both CT1 and the CT-system were in full operation, thus concurrent observations on the same object were possible. Since a large number of γ-like shower events was recorded by both detectors ($\sim$ 30%), this data is well suited to compare the obtained results, as well as the telescope performance. Due to the lower energy threshold of the CT-system, it also allows a cross check of the performance of the CT1 analysis methods for overlapping energies. In the following a comparison of the reconstructed shower energy and impact parameter will be presented, while the derived flux values will be compared in sec. 6.4.

In order to compare the energy of individual showers, the first step is to search for coincident events (both detectors have unsynchronized deadtime, different collection areas and different energy thresholds). Since both detectors are operated completely independently, coincident events have to be found by comparing the recorded UTC time of the events. Two events are regarded coincident, if the difference of their recording time lies within a given coincidence window of typically 0.4 s (see below).

Some complications arise from the fact that the recording time of a shower event is determined in different ways for the CT-system and CT1. The former records the time signal of a GPS receiver while CT1 records the signal of a rubidium clock. Since sometimes occurring leap seconds (see `maia.usno.navy.mil/eo/leapsec.html`) are added to the GPS time, but not to the rubidium clock time, the time standards show an offset to each other, 10 s and 11 s in 1997. Another contribution to the time offset is caused by some inaccuracy of the rubidium clock. This contribution is monitored on a daily basis and is of the order of 1 ms. Unfortunately, only the PC internal clock time is available for about 8% of the events recorded with the CT-system and some 9% of the events have their observation time recorded only in units of seconds (e.g., altogether $\sim$ 12% of the events have a spoiled time information). In order not to loose too many coincident events, it was therefore necessary to enlarge the coincident window to 0.4 s.

Given that time window, the number of coincident events (after applying γ-hadron selection cuts) was calculated for a set of different time offsets in order to detect the 10 s and 11 s offset (see fig. 6.3.2 a). As expected, most of the coincident events occur at 10 s and 11 s but the additional smaller peak at 12 s offset is not understood yet. All coincident events at 10 s and 11 s offset have been used for the comparison. The amount of random coincidences in the 0.4 s coincidence time window can be estimated from fig. 6.3.2 a) as $\sim$ 7%. To further reduce the number of random coincidences, the azimuth ϕ of a given shower event can be used (see fig. 6.3.1 and 6.3.2 b). Since random coincidences are not likely to give matching azimuth values, all shower events within the two areas defined by the dashed lines in fig. 6.3.2 b) are considered as uncorrelated background and therefore rejected. The region in the upper and lower corner contains valid coincidences, because of an ambiguity at e.g. $\phi_1 \simeq -\pi$ and $\phi_2 \simeq +\pi$. After rejecting events with inappropriate azimuth values, the amount of random

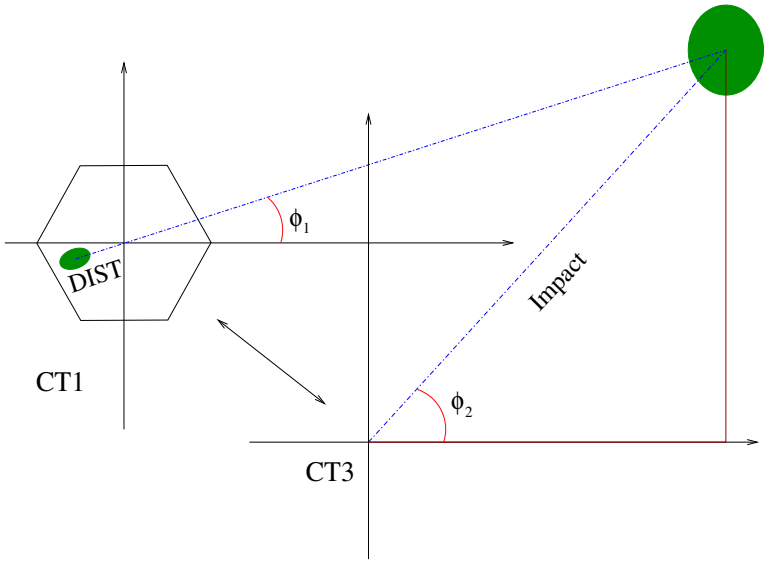

Fig. 6.3.1: Estimation of the azimuth ϕ of individual EAS using the x- and y-coordinates of the DIST (CT1) and impact parameter (CT-system with respect to CT3). After taking the offset between the two reference frames into account, real coincident events should give comparable azimuth values $\phi_1 \simeq \phi_2$.

coincidences is reduced to $\sim$ 3%. The final data sample contains 624 events fulfilling all cuts for γ-candidates.

A comparison of the derived energy and impact parameter[2] values for the coincident events is shown in fig. 6.3.2 c) and d). The 1σ confidence band, using an energy resolution of 29% (CT1) and 20% (CT-system) and impact parameter resolution of 20% (CT1 alone) is shown as dashed lines. As can be seen, the derived shower energies agree very well over the whole energy range, even at the CT1 threshold energy. The 1σ confidence band is too wide when compared with the reconstructed energies in CT1 and the CT-system ($\sim$ 93% of the data points lie within the dashed lines). The reason is that both detectors observe the same shower and are therefore subject to the same fluctuations in the shower development and atmospheric conditions. From this result, the following conclusions can be drawn.

- The energy resolution does not solely depend on the quality of the shower reconstruction, but is also strongly affected by shower fluctuations in the atmosphere. The deterioration of the energy resolution due to these fluctuations is about 70%.
- The energy reconstruction for both instruments shows a remarkable agreement throughout the whole energy range, although completely different calibration methods have been used.
- No large outliers (i.e. $|(E_{CTsys} - E_{CT1})/E_{CTsys}| < 1.2$ for all events with $E_{CTsys} > 2$ TeV) were reconstructed for CT1, therefore only a few misinterpreted high energy showers are expected.

In the case of the impact parameter, the agreement is reasonably good, but the distribution of the CT1 data points shows a slight bending at larger impact parameters. The main reason are the leakage effects of the small CT1 camera (see sec. 5.3.1), i.e. the truncated images have a

[2] The methods, used to estimate the energy and impact parameter for the CT-system are described in [3, 8].

smaller $DIST$-value. The width of the 1σ confidence band is again too large when compared to the data ($\sim 78\%$ of the data points lie within the dashed lines).

In summary, the relative energy and impact parameter calibration between CT1 and the CT-system is surprisingly good, although completely different methods were used. Given the higher energy threshold of CT1 and the resulting small photon statistics, the CT1 results are comparable to the CT-system data.

6.4 Discussion

In comparison to the published CT1 results from Mkn 501 [2] some significant improvements were achieved by means of the newly introduced analysis techniques (sec. 5.3). In the case of overlapping data, taken at the same day, the integral flux values are now in better agreement with the CT-system results. A comparison of the Mkn 501 flux values derived from CT1 and CT-system observations taken during the same night is shown in fig. 6.4.1. Since most of the CT1 and CT-system data have been taken at about the same time, a very good correlation is expected and indeed present in the data. The correlation coefficient (0.96 ± 0.05) is consistent with unity. A straight line fit shows somewhat larger deviations from a one-to-one correspondence:

$$\frac{flux_{CT1}}{10^{-11}\,\mathrm{cm^{-2}s^{-1}}} = (0.13 \pm 0.17) + (0.88 \pm 0.03) \cdot \frac{flux_{CT-system}}{10^{-11}\,\mathrm{cm^{-2}s^{-1}}}\,. \qquad (6.4.1)$$

Nevertheless, the mean flux ratio $flux_{CT1}/flux_{CT-system} = 1.01 \pm 0.07$ is consistent with unity and has significantly improved compared to [2] where its value was derived as 0.73 ± 0.02.

In the case of the energy spectra, there is good agreement with the published CT1 results [2]. In addition, some significant improvements could be made. At first, it was possible to track down the inadequate trigger simulation in the MC data which ignores the arrival time distribution of the individual photo-electrons. Furthermore, a pure power law spectrum is now ruled out by the CT1 data at the 4.5σ level, in contrast to the old results. Finally, for the first time, an energy spectrum from moon observation data could be derived. Excellent agreement between the spectra derived from dark night and moonshine data has been found. The combination of the data allows the rejection of the pure power law spectrum and increases the precision at energies above, say, 5 TeV.

A significant γ-ray flux up to $\sim$ 14TeV could be detected, consistent with the corresponding results from the CT-system (γ-ray flux up to $\sim$ 16 TeV). This is an important result with respect to the discussion on the DEBRA density. Due to a lack of time, this is not discussed any further and the reader is referred to [4, 18, 92] instead. The final figure of this chapter shows the time averaged TeV energy spectrum of Mkn 501 during 1997 as obtained with CT1 (this thesis), CT-system [4], CAT [12], Telescope Array [70] and the Whipple telescope [148].

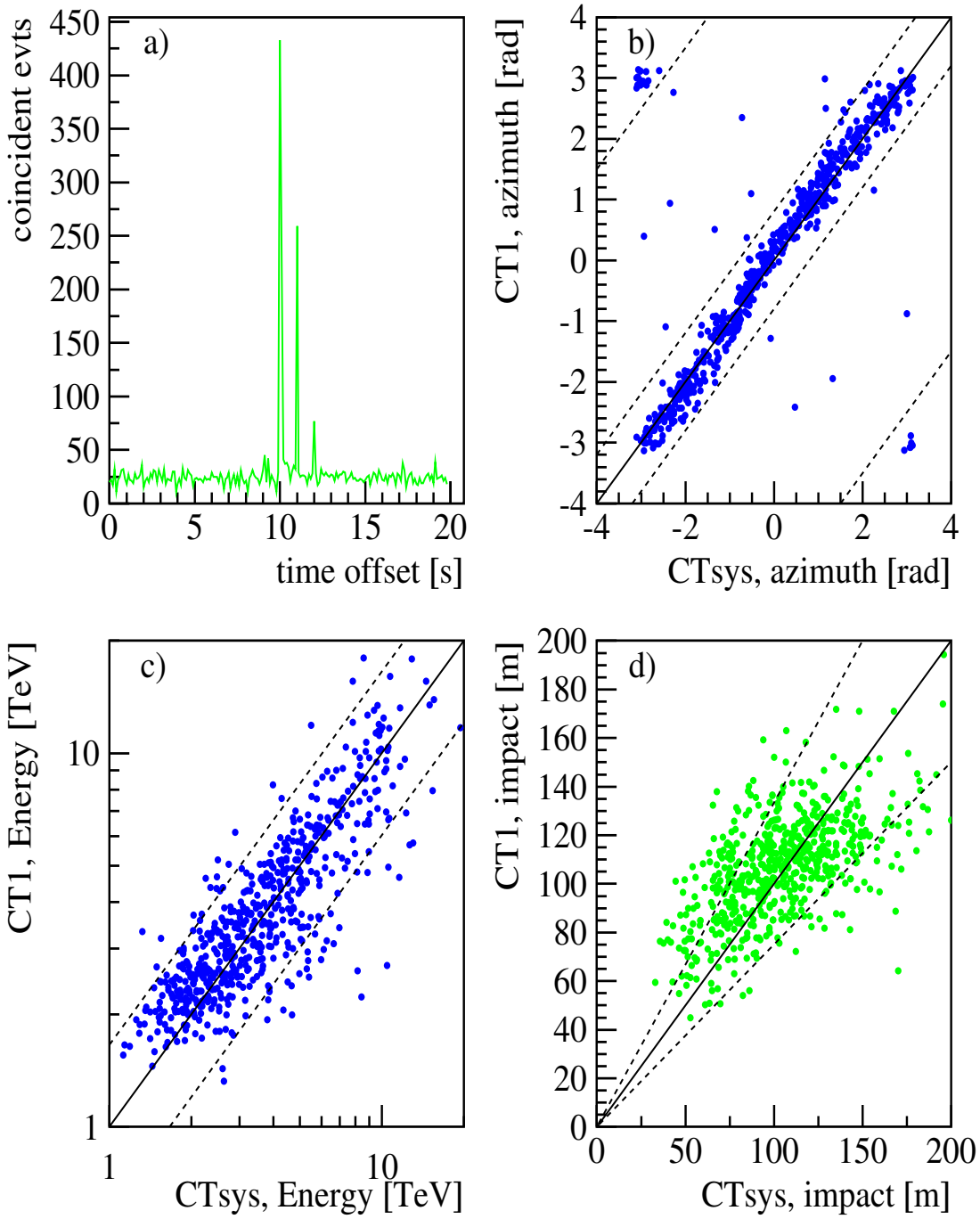

Fig. 6.3.2: Figure a) shows the number of coincident events as a function of the time offset between CT1 and CT-system (see text for further explanation). A comparison of the azimuth angle of all coincident events, as derived with CT1 and CT-system is given in fig. b). The upper and lower bands between the two dashed lines mark the region of random coincidences. Figure c) and d) show a comparison of the reconstructed energy and impact parameter. The dashed lines mark the 1σ confidence band for an energy resolution of 29% (CT1) and 20% (CT-system) and an impact parameter resolution of 20% (CT1 alone).

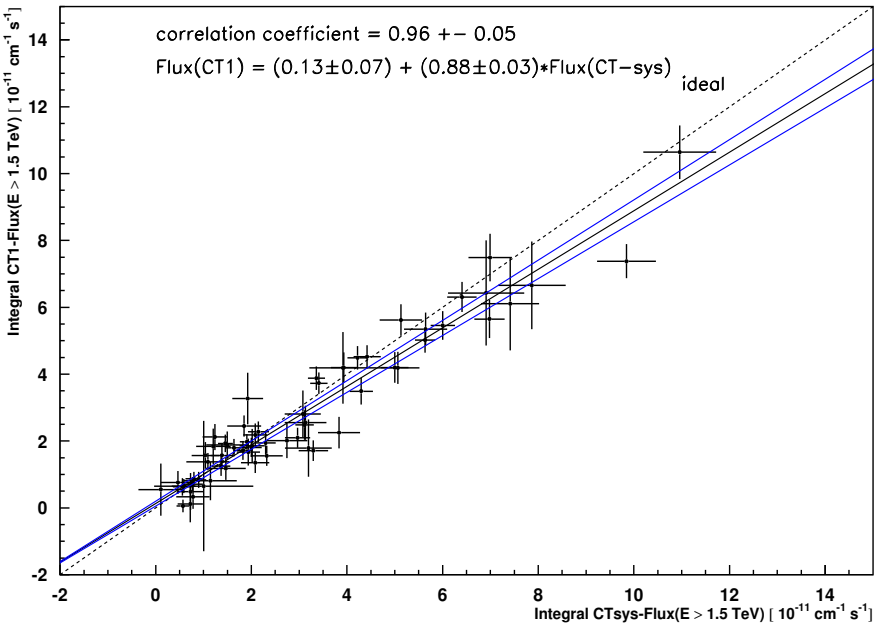

Fig. 6.4.1: Comparison of the Mkn 501 flux from CT1 and CT-system observations taken during the same night. The black line is a linear fit to the data and the blue lines mark the 1σ errors from the fit. The dashed line indicates a perfect correlation.

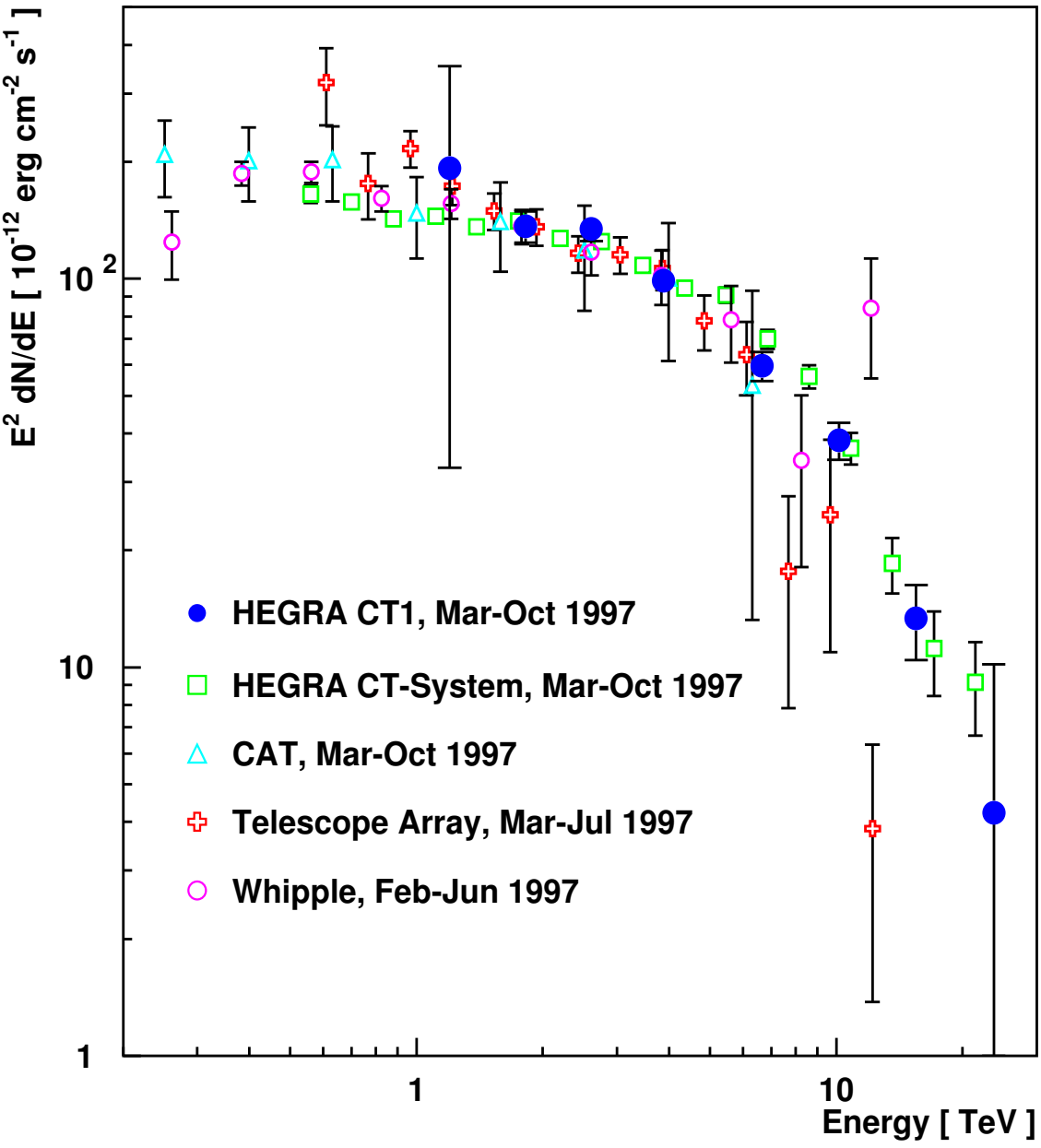

Fig. 6.4.2: The time averaged TeV spectrum of Mkn 501 during 1997 as obtained with CT1, CT-system and other experiments. The individual differential energy spectra were normalized at 2 TeV.

7. TEMPORAL CHARACTERISTICS OF THE MKN 501 DATA

The temporal characteristics of the γ-ray emission from AGN is another important topic which provides new information on these objects. Since several dynamic processes are involved in the production of high-energy γ-rays (accretion of matter, shock acceleration, etc.) their characteristic timescales might show up in the observed data. The investigation of periodic or *Quasi Periodic Oscillations* (QPO[1]) for example might provide information on accretion processes and/or the structure of binary systems (e.g. [136, 138]). Another example is the rise and decay time of individual flares, which yields information on the size of the emission region.

The investigation of possible QPO is quite common in X-ray astronomy, but have not been carried out for TeV data yet, the main reason being the lack of suitable data. The 1997 light curve of Mkn 501 with its long duration and significant flux variation, however, opens the opportunity to try such an analysis in the TeV region, too. Already at the XXV ICRC in Durban (1997), two groups (*Utah Telescope Array* (TA) and HEGRA) reported indications for a periodic structure in the TeV lightcurve (clearly visible in the TeV lightcurve, see fig. 6.1.1). Later, the TA group published a periodicity analysis of the Mkn 501 data [70] where they found indications for a 10-12 or 24-26 day periodicity. The basic problem of this analysis is, as the authors state, the gaps in the observational data caused by the moonlight periods. Due to the CT1 observations carried out during the presence of moonlight we have a nearly complete coverage of the 1997 outburst and may therefore be able to give more reliable results. One point, not taken into account in [70] refers to the calculation of probabilities for the observed periodic structure. Since BL Lac objects show the phenomenon of flaring the probability for a given period should not be calculated against the null hypothesis of Gaussian white noise[2] in the data, but against the null hypothesis of randomly distributed flares.

This chapter describes the methods used for analyzing the temporal characteristics of Mkn 501 in the TeV as well as in the X-ray data. The TeV data used are those taken with all 6 Cherenkov telescopes of the HEGRA collaboration. They were described in chapter 6. In the case of the X-ray data, the 'definitive products' RXTE/ASM data as provided on the web at `http://legacy.gsfc.nasa.gov/docs/xte/asm_products.html` have been used. I gratefully thank the RXTE team for this service.

First results of the timing analysis have already been presented at the XXVI ICRC in Salt Lake City [45, 90] in 1999. Since then the timing analysis has been refined and a large number of simulations have been carried out. The results of the complete analysis are presented here. Starting with a short description of the standard time series analysis, sec. 7.2 then deals with the *Lomb-Scargle Periodogram* (LSP) used to derive power spectra for unevenly sampled data. The next section is dedicated to the Shot Noise Model, an extension to the LSP, which assigns meaningful probabilities to the derived power spectra in case of flaring activity. The results from the Shot Noise Model and their implications are presented in the last two sections.

[1] The term QPO denotes the presence of a band of adjacent, prominent frequencies in the data in contrast to individual separated frequencies.

[2] A time series of independent (Gaussian) random numbers is denoted as (Gaussian) white noise.

7.1 Time series analysis

The main interest of a time series analysis is threefold:

- characterization of random flares in the frequency space.
- the search for possible signals (hidden by the data spacing, noise or both)
- estimation of the characteristic parameters of the signal (errors, model parameters, etc.)

The signals can be roughly classified into stochastic and deterministic signals. Depending on the signal type, it is preferable to work in the time domain (the observed quantity is given as a function of time $X_j = X(t_j)$, e.g. stochastic signals at discrete times t_j, $j = 1, ..., N$) or in the frequency domain (the process is specified as a function of the angular frequency ω: $FT_X = FT_X(\omega)$, e.g. deterministic signals). The connection between both representations is given by the *discrete Fourier transform* DFT which can be defined as:

$$FT_X(\omega) = \sum_{j=1}^{N} X_j \exp(-i\omega t_j) \tag{7.1.1}$$

($X_j = X(t_j)$, $j = 1, ..., N$ denotes values of the physical quantity, e.g. the flux of an AGN, measured at times t_j). In the case of even data spacing ($t_j = j\Delta$, $\Delta = const.$, $j = 1, ..., N$), eq. 7.1.1 becomes

$$FT_X(\omega) = \sum_{j=1}^{N} X_j \exp(-ij\omega\Delta) \tag{7.1.2}$$

and the inverse Fourier transform, which recovers the set of data points X_j from the DFT evaluated at a certain set of frequencies $\omega_n = 2\pi n/T$, $n = 1, ...N$ (T is the total time interval), is (see Appendix A.1):

$$X_j = \frac{1}{N} \sum_{n=1}^{N} FT_X(\omega_n) \exp(ij\omega_n\Delta) \tag{7.1.3}$$

(this may not hold for unevenly sampled data).

A basic tool to search for periodic signals in a given data sample is the so-called (classical) periodogram, which is conventionally defined as:

$$\begin{aligned} P_X(\omega) &= \frac{1}{N} |FT_X(\omega)|^2 \\ &= \frac{1}{N} \left| \sum_{j=1}^{N} X_j \exp(-i\omega t_j) \right|^2 \\ &= \frac{1}{N} \left[\left(\sum_{j=1}^{N} X_j \cos(\omega t_j) \right)^2 + \left(\sum_{j=1}^{N} X_j \sin(\omega t_j) \right)^2 \right] \end{aligned} \tag{7.1.4}$$

([150] and reference therein). In case there is a sinusoidal component (hereafter called sinusoid) with angular frequency ω_0 present in the data, the factors X_j and $\exp(-i\omega_0 t_j)$ are in phase. As a result, the sums in eq. 7.1.4 and therefore the periodogram $P_X(\omega)$ becomes rather large at and close to $\omega = \omega_0$. At frequencies ω significantly different from ω_0 the factors X_j and

$\exp(-i\omega t_j)$ are out of phase, therefore the individual factors of the sum basically cancel each other and the periodogram $P_X(\omega)$ has a small value. Thus prominent frequency components are visible as large peaks in the power spectrum[3] of the data sample. In the case of even data spacing, a sinusoid with amplitude A and angular frequency $\omega_n = 2\pi n/T$, $n = 1, .., (N-1)/2$ (T is the total time interval) results in a Fourier power $P_X(\omega_n) = NA^2/4$ or $P_X(\omega_n) = (N-1)/2$ when normalized onto the sample variance (see Appendix A.2).

According to eq. 7.1.3, all values X_j can be recalculated from the DFT derived at the N frequency components ω_n in the case of even data spacing. The Fourier power values at additional frequencies are therefore not independent and do not contain additional information[4]. Since half of the information is lost in the calculation of the periodogram (since $\omega_{n+N/2} = \omega_n + \pi/\Delta$ we have $\omega_{n+N/2} \cdot t_j = \omega_n \cdot t_j + \pi j$ and therefore $P_X(\omega_{n+N/2}) = P_X(\omega_n)$) it is sufficient to calculate the power spectrum for the $N/2+1$ angular frequencies[5] $\omega_n = 2\pi n/T$, $n = 0, ..., N/2$. Of special interest is the so-called **Nyquist frequency** $f_c = \omega_{N/2}/2\pi = 1/(2\Delta)$ characterizing the largest frequency component, which can be resolved by the given data spacing Δ. All frequency components above the Nyquist frequency spuriously show up in the frequency range $(0, f_c)$.

The significance of a certain frequency component is estimated by means of hypothesis testing. Given the null hypothesis that the data sample only consists of Gaussian white noise one can show (Appendix A.3.3), that $P_X(\omega)$ has a theoretical exponential probability distribution[6]:

$$\mathrm{d}\mathcal{P}(z < P_X(\omega) < z + \mathrm{d}z) = \exp(-z)\,\mathrm{d}z \tag{7.1.5}$$

It follows that the probability to obtain no Fourier power value above a certain limit z_0 in M **independent** frequencies is:

$$\mathcal{P}_M(P_X(\omega_n) < z_0, \text{ for all } n) = (1 - \exp[-z_0])^M \ . \tag{7.1.6}$$

The "false alarm probability" of the null hypothesis, i.e. the significance level of a certain frequency peak then becomes:

$$1 - \mathcal{P}_M(P_X(\omega_n) < z_0, \text{ for all } n) = 1 - (1 - \exp[-z_0])^M \ . \tag{7.1.7}$$

It should be noted, that this false alarm probability is only valid for the null hypothesis of Gaussian white noise and may dramatically change when different models are used[7].

In the case of uneven data spacing, the situation becomes more complex. It is reasonable to use the same independent Fourier spacing $\Delta\omega = 2\pi/T$, as the time interval T is still well defined, but the value of the Nyquist frequency might change with the data spacing (especially, when the data points are closely clumped together). The Nyquist frequency can be estimated by means of the *windowing function*

$$W(\omega) = \frac{1}{N}\left|\sum_{j=1}^{N} \exp(-i\omega t_j)\right|^2 \tag{7.1.8}$$

[3] "We use the terms (*power*) *spectrum* and *periodogram* interchangeably, although strictly speaking the power spectrum is a theoretical quantity defined as an integral over continuous time, and of which the periodogram is merely an estimate based on a finite amount of discrete data." (footnote from [150])

[4] Nevertheless, sometimes they are calculated in order to produce smooth graphs (oversampling).

[5] The frequency component ω_0 can be omitted by subtracting the mean $\overline{X}$ from the data values X_j.

[6] For simplicity a Gaussian random noise distribution with unit variance is assumed. Otherwise one has to renormalize eq. 7.1.4 on the variance.

[7] As will be shown in this chapter a 200σ signal can easily drop down to 3σ that way.

which characterizes periodicities inherent in the data spacing (e.g. day-night effects). Another possibility is to derive the number of independent frequencies M (according to [130, p. 578]) and to estimate the Nyquist frequency f_c according to $f_c = M/T$.

A more critical feature of unevenly sampled data is that the exponential probability distribution for $P_X(\omega)$ (eq. 7.1.5) is not strictly valid anymore. Either one has to work with a considerably more complicated statistics or one could try to reconstruct a relatively simple behavior with a slightly modified definition of the periodogram. The latter approach was chosen here.

All the lightcurve simulations presented in this chapter have been done in the following way: the observation times t_i were taken from the real data but the observed flux values/count rates were replaced by the simulation (e.g. Gaussian white noise, a Sinusoid of a given period and phase, etc.). Depending on the original data, this simulation is then referred to as simulation with TeV or X-ray data spacing. For simulations with even data spacing, the data points of the original data (i.e. the observation times) were evenly distributed over the corresponding time interval T.

7.2 The Lomb-Scargle Periodogram

In order to test for possible quasi-periodic structures in the TeV and X-ray light curves the formalism developed by Lomb and Scargle [98, 150] has been used. The *Lomb-Scargle periodogram* (as I will call it) is a modification of the classical periodogram (eq. 7.1.4) and has some improved properties compared to the latter in the case of unevenly sampled data.

7.2.1 Definition and properties

The Lomb-Scargle periodogram P_X as a function of the angular frequency ω is defined as[8]:

$$P_X(\omega) = \frac{1}{2\sigma_X^2}\left[\frac{\left[\sum_{j=1}^{N}\left(X_j-\overline{X}\right)\cos\left(\omega\left(t_j-\tau\right)\right)\right]^2}{\sum_{j=1}^{N}\cos^2\left(\omega\left(t_j-\tau\right)\right)}+\frac{\left[\sum_{j=1}^{N}\left(X_j-\overline{X}\right)\sin\left(\omega\left(t_j-\tau\right)\right)\right]^2}{\sum_{j=1}^{N}\sin^2\left(\omega\left(t_j-\tau\right)\right)}\right] \tag{7.2.1}$$

with the phase factor τ given by the equation:

$$\tau = \frac{1}{2\omega}\arctan\left(\frac{\sum_{j=1}^{N}\sin\left(2\omega t_j\right)}{\sum_{j=1}^{N}\cos\left(2\omega t_j\right)}\right) \tag{7.2.2}$$

N : number of data points
t_j : individual observation times
X_j : individual flux value at time t_j
$\overline{X}$: mean flux
σ_X^2 : flux variance

The introduction of the phase factor τ is necessary in order to preserve time translation invariance (as $t_j \to t_j + \Delta t$ for all j, see Appendix A.3.1) from the classical definition in eq.

[8] There exists a modification of the Lomb-Scargle periodogram using a normalization based on the residual variance instead of the sample variance ($\sigma_X^2 \to 1$, $X_j - \overline{X} \to \left(X_j - \overline{X}\right)/\sigma_j^2$). The main difference to the definition in eq. 7.2.1 is a different probability distribution (Fisher-Snedecor instead of the beta distribution, see [153]). In the framework of the shot noise model (sec. 7.3), however, this approach gives inferior results.

7.1.4. Its special form can be derived from least squares analysis as shown in [150, Appendix C] .

The Lomb-Scargle periodogram has the same theoretical exponential probability distribution as the classical periodogram[9]. In fact, eq. 7.2.1 can be derived from a generalized DFT by demanding the same exponential probability distribution as in the case of the classical periodogram (see Appendix A.3.3). In the case of even data spacing, the Lomb-Scargle periodogram converges to the classical periodogram (Appendix A.3.2). Due to the normalization on the variance, the mean of the probability distribution for the hypothesis of Gaussian white noise is unity:

$$\mathrm{d}\mathcal{P}\left(z < P_X(\omega) < z + \mathrm{d}z\right) = \exp(-z)\,\mathrm{d}z \tag{7.2.3}$$

Again the false alarm probability for the null hypothesis is (see sec. 7.1):

$$\begin{aligned} 1 - \mathcal{P}_M\left(P_X(\omega) < z_0 \text{ for all } n\right) &= 1 - \left(1 - \exp\left[-z_0\right]\right)^M \\ &\approx M \exp\left[-z_0\right] \quad (\text{for } z_0 \gg 1). \end{aligned} \tag{7.2.4}$$

a) the effect of aliasing:

One of the main problems of a periodicity analysis of unevenly sampled data is that even a single period can result in a complex power spectrum with a large number of aliasing peaks (fig. 7.2.1 b). The simulated period is clearly resolved in the power spectrum, but due to the strong aliasing peaks (e.g. introduced by the moon period interruptions) it is difficult to find additional frequency components. Lomb [98] therefore suggested that "subsequent periods have to be found by successively subtracting the previously found periodicities from the data and calculating the 'prewhitened' spectrum". This is not an issue for the TeV data with only one prominent frequency mode, but it was used for the X-ray periodicity analysis (despite the fact that it did not change the results too much, see sec. 7.2.2). Note that the Fourier power at the sinusoid period in the power spectrum of fig. 7.2.1 b) is close to the theoretical expectation of $P_X(\omega_{sin}) = (N-1)/2 = 99$, given the 199 data points in the TeV data sample. Furthermore, the Fourier power of the aliasing peaks is $\lesssim 10\%$ of the Fourier power of the main peak.

An example of a simulation with 2 different sinusoids and a Gaussian white noise component (here and in the following always simulated with zero mean and unit variance) is shown in fig. 7.2.2. The sinusoid amplitudes were 0.5. As can be seen, both power spectra show the two simulated frequencies (at the chosen 10.49 and 5.25 day period) and some additional peaks introduced by the noise component. Nevertheless, in order to remove doubts the subtraction method should be used as a cross check in case of multiple prominent frequencies. The significance of the two peaks in the uneven case is 2.2σ and 3.0σ respectively.

b) the influence of the data spacing:

In order to test the effect of the data spacing on the power spectrum one usually calculates the windowing function (eq. 7.1.8). The straightforward generalization of the windowing function to the Lomb-Scargle periodogram (replacing the term $X_j - \overline{X}$ in eq. 7.2.1 by unity) is not a correct window function [150, Appendix D], but nevertheless gives some hints on the critical frequency components. Some characteristic frequencies in the TeV data show up at $f = 1\,\mathrm{d}^{-1}$ (day-night interruptions) and at the moon period of about $f = \frac{1}{28}\mathrm{d}^{-1} = 0.036\mathrm{d}^{-1}$ (see fig. 7.2.3

[9] From now on, the term 'classical periodogram' always refers to even data spacing.

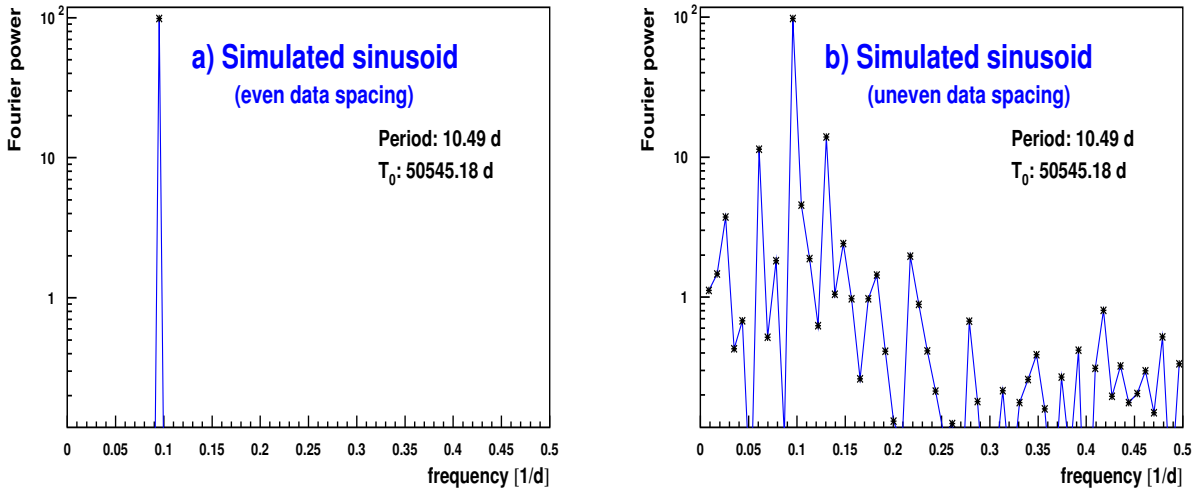

Fig. 7.2.1: Test of the power spectrum analysis for a sinusoid of a given period and phase (fixed by the time origin T_0) in the case of even a) and uneven b) data spacing as in the TeV data. Note the log scale on the ordinate.

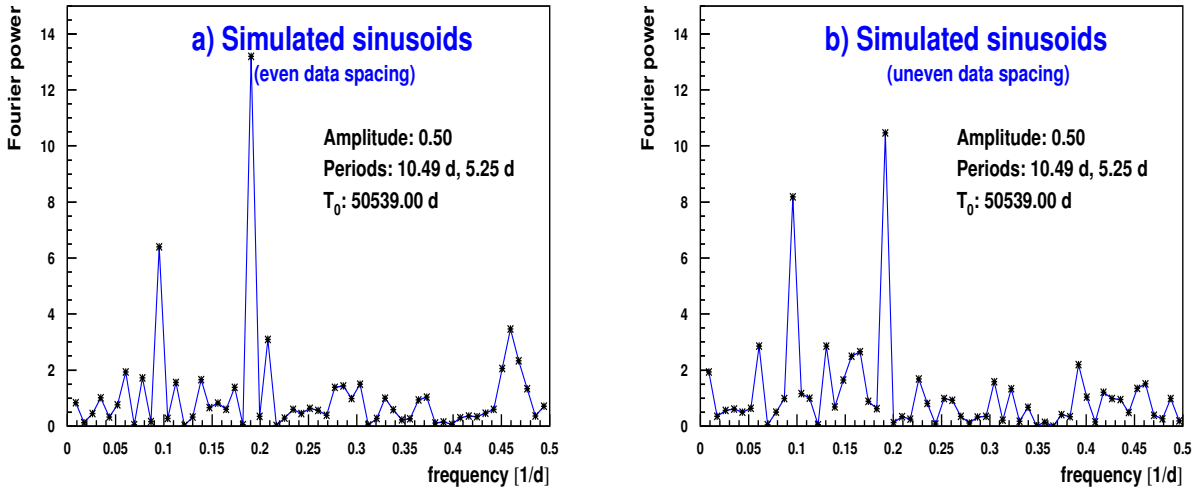

Fig. 7.2.2: Power spectrum for a signal built up from two different sinusoids (10.49 and 5.25 day period) in the case of even a) and uneven b) data spacing. The TeV data spacing was used here since it shows larger deviations from the even data spacing than the X-ray data.

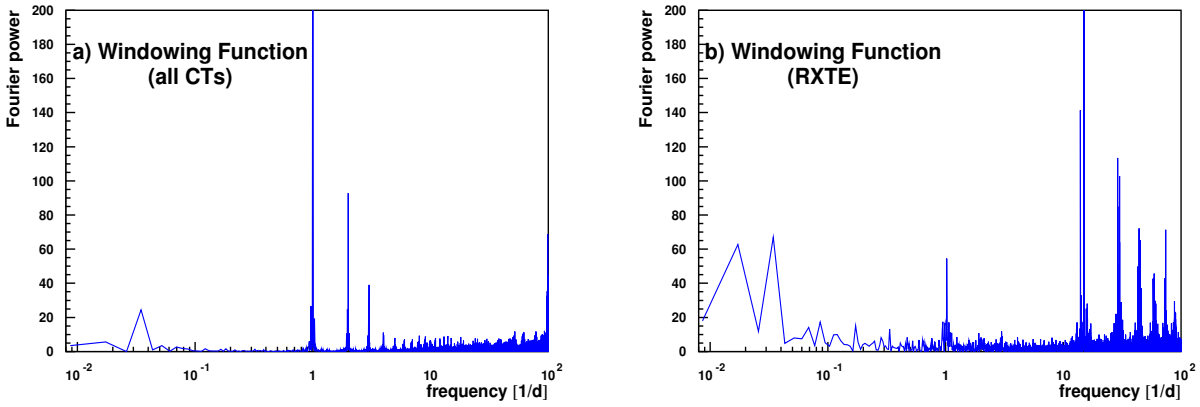

Fig. 7.2.3: Windowing function as derived for the TeV a) and X-ray b) data spacing. The y-scale is limited to 200 in order to reveal finer structures (although the highest peak goes to 400 in a) and 580 in b)).

a)[10]. In the case of the X-ray data, the most prominent frequencies, $f = \frac{1}{96}\,\mathrm{min}^{-1} = 15\,\mathrm{d}^{-1}$ and its harmonics, are related to the satellite's orbital period of 96 min. Some additional periods show up at $f = 1\,\mathrm{d}^{-1}$, at the moon period (which cannot be related to data gaps as can be seen from fig. 7.2.8) and at $f = 0.017\,\mathrm{d}^{-1}$ (59 days), the reason of which is not clear yet.

Another way to investigate critical periods is by means of sinusoid simulations with certain periods and phases (the individual phase values are specified by the time origin T_0, as $flux^{sim}(t_j) \propto \sin(\omega(t_j + T_0))$). Since the following explanation refers to the three figures 7.2.4, 7.2.5 and 7.2.6, they are introduced beforehand. Figure 7.2.4 shows the Fourier power $P_X(\omega)$ at the simulated sinusoid frequency ω as a function of this frequency ω (this is therefore not a power spectrum). The results for four different phase values are shown in one plot. The individual plots in fig. 7.2.4 cover different data spacings (RXTE, CTs and even[11]) and different settings for the mean $\overline{X}$ in eq. 7.2.1 (either the theoretical $\overline{X} = 0$ or the sample mean as estimated from the simulated data). Figures 7.2.5 a) and 7.2.6 a) show the power spectra for two different phase values from fig. 7.2.4 a). The corresponding "light curves", together with the most prominent mode from the power spectrum (green line) are shown in fig. 7.2.5 b) and 7.2.6 b). In addition, fig. 7.2.6 c) shows the 2nd most prominent mode from the power spectrum in fig. 7.2.6 a).

As can be seen in fig. 7.2.4 a), the effect of the moon period is again clearly visible in the TeV data, but obviously not for all phase values. The reason for this behavior is related to the mean $\overline{X}$ and variance σ_X^2 (in eq. 7.2.1) which are estimated from the data itself and whose values may differ strongly from the true values. If some of the sinusoid extrema are only covered by a few data points (see fig. 7.2.6 b), the sample mean and variance may not reveal the true value[12]. The effect of the variance estimation is shown in fig. 7.2.4 c), where

[10] The moon period is a mixture of the siderical (27.3 d) and the synodical month (29.5 d). The former affects the angular distance between the source and the moon, the latter affects the brightness of the moon and both influence the NSB noise during observations which is the main reason for the moon gaps in the data sample.

[11] In the case of the even data spacing, the number of data points and the covered time range of the RXTE and CTs data was kept, but the data points were evenly distributed in time.

[12] Another effect of the 'uncovered' extrema is that the 2nd harmonics are not rejected as much and aliasing effects are therefore increased (see fig. 7.2.6 a and c).

the mean was fixed at the theoretical $\overline{X} = 0$. In the case of fig. 7.2.4 c) the sample variance is always underestimated and the Fourier power therefore overestimated. However, due to the incorrect mean estimation, the sinusoids may not fit well to the data (see 7.2.6 b), and the Fourier power may be reduced. These effects were not investigated further, but the influence of the incorrect mean on the Fourier power calculation seems to dominate the effect of the incorrect variance as shown in fig. 7.2.4 a), where both effects are included. As a result, the Fourier power at the moon period is underestimated.

Nevertheless, the derived Fourier power values are very close to the theoretical expectation ($(N-1)/2$ for even data spacing, see Appendix A.2) for all other frequencies. The Lomb-Scargle periodogram therefore provides a nearly unbiased estimator[13] of the real Fourier power. The second column of fig. 7.2.4 shows the results for the X-ray data sample. Due to the better time coverage, the effects of the sample mean and variance on the Fourier power are much weaker (7% vs. 38% at the moon period and $T_0 = 50539\,\mathrm{d}$). The critical frequencies are again the same as in the windowing function (fig. 7.2.3 b).

c) Probability distribution

Due to the estimation of the mean $\overline{X}$ and variance σ_X^2 (in eq. 7.2.1) from the data, the probability distribution of the Lomb-Scargle periodogram has to be modified [153]. The periodogram then follows the beta distribution and the exponential probability distribution changes (instead of eq. 7.1.5) into:

$$\mathrm{d}\mathcal{P}\left(z < P_X(\omega) < z + \mathrm{d}z\right) = \left(1 - \frac{2z}{N}\right)^{N/2} \mathrm{d}z \tag{7.2.5}$$

[153]. For small Fourier power values z and a large number data points N, this distribution converges to the exponential distribution (eq. 7.1.5) and the differences are small. In the case of small data samples and large Fourier power values, however, the differences can be quite substantial. Figure 7.2.7 shows the *Probability Density Function* (PDF) $\mathrm{d}\mathcal{P}/\mathrm{d}z$ which was derived for the TeV and X-ray data spacing by means of the power spectra from a set of 10^8 simulated light curves (replacing the fluxes/count rates with Gaussian white noise; a modified version of the *gasdev* routine from [130] was used as random number generator[14]). The difference between the exponential and beta distribution probability is small but clearly visible in the TeV data ($N = 199$), but is negligible for the X-ray data ($N = 1894$). Besides the moon period, where differences are expected, the beta distribution describes the simulations quite well in both cases[15].

The results from the Fourier analysis of the TeV and X-ray data are presented in the next section.

[13] In principle the statement is only justified for the given data samples, but since these samples already show large deviations from the even data spacing this statement should apply to most other data sets as well.

[14] The changes were, that *ran2* instead of *ran1* was used to generate uniformly distributed random numbers and that all calculations were carried out in double precision. The *ran2* is a "long period ($> 2 \cdot 10^{18}$) random number generator of L'Ecuyer with Bays-Durham shuffle and added safeguards". ... "We think that, within the limits of its floating-point precision, *ran2* provides perfect random numbers" (from [130]). All simulations presented here are based on this routine.

[15] The agreement between the beta distribution and the simulated PDF can also be regarded as a test for the random number generator [153].

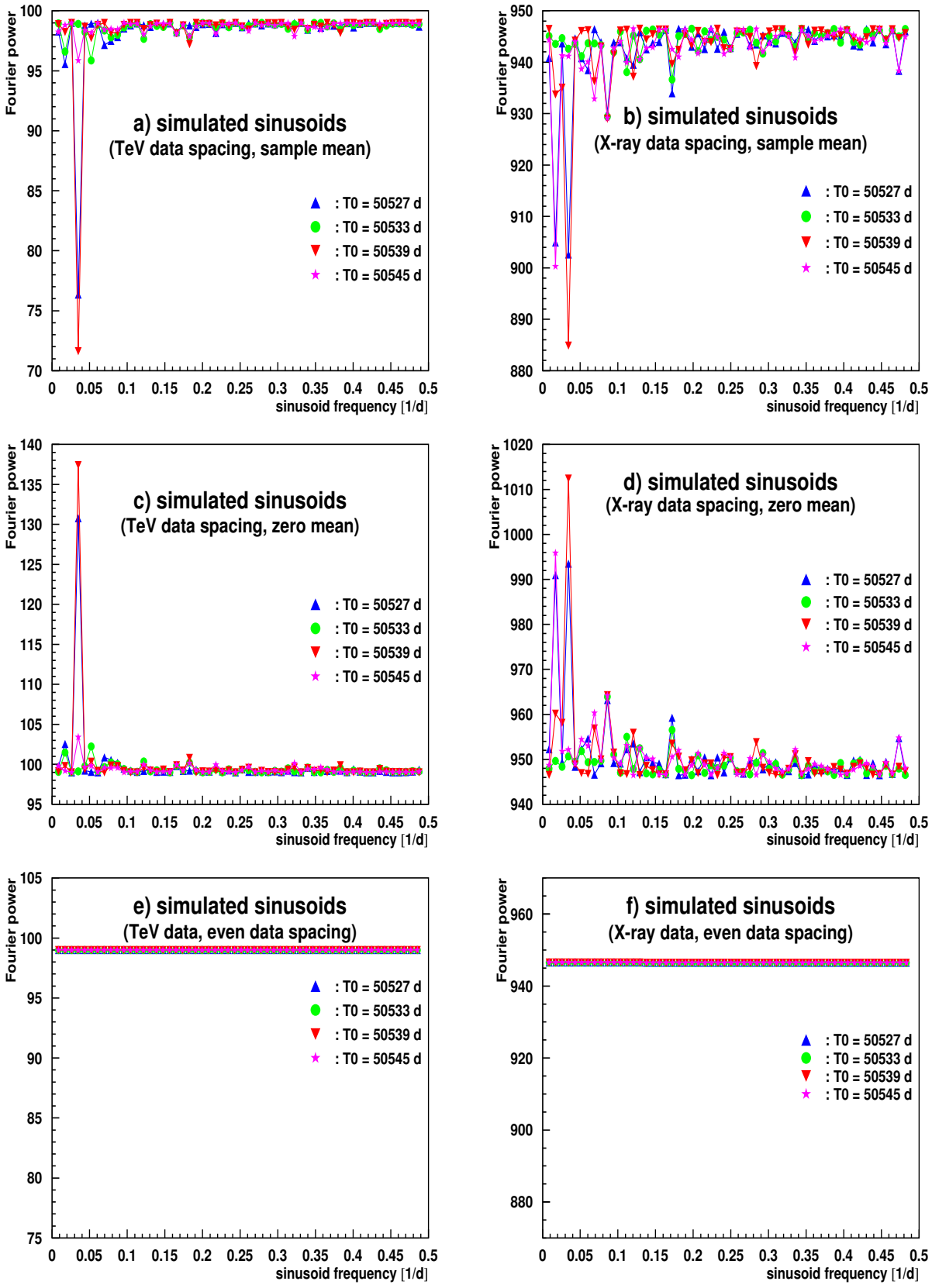

Fig. 7.2.4: Fourier power $P_X(\omega)$ at the sinusoid frequency ω as a function of the sinusoid frequency ω for different phase values (fixed by the time origin T_0). See text for further explanation. Note that the y-scale does not start at zero.

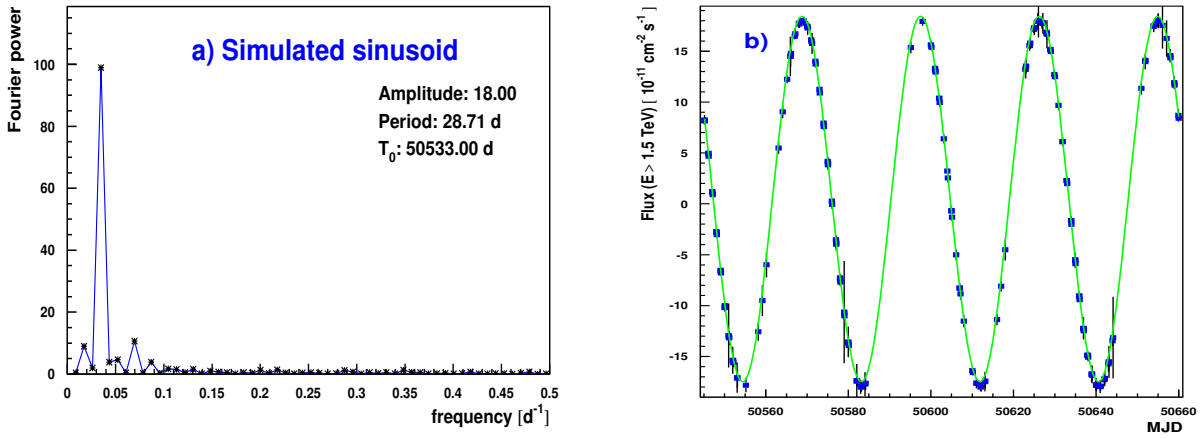

Fig. 7.2.5: Power spectrum a) and corresponding "lightcurve" b) for a simulated sinusoid (TeV data spacing) with a period close to the moon period and given phase value (fixed by the time origin T_0). The green line corresponds to the most prominent mode in the power spectrum a).

7.2.2 Results for the X-ray and γ-ray data

For the timing analysis of the TeV and X-ray data of Mkn 501, two pre-selections have been made:

- Only data from the first two shadow-cameras of RXTE have been used. The data sample of the 3rd camera is rather incomplete having large data gaps and was therefore not used.
- The timing analysis was restricted to the time region of $50545 \leq MJD \leq 50660$ (blue lines in fig. 7.2.8), i.e. a time range $T = 115$ d. As lower limit the beginning of the large flaring activity was selected and as upper limit the time of the start of the data gap in the X-ray data was used. This limit also excludes the data taken at the end of the observation period (of ACTs[16]), i.e., data which were obtained from short-time observations and therefore had larger errors. Since the individual data errors are not taken explicitly into account in the Lomb-Scargle periodogram, adding a small fraction of data with much larger errors might spoil the results. Furthermore, this data was taken at large zenith angles and systematic errors were therefore larger (in part due to the small MC statistics and in part due to higher influence of optical transmission variations of the atmosphere).

The time limit selection has been made in the very beginning of the investigation and has been used since then.

Once the data sample is defined for the timing analysis, the first issue concerns the Nyquist frequency (see sec. 7.1) and the related problem of the number of independent frequencies M in the data sample. As can be seen from fig. 7.2.8, the TeV lightcurve is composed of small groups of typically 3 data points separated by 1 day (no observations during daylight). This characteristic 1 day timescale is also visible in the windowing function (fig. 7.2.3 a) of the TeV

[16] At the end of the observation period, any object under study culminates well before sunset and has a rather large zenith angle when the observation starts. Therefore it can be observed only for a short time until the zenith angle becomes too large.

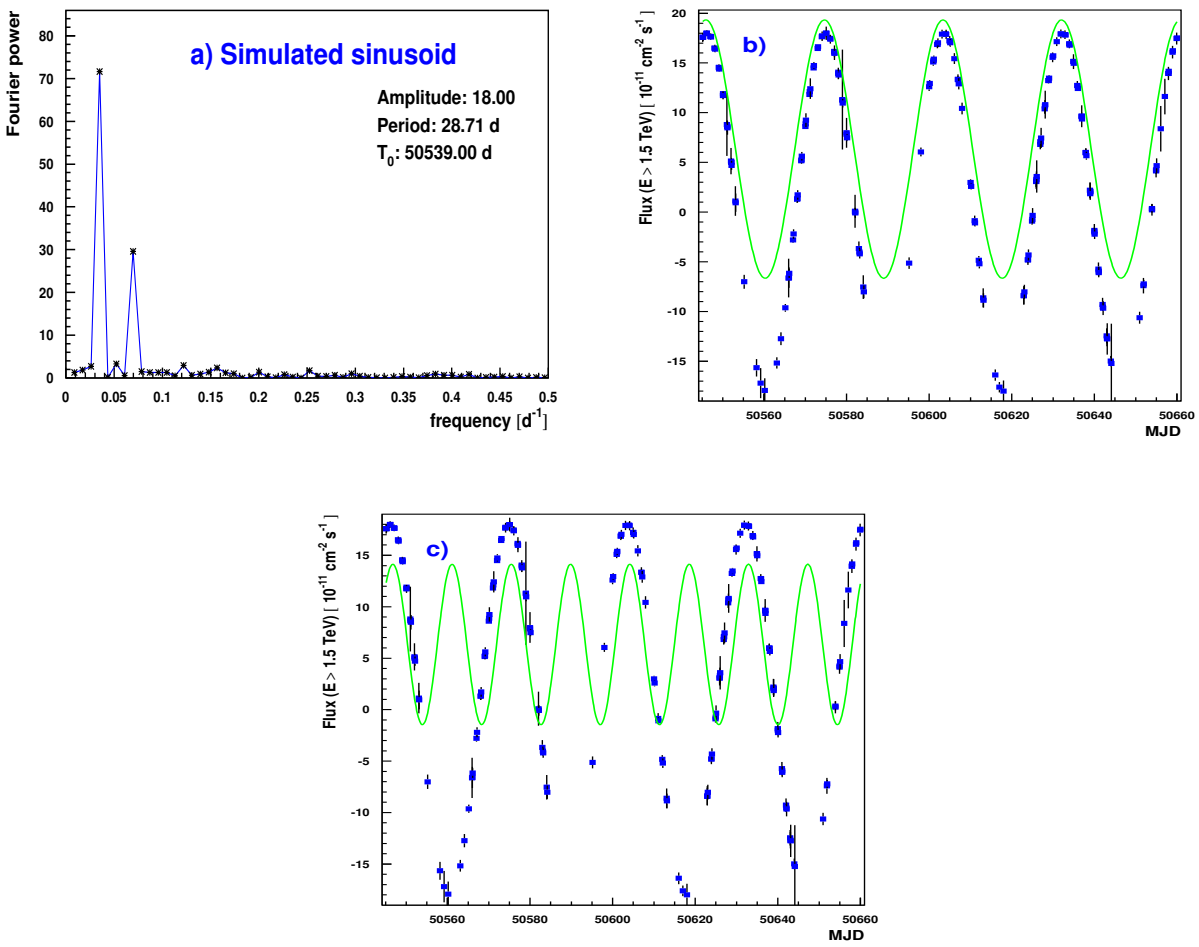

Fig. 7.2.6: Power spectrum a) and corresponding "lightcurve" b) for a simulated sinusoid (TeV data spacing) with a period close to the moon period and given phase value (fixed by the time origin T_0). The green line corresponds to the most prominent mode in the power spectrum a). The last plot c) shows the simulated lightcurve using the 2nd most prominent mode from the power spectrum a).

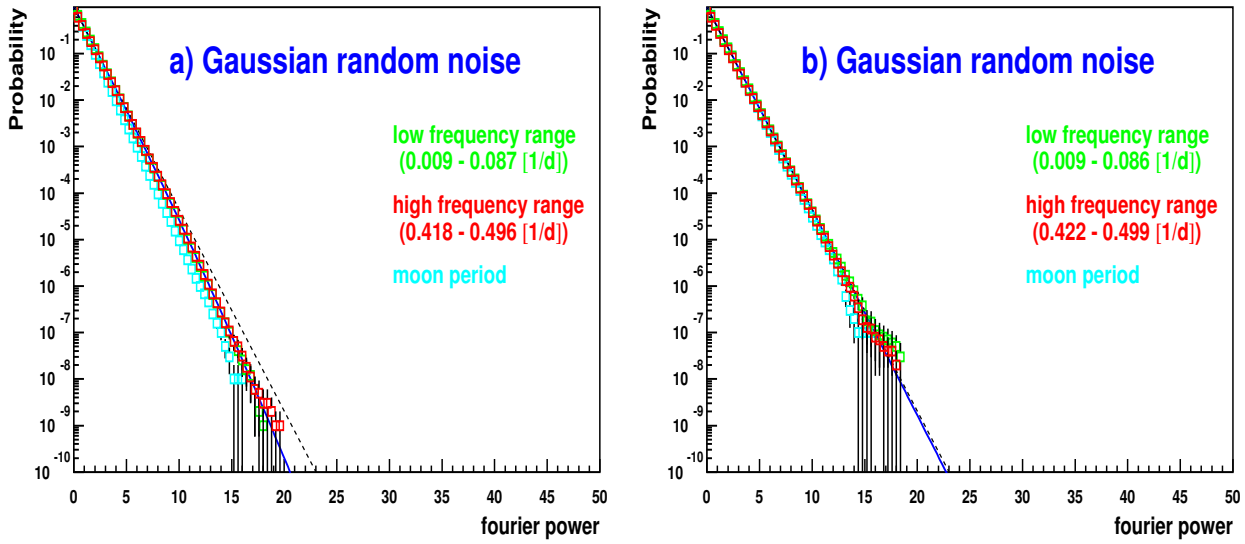

Fig. 7.2.7: Probability density function for the Lomb-Scargle periodogram for 2 frequency ranges and the moon frequency in the case of the TeV a) and X-ray b) data spacing. The different PDFs were derived from the data by replacing the observed fluxes/count rates with Gaussian white noise. The dashed line denotes the exponential probability distribution whereas the blue line denotes the beta distribution probability (taking into account the indeterminacy of the variance) from eq. 7.2.5. In order to increase statistics, 10 consecutive frequencies have been combined (except for the moon period).

data. The 'Nyquist frequency' f_c was therefore set to $f_c = 0.5\,\mathrm{d}^{-1}$ [17]. This is also supported by simulations of sinusoids close above f_c (where significant aliasing effects are supposed to show up). As can be seen from fig. 7.2.9, the corresponding peak in the power spectrum is folded back into the frequency range $(0, f_c)$. Since the sinusoid peak starts forking at $f \simeq 0.5\,\mathrm{d}^{-1}$ the choice of f_c is reasonable.

The number of independent frequencies M was estimated by means of MC simulations. Again a set of light curves (replacing the fluxes/count rates with Gaussian white noise) was used to estimate the probability $\mathcal{P}_{ex}\left(P_X\left(\omega\right) > z_0\right)$ that at least one of the test frequencies has a Fourier power value above z_0. This probability has to be compared with the analytical expectation, which can be taken according to eq. 7.2.4 in case the mean is set to zero and the variance to unity. Replacing $1 - \mathcal{P}_M$ by $\mathcal{P}_{ex}$ and solving for M gives:

$$M = \frac{\ln\left(1 - \mathcal{P}_{ex}\right)}{\ln\left(1 - \exp\left(-z_0\right)\right)} \tag{7.2.6}$$

A test with an even data spacing and with frequencies restricted to $f_{max} \leq 0.5\,\mathrm{d}^{-1}$ revealed $M = 57.2 \pm 0.7$ (a Fourier power of $z_0 = 8$ was used) which perfectly agrees with the theoretical value $M = INT\left(f_{max}/\Delta f\right) = INT\left(f_{max} \cdot T\right) = INT\left(0.5 \cdot 115\right) = 57$. The value of M for the uneven sampled TeV data was derived as $M = 57.6 \pm 0.6$ so all the frequencies $f_i = i/T$ (with $i = 1, \ldots, M$) equal or below the 'Nyquist frequency' $f_c = 0.5\,\mathrm{d}^{-1}$ are considered to be independent.

In order to compare the results from the TeV and X-ray data, the maximum frequency for the X-ray data was also set to $0.5\,\mathrm{d}^{-1}$. Since the X-ray data covers the same time region as the

[17] In contrast to the case of even data spacing, the Nyquist frequency is not clearly defined for uneven data spacing but approximately correct for our type of binning.

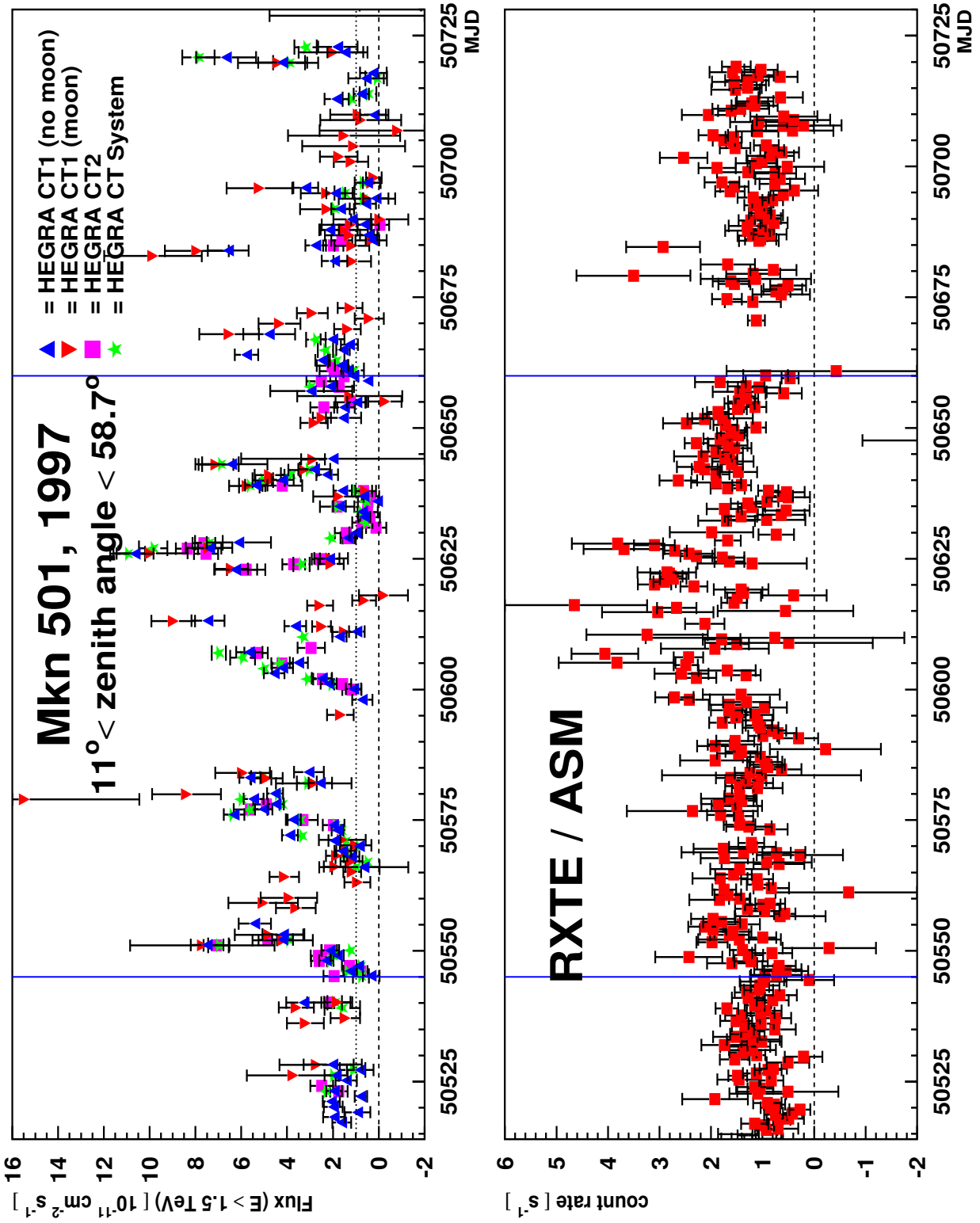

Fig. 7.2.8: TeV (upper) and X-ray (lower) lightcurve for Mkn 501 in 1997. The data within the two blue lines was used for the timing analysis (see text). The RXTE data was binned for visual purposes.

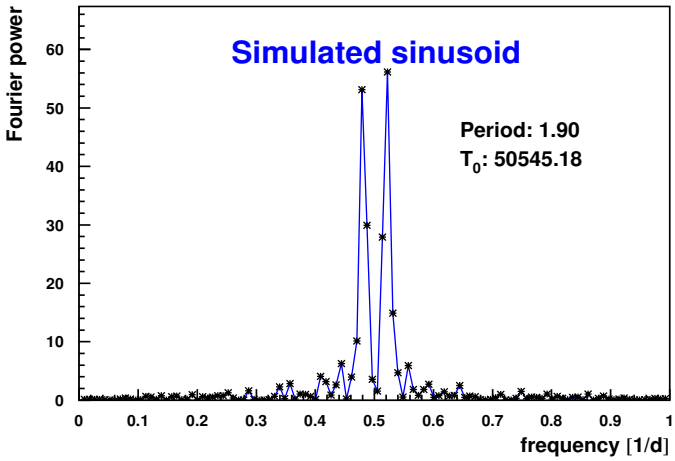

Fig. 7.2.9: Power spectrum for a simulated sinusoid above the 'Nyquist frequency' $f_c = 0.5\,\mathrm{d}^{-1}$ (TeV data spacing). The second peak below f_c is due to aliasing.

TeV data, the number M_X of independent frequencies equal or below $f = 0.5\,\mathrm{d}^{-1}$ is 57, too.

The power spectra for the measured TeV and X-ray data samples are shown in fig. 7.2.10 a) and c). Also shown are the corresponding light curves (b and d; binned in the case of the X-ray data) and, as a green line, the prominent modes from the corresponding power spectrum (frequencies with a Fourier power above 20). As can be seen, both power spectra have a prominent peak at $\sim$ 23 days. In contrast to the TeV data, however, the periodic structure is not as clearly visible in the X-ray lightcurve. In order to remove the contribution of the first prominent frequency at $1/T$ in the X-ray power spectrum[18], this mode was subtracted from the data[19]. The resulting power spectrum is shown in fig. 7.2.10 e). The Fourier power at the removed frequency component is nearly zero, but all other frequencies are only slightly affected.

The main results of the power spectrum analysis are shown in tab. 7.2.1. The given period corresponds to the position of the maximum Fourier power using an oversampling factor of 20. The errors are estimated from the FWHM of the individual peaks (TeV and X-ray data) at the 23 day period. In the case of small data samples (TeV data), there is a big difference in the probability derived from the exponential and the beta distribution (nearly a factor 4 in significance) whereas the effect is rather small for large data sets (X-ray data). Given the null hypothesis of Gaussian white noise, the 23-day period in the data is beyond any doubts.

As can be seen from the light curves in fig. 7.2.10, both data samples do not only have the same prominent frequency, but are also close in phase. This can be seen more clearly by means of a phase plot. Here, the measured lightcurve is folded with a given period p and the individual data points are then distributed to the corresponding phase bin $(phase = (t_j\, modulo\, p)\,/p)$. The flux/count rate for each phase bin is calculated as weighted mean. Figure 7.2.11 shows the phase plots for a set of periods p corresponding to the largest Fourier power values of the

[18] The large Fourier power at $1/T$ is addressed to the overall shape of the Mkn 501 X-ray lightcurve in 1997 (significant increase until mid 1997 and then a falling tendency until the end of the year).

[19] The contribution of a single frequency component k to the lightcurve can be derived from eq. 7.1.3 as: $X_j\,(\omega_n) = \frac{1}{N} FT_x\,(\omega_n) \exp\,(ij\omega_n \Delta)$. Since eq. 7.1.3 may not hold for uneven sampled data, the frequency component may not be completely removed from the data. In the case of the X-ray data, the remaining contribution is negligible.

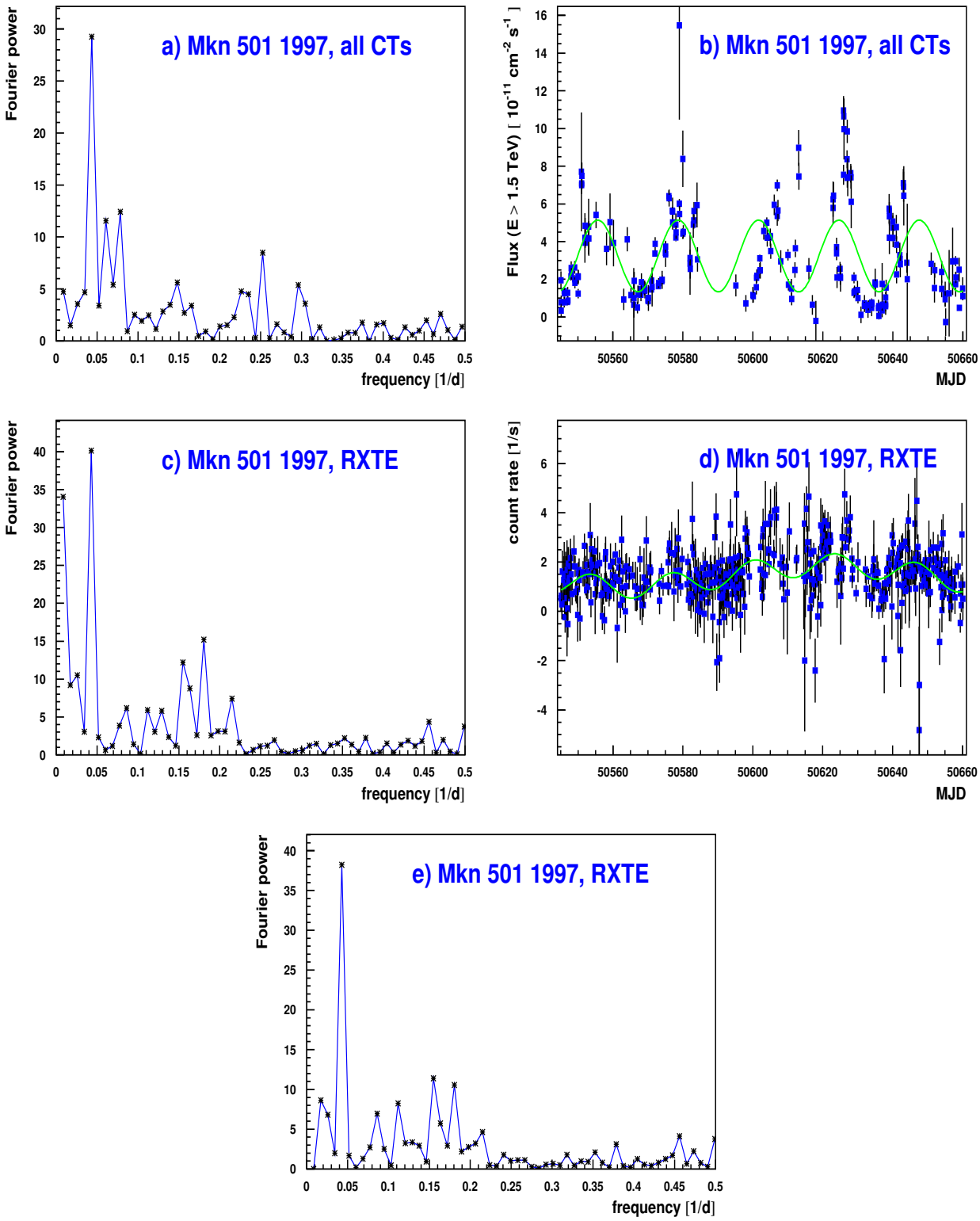

Fig. 7.2.10: The left side shows the power spectrum as derived from the measured TeV a) and X-ray c) data. The strongest peak in both data samples is located at a period of ~ 23 days. The right side (fig. b and d) shows the corresponding light curves (the X-ray data are binned for visual purposes) and the prominent modes from the power spectrum (frequencies with a Fourier power above 20) as a green line. Figure e) shows the X-ray power spectrum after subtracting the prominent mode at $1/T$.

data sample	period p [d]	Fourier power (at period p)	probability	
			exponential	beta distribution
X-ray:	$23.0^{+1.8}_{-2.0}$	38.2	$141.3\,\sigma$	$163.8\,\sigma$
TeV:	$22.5^{+1.8}_{-1.7}$	29.3	$19.1\,\sigma$	$69.4\,\sigma$

Tab. 7.2.1: Main results of the TeV and X-ray power spectrum. The stated significance is for the null hypothesis of Gaussian white noise.

TeV power spectrum (fig. 7.2.10 a). While there is a periodic structure visible at 12.8, 16.4 and 23 days in the TeV data, the X-ray data shows a periodicity only at 23 days. In that case both data samples are in phase. According to the phase plot at $p = 4$ d the peak in the TeV power spectrum is mainly due to the data spacing.

7.2.3 Conclusions

In summary the following conclusions can be drawn for the Lomb-Scargle periodogram:
Even in the case of simple periodic signals (i.e. sinusoids), the Lomb-Scargle periodogram shows a rather complex power spectrum (fig. 7.2.1 b). Nevertheless, since the Fourier power of the aliasing peaks has been found to be only about 10% of the main signal Fourier power (in the worst case of the TeV data with large moon gaps) all signal components could be clearly identified in the simulations down to a signal to noise ratio (i.e. ratio between the sinusoid amplitude and the noise variance) of 0.5 (fig. 7.2.2 b). In case of several prominent modes in the power spectrum it is advisable to derive the power spectra after removing these modes one by one from the data. Thus one can be sure that a certain prominent mode is not caused by aliasing of a stronger mode.

A big advantage of the Lomb-Scargle periodogram is the simple PDF which is basically given by the exponential distribution. In practice deviations from this distribution show up, since the mean and variance of eq. 7.2.1 have to be estimated from the data itself. The PDF then changes into the beta distribution probability (eq. 7.2.5). In the case of small Fourier power values or large data sets however, the difference between both PDFs becomes marginal.

When applied to data with large gaps the Lomb-Scargle periodogram might show a strong phase dependence for certain frequencies (fig. 7.2.4 a - d). The reason is that the calculation of the sample mean and variance is strongly affected then. In the case of the TeV data the only critical frequency corresponds to the moon period. Depending on the phase, the effect might be negligible or strong (Fourier power reduced by 38%, see fig. 7.2.4 a). Since the Fourier power is underestimated then, the beta distribution does not hold for this special frequency. It seems that the Lomb-Scargle periodogram never overestimates the Fourier power, but this has to be investigated further. In order to reduce the effect of the moon gaps in the TeV data, moon observations have proven to be of great importance. Figure 7.2.12 shows the results from a worst case scenario, where the period and phase of the simulated sinusoid was chosen in order to maximize the effect of the moon data gaps. As can be seen, including the moon data points in the power spectrum calculation increases the Fourier power at the sinusoid frequency and decreases the Fourier power of the largest aliasing peak by about a factor 2.5.

The results of the timing analysis of the TeV and X-ray data are as follows:

- Both the TeV and X-ray data samples show a strong peak in the power spectrum at a 23 day period (fig. 7.2.10 a and c). The exact periods were derived from oversampled

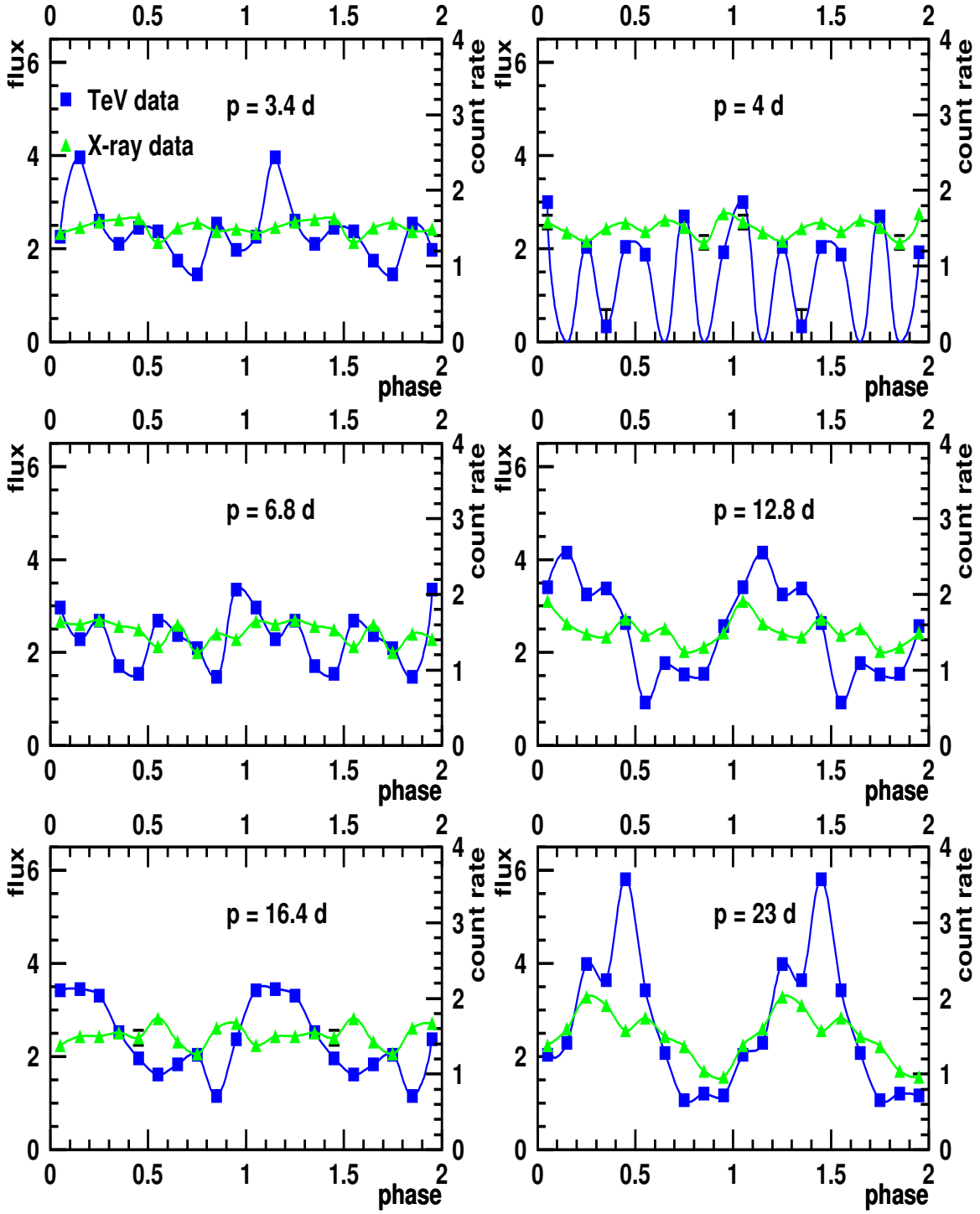

Fig. 7.2.11: Phase plots for the Mkn 501 TeV (blue boxes) and X-ray (green triangles) lightcurve. The data points denote the weighted mean as derived from the folded light curves. The chosen periods p (in days) correspond to the largest Fourier power values from fig. 7.2.10 a). In the case of the TeV data, the flux is given as integral flux above 1.5 TeV in units of $10^{-11}\mathrm{cm}^{-2}\mathrm{s}^{-1}$, in case of the X-ray data, the count rate is in *counts*/s. For visual purposes, two identical cycles are shown (common in astronomy).

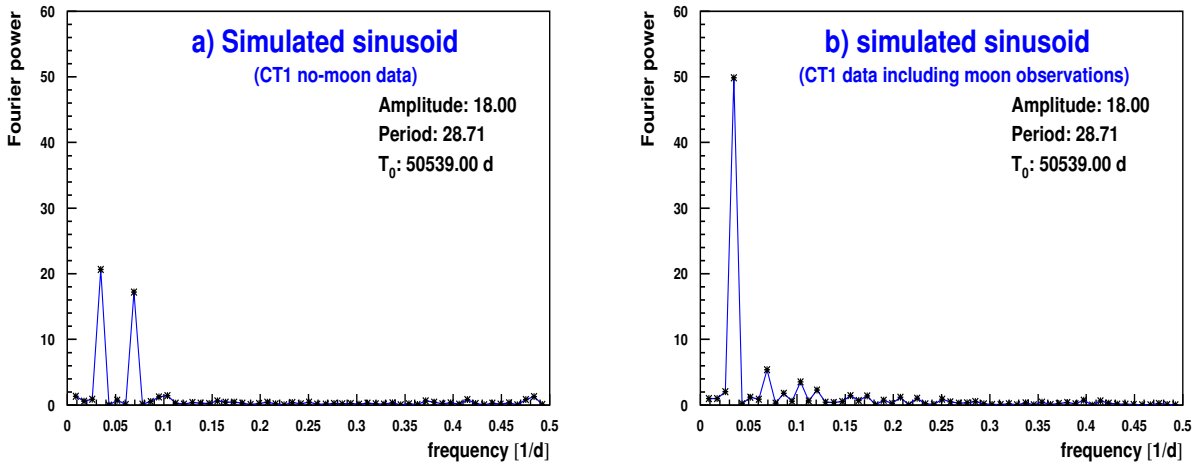

Fig. 7.2.12: The power spectrum for a simulated sinusoid sampled at the CT1 no-moon data points a) and at the combined moon and no-moon data points b). The chosen period and phase (fixed by the time origin T_0) denotes the worst case scenario.

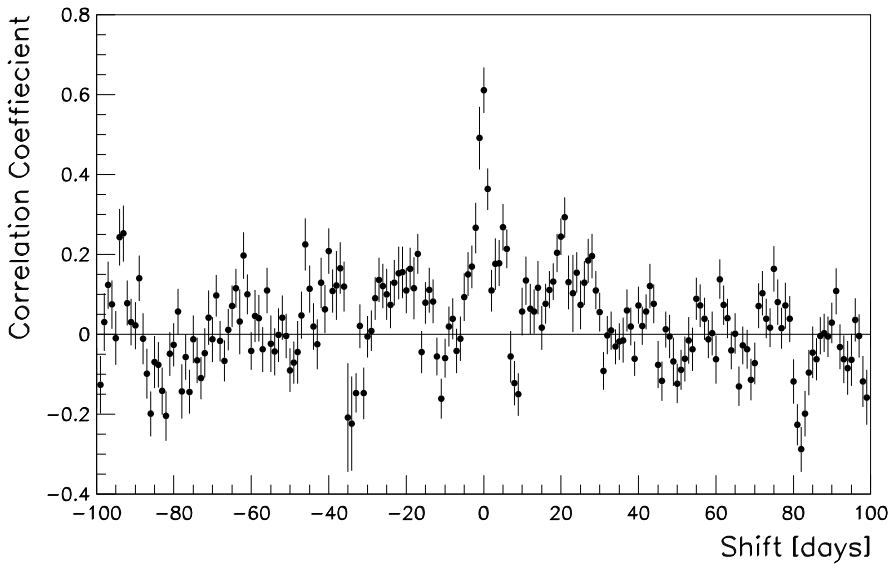

Fig. 7.2.13: Correlation coefficient as a function of the artificially introduced time shift between the RXTE and CT1 data. Taken from [2, p. 37].

power spectra as $p_{X-ray} = 23.0^{+1.8}_{-2.0}$ d and $p_\gamma = 22.5^{+1.8}_{-1.7}$ d. The errors denote the FWHM of the individual peaks in the power spectrum.

- For the 23 day period, the X-ray and TeV data also have the same phase. This can also be seen from fig. 7.2.13, which shows the correlation coefficient between the RXTE and CT1 data as a function of an artificial time shift between the RXTE and CT1 time. Since the maximum correlation coefficient is obtained at a time lag of 0 d, both data samples are in phase.

- The periodic structure is well visible in the TeV, but not so clearly in the X-ray lightcurve (fig. 7.2.8).

- The 23 day period in the TeV data is not caused by the data gaps due to the full moon interruption.

- Given the null hypothesis of Gaussian white noise, the significance of the 23 day period becomes $163.8\,\sigma$ for the X-ray and $69.4\,\sigma$ for the TeV data (eq. 7.2.5, taking into account the number of 57 independent test frequencies).

As will be shown in the next main section, these significances will dramatically change in case of another physics motivated assumption on the null hypothesis. Consequences of the observed periodicity will also be discussed then.

7.3 The shot noise model

In the case of Gaussian white noise the Lomb-Scargle periodogram has quite a simple statistical behavior. As was shown in the last chapter, its PDF basically follows the PDF of the beta distribution being (in the case of the TeV and X-ray data) close to the exponential distribution with unit mean and variance. Due to the known PDF it is then possible to assign probabilities to the individual Fourier power values.

In the case of Mkn 501 however, the basic assumption of Gaussian white noise of the previous chapter does not strictly hold. Since AGN show the phenomenon of flaring, consecutive data points are not independent anymore and the assumption of white noise is therefore invalid. One way to handle this problem is to estimate the number of correlated consecutive data points k and replace each group of k data points by its average [153]. This procedure, however, may either introduce new or remove existing periodicities from the power spectrum (Slutzky's Theorem, [66, p. 97]). A different approach was therefore used here:

The *shot effect* or *shot noise model* is well known in electronics [17] and X-ray astronomy[20] ([168] and reference therein) and denotes the response of a linear system to input data which consists of a large number of randomly distributed shots with random amplitude. This model can be easily adopted to Blazars by identifying the shock waves, or more precisely the interactions of a shock wave with a plasma 'blob' in the jet, with the random shots. The system response function is then given by the γ-production model and reveals itself in the shape of the individual flares. From a physics viewpoint, the rapid variability of the flares can be understood by means of shock acceleration of electrons, leading to short flare rise times, while the short decay time scales may be due to radiative cooling of the electrons.

Once the response function is known, the power spectrum and PDF of the system can be calculated. Given the PDF, it is then possible to reassign probabilities to the Fourier power

[20] Where it was used to explain the power spectra of low-mass X-ray binaries.

peaks. Thus the main idea is to
replace the null hypothesis of Gaussian white noise by that of randomly distributed flares with a certain shape.
As will be shown below, the normalization of the Mkn 501 power spectra on the shot noise model leads to white noise residuals, except for the 23-day effect, which imply an exponential probability distribution of the normalized Fourier power values. Since the shape of the individual flares also determines the shape of the mean power spectrum, it should be possible to distinguish between different types of flares, thus giving further insight into the physical processes involved.

In summary, the input data $x(t)$ is given by the following Ansatz:

$$x(t) = \sum_{i=1}^{K} a_i \cdot \delta(t - \tau_i) \tag{7.3.1}$$

and the system response $f(t)$ represents the convolution of the response function $h(t)$ with the input data $x(t)$:

$$\begin{aligned} f(t) &= h(t) * x(t) := \int x(\tau)\, h(t-\tau)\, \mathrm{d}\tau \\ &= \sum_{i=1}^{K} a_i \int \delta(\tau - \tau_i)\, h(t-\tau)\, \mathrm{d}\tau \\ &= \sum_{i=1}^{K} a_i \cdot h(t - \tau_i) \end{aligned} \tag{7.3.2}$$

$h(t)$	-	response function to δ -type shots at time 0
τ_i	-	time of i-th flare/shot
a_i	-	Amplitude of i-th flare/shot (replace a_i by $(a_i - \overline{a})$ in case $\overline{a} \neq 0$)
K	-	denotes the number of independent flares/shots which contribute to the observed data

Please note, that the a_i and τ_i values are not completely independent if each shock wave produces several flares through interaction with a set of plasma 'blobs'.

Due to the Convolution theorem [130, p. 498], the Fourier transform $F(\omega)$ of the system response $f(t)$ is given by:

$$F(\omega) = \int_{-\infty}^{\infty} f(t) \exp(i\omega t)\, \mathrm{d}t = H(\omega)\, X(\omega) \tag{7.3.3}$$

with $H(\omega)$ and $X(\omega)$ being the Fourier transforms of $h(t)$ and $x(t)$ respectively. Since

$$X(\omega) = \sum_{i=1}^{K} a_i \exp(i\omega\tau_i) \tag{7.3.4}$$

the Fourier power of the shot noise model becomes

$$\begin{aligned} |FF^*| &= |H(\omega)|^2 \cdot |X(\omega)|^2 \\ &= |H(\omega)|^2 \cdot \left[\left(\sum_{i=1}^{K} a_i \cos(\omega\tau_i) \right)^2 + \left(\sum_{i=1}^{K} a_i \sin(\omega\tau_i) \right)^2 \right] \end{aligned} \tag{7.3.5}$$

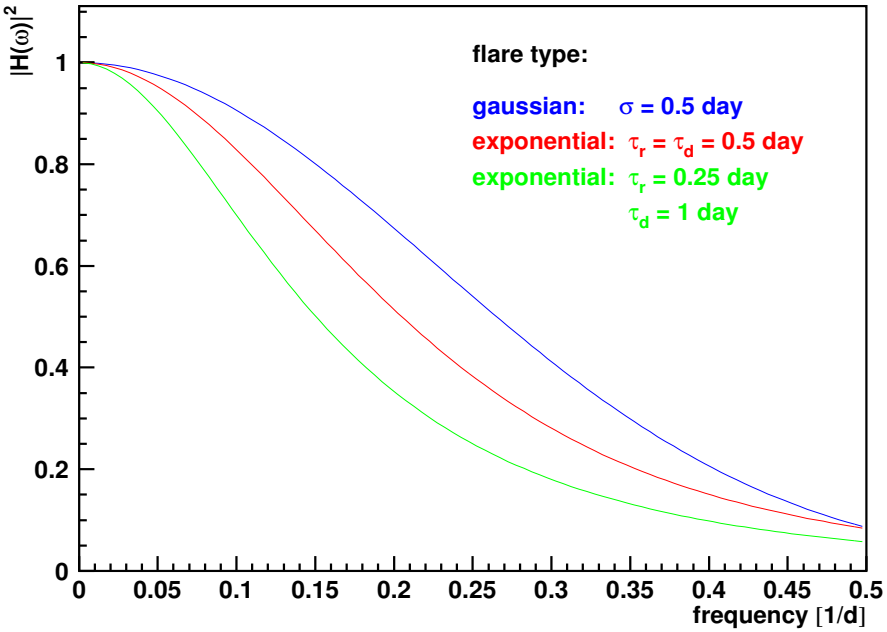

Fig. 7.3.1: Frequency dependence of the mean Fourier power for different flare types. For Gaussian type flares the power spectrum is proportional to $\exp\left(-\omega^2\sigma^2\right)$ and in the case of exponential type flares proportional to $\left(1+\omega^2\tau_r^2\right)^{-1}\cdot\left(1+\omega^2\tau_d^2\right)^{-1}$.

Since the variables a_i, τ_i and therefore $a_i\cos\left(\omega\tau_i\right)$ and $a_i\sin\left(\omega\tau_i\right)$ are randomly distributed, the two sums in eq. 7.3.5 are approximately normally distributed according to the central limit theorem [38, p. 147]. The mean of each sum is zero (by definition of the amplitudes a_i) and the variance is $\sigma_a^2 = 0.5K\overline{a^2}$. Therefore

$$\left|FF^*\right| = K\overline{a^2}\left|H\left(\omega\right)\right|^2\left[\frac{\left(\sum_{i=1}^{K}a_i\cos\left(\omega\tau_i\right)\right)^2}{2\sigma_a^2}+\frac{\left(\sum_{i=1}^{K}a_i\sin\left(\omega\tau_i\right)\right)^2}{2\sigma_a^2}\right] \tag{7.3.6}$$

is χ^2-distributed with 2 degrees of freedom and has a mean and variance equal to $K\overline{a^2}\left|H\left(\omega\right)\right|^2$. This means that the exponential probability distribution for $\left|FF^*\right|$ is still valid here and holds **independently of the flare type**. In contrast to the case of Gaussian white noise, however, the mean and variance of the Fourier power is now also frequency dependent. Figure 7.3.1 shows the power spectrum for Gaussian ($\left|H\left(\omega\right)\right|^2 \propto \exp\left(-\omega^2\sigma^2\right)$) and exponential type flares ($\left|H\left(\omega\right)\right|^2 \propto \left(1+\omega^2\tau_r^2\right)^{-1}\cdot\left(1+\omega^2\tau_d^2\right)^{-1}$, with rise time τ_r and decay time τ_d[21]). As can be seen, the individual power spectra are quite different. It should therefore be possible to distinguish between certain γ-production or flare models [46, 88, 157] by means of the observed power spectra. All the following calculations are carried out for Gaussian type flares ($h\left(t\right) = \exp\left(-t^2/2\sigma^2\right)$), but can be easily applied to other flare types.
In order to compare the Lomb-Scargle Fourier power (eq. 7.2.1) with the theoretical expectation (eq. 7.3.6) one has to take into account all the normalization factors. The estimate

[21] Since the power spectrum is symmetric in τ_d and τ_r it can not be used to distinguish between both time parameters.

of the Lomb-Scargle Fourier power for the shot noise process, assuming Gaussian type flares with width σ, then becomes:

$$\begin{aligned} P_X(\omega) &\simeq \frac{1}{2\frac{N}{2}s_X^2} \cdot |FF^*| / \triangle t^2 \\ &\simeq \frac{2\pi\sigma^2 NK}{s_X^2 T^2} e^{-\omega^2\sigma^2}\overline{a^2} \cdot \left[\frac{\left(\sum_{i=1}^K a_i \cos(\omega\tau_i)\right)^2}{2\sigma_a^2} + \frac{\left(\sum_{i=1}^K a_i \sin(\omega\tau_i)\right)^2}{2\sigma_a^2} \right] \end{aligned} \quad (7.3.7)$$

N : number of flux data points
K : number of independent flares which contribute to the observed data
T : time range of the observation
σ_a^2: $\sigma_a^2 = 0.5K\overline{a^2}$ variance of $\sum_{i=1}^K a_i \cos(\omega\tau_i)$ and $\sum_{i=1}^K a_i \sin(\omega\tau_i)$
s_X^2 : sample variance of the flux data

($\triangle t \simeq \frac{T}{N}$ is the sampling interval; it is introduced when going from the continuous Fourier transform to the discrete Fourier transform; see [130, p. 503]). For a given ω, the mean Fourier power is then:

$$\langle P_X(\omega) \rangle = A \cdot \exp\left(-\omega^2\sigma^2\right) \quad (7.3.8)$$

with an amplitude A proportional to the shot rate $\lambda = K/T$ and the mean squared amplitude $\overline{a^2}$ of the flares:

$$A = \frac{2\pi N}{s_X^2 T}\lambda\sigma^2\overline{a^2}\,. \quad (7.3.9)$$

In summary, the PDF of the shot noise process for a certain angular frequency ω_i has an exponential shape

$$\frac{\mathrm{d}\mathcal{P}}{\mathrm{d}z} = pdf_i(z) = \frac{1}{\mu_i} \cdot \exp(-z/\mu_i) \quad \text{with } \mu_i = \mu_i(A,\sigma) := \langle P_X(\omega_i) \rangle \quad (7.3.10)$$

(the parameter i marks the M different test frequencies) and the probability to have a Fourier power value above z_0 for a given angular frequency ω_i is:

$$\mathcal{P}(P_X(\omega_i) > z_0) = \int_{z_0}^{\infty} pdf_i(z)\mathrm{d}z = \exp(-z_0/\mu_i) \quad (7.3.11)$$

Since the shot noise parameters A and σ are not known a priori, they are estimated from the power spectra. This is done by means of *maximum likelihood estimates* (MLEs) through maximizing:

$$\log(L) = \log\left(\prod_{i=1}^M pdf_i(z_i)\right) = -\sum_{i=1}^M (\log\mu_i + z_i/\mu_i) \quad (7.3.12)$$

The expectation value $\langle \log(L) \rangle = -\left(M + \sum_{i=1}^M \log\mu_i\right)$ (Appendix A.4) solely depends on the used model (given by the μ_i values) and does therefore not describe how well the model fits to the data. Thus the maximum likelihood method cannot be used here to validate the model assumptions (e.g. the special shape of the flares). This is done by calculating the χ^2-value $\chi^2 = \sum_{i=1}^M [z_i - \mu_i(A,\sigma)]^2 / \mu_i(A,\sigma)$ between the power spectrum and the model (with A and σ given by the MLEs).

In summary, the procedure is as follows:
If we have a source power spectrum $P_X(\omega)$ which is mainly due to randomly distributed flares (i.e. only one or a few 'disturbed' frequencies, where an additional effect may show up), the 'undisturbed' frequencies can be used to estimate the shot noise parameters A and σ of the mean power spectrum (eq. 7.3.8). This is done by means of MLEs (eq. 7.3.12). Once the mean power spectrum is known, the renormalized Fourier power values $P_X(\omega_i)/\mu_i$ can be calculated. According to eq. 7.3.10 (with $z/\mu_i \to z$), these values are χ^2-distributed with 2 degrees of freedom and with a mean and variance equal to unity. The 'disturbed' frequencies, of course, show deviations from this distribution.

A series of MC simulations has been carried out in order to validate the statements made in this chapter. These simulations are described in the next section.

7.4 Simulations on the shot noise model

The basic assumption of all simulations is an exponential distribution of the shot amplitudes a[22] as well as for the time τ between consecutive shots:

$$\begin{aligned} \frac{\mathrm{d}\mathcal{P}}{\mathrm{d}a} = pdf(a) &= \frac{1}{\overline{a}} \cdot \exp(-a/\overline{a}) \\ \frac{\mathrm{d}\mathcal{P}}{\mathrm{d}\tau} = pdf(\tau) &= \lambda \cdot \exp(-\lambda\tau) \end{aligned} \tag{7.4.1}$$

(λ denotes the shot rate). Each lightcurve was then built up of a superposition of flares of a certain shape. For Gaussian type flares, all simulations are therefore characterized by the parameters λ, σ and $\overline{a}$[23]. The time of the first shot was chosen well before t_{min}, i.e. the time of the first data point, in order to avoid edge effects. Similarly, the time of the last shot was chosen well after t_{max}[24]. If needed, noise has been added to the simulated light curves in the following way:
The flux error of each data point was calculated as the product between the relative error of the real data and the simulated flux ($\Delta flux^{sim} = flux^{sim} \cdot \Delta flux/flux$). If the real or simulated flux was too small ($flux < 1$ or $flux^{sim} < 1$), the absolute error was used instead ($\Delta flux^{sim} = \Delta flux$). The noise was then added to the simulated fluxes according to a Gaussian distribution with a standard deviation $\sigma_{flux} = \Delta flux^{sim}$. Simulations without any noise component are labeled as such.
For most of the simulations presented here, the TeV data spacing (i.e. the observation times t_i) has been used. The reason was the small number of data points compared to the X-ray data which speeds up computation. Another point is that deviations from even data spacing are larger for the TeV data. Simulations using the X-ray data spacing are labeled accordingly.

[22] Here and in the remaining chapter, the shot amplitude a and the flux values $flux$ and $flux^{sim}$ are in units of the corresponding data samples, i.e. s^{-1} for the X-ray data and $10^{-11}\,\mathrm{cm}^{-2}\mathrm{s}^{-1}$ for the TeV data. Similarly, the shot noise parameters A and C are given in units of s^{-2} (X-ray data) or $10^{-22}\,\mathrm{cm}^{-4}\mathrm{s}^{-2}$ (TeV data).

[23] In the case of an exponential amplitude distribution the mean squared amplitude $\overline{a^2} = 2\overline{a}^2$ can be used alternatively.

[24] Given the mean flare duration σ_f as the time when the flare amplitude drops by a factor $1/e$, the time of the first shot was $\tau_{min} = t_{min} - 5\sigma_f + \tau$ (τ is exponentially distributed). Similar $\tau_{max} = t_{max} + 5\sigma_f - \tau$.

a) Introduction of an additional term C in the expression for the mean Fourier power $\langle P_X(\omega)\rangle$ in the shot noise model:

In order to verify the different theoretical predictions of the previous section, the mean power spectrum from 10000 individual simulations was calculated and evaluated. It turned out, that is was necessary to introduce a constant term C to the mean power spectrum in order to bring theory and simulations in agreement. Thus eq. 7.3.8 becomes:

$$\langle P_X(\omega)\rangle = A \cdot \exp\left(-\omega^2\sigma^2\right) + C \tag{7.4.2}$$

The reason for this C-term is twofold:

- The effect of uneven data spacing. As was shown in fig. 7.2.1 b), the power spectrum of a single sinusoid is rather complex in the case of uneven data spacing. Nearly all frequencies have a non-zero Fourier power content. The same problem affects the power spectra in the shot noise model. The large amplitudes at small frequencies give a contribution to the Fourier power values at large frequencies and the corresponding mean Fourier powers are therefore larger than zero.

- Noise content in the data. In case of pure white noise, the mean power spectrum is unity for all frequencies (eq. 7.2.3). The mean power spectrum of the shot noise process therefore tends towards unity when the noise level is increased. Thus, as $\omega\sigma$ becomes large, the mean power spectrum does not reach zero but approaches a constant value, determined by the noise level in the data (see fig. 7.4.1 e and f).
  In combination with an uneven data spacing, the noise component might reduce the contribution of the data spacing to the C-term: In the case of the X-ray data containing a large number of data points with a large noise component, the addition of the noise reduces the mean amplitude A by almost a factor 3 [25]. As a result, the contribution to the Fourier power at large frequencies is also reduced. Another point is that the C-term is above unity for the X-ray simulations. Adding the noise will reduce it towards unity.

In principle the C-term could also be determined as MLE together with A and σ, but this procedure has a drawback. For small σ-values, the power spectrum does not approach the C-term value within the used frequency range $f \leq 0.5\,\mathrm{d}^{-1}$ (fig. 7.4.1 a and b). As a result, the shot noise parameters A, σ and C are strongly correlated, giving rise to large fluctuations in σ and A (an example power spectrum, where a large peak at small frequencies misleads the MLE procedure is shown in fig. 7.4.2). In the case of large σ-values, however, the Fourier power of the high frequency region is at the C-term level and can therefore be used to accurately derive the C-term (fig. 7.4.1 e and f). Thus, the solution to this problem is to derive the C-term from the mean power spectrum once (for a given data spacing and noise content) and use this value for all other simulations (keeping it fixed). Simulations with $\overline{a} = 3.0$, $\sigma = 0.5\,\mathrm{d}$ and $\lambda = 0.5\,\mathrm{d}^{-1}$ (i.e. corresponding roughly to the TeV data results) showed a clear improvement. In the case of a variable C-term the results from 1000 individual power spectrum simulations were $\sigma = 0.64 \pm 0.52\,\mathrm{d}$ and $A = 3.84 \pm 1.45$ in comparison to $\sigma = 0.47 \pm 0.11\,\mathrm{d}$ and $A = 3.64 \pm 0.97$ obtained with a constant $C = 0.43$. Using $\overline{a} = 1.0$, $\sigma = 1.0\,\mathrm{d}$ and $\lambda = 0.5\,\mathrm{d}^{-1}$ in the simulations gives $\sigma = 0.95 \pm 0.19\,\mathrm{d}$ and $A = 35.5 \pm 9.86$ (variable C-term) in comparison to $\sigma = 0.97 \pm 0.15\,\mathrm{d}$ and $A = 35.9 \pm 10.4$ (constant $C = 2.20$). As can be seen the method of keeping C fixed also improves the estimation of the important shot noise parameter σ.

[25] This effect immediately follows from eq. 7.3.9. Since the sample variance σ_X^2 increases with increasing noise level, the amplitude $A \propto 1/\sigma_X^2$ decreases with increasing noise level.

	X-ray		TeV	
	uneven	even	uneven	even
noise	2.20 ± 0.45	0.50 ± 0.12	0.43 ± 0.10	0.17 ± 0.03
no noise	3.23 ± 0.68	0.05 ± 0.02	0.32 ± 0.07	0.01 ± 0.01

Tab. 7.4.1: Constant term C as obtained from simulations with given shot width $\sigma = 1.5\,\mathrm{d}$, shot rate $\lambda = 0.5\,\mathrm{d}^{-1}$ and mean shot amplitude $\overline{a} = 1$ (X-ray data) or $\overline{a} = 3$ (TeV data). The term 'uneven' denotes the real data spacing, whereas the even data spacing was derived thereof (keeping the number of data points and the time range). The used shot amplitudes $\overline{a}$ are in agreement with the real data.

A disadvantage of this approach is that the noise component in the data has to be understood well in order to bring the simulations and the real data in agreement. Table 7.4.1 summarizes the C-values obtained for the different data samples. As already said, both, the data spacing and the noise component contribute to the C-term (not always with the same sign). In the case of even data spacing without noise, the C-term is close to zero.

b) Comparison between the theoretical predictions of the shot noise model and the results from the simulations:

Given the modified mean power spectrum from eq. 7.4.2 the simulations can now be compared with the theory. Figure 7.4.1 shows the mean power spectrum, calculated for 3 different values of the shot width σ (left column: TeV data spacing, right column: even data spacing). As can be seen, all power spectra are well described by the model (green lines), the estimated shot widths σ_{MLE} are in agreement with the simulated σ value. The quoted χ^2 values are a measure of the quality of the fit, but should not be taken too seriously. The reasons are:

- Uneven data spacing produces disturbances in the mean power spectrum
  - The effect of the moon gaps is clearly visible in the power spectra of the TeV sample (fig. 7.4.1 left column).
  - If data points are too close in time compared to the shot width σ, they are not independent and the Fourier power is overestimated. This effect is clearly visible in fig. 7.4.1, where the mean amplitude A drops when going from the uneven to the even case.
- For a given data spacing, the C-term depends on the mean Fourier power at small frequencies (where the mean Fourier power has its maximum). The C-term therefore slightly depends on the mean amplitude $A \propto \sigma^2$. Keeping it fixed for all shot parameters lowers the quality of the fit (using $C_{MLE} = 0.38$ instead of $C_{MLE} = 0.43$ in fig. 7.4.1 c) reduces the χ^2-value from 21.5 to 13.4).
- In the case of even data spacing, the power spectrum is not affected by aliasing (fig. 7.2.1 a) and the C-term only depends on the noise level. Since an increased shot width σ results in larger fluxes in conjunction with larger flux errors, the C-term is also not expected to be constant here. Again the χ^2-value improves by recalculating the C-term (using $C_{MLE} = 0.13$ instead of $C_{MLE} = 0.17$ in fig. 7.4.1 d) reduces the χ^2-value from 36.0 to 2.9).

- As stated in sec. 7.3 the two sums $\sum_{i=1}^{K} a_i \cos(\omega\tau_i)$ and $\sum_{i=1}^{K} a_i \sin(\omega\tau_i)$ in eq. 7.3.5 are only approximately Gaussian distributed. As simulations have shown, the limiting factor is not the number of shots K (as long as $K \gtrsim 10$), but the angular frequency ω. For small frequencies, the sine and cosine terms do not change their sign very often and, as a result, the sums obtain a non-zero mean. The net effect is a mean amplitude A, larger than the theoretical expectation. Since only a few frequencies are affected, this effect has only a small impact on the derived MLEs (see fig. 7.4.3 b and d), but a large impact on the χ^2values (particularly for simulations without noise).

A more thorough comparison between the shot noise parameters A and σ and their MLEs A_{MLE} and σ_{MLE} is given in fig. 7.4.3. The plots show the ratio A/A_{MLE} and σ/σ_{MLE} for several values of the shot width σ in the case of uneven (left column) and even (right column) data spacing. The above mentioned problems concerning the mean amplitude A clearly show up in the uneven case where $A_{MLE} > A$, but, as said before, do not affect the even case. As can be seen, the ratio A/A_{MLE} shows nearly no σ-dependence. A good agreement between A and A_{MLE} however is not required as long as the probability distribution holds (see below). The shot width σ, on the other hand, should be estimated accurately, since it reveals information on the involved physical processes. Fortunately, the ratio σ/σ_{MLE} shows only a small σ-dependence and is close to unity for uneven data spacing (the relevant case). This means that the Lomb-Scargle periodogram in conjunction with the shot noise model can be used to accurately determine this physical quantity. In the case of even data spacing without noise the results for σ_{MLE} are nearly optimal. Note that the large uncertainty at small σ-values is caused by the limited frequency range $f \leq 0.5\,\mathrm{d}^{-1}$ which does not cover the whole drop off of the power spectrum then.

As already mentioned in the previous chapter, it should be possible to distinguish between Gaussian and exponential shaped flares by means of the mean power spectrum. A set of simulations with exponential shaped flares have therefore been carried out. The mean power spectrum of these simulations and the corresponding MLEs are shown in fig. 7.4.4. As can be seen, the hypothesis of Gaussian type flares is clearly ruled out (fig. 7.4.4 a and b), but the discrimination level strongly depends on the number of simulations used for the determination of the mean power spectrum. The Gaussian model cannot be rejected on the basis of a single power spectrum. The model of exponential type flares is in good agreement with the simulations (fig. 7.4.4 c and d) and the derived rise and decay time is in concordance with the simulations (given that the mean power spectrum symmetric in the rise and decay time).

Up to now we only investigated the effect of the shot width σ on the power spectrum. The other two parameters, the shot rate λ and the mean shot amplitude $\overline{a}$ **do not effect the power spectrum** since they are assimilated by the sample variance σ_X^2 in eq. 7.3.7. As a result, the C-term does not depend on λ or $\overline{a}$ and the procedure of keeping the C-term fixed is feasible. This means that the constant C-term approach is not valid for any redefinition of the Lomb-Scargle periodogram which omits the normalization on the sample variance. In that case the C-term strongly depends on the unknown shot parameters λ and $\overline{a}$ and has to be derived from each individual power spectrum (with the above mentioned problems).

c) Investigations on the PDF for the Fourier power $P_X(\omega)$

Another important issue of the MC simulations was to test the theoretical expectations of the PDF (according to eq. 7.3.10). In order to derive the PDF of the Lomb-Scargle Fourier power in the shot noise model, a large number of simulations have been carried out. The power

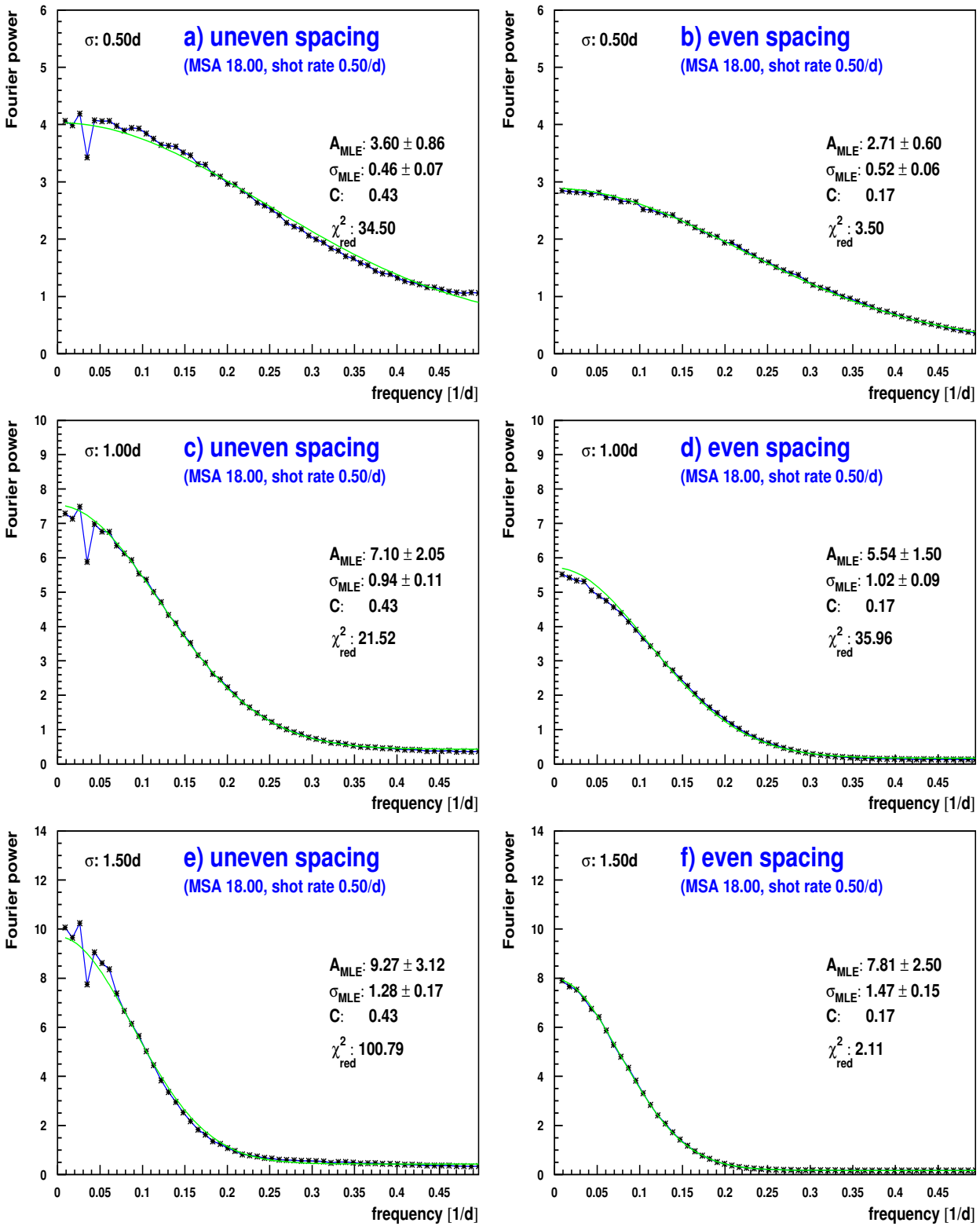

Fig. 7.4.1: Mean power spectrum for different shot widths ($\sigma = 0.5$ d, $\sigma = 1.0$ d and $\sigma = 1.5$ d) in the case of uneven (left column) and even data spacing (right column). The shot rate used in the simulations was $\lambda = 0.5\,\mathrm{d}^{-1}$, the mean squared amplitude (MSA) of the flares was $\overline{a^2} = 18$. The mean power spectrum (blue line) was obtained through superposition of 10000 individual power spectra. The green line denotes the result of the MLE fit, not including the 4th frequency at the moon period (uneven case only). This frequency was also not included in the χ^2 calculation.

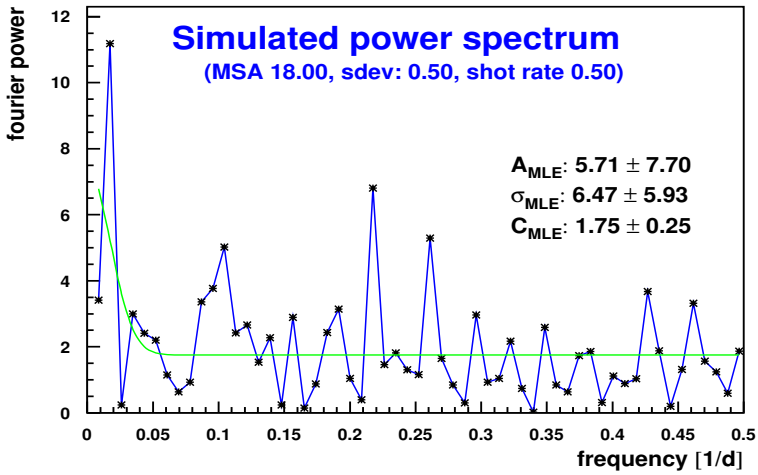

Fig. 7.4.2: Power spectrum for a single simulation ($\sigma = 0.5$ d, $\lambda = 0.5$ d^{-1}, $\overline{a^2} = 18$). In case the C-term (MLE C_{MLE}) is derived for each individual power spectrum, a large peak at small frequencies may mix up the whole procedure. As a result, the MLEs σ_{MLE} and A_{MLE} are then too large.

spectrum was then calculated for each individual lightcurve and the (frequency dependent) Fourier power values were recorded. The probability to have a Fourier power value between z_0 and $z_0 + \mathrm{d}z$ is then given by the number of simulated light curves, resulting in such a Fourier power value divided by the overall number of simulations (the probability is of course frequency dependent):

$$\mathcal{P}\left(z_0 < P_X\left(\omega_i\right) < z_0 + \mathrm{d}z\right) = \frac{N_{sim}\left(z_0 < P_X\left(\omega_i\right) < z_0 + \mathrm{d}z\right)}{N_{sim}} \tag{7.4.3}$$

Figure 7.4.5 shows the obtained PDF for 3 different frequencies in the case of uneven (a) and even (b) data spacing. In contrast to the case of Gaussian white noise it is more likely to produce large Fourier power values in the shot noise model (especially at small frequencies). The underlying PDF (shown as blue line) again originates from the usage of the sample mean and variance in the Lomb-Scargle periodogram (sec. 7.2.1) and is derived in the following way: Under the reasonable assumption that the flux variance s_X^2 is proportional to the shot variance s_a^2 the amplitude A (eq. 7.3.9) becomes $A \propto 1/s_X^2 \propto 1/s_a^2$. Given that the mean amplitude $\overline{A}$ is proportional to $1/\sigma_a^2$, we have $A/\sigma_a^2 \simeq \overline{A}/s_a^2$ and eq. 7.3.7 can be written as:

$$z_\omega := \frac{P_X\left(\omega\right)}{\overline{A}\exp\left(-\omega^2\overline{\sigma}^2\right) + \overline{C}} \simeq \left[\frac{\left(\sum_{i=1}^K a_i \cos\left(\omega\tau_i\right)\right)^2}{2s_a^2} + \frac{\left(\sum_{i=1}^K a_i \sin\left(\omega\tau_i\right)\right)^2}{2s_a^2}\right] \tag{7.4.4}$$

(the C-term was again added to address effects from the uneven data spacing and noise). The normalized Fourier power values z_ω therefore follow the beta distribution

$$\mathrm{d}\mathcal{P}\left(z < z_\omega < z + \mathrm{d}z\right) = \left(1 - \frac{2z}{K}\right)^{K/2} \mathrm{d}z \tag{7.4.5}$$

(see eq. 7.2.5). As can be seen, the agreement with the simulations is quite good for both even and uneven data spacing (fig. 7.4.5). The deviations at small frequencies are related to

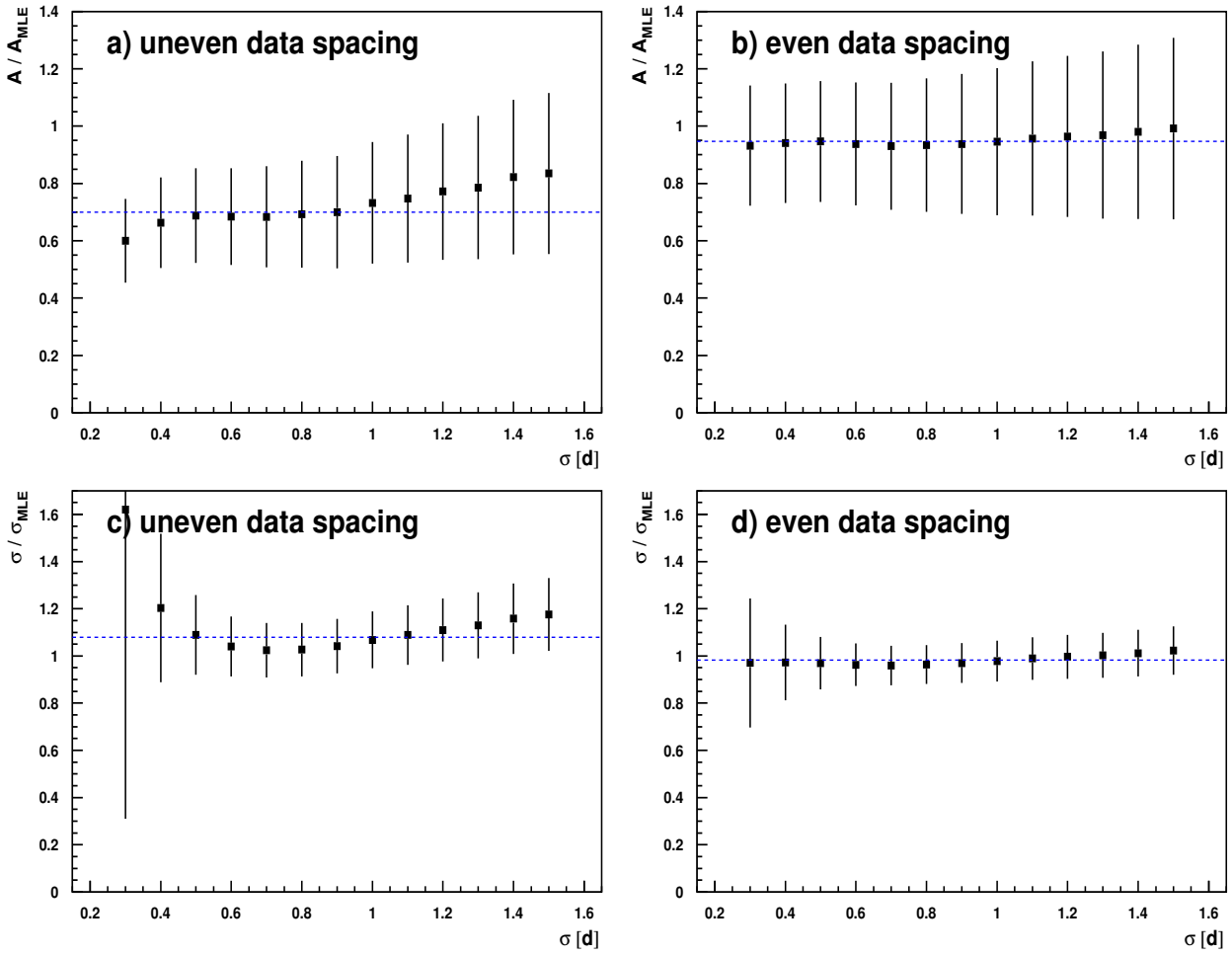

Fig. 7.4.3: Comparison between the shot noise parameters A and σ and their MLEs A_{MLE} and σ_{MLE} for different shot widths σ. The plots on the left side were obtained from an uneven data spacing (TeV data) with added noise, the right column denotes the optimal case with even data spacing and without added noise. The errors were derived from the errors on the MLEs. The blue line denotes the weighted mean.

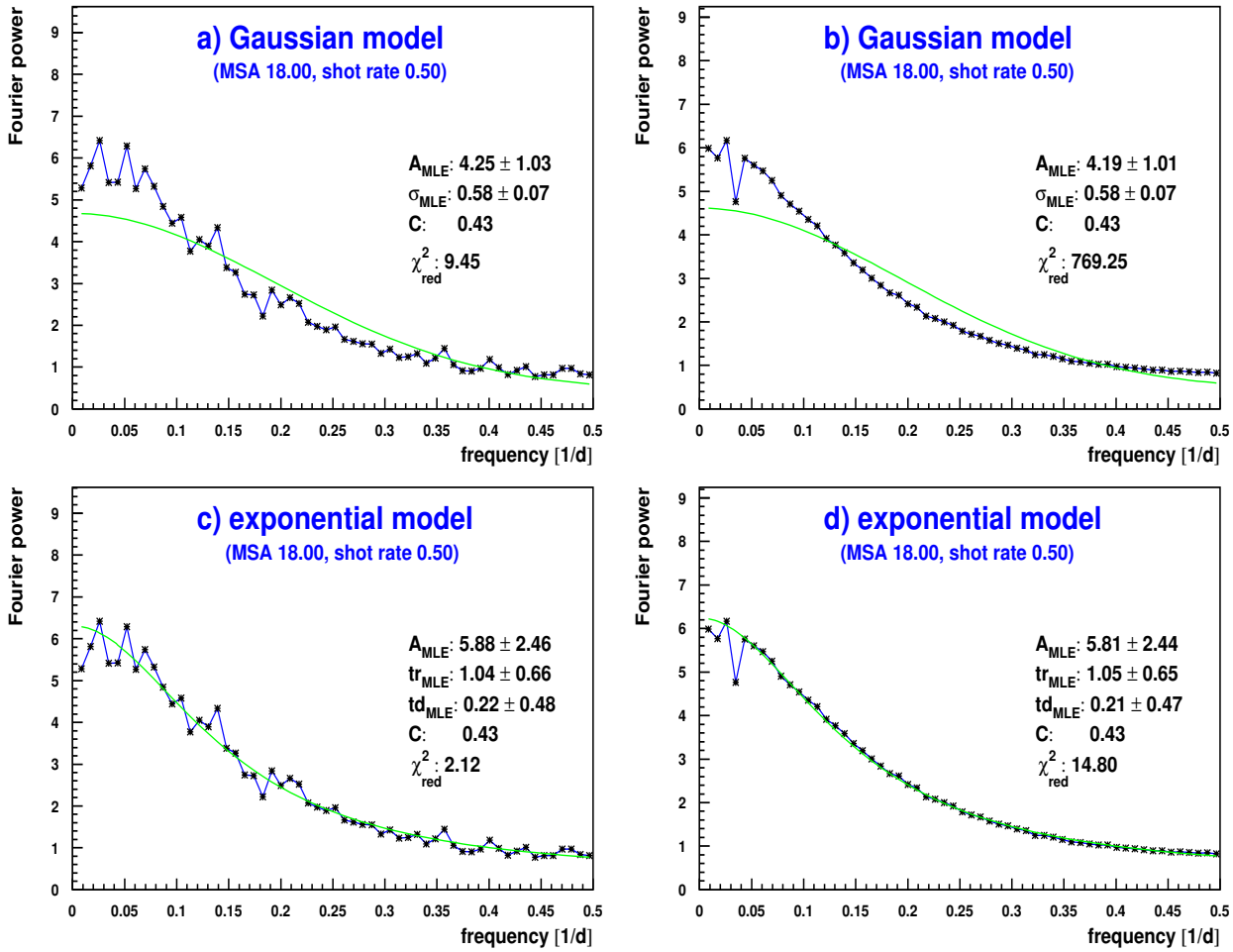

Fig. 7.4.4: Mean power spectrum for exponentially shaped flares with rise time $tr = 0.3$ d and decay time $td = 1.2$ d in comparison with a Gaussian and exponential flare model. The mean power spectrum was derived from 100 (left column) or 10000 (right column) individual power spectra. The shot rate used in the simulations was $\lambda = 0.5$ d^{-1} and the mean squared amplitude of the flares was $\overline{a^2} = 18$. The green line in a) and b) denotes the MLE for Gaussian shaped flares while it shows the MLE for the appropriate exponential shaped flares in c) and d). Note, that the mean Fourier power is symmetric in tr and td, i.e. it is not possible to determine whether tr_{MLE} describes tr or td (and similar for td_{MLE}).

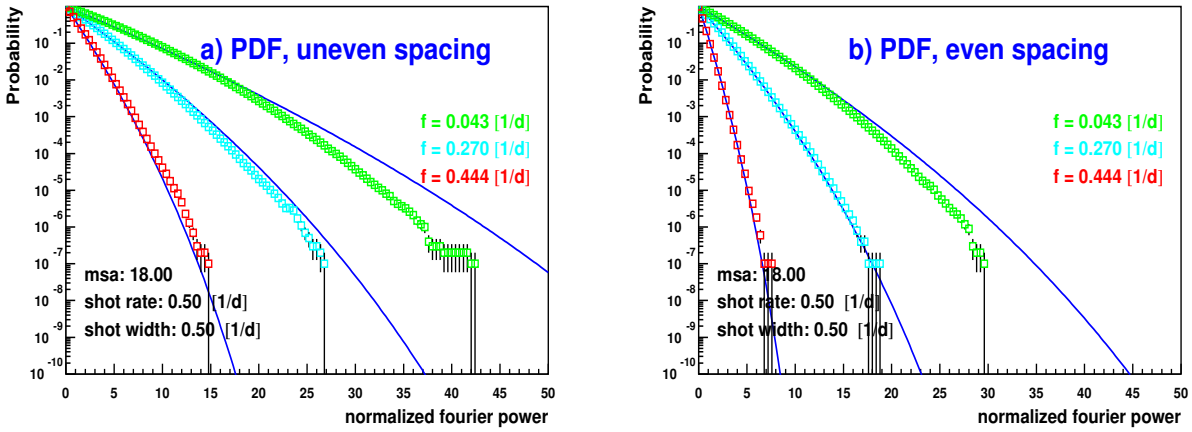

Fig. 7.4.5: PDF of the Lomb-Scargle Fourier power in the shot noise model for 3 different frequencies (a uneven and b even data spacing). The blue lines denote the PDF of the Fourier power z_ω normalized according to eq. 7.4.4 (see text).

the problems concerning the mean amplitude A (see previous comments to the large χ^2-values of the model fit).

A problem of the renormalized Fourier power z_ω is that the normalization factor $\overline{A} \cdot \exp\left(-\omega^2\overline{\sigma}^2\right) + \overline{C}$ must be derived from a large number of similar power spectra. Furthermore, the number of flares K is not known in reality and has to somehow be estimated from the light curves. The solution to this problem is to normalize $P_X(\omega)$ on the mean Fourier power $\langle P_X(\omega)\rangle = A \cdot \exp\left(-\omega^2\sigma^2\right) + C$ derived for each individual power spectrum. Equation 7.4.4 then becomes:

$$z_\omega := \frac{P_X(\omega)}{A\exp\left(-\omega^2\sigma^2\right) + C} \simeq \left[\frac{\left(\sum_{i=1}^{K} a_i \cos(\omega\tau_i)\right)^2}{2\sigma_a^2} + \frac{\left(\sum_{i=1}^{K} a_i \sin(\omega\tau_i)\right)^2}{2\sigma_a^2}\right] \tag{7.4.6}$$

The sample variance s_X^2 (from $\langle P_X(\omega)\rangle$) now cancels against the sample variance s_X^2 (from $P_X(\omega)$) and the normalized Fourier power z_ω follows an exponential distribution with unit mean and variance. As before, deviations from this distribution are expected at large frequencies. Note that in the case of different flare shapes (i.e. exponential shape) all results concerning z_ω are still valid if the mean Fourier power is replaced by the appropriate one (i.e. $\langle P_X(\omega)\rangle = A\left(1+\omega^2\tau_r^2\right)^{-1}\left(1+\omega^2\tau_d^2\right)^{-1} + C$).

The PDF of the normalized Fourier power z_ω (eq. 7.4.6) for two different shot rates is shown in fig. 7.4.6 (a and c TeV data spacing, b and d X-ray data spacing). As can be seen, the small frequency component is in good agreement with the expected exponential distribution (blue line). For larger frequencies the PDF is below the exponential distribution, therefore taking the latter one for any probability calculations is conservative and thus valid. In the case of the X-ray data spacing even the small frequency component shows deviations from the exponential distribution. It can therefore only be used for Fourier power values $z_\omega \lesssim 10$. Note, that the same procedure to derive the mean Fourier power as in the analysis of the measured TeV and X-ray data was used, i.e. the frequency component with the largest Fourier power value in each simulation and the moon period were excluded from the MLE fit.
In the remaining chapter, the term normalized Fourier power always refers to z_ω as defined in

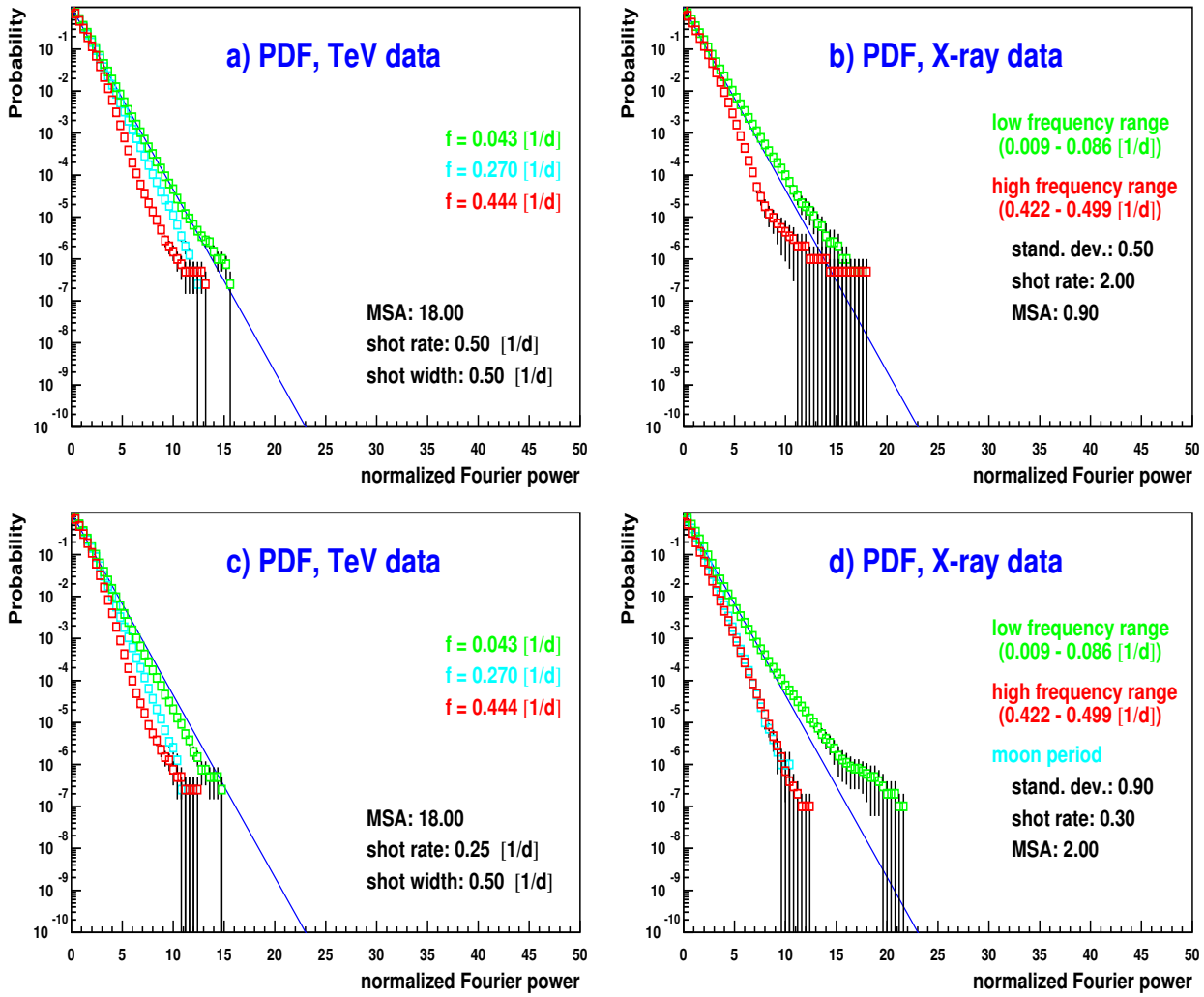

Fig. 7.4.6: PDF of the normalized Fourier power z_ω (eq. 7.4.6) in the shot noise model for 3 different frequencies (left side TeV data spacing, right side X-ray data spacing). The shot parameters $\overline{a^2}$ (MSA) and σ (shot width) were chosen to match the values of the real data. The blue lines denote the exponential probability distribution according to eq. 7.2.3.

eq. 7.4.6.

d) Summary and conclusions

In summary one can conclude that the Lomb-Scargle periodogram in conjunction with the shot noise model is a viable tool for analyzing AGN time series. The characteristic time scales of the shots (i.e. the shot width σ) and, eventually, even the special shape of the flares (Gaussian or exponential with equal or different rise and decay time) can be derived from the power spectrum. This task is strongly simplified due to the normalization on the sample variance, which removes nearly the entire influence of the shot rate and amplitude on the power spectrum. In order to cope with noisy data or uneven data spacing, it was necessary to introduce a constant term C in the definition of the mean Fourier power. The C-term depends on the noise component and the data spacing, but can be estimated from simulations in advance. Again, the normalization on the sample variance is necessary in order to keep this term (nearly) independent of the shot rate and amplitude.
The PDF of the normalized Fourier power z_ω approximately follows an exponential distribution with unit mean and variance. The agreement is good for small frequencies and Fourier power values, but worsens with increased frequency and/or Fourier power. Nevertheless, for $z_\omega \lesssim 10$, the PDF is always in agreement or below the exponential distribution which can therefore be used for the probability calculations. The normalized Fourier power is independent of the special flare shape model (i.e. Gaussian or exponential).

7.5 Results and discussion

With the results of the previous two chapters we can now refine the probability calculation of the 23-day periodicity. As said before, there is strong evidence for a 23-day periodicity, clearly visible in the power spectrum. The question is whether such a periodicity can be produced by randomly distributed flares of a certain shape. If the periodicity holds under this new null hypothesis, it should be related to some intrinsic properties of Mkn 501.

The power spectra of Mkn 501 for the TeV and X-ray data are shown in fig. 7.5.1. The mean Fourier power as derived from the power spectra (using eq. 7.4.2) has been added as a green line. In the case of the TeV data, the moon period and the 23-day period were excluded from the MLE-fit and the χ^2-calculation; in the case of the X-ray data the 23-day period and the smallest frequency mode at $1/T$ were excluded (the latter, since it is also not considered being part of the shot noise process). The model assumption was that of Gaussian type flares. In order to derive the significance for the 23-day period the power spectra are normalized onto the mean Fourier power according to eq. 7.4.6. The results of both data samples can then be easily combined in the following way: As was shown in the previous chapter, the normalized Fourier power z_ω is (nearly) exponentially distributed with unit mean and variance ($\mathcal{P}(z_\omega) = \exp(-z_\omega)$). Given a uniformly distributed probability $\mathcal{P}$, the quantity $-2\ln(\mathcal{P})$ is χ^2-distributed with 2 degrees of freedom ([130, p. 287]) and, as a result, the quantity

$$\chi^2(4) = -2\ln\left(\exp\left(-z_\omega^\gamma\right)\right) - 2\ln\left(\exp\left(-z_\omega^{X-ray}\right)\right) = 2\left(z_\omega^\gamma + z_\omega^{X-ray}\right) \tag{7.5.1}$$

is χ^2-distributed with 4 degrees of freedom. This holds for any (angular) frequency ω. The resulting χ^2-values together with the corresponding probability are shown in fig. 7.5.2. The probability for the 23 day period within the shot noise model (i.e. against the null hypothesis of randomly distributed flares) thus becomes $\mathcal{P} = 6.3 \cdot 10^{-6}$ which corresponds to 4.4σ. This reduces to $\mathcal{P} = 3.6 \cdot 10^{-4}$ or 3.4σ after taking all 57 independent trial frequencies (between

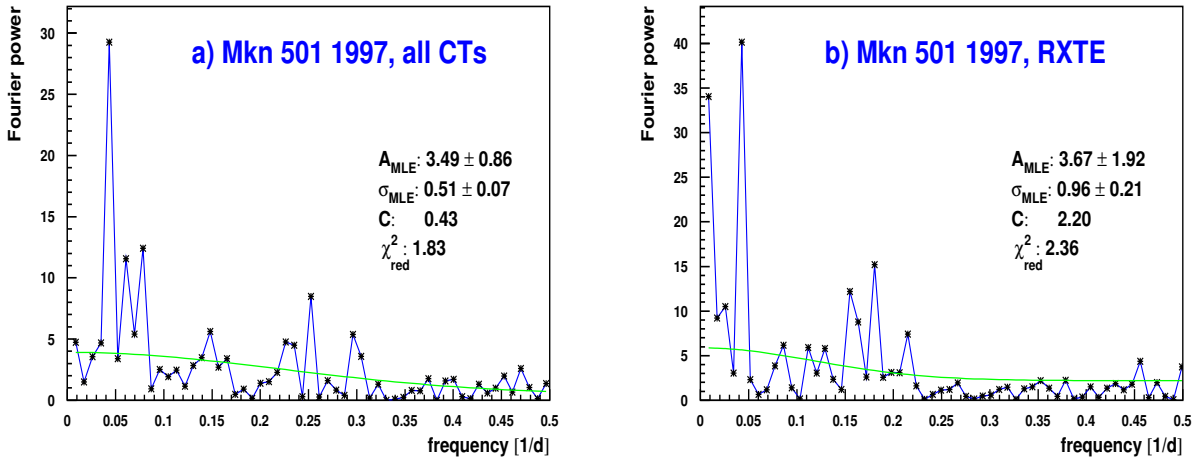

Fig. 7.5.1: The power spectra of the TeV (a) and X-ray (b) data sample and the corresponding mean Fourier power (green line). The latter was determined under the assumption of Gaussian shaped flares with exponentially distributed flare amplitudes and identical shot widths. The 5th frequency, corresponding to the 23-day period was not included in the χ^2 calculation.

1/T and 0.5 per day) into account. Note that the normalized Fourier power values at the 23-day period are small enough ($z^{\gamma} = 7.6$ and $z^{X-ray} = 7.1$) to justify the assumption of an exponential probability distribution for z_{ω} (see fig. 7.4.6).

According to Zhang [175] a 3σ significance limit is, from a statistical point of view, a sufficiently reliable criterion in order to claim a positive result. It should be noted that the lightcurve sample is not the product of a large selection process and can therefore be considered as minimally biased. However, it is essential that the statistical procedure to estimate the significance is correct. In that respect, the uncertainties of the presented significance calculation are discussed in the following:

It was assumed that all flares have a Gaussian shape with shot width σ. Different types of shots yield different mean power spectra (see fig. 7.3.1) and therefore give a different significance. However, since the flare shape determines the shape of the power spectrum but hardly affects the mean Fourier power at small frequencies, the affect of the flare shape on the significance of the 23 day period should be marginal. In the case of exponential type shots (fig. 7.5.3) the combined significance becomes 3.0σ (the same $C = 0.43$ and $C = 2.20$ as in the Gaussian case was used) the resulting χ^2 values however nearly stay the same ($\chi^2_{red}(\gamma) : 1.83 \rightarrow 1.79$, $\chi^2_{red}(X-ray) : 2.36 \rightarrow 2.56$).

As discussed in the previous section, the C-term is calculated from MC simulations and not estimated from the individual power spectra. The main reason was the otherwise increased fluctuations on the shot noise parameters A and σ. The C-term however strongly depends on the noise component of the data sample. In case the noise contribution is not properly simulated, the estimated C-term differs from the 'real' value. A different C-term might give different MLEs for A and σ, and, as a result, the normalized Fourier power and therefore the significance of the signal might be overestimated. In case the C-term is estimated from the power spectrum itself, the combined significance drops to 2.9σ (for exponential type shots, too). This can be regarded as a lower limit of the significance.

On the other hand it could be argued that the 23-day period mode should be subtracted

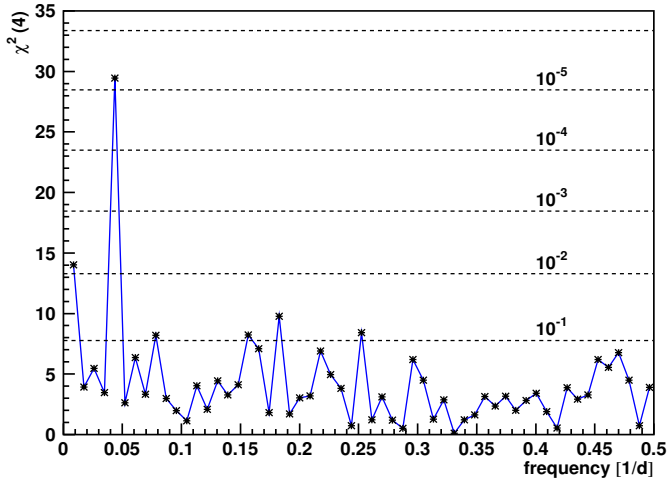

Fig. 7.5.2: The combined normalized power spectrum for the X-ray and TeV data. The dotted lines mark some probability levels.

from the lightcurve before calculating the mean Fourier power. In case there is a real signal present in the data, this signal also affects the other frequencies in the power spectrum (as discussed in sec. 7.2.1) and therefore the MLEs (especially the amplitude A). Removing the whole frequency component, however, is not ideal either and might result in an underestimated mean Fourier power and therefore overestimated significance. Nevertheless, subtracting the 23-day period mode and, in addition, the $1/T$ component from the RXTE data results in a combined significance of 4.1σ[26] (the corresponding power spectra are shown in fig. 7.5.4). This can be regarded as an upper limit.

Another uncertainty is due to the correlation of the TeV and X-ray light curves. In case two data samples are correlated, one would expect to see the correlation also in the derived power spectra. As a result the normalized Fourier power values z_ω^γ and z_ω^{X-ray} would not be independent and eq. 7.5.1 not strictly valid. Simulations however showed, that even when both data sets were taken from the same flare sample (according to the observation times) the mean correlation (determined from the linear correlation coefficients [130, eq. 14.5.1]) was weak ($corr\,(\gamma, X-ray) = 0.33 \pm 0.24$ compared to $corr\,(\gamma, X-ray) = 0.0 \pm 0.22$ for two independent flare samples[27]). In reality both data samples belong to different populations (e.g. synchrotron photons vs. inverse Compton scattered photons) and the correlation is expected to be even smaller. Systematic effects in the determination of the flux values/count rates of the two data samples are also not considered. In case the correlation is calculated for the real power spectra, the correlation is strong when the 23-day period is included in the calculations, but not present otherwise. The results of these correlation studies are shown in tab. 7.5.1.

If, on the other hand, the X-ray and TeV power spectra are correlated, then one would expect to see a deviation from the $\chi^2\,(4)$-distribution in the data points of fig. 7.5.2. An easy way to check this effect is to transfer the $\chi^2\,(4)$-distributed data points into $\chi^2\,(1)$-distributed

[26] Subtracting any frequency mode from the data changes the flux values (or count rates) but not their errors. The C-terms, derived from simulations are therefore not valid anymore and have to be estimated from the power spectra itself.

[27] The calculation of all the correlation coefficients was restricted to small frequencies $f < 0.2\,\mathrm{d}^{-1}$ since this is the important region concerning the 23-day periodicity.

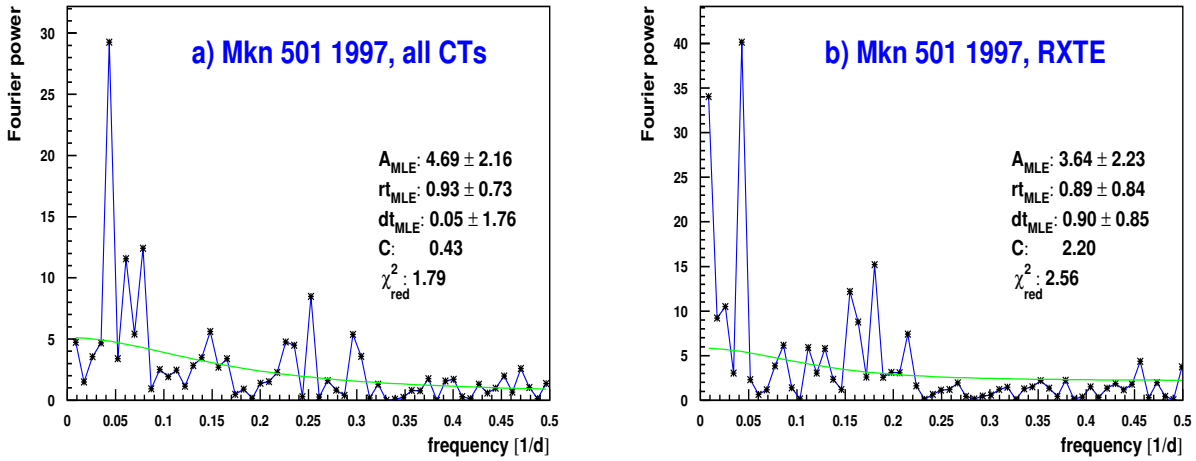

Fig. 7.5.3: The power spectra of the TeV (a) and X-ray (b) data sample and the corresponding mean Fourier power (green line). The latter was determined under the assumption of exponential type flares (with different rise and decay time) with exponential distributed flare amplitudes and identical shot widths.

numbers[28]. In case both power spectra have no significant correlation, the mean of the χ^2 (1)-distributed numbers should be consistent with unity (and significantly different otherwise). Again, the small frequency range $f < 0.2\ \mathrm{d}^{-1}$ was used for this analysis and the 23-day period was excluded. The derived mean value was $\mu_{\chi 1} = 1.04$ with a standard deviation of $\sigma_{\chi 1} = 1.17$. Given the $N = 20$ test frequencies, the error on the mean becomes $\sigma(\mu_{\chi 1}) = \sigma_{\chi 1}/\sqrt{N} = 0.262$ and the deviation of the derived mean from unity is $(\mu_{\chi 1} - 1)/\sigma(\mu_{\chi 1}) = 0.15$ standard deviations. Thus the combined TeV and X-ray probabilities seem to be uncorrelated (excluding the 23-day period) and jointly behave as Gaussian white noise.

In summary there is no indication for a correlation between the power spectra of the TeV and X-ray data sample (the 23-day period is excluded, since it is not considered being part of the shot noise process) and the use of eq. 7.5.1 is therefore reasonable. The main reason for the missing correlation is due to the completely different data spacing for the TeV and X-ray data (see e.g. the ssc1 - ssc2 correlation with similar data spacing in tab. 7.5.1), but also the errors on the TeV and X-ray data cause some deviations.

The power spectra of all the data subsamples (i.e. CT1 moon/no-moon, CT2, etc., see fig. 7.5.5, with the C-term values being derived as described in sec. 7.4) clearly show a maximum at 23 days. Given the strong correlation between the two X-ray data samples (see tab. 7.5.1, 2nd column), it is not surprising to obtain similar power spectra. The TeV data samples however, are only moderately correlated and it is therefore unlikely that the shot noise process generates all maxima at the same frequency. This was not investigated further. The large deviation between the simulation and real data in the case of the ssc1 - ssc2 correlation coefficient is attributed to the inexact noise simulation.

Two points which are not expected to influence the reliability of the significance calculation very much are the selected time range of the data (sec. 7.2.2) and a possible correlation between consecutive flares [168]. As already said, the time range was chosen in the beginning of the

[28] Calculate the upper probability p_i for the individual data points from the χ^2 (4)-distribution and deduce the percentage points for a χ^2 (1)-distribution from p_i.

	simulations	simulations (max. power excluded)	real data	real data (max. power excluded)
CT1nm - CT1m	0.08 ± 0.24	0.06 ± 0.24	0.42	0.04
CT1 - CT2	0.33 ± 0.23	0.27 ± 0.24	0.58	0.13
CT1 - CTsys	0.57 ± 0.20	0.21 ± 0.24	0.68	0.50
CT2 - CTsys	0.44 ± 0.26	0.15 ± 0.25	0.56	0.35
CT - RXTE	0.33 ± 0.24	0.27 ± 0.23	0.57	-0.01
ssc1 - ssc2	0.95 ± 0.03	0.93 ± 0.04	0.83	0.69

Tab. 7.5.1: Correlation coefficients for the power spectra of several subsamples of the TeV and X-ray data sets (CT1nm denotes the CT1 no-moon data, CT1m the CT1 moon data; ssc1 and ssc2 denotes data from the 1st and 2nd shadowing camera of RXTE). In the case of the simulations ($\sigma = 0.5$ d, $\lambda = 0.5\ \mathrm{d}^{-1}$ and $\overline{a^2} = 18$), the correlation coefficient is the mean from 1000 simulations and the error denotes the RMS thereof. The 3rd and 5th column show the results after excluding the frequency connected to the maximum Fourier power from the coefficient calculations (this corresponds to the 23-day period in the case of the real data).

analysis in order to reject the data with large errors and large systematic uncertainties. Since the normalization factor (i.e. the mean Fourier power) is derived from the power spectrum itself, the selected data range is implicitly taken into account in the significance calculation.

It was shown in [168] that quasi-periodic oscillations (QPOs) can appear in the framework of the shot noise model if consecutive shots are not completely independent. The basic idea is that "in order to keep the average energy release (accretion rate) at a constant level on long time scales, the presence of a strong shot at any given moment must reduce the probability of the appearance of another strong shot just after the first one and/or reduce its amplitude." In the case of a 'probability interaction' the Fourier power component $|X(\omega)|$ (see eq. 7.3.5) becomes [168, eq. 8][29] :

$$|X(\omega)|^2 \propto 1 - 2\frac{\lambda^2(1-\cos(\omega\tau_d)) + \lambda\omega\sin(\omega\tau_d)}{\lambda^2(1-\cos(\omega\tau_d))^2 + (\lambda\sin(\omega\tau_d) + \omega)^2} \tag{7.5.2}$$

(λ is the mean shot rate and τ_d is the 'dead time', i.e. the minimum time between consecutive shots) thus adding an oscillating component to the power spectrum. The QPO peak frequency f_{QPO} is defined by the 'dead time' τ_d as $f_{QPO} \approx 1/\tau_d$ and the peak strength increases with increasing $\lambda\tau_d$. According to the Mkn 501 lightcurve (fig. 7.2.8) τ_d is of the order of 1-2 days at most and, as a result, $f_{23} = 0.043\ \mathrm{d}^{-1} \ll f_{QPO} \approx 0.5\ \mathrm{d}^{-1}$ (see fig. 7.5.6 a and b). The reliability of the 23-day periodicity is therefore not affected by this process.
If the shots are subject to 'amplitude interaction', we have [168, eq. 11]:

$$\left\langle |X(\omega)|^2 \right\rangle \propto \frac{1}{\lambda^2} - \frac{1}{\lambda^2 + \omega^2} \tag{7.5.3}$$

which again gives rise to a broad QPO peak in the power spectrum. In the case of Gaussian type shots, the maximum of the QPO peak is obtained at

$$f_{QPO} = \frac{\lambda}{2\pi}\sqrt{\sqrt{\frac{1}{4} + \frac{1}{\lambda^2\sigma^2}} - \frac{1}{2}}\,. \tag{7.5.4}$$

[29] Here, the Greek letter λ instead of ν is used to denote the mean shot rate.

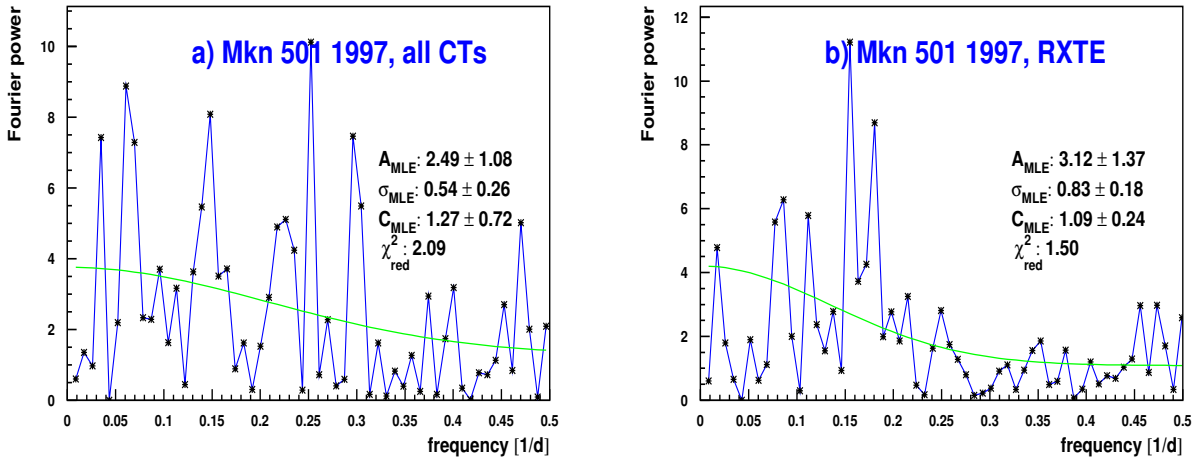

Fig. 7.5.4: The power spectra of the TeV (a) and X-ray (b) data sample after subtracting the 23-day period mode. In addition, the $1/T$ frequency mode was subtracted from the X-ray data. The corresponding mean Fourier power is shown as green line. The latter was determined under the assumption of Gaussian shaped flares with exponential distributed flare amplitudes and identical shot widths. The removed frequency component were excluded from the MLE calculations.

As can be seen from fig. 7.5.6 (c and d), the QPO peak is well above the 23-day period $f_{23} = 0.043\,\mathrm{d}^{-1} \ll 0.1\,\mathrm{d}^{-1} \lesssim f_{QPO}$ in all relevant cases ($\sigma = 0.5\,\mathrm{d}$, $\sigma = 1.0\,\mathrm{d}$ and $0.5\,\mathrm{d}^{-1} \lesssim \lambda$). Furthermore, the obtained power spectra seem to be inconsistent with the results shown in fig. 7.5.1 (no drop-off at small frequencies).

In summary, there is an indication for a real, i.e. not introduced by a set of randomly distributed flares, periodicity in the 1997 lightcurve of Mkn 501. The period is given by $p_{X-ray} = 23.0^{+1.8}_{-2.0}$ d and $p_\gamma = 22.5^{+1.8}_{-1.7}$ d for the X-ray and TeV range respectively. The significance of this periodicity is $3.4^{+0.7}_{-0.5}\,\sigma$ when the error is estimated from the uncertainties of the significance calculation or $3.4^{+1.1}_{-1.0}\,\sigma$ when the error on the MLE A is used ($A_\gamma = 3.49^{+1.0}_{-0.75}$ and $A_{X-ray} = 3.67^{+2.44}_{-1.56}$). In case the 23-day period is related to some intrinsic properties of Mkn 501, it should show up in the next high state of the object (see discussion below). It should also be possible to give the final answer concerning the 23-day periodicity then.

The biggest obstacle in the analysis of the power spectrum is due to the large variations introduced by the shot noise model. As was shown in sec. 7.3, the variance of the Fourier power is given by its mean value ($V\left[P_X\left(\omega\right)\right] = \left\langle P_X\left(\omega\right)\right\rangle$). It is therefore not possible to resolve finer structures like the difference between Gaussian and exponential type shots (see fig. 7.3.1) in individual power spectra. In fact, the analysis of the X-ray and TeV data gives similar results for both models (Gaussian: $\chi^2_{red}\left(\gamma\right) = 1.83$, $\chi^2_{red}\left(X-ray\right) = 2.36$, exponential: $\chi^2_{red}\left(\gamma\right) = 1.79$, $\chi^2_{red}\left(X-ray\right) = 2.56$, see fig. 7.5.1 and 7.5.3 respectively). Larger modifications of the power spectra, as introduced for example by the 'amplitude interaction' model (fig. 7.5.6) are clearly rejected by the data.

As was shown in sec 7.4 (fig. 7.4.4) it is possible to resolve minor differences in the spectral shape by means of the superposition of several similar power spectra. In the case of the TeV data this can be done by using the power spectra from different years. Problems arise, however, from the fact that the source was in different emission states, thus leading to different values for the shot noise parameter A. The power spectra then have to be normalized before being

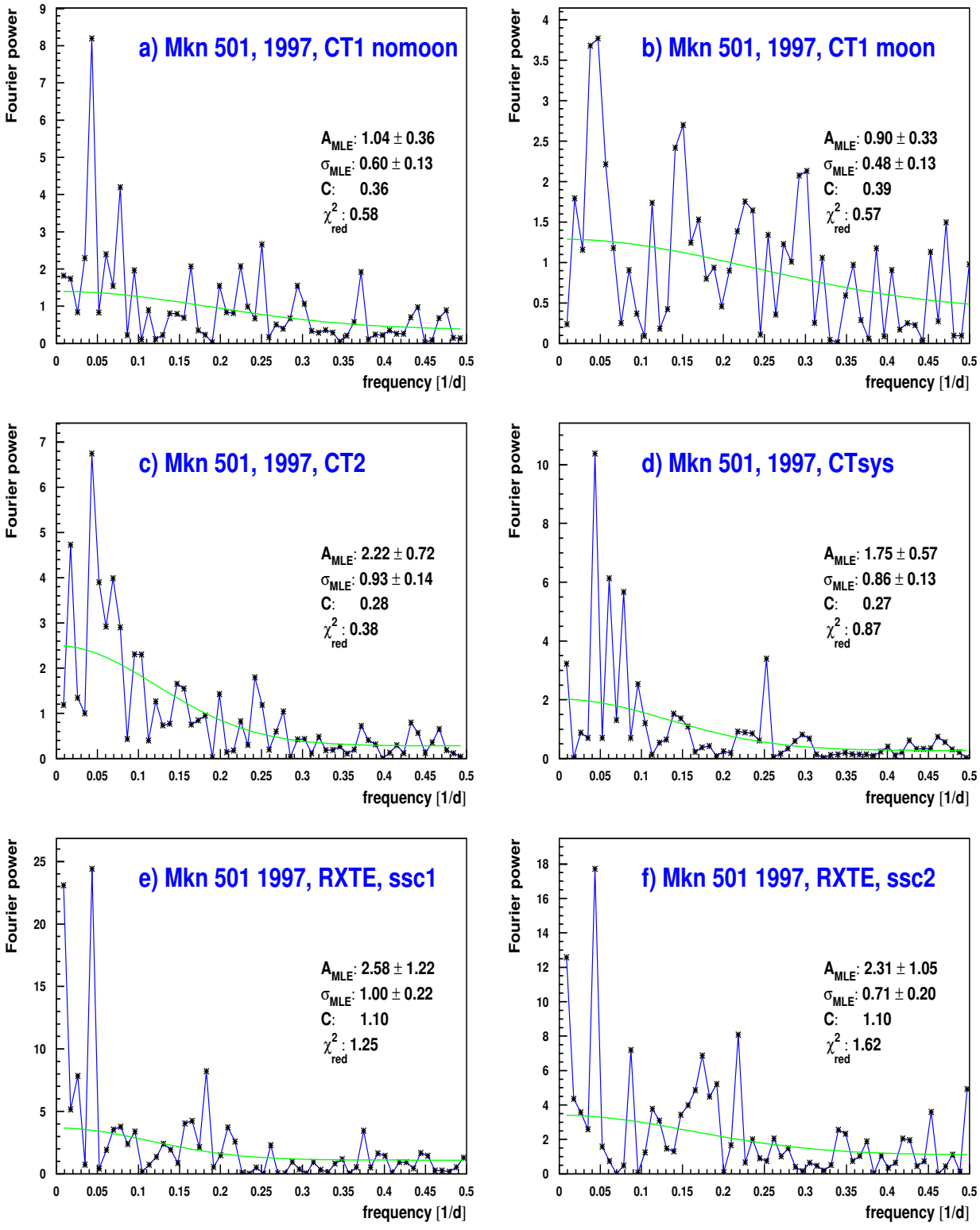

Fig. 7.5.5: The power spectra of the individual TeV (CT1, CT2 and CT-system) and X-ray (1st and 2nd shadowing camera) data samples and the corresponding mean Fourier power (green lines). The latter were determined under the assumption of Gaussian shaped flares with exponential distributed flare amplitudes and identical shot widths. It should be noted that there is a small overlay from events detected simultaneously by 2 instruments ($\sim$ 10% of the TeV data).

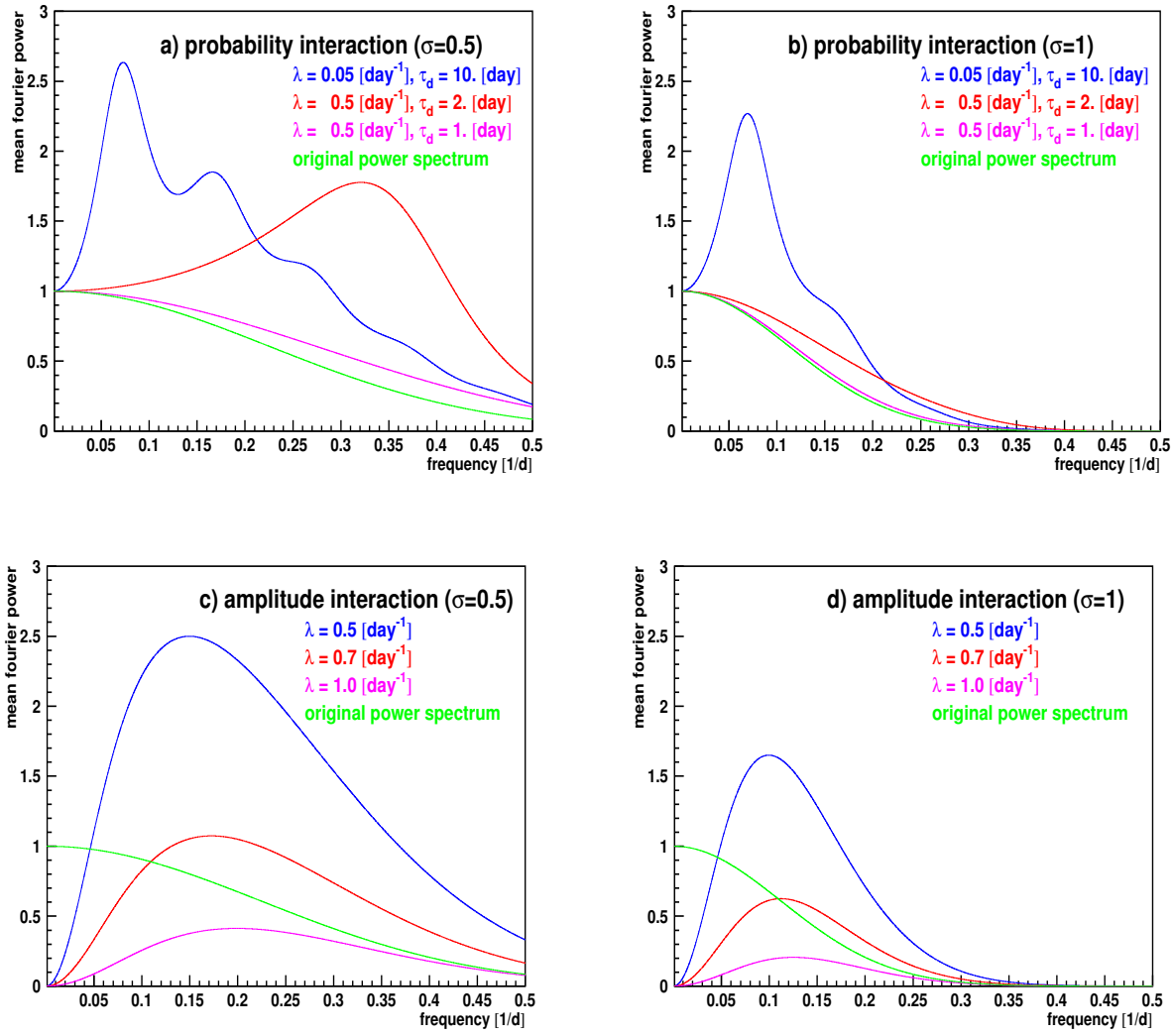

Fig. 7.5.6: Effect of the 'probability' and 'amplitude interaction' (see text) on the mean power spectrum. The original power spectrum is that of Gaussian type flares with $\sigma = 0.5$ day (left column) and $\sigma = 1.0$ day (right column) shot width. The disturbed power spectra are shown for different shot rates λ and decay times τ_d.

combined. In the case of the RXTE data, individual power spectra can be obtained more easily. Since the data density is about 10 times that of the CT data (1894 compared to 199 data points), one simply has to split up the data sample into several randomly chosen subsamples. The power spectrum can then be derived for each individual subsample. This analysis has not been carried out yet.

The results obtained for the shot width σ (fig. 7.5.1, $\sigma_\gamma = (0.51 \pm 0.07)$ d and $\sigma_{X-ray} = (0.96 \pm 0.21)$ d) give indications for another (besides the amplitude) real difference between the X-ray and TeV flares. These values are also supported by most of the results obtained from the individual subsamples (fig. 7.5.5), the frequency subtracted power spectra (fig. 7.5.4) and the overall Mkn 501 RXTE data[30] (fig. 7.5.11). Care must be taken, however, in the first two cases. On the one hand, the subtraction procedure might alter the power spectra in an uncontrolled way and lead to different results. For the TeV range on the other hand, only the CT1 no-moon data contain enough data points to really allow for frequencies up to $0.5\,\mathrm{d}^{-1}$. These results therefore serve only as a rough estimate.

Physics Discussion

In this section, the physical implications of a 23-day periodicity in the Mkn 501 data sample are discussed. Conclusions concerning the shape of the TeV and X-ray power spectra are also presented.

a) periodicity:

In 1997, Bednarek and Protheroe [15] proposed a model to explain a possible periodic structure of $\sim$ 3.3 days in the Mkn 421 light curves ([27] and reference therein). In this model, the observed correlated variable γ- and X-ray emission is explained as the result of photon-photon pair production interactions ($\gamma\gamma \rightarrow e^+e^-$) between γ- and X-ray photons which leads to a disappearance of γ- and X-ray photons (see below). The γ-rays are expected to be produced within the jet of the AGN while, in contrast to synchrotron self-Compton models (e.g. [27, 79]), the X-rays originate in a hot spot in the accretion disk. The variability in the observed X-ray and γ-ray light curves then originates in the orbital motion of the hot spot around the black hole. Several scenarios leading to hot spots in the accretion disk are proposed in [15]. One of them is the collision of a star or its debris with the accretion disk.
Assume an X-ray emitting hot spot is orbiting at distance r_s around the central engine of the AGN (see fig. 7.5.7). Because of strong absorption, the γ-rays cannot be produced within the hot spot, but must originate in the jet (at distance x to the hot spot). If the γ-ray emission is not too far away from the hot spot, the γs can be absorbed through pair production interaction. According to [15], the optical depth, measured from the point of injection to infinity, for a γ-ray photon with energy E_γ is then given by:

$$\tau\left(r_s, E_\gamma, \alpha, l\right) = \frac{d_s^2}{c r_s} \int \frac{(1-\cos\chi)}{D^2} \mathrm{d}H \int F_X\left(\epsilon\right) \sigma_{\gamma\gamma}\left(s\right) \mathrm{d}\epsilon \,. \tag{7.5.5}$$

Here χ denotes the angle between the γ-rays (on their way to the observer) and the interacting X-rays, $D = \sqrt{1 + H^2 + L^2 + 2HL\sin\alpha\cos\phi}$ the distance hot spot - interaction and $H = D\cos\chi - L\cos\alpha + \sin\alpha\cos\phi$ the distance emission region - interaction in units of r_s (see fig.

[30] The 1998 and 1999 Mkn 501 data from the CTs have not been completely analyzed yet. The 1996 data, solely taken by CT1, has a poor signal to noise ratio ($\sim$ 0.3 crab [126]) and large moon gaps (CT1 moon observations began in 1997).

7.5.7 a and b, $L = l/r_s$). The parameter d_s denotes the distance to earth, $\sigma_{\gamma\gamma}$ the photon-photon pair production cross section and $s = 2\epsilon E_\gamma (1 - \cos\chi)$ the center of momentum frame energy squared. The X-ray spectrum of the hot spot is given by $F_X(\epsilon)$.
In case α, the viewing angle with respect to the jet axis, is non zero, the angle ψ and therefore the optical depth τ become phase dependent (phase $\phi = \phi_0 + \omega_s t$, see fig. 7.5.7). As a result, both, the γ-rays and X-rays show a periodic structure with angular frequency ω_s. A relation between the hot spot orbital radius r_s and the black hole mass can then be established by means of Kepler's third law:

$$\omega_s = \sqrt{\frac{G(M+m)}{r_s^3}} \simeq \sqrt{\frac{GM}{r_s^3}} = c\sqrt{\frac{r_g}{2r_s^3}} \tag{7.5.6}$$

($r_g = 2GM/c^2 \simeq 3.0 \cdot 10^{11} M_8$ m denotes the Schwarzschild radius, m the hot spot mass and M_8 the black hole mass in units of 10^8 solar masses - $M_\odot \simeq 2.0 \cdot 10^{30}$ kg). Given a minimum inner disk radius $r_i \sim$ (0.5-3)r_g, for maximally rotating Kerr and Schwarzschild black holes respectively [15], an upper limit for the black hole mass can be derived. In the case of the 23 day period of Mkn 501, the hot spot orbital radius is derived as

$$r_s \simeq 1.1 \cdot 10^{13} M_8^{1/3} \text{ m} \tag{7.5.7}$$

and the upper limit for the black hole mass becomes $M < 6.3 \cdot 10^{10} M_\odot$ (Kerr black hole) and $M < 4.3 \cdot 10^9 M_\odot$ (Schwarzschild black hole).

A more severe restriction on the black hole mass, however, comes from the limited velocity v_s of the orbiting hot spot. Given the 23 day period of Mkn 501 and a reasonable upper limit on the hot spot velocity of $v_s \lesssim 0.1 \cdot c$ the upper limit on the orbital radius r_s becomes $r_s \lesssim 0.1 \cdot c \cdot 23\,\text{d}/2\pi = 9.5 \cdot 10^{12}$ m. A comparison with eq. 7.5.7 then yields an upper limit on the black hole mass of $M \lesssim 6 \cdot 10^7 M_\odot$.

Another result from [15] is a predicted time delay Δt of the peak γ-ray flux with respect to the peak X-ray flux (see fig. 7.5.7):

$$\Delta t = \frac{1}{c}\sqrt{r_s^2 + l^2}\,[1 - \cos(\theta - \alpha)] \tag{7.5.8}$$

(with $\tan\theta = r_s/l$). For $r_s = 1.0 \cdot 10^{13}$ m, $\alpha = 7°$ and $l = 30 r_s$, the expected delay is $\Delta t \approx 1$ h and for $l = 10 r_s$ the delay becomes $\Delta t \approx 1.4$ min. These values are too small to be resolved by either the phase plot (fig. 7.2.11) or the correlation analysis (fig. 7.2.13).
The main problem with this model seems to be the observed non-thermal X-ray spectra for Mkn 421 [27, 101, 162] and Mkn501 [30, 128, 146] which is in contrast to an expected thermal emission from the hot spot.

In order to explain the observed periodic structure in the Mkn 501 1997 lightcurve [70, 90] Rieger and Mannheim [142] have proposed another model, where Mkn 501 is assumed to be a *binary black hole system* BBHS. This assumption is based on the fact that BBHSs are expected from galaxy merger scenarios ([142] and reference therein) while giant elliptical galaxies, like the host galaxy of Mkn 501, seem to be the result of spiral galaxy mergers [59]. In case the jet from Mkn 501 originates in the less massive black hole, the orbital motion of the latter would naturally lead to a helical jet structure (an example is shown in fig. 7.5.8). In fact, a helical jet model has already been proposed in order to explain the misalignment of the radio jet on parsec and kiloparsec scales [36][31] (see fig. 7.5.9) and the X-ray variations in the *spectral*

[31] However, in a more recent VLBI observation of Mkn 501 Giovannini et al. [63] conclude: "No evidence of a helical structure is visible in our maps."

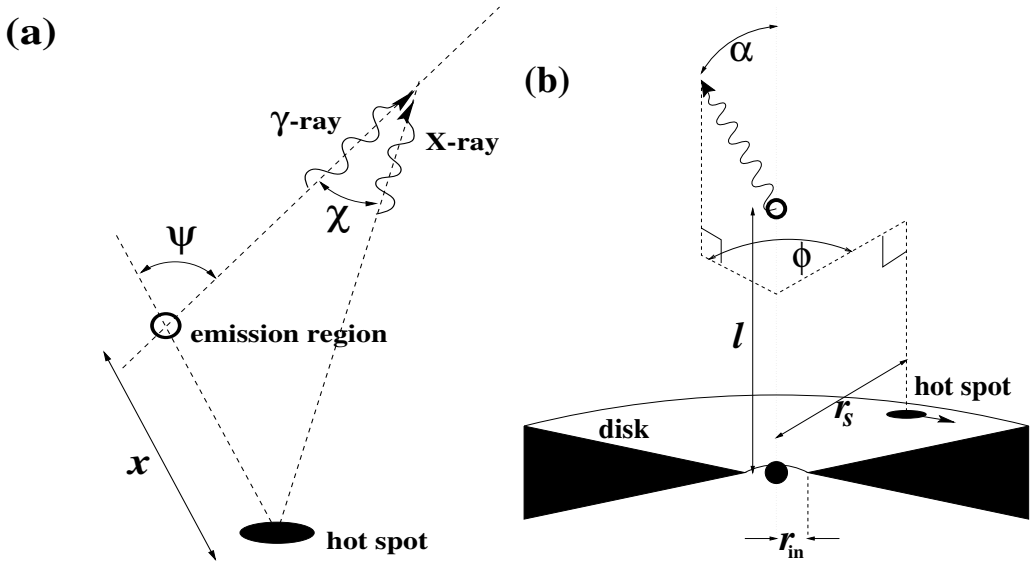

Fig. 7.5.7: (a) Simple picture of X-ray emitting hot spot and emission region of VHE γ-rays located at a distance x from the hot spot. The γ-rays, injected at an angle ψ to the direction from the hot spot, interact with the X-ray radiation from the hot spot. (b) Schematic representation (not to scale) of the central region of AGN. The X-ray emitting hot spot orbits with the accretion disk at a distance r_s from a massive black hole. The γ-rays emitted at angle α to the jet axis and at different distances l along the jet can interact with X-rays from the hot spot. The location of the hot spot on the disc is defined by its phase ϕ. (figure and caption taken from [15])

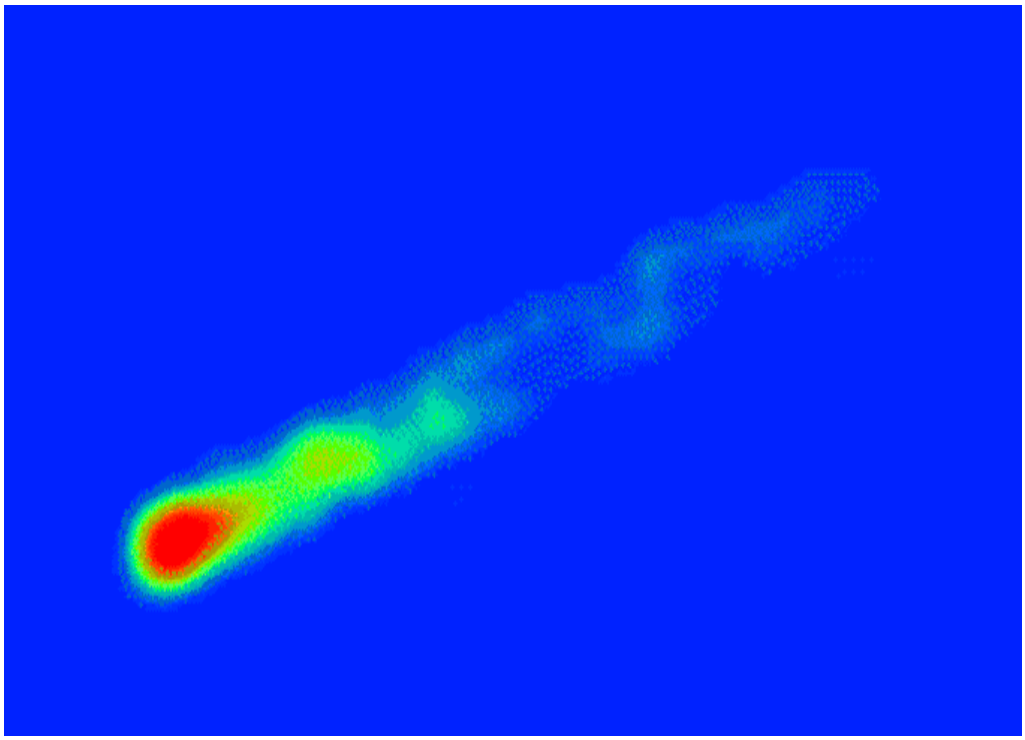

Fig. 7.5.8: Radio jet of the elliptical galaxy M87, observed with the 'World Array' of radio telescopes at a wavelength of 18 cm. The image covers about 100 milli-arc-seconds of sky with a resolution of about 4 milli-arc-seconds. The jet is clearly resolved and shows quasi-helical structures and limb brightening. (taken from [140])

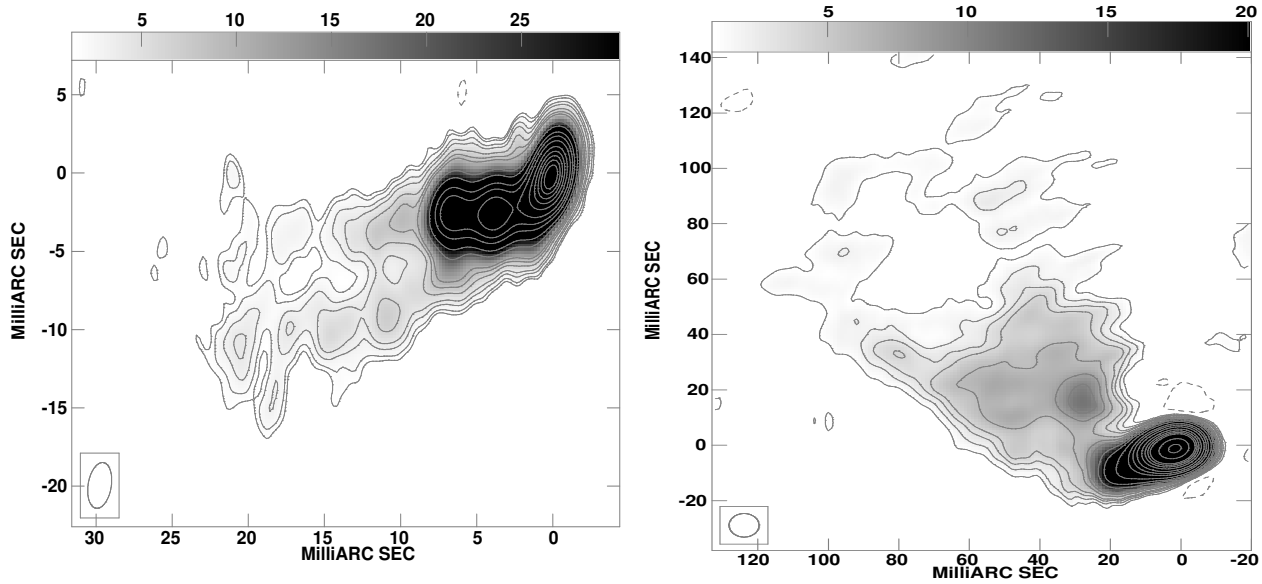

Fig. 7.5.9: Left: Space VLBI map of Mkn 501 at 18 cm. The *half power beam widths* (HPBW) is 2.9x1.5 mas (milli arc seconds) at $PA = -10°$. The noise level is 0.3 mJy/beam. Right: VLBI map of Mkn 501 at 18 cm using only ground stations. The HPBW is 8.5 mas and the noise level is 0.35 mJy/beam. (figure and caption taken from [63])

energy distribution SED of Mkn 501 in 1997 [169]. Assuming that the non-thermal X-ray and γ-ray radiation is produced within an emission region propagating along the jet (with bulk Lorentz factor γ_b), the observed flux is Doppler boosted according to [142]:

$$S(\nu) = \delta^3 S'(\nu') = \delta^{3+\alpha} S'(\nu) \tag{7.5.9}$$

This equation gives the spectral flux density as a function of α, the spectral index of the object and S', the spectral flux density in the comoving frame; $\delta = \left(\gamma_b \left[1 - v\cos\theta(t)/c\right]\right)^{-1}$ denotes the Doppler factor and $\theta(t)$ the angle between the velocity vector $\overrightarrow{v}$ of the emission region and the direction to the observer. In case of a helical jet structure the angle $\theta(t)$ and therefore the Doppler factor δ change periodically (see fig. 7.5.10) and, as a result, the observed flux shows the same modulation. In the simple case, where the angle between the jet axis and the normal of the orbiting plane is zero, the Doppler factor becomes:

$$\delta = \frac{\sqrt{1 - v^2/c^2}}{1 - v\cos(\theta(t))/c} = \frac{\sqrt{1 - (v_z^2 + \Omega_k^2 R^2)/c^2}}{1 - (v_z\cos(i) - \Omega_k R\sin(i)\sin(\Omega_k t))/c} \tag{7.5.10}$$

(Ω_k is the orbital frequency, R the center-of-mass distance and i the inclination angle of the jet with respect to the observer[32]). As can be seen, the Doppler factor has the same period

[32] The second part of eq. 7.5.10 follows from the velocity vector $\overrightarrow{v} = \begin{pmatrix} -\Omega_k R\cos(\Omega_k t) \\ \Omega_k R\sin(\Omega_k t) \\ v_z \end{pmatrix}$, the position of the observer $\overrightarrow{d_s} = \begin{pmatrix} d_s\sin(i) \\ 0 \\ d_s\cos(i) \end{pmatrix}$ and $\overrightarrow{v}\cdot\overrightarrow{d_s} = v d_s\cos(\theta(t))$.

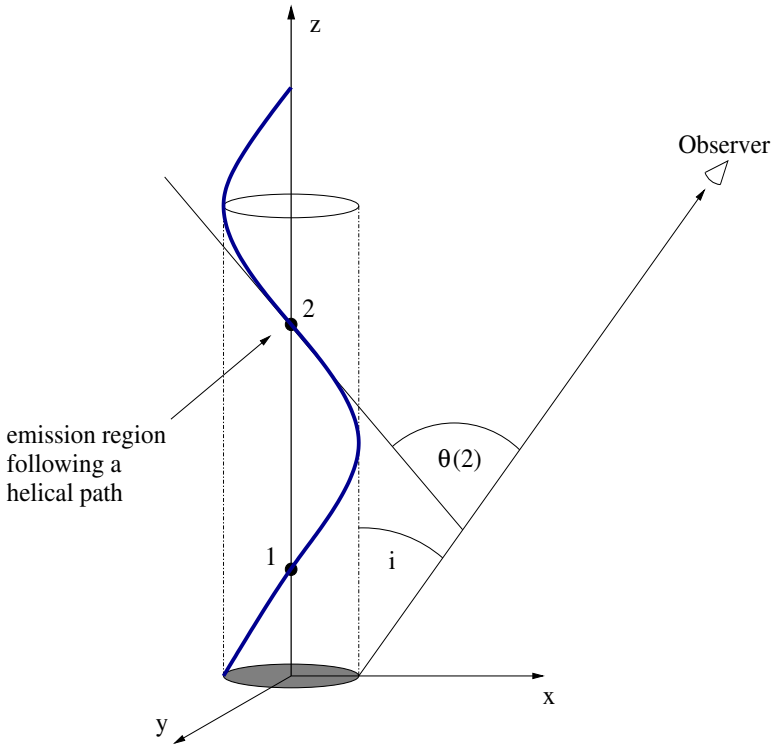

Fig. 7.5.10: Simple sketch of a helical jet path caused by the orbital motion in a BBHS. (adopted from [143])

$P_k = 2\pi/\Omega_k$ as the orbiting black hole. The observed X-ray and γ-ray flux shows a Doppler shortened period proportional to P_k, which is according to [142]:

$$P_{obs} = (1+z)\left(1 - \frac{v_z}{c}\cos(i)\right) P_k \tag{7.5.11}$$

(the first term takes into account the redshift of Mkn 501 with $z = 0.034$). Reasonable numbers for the constituents of eq. 7.5.11 are: $i \simeq 1/\gamma_b$ [157], $\gamma_b \simeq 10 - 15$ [77, 104, 157] and $v_z/c \simeq \sqrt{\left(1 - \gamma_b^{-2}\right)}$. Given an observed period of 23 days, the intrinsic period P_k then becomes $P_k = (6 - 10)$ yrs.

The center-of-mass distance $R = Md/(m+M)$ (m and M denote the mass of the smaller and larger black hole) can be calculated from eq. 7.5.9 and 7.5.10. According to eq. 7.5.10, the Doppler factor is maximal for $t = 3P_k/4$ and minimal for $t = P_k/4$. If the observed periodicity is mainly due to Doppler modulation, eq. 7.5.9 leads to the following condition for the flux ratio f (maximum flux / minimum flux): $f^{1/(3+\alpha)} \simeq \delta_{max}/\delta_{min}$. Equation 7.5.10 then gives:

$$\Omega_k R = \frac{f^{1/(3+\alpha)} - 1}{f^{1/(3+\alpha)} + 1}\left(\frac{1}{\sin(i)} - \frac{v_z}{c}\cot(i)\right) c \tag{7.5.12}$$

and finally (using eq. 7.5.11):

$$R = \frac{P_{obs}}{2\pi(1+z)}\frac{f^{1/(3+\alpha)} - 1}{f^{1/(3+\alpha)} + 1}\frac{c}{\sin(i)}\,. \tag{7.5.13}$$

Given a flux ratio of $f \sim 8$ [131], the 23 day period, an inclination angle $i \simeq 1/\gamma_b \simeq 1/10 - 1/15$ and a TeV spectral index of $\alpha \simeq (1.2 - 1.7)$ [2] the center-of-mass distance R becomes: $R \simeq (2.3 - 3.5) \cdot 10^{16}$ cm.

$i = 1/\gamma_b$	1/10		1/15	
m $[10^8 M_\odot]$	0.040	(0.061)	0.33	(0.42)
M $[10^8 M_\odot]$	0.96	(0.75)	1.03	(0.91)
d $[10^{16}\mathrm{cm}]$	2.40	(2.24)	4.57	(4.54)
P_k [yrs]	6.10		13.7	
τ_{grav} $[10^7\mathrm{yrs}]$	5.46	(4.25)	5.86	(5.18)
P_p $[10^4\mathrm{yrs}]$	0.52	(0.39)	3.03	(2.93)

Tab. 7.5.2: Maximum binary masses, separation d, intrinsic orbital period P_k, gravitational lifetime τ_{grav} and precessional period P_p for inclination angles i , accretion rate $\dot{M} = 2M_\odot/yr$ and spectral index $\alpha = 1.2\,(1.7)$. (taken from [142])

Table 7.5.2 summarizes the results obtained from two different gamma factors and spectral indices. The authors [142] also give estimates for the two black hole masses m and M, the gravitational lifetime τ_{grav} and the precession period P_p. In case of $N \lesssim 6$ periodic oscillations (see fig. 7.2.8), the derived (projected) propagation length l_p for the emitting component becomes (using $i = 1/15 - 1/10$ rad): $l_p \simeq 1.4 - 2.1$ mas. The observed change in the jet parameters at 3 mas (7.5.9 left) might therefore be the reason for the termination of the observed periodicity [142].

The BBHS model gets further support from the timing analysis of the overall RXTE Mkn 501 data. As can be seen from fig. 7.5.11 and 7.5.12 there are several strong modes at small frequencies in the power spectrum of Mkn 501 ($f_n = n/T$ and $T = 1616$ d: $P_X(f_1) = 377$, $P_X(f_2) = 57$ and $P_X(f_3) = 163$). These modes do not correspond to the precession frequency (with $P_p^{obs} = \mathcal{O}(50)$ yrs according to eq. 7.5.11 and tab. 7.5.2) but are addressed to precessional modulations. Since there are only 3 prominent cycles present in the lightcurve, it is too early to draw decisive conclusions yet. Note that the power spectrum even shows a small peak at the 23-day period.

Another interesting result is obtained from the Mkn 421 timing analysis (same figures). The strongest frequency modes are less pronounced than in the Mkn 501 power spectrum ($T = 1613$ d: $P_X(f_2) = 122$, $P_X(f_4) = 93$ and $P_X(f_5) = 85$), but there seems to be a periodic structure present too (especially in the 2nd half of the lightcurve). Given the similarities between Mkn 501 and Mkn 421 (similar redshift and bulk Lorentz factor γ_b [63]) it could be possible that Mkn 421 shows a periodicity comparable to the 23 days of Mkn 501. In fact, the Whipple data from the 1995 observation of Mkn 421 [27] show evidence for a ~ 30 day periodicity (see fig. 7.5.13). As far as I know, a timing analysis of this data has not been carried out yet.

Another possibility to explain the 23-day periodicity can be attributed to disk jet interactions in the AGN: In the case of the microquasar GRS 1915+105 evidence has been found that the observed plasma ejection into the jet is intimately linked to activity in the inner accretion disk [51, 53, 109]. Due to the close similarity between AGN and microquasars, this effect might also show up in AGN. In that scenario, a periodic γ-ray flux might be produced by an orbiting massive star. If the star has an elliptical orbit, the mass outflow onto the central black hole increases each time the star passes through the perihelion. As a result, the mass ejection rate into the jet shows the same periodic structure. Each mass ejection is accompanied by a shock wave which is then responsible for the high-energy γ-ray emission. Similar to the hot spot scenario and in contrast to the BBHS model, the observed periodicity is not Doppler shortened and reveals the true period of the orbiting object.

Two other models, which have been proposed to explain the production of high-energy γ-

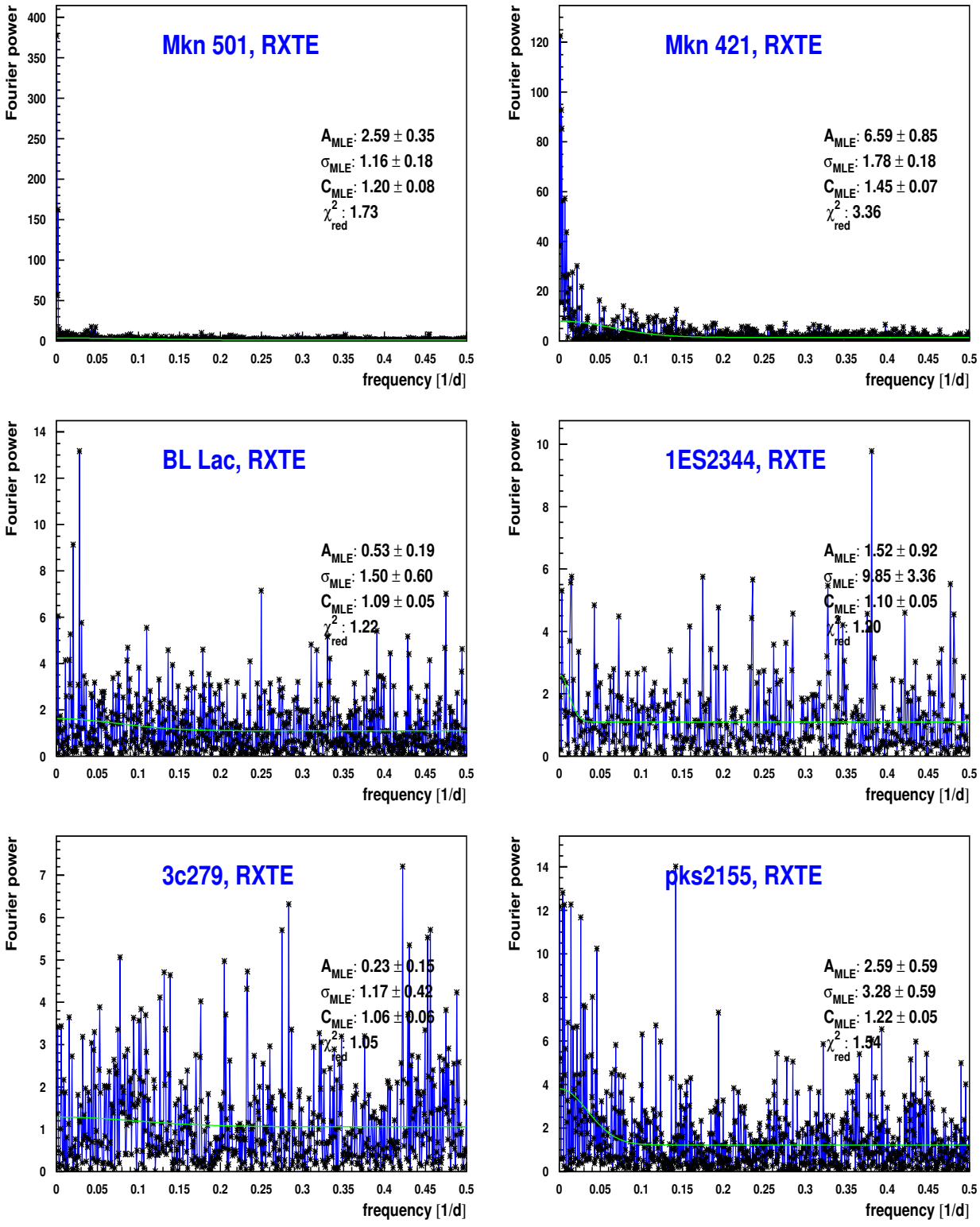

Fig. 7.5.11: Power spectrum for several prominent BL Lac objects (derived from all available RXTE data). The corresponding mean Fourier power (shown as green line) was determined under the assumption of Gaussian shaped flares with exponential distributed flare amplitudes and identical shot widths. In the case of Mkn 501 and Mkn 421 all modes with a Fourier power above 60 have been excluded from the MLE calculation and χ^2-fit.

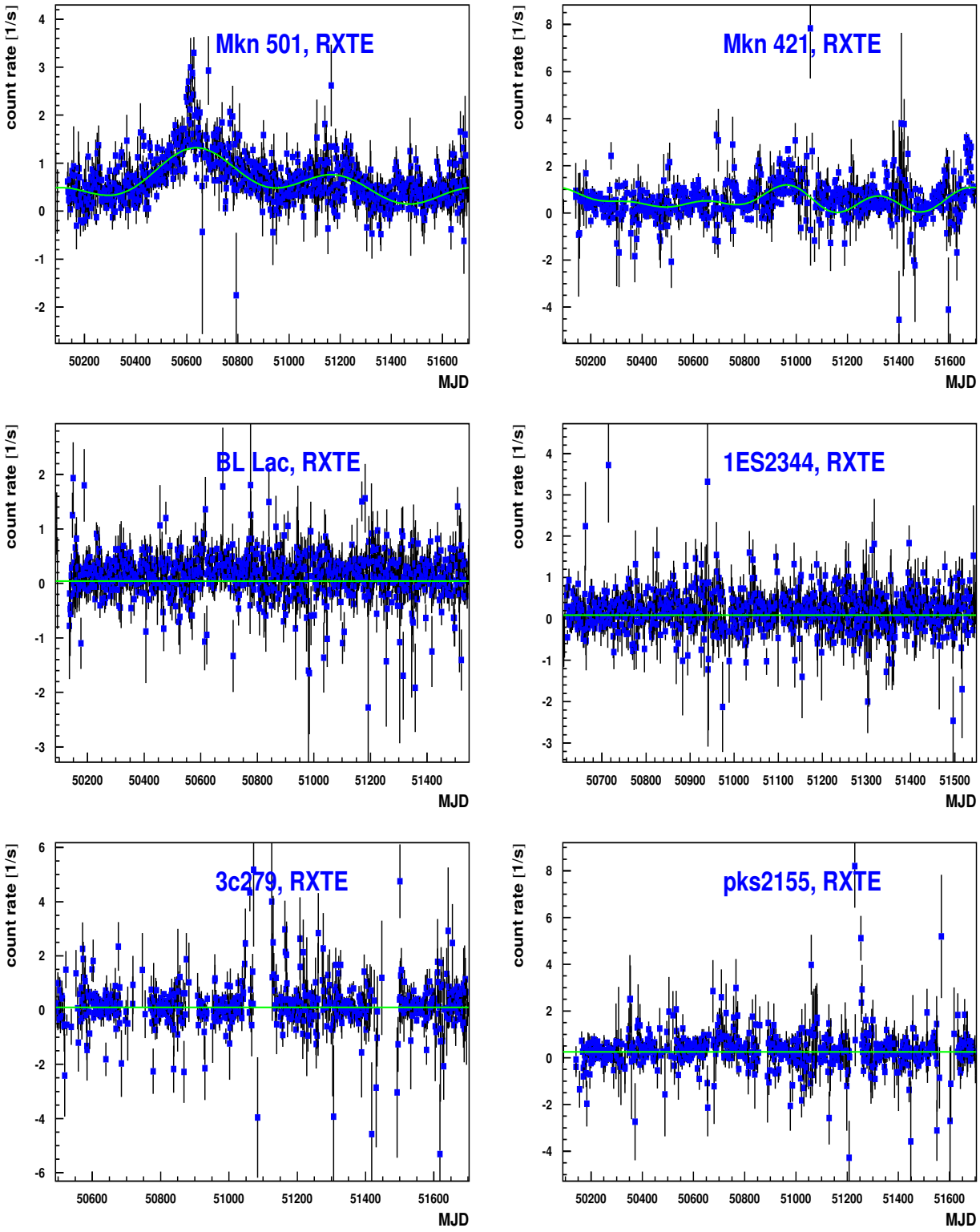

Fig. 7.5.12: RXTE light curves for several prominent BL Lac objects (derived from all available data) and the prominent modes from the power spectrum (frequencies with a Fourier power above 60) as a green line. The data was binned for visual purposes.

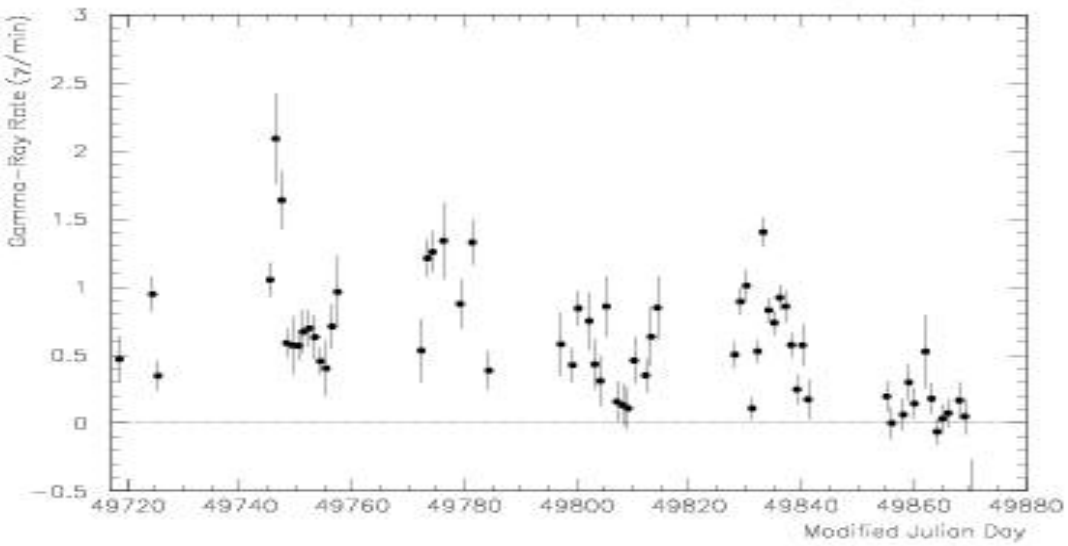

Fig. 7.5.13: Whipple lightcurve of the Mkn 421 observation in 1995. The daily rates at $E > 300\,\mathrm{GeV}$ are shown. (taken from [27])

rays in AGN, are essentially ruled out, if the observed periodicity holds. The basic assumption in these models is, that high-energy γ-ray photons are produced in collisions of small clouds [40] or stars [14] surrounding the black hole with the jet. Unless these clouds or stars are regularly arranged, no periodic emission will emerge from the jet.

b) power spectra:

As was already said before, it is not possible to resolve minor differences in the flare shape (e.g. between Gaussian or exponential type flares) from a single power spectrum. It is therefore not possible to draw conclusions on the predictions of the different variability models [46, 88, 108, 157] yet. For strong flares (see fig. 7.5.14), it is therefore more appropriate to work out this analysis in the time domain [108]. In the case of a poor signal to noise ratio or overlayed flares the Fourier analysis may still prove valuable: given the Mkn 501 lightcurve (see fig. 7.2.8), the shot width $\sigma_\gamma \simeq 0.5\,\mathrm{d}$ is barely visible in the TeV data, but $\sigma_{X-ray} \simeq 1.0\,\mathrm{d}$ not at all in the X-ray data.

The effect of an amplitude or probability interaction of the individual flares is not visible in the X-ray and γ-ray power spectra. The reason is as follows: The amplitude and probability interaction was introduced in order to keep the average energy release on a constant level on long time scales. The one year duration of the 1997 outburst, however, does not represent a long time scale for the accretion processes within an AGN, even when a Doppler factor of O(10) is assumed. Therefore none of these effects is expected to show up in the power spectrum.

The difference in the derived shot width $\sigma_\gamma = (0.51 \pm 0.07)\,\mathrm{d}$ and $\sigma_{X-ray} = (0.96 \pm 0.21)\,\mathrm{d}$ seems to be also supported by recent Mkn 501 multi-wavelength observations [146, Fig. 1]. Furthermore, a similarity in the difference between σ_γ and σ_{X-ray} is also observed in a recent flare of Mkn 421 (fig. 7.5.14). An explanation for this difference could be photon-photon absorption in the emitting hot blob [16]. Depending on the size of the optical depth, only γ-ray photons from the outer region of the blob are able to escape. As a result, the emitting volume, and therefore the rise and decay time of a flare, is smaller for γ-rays compared to X-rays.

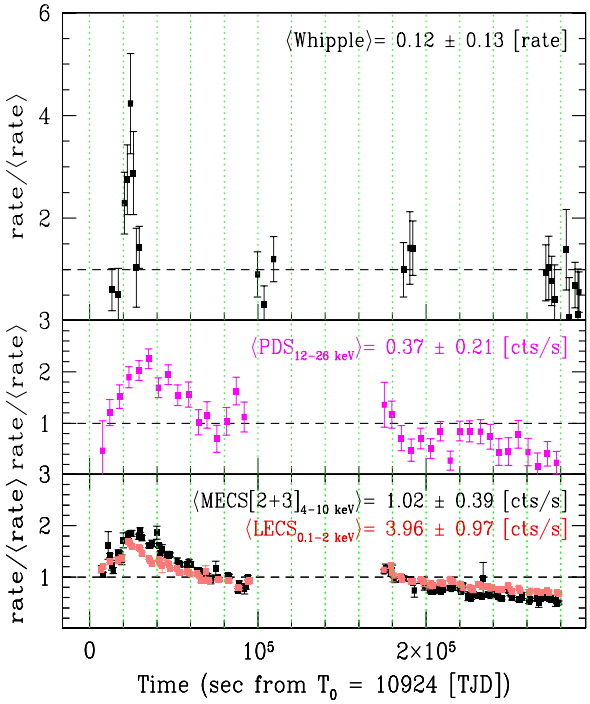

Fig. 7.5.14: Mkn 421 light curves at TeV and X-ray energies. The top part of the figure shows the Whipple data ($> 2\,\mathrm{TeV}$), the second and third section show BeppoSAX data with energy ranges as specified. All the count rates are normalized to their respective averages (given in each section) over the observations shown. (taken from [105])

	3C279	BL Lac	PKS2155	1ES2344	Mkn 421	Mkn 501
σ_{mle} $[d]$	1.17 ± 0.42	1.50 ± 0.60	3.28 ± 0.59	9.85 ± 3.36	1.78 ± 0.18	1.16 ± 0.18
χ^2_{red}	1.05	1.22	1.54	1.20	3.36	1.73
μ $[\mathrm{s}^{-1}]$	0.10	0.05	0.25	0.09	0.53	0.61

Tab. 7.5.3: Shot width σ_{mle} for several prominent BL Lac objects (derived from the overall RXTE data). The χ^2-value for the mean Fourier power and the mean photon count rate μ for each individual lightcurve is also given.

The X-ray power spectra for several BL Lac objects show rather similar values for the shot width σ (see fig. 7.5.11 and tab. 7.5.3). The result for the main outlier, 1ES2344, is addressed to its poor signal (mean photon count rate $\mu = 0.09\,\mathrm{s}^{-1}$). The results obtained for Mkn 421 and Mkn 501 are somewhat surprising, since the shortest variability time scales in the TeV range are $\Delta t_{501} \sim 5 - 15$ h [3] compared to $\Delta t_{421} \sim 1$ h [105], e.g. in reverse order to tab. 7.5.3. The shot width, derived from the power spectrum, however, denotes the mean variability time scale and not its minimum. Furthermore, tab. 7.5.3 only shows the results from the X-ray data. Different contributions of the photon-photon absorption process might result in the observed TeV variability time scales.

APPENDIX

A. FOURIER TRANSFORMATIONS AND THE LOMB-SCARGLE PERIODOGRAM

A.1 Validation of the inverse Fourier transform

The aim of this section is to validate eq. 7.1.3 of sec. 7.1. With

$$FT_x(\omega_n) = \sum_{k=1}^{N} X_k \exp(-ik\omega_n\Delta) \tag{A.1.1}$$

and the inverse Fourier transform

$$X_j = \frac{1}{N}\sum_{n=1}^{N} FT_x(\omega_n) \exp(ij\omega_n\Delta) \tag{A.1.2}$$

($t_j = j\Delta,\ j = 1,...,N,\ \omega_n = 2\pi n/T,\ n = 1,...N$ and $T = N\Delta$ is the total time interval) we have:

$$\begin{aligned} X_j &= \frac{1}{N}\sum_{n=1}^{N}\sum_{k=1}^{N} X_k \exp[-2\pi i n(k-j)\Delta/T] \\ &= \frac{1}{N}\left[\sum_{n,k} X_k\delta_{kj} + \sum_{n,k,k\neq j} X_k \exp[-2\pi i(k-j)/N]\frac{1-\exp[-2\pi i(k-j)]}{1-\exp[-2\pi i(k-j)/N]}\right] \\ &= \frac{1}{N}\sum_{n} X_j = X_j \end{aligned} \tag{A.1.3}$$

(since $1-\exp[-2\pi i(k-j)] \equiv 0\ \forall k, j\epsilon N$ and $1-\exp[-2\pi i(k-j)/N] \neq 0$ for $k \neq j$ and $|k-j| \leq N-1$)

A.2 Fourier power for simulated sinusoids with angular frequency ω_k

In the case of even data spacing ($t_j = j\Delta,\ j = 1,...,N$, $T = N\Delta$ is the total time interval) a sinusoid with amplitude A and angular frequency $\omega_k = 2\pi k/T,\ k = 0,...N/2$ gives $X_j = Acos(2\pi kj/N + \varphi)$. The resulting Fourier power (eq. 7.1.4) at ω_k becomes (phase φ can be set to zero):

$$\begin{aligned} P_X(\omega_k) &= \frac{1}{N}\left[\left(\sum_{j=1}^{N} A\cos^2(2\pi kj/N)\right)^2 + \left(\sum_{j=1}^{N} A\cos(2\pi kj/N)\sin(2\pi kj/N)\right)^2\right] \\ &= \frac{A^2}{4N}\left[\left(\sum_{j=1}^{N}[1+\cos(4\pi kj/N)]\right)^2 + \left(\sum_{j=1}^{N}\sin(4\pi kj/N)\right)^2\right] \end{aligned} \tag{A.2.1}$$

If $0 < k < N/2$:

$$\begin{aligned}\sum_{j=1}^{N} \cos\left(4\pi kj/N\right) + i \cdot \sum_{j=1}^{N} \sin\left(4\pi kj/N\right) &= \sum_{j=1}^{N} \exp\left(4\pi ikj/N\right) \\ &= \exp\left(4\pi ik/N\right) \frac{1-\exp\left(4\pi ik\right)}{1-\exp\left(4\pi ik/N\right)} \\ &= 0 \end{aligned} \tag{A.2.2}$$

(since $1 - \exp(4\pi ik) \equiv 0 \; \forall \; k = 1, ..., N/2 - 1$) and therefore $P_X(\omega_k) = A^2 N/4$.
In case $k = 0$ or $k = N/2$, eq. A.2.1 becomes $P_X(\omega_k) = A^2 N$.
If the periodogram is normalized onto the sample variance $\sigma_X^2 = \frac{1}{N-1} \sum_{j=1}^{N} A^2 cos^2 2\pi kj/N = \frac{NA^2}{2(N-1)}$, we have $P_X(\omega_k) = (N-1)/2$ for $0 < k < N/2$ or $P_X(\omega_k) = N - 1$ for $k = 0$ or $k = N/2$.

A.3 Properties of the Lomb-Scargle periodogram

The most important properties of the Lomb-Scargle periodogram are derived in this section. Section A.3.3 is a short summaries of [150, App. A] and is repeated here for completeness.

A.3.1 Time-translation invariance

Proof of the time - translation invariance of eq. 7.2.1. The proof is produced by showing that as $t_j \to t' = t_j + \Delta t$ we have $\tau \to \tau' = \tau + \Delta t$ because then Δt cancels out in the argument $\omega(t_j - \tau)$:

$$\begin{aligned}\tan 2\omega\tau' &:= \frac{\sum_{j=1}^{N} \sin 2\omega\left(t_j + \Delta t\right)}{\sum_{j=1}^{N} \cos 2\omega\left(t_j + \Delta t\right)} \\ &= \frac{\sum_{j=1}^{N} \left(\sin 2\omega t_j \cos 2\omega\Delta t + \cos 2\omega t_j \sin 2\omega\Delta t\right)}{\sum_{j=1}^{N} \left(\cos 2\omega t_j \cos 2\omega\Delta t - \sin 2\omega t_j \sin 2\omega\Delta t\right)} \\ &= \frac{\frac{\sum_{j=1}^{N} \sin 2\omega t_j}{\sum_{j=1}^{N} \cos 2\omega t_j} + \frac{\sin 2\omega\Delta t}{\cos 2\omega\Delta t}}{1 - \frac{\sum_{j=1}^{N} \sin 2\omega t_j}{\sum_{j=1}^{N} \cos 2\omega t_j} \frac{\sin 2\omega\Delta t}{\cos 2\omega\Delta t}} \\ &= \frac{\tan 2\omega\tau + \tan 2\omega\Delta t}{1 - \tan 2\omega\tau \tan 2\omega\Delta t} \\ &= \tan 2\omega\left(\tau + \Delta t\right) \end{aligned} \tag{A.3.1}$$

A.3.2 Conformity with the classical periodogram

In order to proof the conformity between the Lomb-Scargle periodogram (eq. 7.2.1) and the classical periodogram (eq. 7.1.4) in the case of even data spacing, it is sufficient to shown that:

$$\mathrm{I}: \quad \sum_{j=1}^{N} \cos^2 \omega_k \left(t_j - \tau\right) = \sum_{j=1}^{N} \sin^2 \omega_k \left(t_j - \tau\right) = N/2 \tag{A.3.2}$$

(for $\omega_k = 2\pi\frac{k}{T},\ k = 1, ..., N/2-1$ and $t_j = t_0 + j\frac{T}{N};\ j = 1, ..., N$, T denotes the covered time range)
and

$$\text{II}: \quad P_X\left(\omega_{N/2}\right) = \frac{1}{N}\left[\sum_{j=1}^{N} X_j\,(-1)^j\right]^2 \quad . \tag{A.3.3}$$

($\sigma_X^2 = 1$ and $\overline{X} = 0$ can be assumed without loss of generality[1])

part I:

$$\sum_{j=1}^{N} \sin^2\omega_k\,(t_j-\tau) = \sum_{j=1}^{N} \cos^2\omega_k\,(t_j-\tau) = \frac{N}{2} \tag{A.3.4}$$

(for $k = 1, ..., N/2-1$).
Since $\sum_{j=1}^{N}\left(\sin^2\alpha_j + \cos^2\alpha_j\right) = N$, it is sufficient to show that $\sum_{j=1}^{N}\sin^2\omega_k\,(t_j-\tau) = N/2$. With $\sum_{j=1}^{N}\sin^2\alpha = \sum_{j=1}^{N} 0.5\,(1-\cos 2\alpha)$ and $\cos(\alpha-\beta) = \cos\alpha\cos\beta + \sin\alpha\sin\beta$ eq. A.3.4 is equivalent to:

$$\cos 2\omega_k\tau \cdot \sum_{j=1}^{N}\cos 2\omega_k t_j + \sin 2\omega_k\tau \cdot \sum_{j=1}^{N}\sin 2\omega_k t_j = 0 \tag{A.3.5}$$

The proof of eq. A.3.5 immediately follows from eq. A.2.2 (t_0 can be set to zero due to Appendix A.3.1). Please note that the definition of t_j determines T as $T = \frac{N}{N-1}(t_N - t_1)$. The definition $T = t_N - t_1$ is not correct (in the sense that the LSP does not converge to the classical periodogram then) since $t_j = t_0 + j\frac{T}{N-1};\ j = 1, ..., N$ then and eq. A.2.2 is not fulfilled. In other words, since t_1 ... t_N correspond to certain time bins (they denote for example the bin mean), taking $T = t_N - t_1$ neglects one bin.

part II:

In case of $k = N/2$, we have $\omega = \pi N/T$, $t_j = jT/N$ (t_0 can be set to zero without loss of generality, see sec. A.3.1) and $\tau = mT/2N\ m\epsilon\mathbb{Z}$ (since $\tan 2\omega\tau = 0$, eq. 7.2.2). Actually, eq. 7.2.1 is not defined at $\omega = \pi N/T$, but it can be continuously extended by using $\omega t_j = \pi j + \epsilon$ and taking the limit $\epsilon \to 0$. It then becomes (using $\sigma^2 = 1$ and $\overline{X} = 0$):

$$P_X = \lim_{\varepsilon\to 0}\frac{1}{2}\left[\frac{\left[\sum_{j=1}^{N} X_j\cos\left(\pi\left(j-m/2\right)+\epsilon\right)\right]^2}{\sum_{j=1}^{N}\cos^2\left(\pi\left(j-m/2\right)+\epsilon\right)} + \frac{\left[\sum_{j=1}^{N} X_j\sin\left(\pi\left(j-m/2\right)+\epsilon\right)\right]^2}{\sum_{j=1}^{N}\sin^2\left(\pi\left(j-m/2\right)+\epsilon\right)}\right] \tag{A.3.6}$$

Without loss of generality $m = 0$ can be used, so that

$$\begin{aligned} P_X &= \frac{1}{2}\left[\frac{\left[\sum_{j=1}^{N} X_j\,(-1)^j\right]^2}{N} + \lim_{\epsilon\to 0}\frac{\sin^2\epsilon\left[\sum_{j=1}^{N} X_j\,(-1)^j\right]^2}{N\sin^2\epsilon}\right] \\ &= \frac{1}{N}\left[\sum_{j=1}^{N} X_j\,(-1)^j\right]^2 \end{aligned} \tag{A.3.7}$$

which is in concordance with the classical definition.
Please note, that for any frequencies ω different from ω_k the proof may not hold.

[1] A nonzero $\overline{X}$ does not affect the classical periodogram (see end of A.3.3) and normalization on the variance is needed for both periodograms to have an exponential probability distribution with unity mean (see A.3.3).

A.3.3 Statistical distribution of the periodogram

This section is mainly a summary of appendix A of [150]. It is shown, that the Lomb-Scargle periodogram (as defined in eq. 7.2.1) possesses an exponential probability distribution in the case of independent (white) Gaussian noise. In fact, the requirement of this simple statistical distribution leads to the definition of the LS periodogram.
Starting with a generalization of the discrete Fourier transform (eq. 7.1.1)

$$FT_x(\omega) = \left(\sqrt{N/2}\right) \sum_{j=1}^{N} X_j \left[A \cos \omega t_j + iB \sin \omega t_j\right] \tag{A.3.8}$$

the corresponding periodogram becomes:

$$\begin{aligned} P_X(\omega) &= \frac{1}{N} \left|FT_X(\omega)\right|^2 \\ &= \frac{A^2}{2} \left(\sum_{j=1}^{N} X_j \cos \omega t_j\right)^2 + \frac{B^2}{2} \left(\sum_{j=1}^{N} X_j \sin \omega t_j\right)^2 \end{aligned} \tag{A.3.9}$$

In the case, that X is independent Gaussian noise with zero mean and variance σ^2, the quantity

$$C(\omega) = A \sum_{j=1}^{N} X_j \cos \omega t_j \tag{A.3.10}$$

is also normally distributed with zero mean and variance

$$\begin{aligned} \sigma_c^2 = \left\langle C(\omega)^2 \right\rangle &= A^2 \sum_{j=1}^{N} \sum_{k=1}^{N} \langle X_j X_k \rangle \cos \omega t_j \cos \omega t_k \\ &= A^2 N \sigma^2 \sum_{j=1}^{N} \cos^2 \omega t_j \end{aligned} \tag{A.3.11}$$

(the cross terms vanish since X is assumed to be independent). Similarly,

$$S(\omega) = A \sum_{j=1}^{N} X_j \sin \omega t_j \tag{A.3.12}$$

is normally distributed with zero mean and variance

$$\begin{aligned} \sigma_s^2 = \left\langle S(\omega)^2 \right\rangle &= A^2 \sum_{j=1}^{N} \sum_{k=1}^{N} \langle X_j X_k \rangle \sin \omega t_j \sin \omega t_k \\ &= A^2 N \sigma^2 \sum_{j=1}^{N} \sin^2 \omega t_j \, . \end{aligned} \tag{A.3.13}$$

The periodogram can now be written as the sum of squares of two normally distributed variables with zero mean and variances σ_c and σ_s:

$$P_X(\omega) = \frac{1}{2} \left[C^2(\omega) + S^2(\omega)\right] \, . \tag{A.3.14}$$

The random variable $Z = C^2(\omega)/\sigma_c^2 + S^2(\omega)/\sigma_s^2$ is therefore χ^2 -distributed with 2 degrees of freedom and its probability distribution is:

$$\mathcal{P}_Z(z) = (1/2)\exp(-z/2) \ . \tag{A.3.15}$$

For $\sigma_c = \sigma_s = \sigma$, eq. A.3.14 can be renormalized to σ^2 and thus obtains the exponential probability distribution:

$$\mathcal{P}(z < P_X(\omega) < z + \mathrm{d}z) = \exp(-z)\,\mathrm{d}z \tag{A.3.16}$$

(The factors 1/2 in eq. A.3.14 and A.3.15 cancel each other). With $\sigma_c = \sigma_s = \sigma$ eq. A.3.10 and A.3.12 yields:

$$A \propto \left(\sum_{j=1}^{N} \cos^2 \omega t_j\right)^{-1/2} \tag{A.3.17}$$

and

$$B \propto \left(\sum_{j=1}^{N} \sin^2 \omega t_j\right)^{-1/2} \tag{A.3.18}$$

The proportionality constants are fixed to unity by demanding conformity with the classical periodogram in the case of evenly spaced data (see also appendix A.3.2). The resulting periodogram is then:

$$P_X(\omega) = \frac{1}{2\sigma^2}\left[\frac{\left(\sum_{j=1}^{N} X_j \cos\omega t_j\right)^2}{\sum_{j=1}^{N}\cos^2\omega t_j} + \frac{\left(\sum_{j=1}^{N} X_j \sin\omega t_j\right)^2}{\sum_{j=1}^{N}\sin^2\omega t_j}\right] \ . \tag{A.3.19}$$

In case of data samples with non-zero mean μ, eq. A.3.11 and A.3.13 becomes:

$$\sigma_c^2 = \left\langle C(\omega)^2 \right\rangle = A^2 N\sigma^2 \sum_{j=1}^{N} \cos^2\omega t_j - \left(\mu \sum_{j=1}^{N} \cos\omega t_j\right)^2 \tag{A.3.20}$$

$$\sigma_s^2 = \left\langle S(\omega)^2 \right\rangle = B^2 N\sigma^2 \sum_{j=1}^{N} \sin^2\omega t_j - \left(\mu \sum_{j=1}^{N} \sin\omega t_j\right)^2 \tag{A.3.21}$$

For even data spacing ($t_j = t_0 + j\frac{T}{N}$; $j = 1, ..., N$, T denotes the covered time range) and for the set of frequencies $\omega = \omega_k = 2\pi\frac{k}{T}$, $k = 1, ..., N/2$ the terms $\sum_{j=1}^{N}\cos\omega_k t_j$ and $\sum_{j=1}^{N}\sin\omega_k t_j$ are zero (proof by replacing $2 \to 1$ and $4 \to 2$ in eq. A.2.2), but for uneven data spacing these terms spoil the exponential probability distribution[2]. The solution to this problem is to replace X_j by $X_j - \overline{X}$. Since adding a phase term τ in eq. A.3.8 does not affect the calculations, the proof is completed. The special form of the τ can be derived from least squares analysis as presented in [98].

[2] If one does not want to deal with 4th order cos and sin terms in eq. A.3.9.

A.4 Mean and variance of the log-likelihood function for the shot noise model

The mean and variance of the (maximized) log-likelihood function can be calculated under the assumption of an exponential *probability density function* PDF (the parameter i marks the M different test frequencies):

$$f(z_i) = \frac{1}{\mu_i} \exp(-z_i/\mu_i) \ . \tag{A.4.1}$$

The shape of the mean values μ_i might be given (according to the shot noise model with Gaussian type flares) as:

$$\mu_i = A \cdot \exp\left(-\omega_i^2 \sigma^2\right) + C \tag{A.4.2}$$

(see sec. 7.3 for details). The log-likelihood function is then defined by [38]:

$$l := \log L = log \prod_{i=1}^{M} f(z_i) = \sum_{i=1}^{M} \left(\log \frac{1}{\mu_i} - \frac{z_i}{\mu_i} \right) \tag{A.4.3}$$

The calculation of the mean $E[l]$ and variance $V[l] = E[l^2] - E[l]^2$ is now straight forward:

$$\begin{aligned} E[l] &= -\sum_{i=1}^{M} \left(\log \mu_i + \frac{1}{\mu_i} E[z_i] \right) \\ &= -\left(M + \sum_{i=1}^{M} \log \mu_i \right) \end{aligned} \tag{A.4.4}$$

$$\begin{aligned} E\left[l^2\right] &= \sum_{i=1}^{M} \sum_{j=1}^{M} E\left[\left(\log \mu_i + \frac{z_i}{\mu_i} \right) \left(\log \mu_j + \frac{z_j}{\mu_j} \right) \right] \\ &= \sum_{i=1}^{M} \sum_{j=1}^{M} \left(\log \mu_i \log \mu_j + \log \mu_i \frac{1}{\mu_j} E[z_j] + \log \mu_j \frac{1}{\mu_i} E[z_i] + \frac{1}{\mu_i \mu_j} E[z_i z_j] \right) \\ &= \sum_{i=1}^{M} \sum_{j=1}^{M} \left(\log \mu_i \log \mu_j + \frac{1}{\mu_i \mu_j} E[z_i z_j] \right) + 2M \sum_{i=1}^{M} \log \mu_i \end{aligned} \tag{A.4.5}$$

In case $i \neq j$ the two random numbers z_i and z_j are independent and the joint PDF is the product of the individual PDFs [25, p. 28]. We therefore have

$$\frac{1}{\mu_i \mu_j} E[z_i z_j] = \frac{1}{\mu_i \mu_j} E[z_i] \, E[z_j] = 1 \ . \tag{A.4.6}$$

If $i = j$:

$$\frac{1}{\mu_i^2} E[z_i z_i] = \frac{1}{\mu_i^2} \int_0^\infty z_i^2 f(z_i) \, \mathrm{d}z_i = \int_0^\infty \frac{z_i^2}{\mu_i^2} \exp(-z_i/\mu_i) \frac{\mathrm{d}z_i}{\mu_i} = 2 \ . \tag{A.4.7}$$

The 2nd algebraic moment $E[l^2]$ then becomes:

$$E\left[l^2\right] = \sum_{i=1}^{M} \sum_{j=1}^{M} \log \mu_i \log \mu_j + 2M \sum_{i=1}^{M} \log \mu_i + M(M-1) + 2M \tag{A.4.8}$$

and the variance of the log-likelihood function is $V[l] = E[l^2] - E[l]^2 = M$.

B. MKN 501 DIURNAL INTEGRAL FLUX VALUES ABOVE 1.5 TEV

The Mkn 501 diurnal flux values above 1.5 TeV as measured by CT1 (only statistical flux errors given)

MJD[a]	$F\,(E > 1.5\ \mathrm{TeV})^{b}$	Δt^{c}	HV[d]	MJD[a]	$F\,(E > 1.5\ \mathrm{TeV})^{b}$	Δt^{c}	HV[d]
517.1899	1.62 ± 0.41	2.49	NOM06	565.1313	1.16 ± 0.39	4.00	HV06
518.1843	1.94 ± 0.48	2.00	NOM06	565.9881	0.65 ± 1.95	1.00	NOM06
519.1399	0.93 ± 0.57	2.00	NOM06	566.1169	1.92 ± 0.47	3.99	HV06
520.1771	1.98 ± 0.41	2.88	NOM06	567.1515	1.19 ± 0.48	2.99	HV06
521.1746	2.07 ± 0.37	3.48	NOM06	568.0377	1.18 ± 0.34	2.49	NOM00
522.1709	0.78 ± 0.27	3.50	NOM06	568.1509	1.84 ± 0.47	2.82	HV06
523.1748	1.94 ± 0.34	3.99	NOM06	569.0643	1.57 ± 0.36	2.32	NOM00
525.2082	1.42 ± 0.47	1.66	NOM06	569.1650	1.42 ± 0.44	2.16	HV06
526.1481	3.75 ± 2.01	1.00	HV10	570.0712	0.84 ± 0.24	3.50	NOM00
526.2175	1.86 ± 0.50	1.66	NOM06	570.1781	1.01 ± 0.69	1.33	HV06
527.2310	0.81 ± 0.58	0.92	NOM06	571.0869	1.93 ± 0.26	4.25	NOM00
528.2050	2.72 ± 1.62	0.75	HV10	571.1917	1.59 ± 1.03	0.66	HV06
528.2395	2.01 ± 1.27	0.42	NOM06	572.1026	3.88 ± 0.35	5.00	NOM00
536.1538	3.20 ± 0.81	2.99	HV10	573.0997	1.80 ± 0.26	4.75	NOM00
537.1659	1.46 ± 0.64	3.28	HV10	574.0821	1.98 ± 0.23	6.49	NOM00
539.1724	3.60 ± 0.77	2.82	HV10	575.0885	3.73 ± 0.32	5.99	NOM00
540.1144	3.27 ± 0.77	1.50	NOM06	576.0825	6.31 ± 0.45	5.83	NOM00
540.1890	1.81 ± 0.57	1.83	HV06	577.0806	5.02 ± 0.38	6.15	NOM00
545.2053	0.33 ± 0.36	1.25	NOM06	578.0801	4.49 ± 0.35	6.33	NOM00
546.1545	1.25 ± 0.29	3.66	NOM06	578.9602	15.48 ± 5.02	0.50	HV06
547.1279	0.87 ± 0.21	5.39	NOM06	579.0774	5.46 ± 0.43	4.98	NOM00
548.1288	2.28 ± 0.31	5.23	NOM06	579.9669	8.39 ± 1.50	1.91	HV06
549.1264	1.81 ± 0.29	5.40	NOM06	580.1084	4.52 ± 0.35	4.25	NOM00
550.1131	2.12 ± 0.39	2.99	NOM06	582.0472	2.83 ± 1.65	0.49	HV06
551.0212	7.70 ± 3.15	1.00	HV06	582.0904	2.55 ± 0.51	1.16	NOM00
551.1127	7.49 ± 0.71	3.24	NOM06	583.0032	4.90 ± 0.70	3.99	HV06
552.0352	4.19 ± 1.32	1.66	HV06	583.1444	5.62 ± 0.47	2.70	NOM00
552.1501	4.20 ± 0.45	3.66	NOM06	584.0444	5.94 ± 1.19	1.29	HV06
553.0705	4.79 ± 1.49	0.99	HV06	584.1812	3.05 ± 0.65	0.99	NOM00
553.1180	4.16 ± 0.92	1.00	NOM06	595.1070	1.67 ± 0.58	2.00	HV06
555.1850	5.41 ± 0.70	1.66	NOM06	597.9936	0.72 ± 0.44	0.99	NOM00
558.1742	3.62 ± 0.87	2.27	HV10	600.0898	1.10 ± 0.33	1.49	NOM00
559.1661	5.04 ± 1.52	0.94	HV10	601.1110	2.18 ± 0.35	2.50	NOM00
560.1620	3.92 ± 1.23	2.74	HV16	602.1017	2.48 ± 0.44	1.50	NOM00
563.1273	0.93 ± 0.57	4.30	HV14	603.1197	4.56 ± 0.45	3.50	NOM00
564.1199	4.12 ± 0.64	4.32	HV10	604.1314	4.20 ± 0.46	2.99	NOM00

MJD[a]	$F\,(E>1.5)^{b}$	Δt^{c}	HV[d]	MJD[a]	$F\,(E>1.5)^{b}$	Δt^{c}	HV[d]
605.1136	3.49 ± 0.40	3.50	NOM00	642.9653	7.23 ± 0.90	2.33	HV06
607.1286	5.65 ± 0.57	2.49	NOM00	643.0575	6.78 ± 1.44	0.66	HV00
610.1253	1.71 ± 0.31	2.49	NOM00	643.0956	6.43 ± 1.57	0.90	NOM00
611.0015	1.50 ± 0.52	1.00	HV00	643.9883	2.87 ± 0.52	3.63	HV06
611.0581	0.96 ± 0.34	1.49	NOM00	644.1039	2.00 ± 4.01	0.38	NOM00
612.0249	2.49 ± 0.41	2.00	HV00	650.9280	3.59 ± 0.68	2.00	HV06
612.1226	3.64 ± 0.47	2.50	NOM00	650.9953	0.27 ± 1.24	0.99	HV10
613.0607	8.97 ± 0.95	1.00	HV00	651.0331	3.01 ± 5.79	0.65	HV14
613.1365	7.46 ± 0.72	2.50	NOM00	651.9125	1.54 ± 0.77	0.41	NOM00
615.9310	0.54 ± 2.87	0.99	HV14	651.9258	2.40 ± 0.47	1.37	HV00
615.9849	2.39 ± 1.03	1.32	HV10	652.0003	2.68 ± 0.75	1.66	HV06
616.0734	2.76 ± 0.71	1.99	HV06	653.9432	1.49 ± 0.45	1.00	NOM00
616.9660	0.24 ± 0.71	2.63	HV14	654.9364	0.95 ± 0.42	1.00	NOM00
617.0753	1.09 ± 0.76	1.66	HV10	655.0508	-0.27 ± 0.73	1.49	HV06
617.9806	-0.21 ± 1.07	3.26	HV16	656.0619	1.26 ± 2.29	0.50	HV00
622.9270	6.25 ± 0.94	0.83	NOM00	657.0603	2.95 ± 1.79	0.50	NOM00
623.0263	6.43 ± 0.72	2.99	HV06	657.9867	2.10 ± 0.30	3.49	NOM00
624.0328	2.09 ± 0.56	2.32	HV06	658.9802	0.48 ± 0.17	4.00	NOM00
624.9534	2.14 ± 0.43	1.33	NOM00	659.9806	1.10 ± 0.22	3.99	NOM00
625.0559	2.08 ± 0.74	1.66	HV06	660.9710	1.38 ± 0.26	3.49	NOM00
625.9763	10.64 ± 0.80	1.50	NOM00	661.9684	1.62 ± 0.30	3.50	NOM00
626.0535	9.97 ± 1.62	0.99	HV06	662.9680	2.45 ± 0.32	3.49	NOM00
626.9929	7.38 ± 0.51	2.50	NOM00	663.9696	5.77 ± 0.51	3.50	NOM00
627.0894	7.41 ± 1.01	1.00	HV00	664.9476	1.56 ± 0.30	2.50	NOM00
628.0832	6.11 ± 1.40	0.50	NOM00	665.9414	1.28 ± 0.37	1.50	NOM00
629.0035	1.35 ± 0.31	2.00	NOM00	666.9327	2.01 ± 0.52	1.00	NOM00
629.9895	1.00 ± 0.28	1.84	NOM00	667.9146	6.53 ± 1.30	0.83	HV06
632.9870	0.63 ± 0.26	2.00	NOM00	667.9436	4.78 ± 1.13	0.50	NOM00
634.0065	0.71 ± 0.21	3.00	NOM00	668.9247	1.36 ± 0.58	1.50	HV06
635.0109	1.72 ± 0.28	3.00	NOM00	669.9333	4.33 ± 0.91	1.49	HV06
636.0078	0.06 ± 0.19	2.50	NOM00	670.9271	0.41 ± 0.64	1.50	HV06
636.9104	1.76 ± 1.10	0.33	HV00	671.9428	2.90 ± 0.68	2.49	HV06
636.9945	0.65 ± 0.21	3.00	NOM00	672.9512	1.25 ± 0.54	3.00	HV06
637.9447	0.57 ± 0.45	0.83	HV00	681.8733	1.15 ± 0.82	0.50	HV00
638.0325	1.57 ± 0.40	1.49	NOM00	681.9051	1.93 ± 0.56	1.00	NOM00
638.9353	5.74 ± 0.79	0.99	HV00	682.8691	9.86 ± 2.13	0.50	HV06
639.0244	5.35 ± 0.49	3.00	NOM00	683.8735	7.94 ± 1.39	0.50	HV00
639.9390	5.04 ± 1.43	0.65	HV06	683.9056	6.57 ± 0.89	1.00	NOM00
639.9761	4.67 ± 0.71	1.00	HV00	684.8702	1.17 ± 0.76	0.50	HV00
640.0601	4.19 ± 0.48	3.19	NOM00	684.9262	2.75 ± 0.45	2.25	NOM00
640.9488	5.83 ± 0.95	1.33	HV06	685.8719	0.33 ± 0.68	0.50	HV00
641.0103	3.86 ± 0.88	0.67	HV00	685.9134	0.27 ± 0.29	1.50	NOM00
641.0696	2.25 ± 0.47	2.14	NOM00	686.8685	1.28 ± 1.07	0.33	HV00
641.9562	3.65 ± 0.75	1.98	HV06	686.8970	0.44 ± 0.38	0.99	NOM00
642.0417	2.04 ± 1.37	0.33	HV00	687.8675	1.54 ± 1.06	0.33	HV00
642.0802	2.81 ± 0.71	1.50	NOM00	687.9154	2.13 ± 0.40	2.00	NOM00

MJD[a]	$F\,(E>1.5)^b$	Δt^c	HV[d]	MJD[a]	$F\,(E>1.5)^b$	Δt^c	HV[d]
688.8683	1.24 ± 1.25	0.33	HV00	706.8616	-0.83 ± 3.41	0.65	HV14
688.9165	0.62 ± 0.31	2.00	NOM00	708.8502	1.26 ± 2.26	0.33	HV06
689.8678	-0.05 ± 1.25	0.3	HV00	708.8938	0.02 ± 2.83	1.31	HV14
689.8902	1.16 ± 0.82	0.50	NOM00	709.8547	0.19 ± 0.62	0.66	NOM00
691.8663	2.26 ± 1.18	0.33	HV00	709.8808	0.85 ± 1.25	0.50	HV00
691.9196	1.67 ± 0.40	2.16	NOM00	709.9021	1.65 ± 4.86	0.33	HV06
692.9082	0.57 ± 0.46	1.00	NOM00	712.8795	1.84 ± 0.53	1.66	NOM00
693.8645	0.51 ± 1.23	0.33	HV00	713.8781	0.76 ± 0.34	1.99	NOM00
693.8913	0.12 ± 0.55	0.83	NOM00	716.8796	0.55 ± 0.78	1.00	NOM00
694.8635	2.27 ± 1.13	0.33	HV00	717.8677	0.24 ± 0.58	1.00	NOM00
694.9142	1.88 ± 0.41	1.99	NOM00	719.8425	4.40 ± 1.75	0.32	HV00
695.8656	5.21 ± 1.43	0.33	HV00	719.8695	4.19 ± 1.07	1.00	NOM00
695.9113	3.19 ± 0.54	1.83	NOM00	720.8684	6.66 ± 1.31	1.00	NOM00
696.8797	0.30 ± 0.39	1.00	HV00	721.8409	1.99 ± 1.50	0.33	HV00
696.9215	0.49 ± 0.55	1.00	NOM00	721.8679	1.46 ± 0.78	1.00	NOM00
697.8879	0.21 ± 0.34	1.50	HV00	722.8648	1.79 ± 0.86	0.99	NOM00
700.8942	1.21 ± 0.75	1.50	HV06	728.8541	0.98 ± 3.78	0.50	HV06
701.8833	1.74 ± 0.82	1.49	HV06	730.8489	-0.51 ± 1.34	0.99	HV06
703.8813	1.09 ± 2.25	1.49	HV14	731.8544	-0.75 ± 2.05	0.99	HV06
705.8938	1.51 ± 2.45	1.49	HV14	732.8525	-1.09 ± 1.67	1.00	HV06

[a] MJD + 50000

[b] in $(10^{-11}\,\mathrm{cm}^{-2}\mathrm{s}^{-1})$

[c] observation time in hours

[d] moon (HVxx) and no-moon (NOMxx) data, xx denotes the HV reduction

BIBLIOGRAPHY

[1] F. Aharonian, A. Akhperjanian, J. Barrio et al. *The TeV Energy Spectrum of Markarian 501 Measured with the Stereoscopic Telescope System of HEGRA during 1998 and 1999*. Astrophysical Journal, **546**: 898–902, January 2001.

[2] F. Aharonian, A. G. Akhperjanian, J. A. Barrio et al. *The temporal characteristics of the TeV gamma -emission from MKN 501 in 1997. II. Results from HEGRA CT1 and CT2*. Astronomy and Astrophysics, **349**: 29–44, September 1999.

[3] F. A. Aharonian, A. G. Akhperjanian, J. A. Barrio et al. *The temporal characteristics of the TeV gamma-radiation from MKN 501 in 1997. I. Data from the stereoscopic imaging atmospheric Cherenkov telescope system of HEGRA*. Astronomy and Astrophysics, **342**: 69–86, February 1999.

[4] F. A. Aharonian, A. G. Akhperjanian, J. A. Barrio et al. *The time averaged TeV energy spectrum of MKN 501 of the extraordinary 1997 outburst as measured with the stereoscopic Cherenkov telescope system of HEGRA*. Astronomy and Astrophysics, **349**: 11–28, September 1999.

[5] F. A. Aharonian, A. G. Akhperjanian, J. A. Barrio et al. *The Energy Spectrum of TeV Gamma Rays from the Crab Nebula as Measured by the HEGRA System of Imaging Air Cerenkov Telescopes*. Astrophysical Journal, **539**: 317–324, August 2000.

[6] F. A. Aharonian, A. G. Akhperjanian, J. A. Barrio et al. *Evidence for TeV gamma ray emission from Cassiopeia A*. Astronomy and Astrophysics, **to be submitted**, 2001.

[7] F. A. Aharonian and H. E. S. S. Collaboration. *H.E.S.S.- The High Energy Stereoscopic System*. AAS/High Energy Astrophysics Division, **32**: 4311+, October 2000.

[8] F. A. Aharonian, W. Hofmann, A. K. Konopelko et al. *The potential of ground based arrays of imaging atmospheric Cherenkov telescopes. I. Determination of shower parameters*. Astroparticle Physics, **6**: 343–368, March 1997.

[9] O. C. Allkofer and P. K. F. Grieder. *Cosmic Rays on Earth*. Physics Data, Fachinformationszentrum Energie Physic Mathematik Karlsruhe, **25-1**, 1984.

[10] M. Amenomori, S. Ayabe, P. Y. Cao et al. *Detection of Multi-TeV Gamma Rays from Markarian 501 during an Unforeseen Flaring State in 1997 with the Tibet Air Shower Array*. Astrophysical Journal, **532**: 302–307, March 2000.

[11] R. Antonucci. *Unified models for active galactic nuclei and quasars*. Annual Review of Astronomy and Astrophysics, **31**: 473–521, 1993.

[12] A. Barrau. *Astrophysique gamma de tres haute energie: etude du noyau actif de galaxie Mrk 501 et implications cosmologiques*. Ph.D. thesis, Universite de Grenoble, 1998.

[13] J. A. Barrio, G. Blanchot, H. Börst et al. *The Magic Telescope*. Technical Report MPI-PhE/98-5, Max-Planck-Institut für Physik (Werner-Heisenberg-Institut), March 1998.

[14] W. Bednarek and R. J. Protheroe. *Gamma-rays from interactions of stars with active galactic nucleus jets*. Monthly Notices of the Royal Astronomical Society, **287**: L9–L13, May 1997.

[15] W. Bednarek and R. J. Protheroe. *Modulation of AGN gamma-rays by interaction with X-rays from an accretion disc hotspot*. Monthly Notices of the Royal Astronomical Society, **290**: 139–144, September 1997.

[16] W. Bednarek and R. J. Protheroe. *The physical parameters of Markarian 501 during flaring activity*. Monthly Notices of the Royal Astronomical Society, **310**: 577–584, December 1999.

[17] J. S. Bendat. *Principles and Applications of Random Noise Theory*. John Wiley & Sons, 1958.

[18] S. D. Biller, J. Buckley, A. Burdett et al. *New Limits to the Infrared Background: Bounds on Radiative Neutrino Decay and on Contributions of Very Massive Objects to the Dark Matter Problem*. Physical Review Letters, **80**: 2992–2995, April 1998.

[19] R. D. Blandford and J. P. Ostriker. *Particle acceleration by astrophysical shocks*. Astrophysical Journal Letters, **221**: L29–L32, April 1978.

[20] S. D. Bloom and A. P. Marscher. *An Analysis of the Synchrotron Self-Compton Model for the Multi–Wave Band Spectra of Blazars*. Astrophysical Journal, **461**: 657+, April 1996.

[21] R. K. Bock and A. Vasilescu. *The Particle Detector BriefBook*. Springer-Verlag Berlin Heidelberg, 1998.

[22] M. Böttcher. *Zeitabhängiger Strahlungstransport in Jets von aktiven galaktischen Kernen*. Ph.D. thesis, Rheinische Friedrich-Wilhelms-Universität Bonn, January 1997.

[23] S. M. Bradbury, T. Deckers, D. Petry et al. *Detection of γ-rays above 1.5TeV from MKN 501*. Astronomy and Astrophysics, **320**: L5–L8, April 1997.

[24] H. V. Bradt, R. E. Rothschild and J. H. Swank. *X-ray timing explorer mission*. Astronomy and Astrophysics, Supplement Series, **97**: 355–360, January 1993.

[25] S. Brandt. *Data Analysis*. Springer-Verlag Berlin Heidelberg, 3 edition, 1998.

[26] K. A. Brownlee. *Statistical Theory and Methodology in Science and Engineering*. John Wiley & Sons, 2 edition, 1965.

[27] J. H. Buckley, C. W. Akerlof, S. Biller et al. *Gamma-Ray Variability of the BL Lacertae Object Markarian 421*. Astrophysical Journal Letters, **472**: L9+, November 1996.

[28] P. Carruthers and M. Duong-van. Physics Letters B, **41**: 597+, 1972.

[29] M. Catanese, C. W. Akerlof, H. M. Badran et al. *Discovery of Gamma-Ray Emission above 350 GeV from the BL Lacertae Object 1ES 2344+514*. Astrophysical Journal, **501**: 616+, July 1998.

[30] M. Catanese, S. M. Bradbury, A. C. Breslin et al. *Multiwavelength Observations of a Flare from Markarian 501*. Astrophysical Journal Letters, **487**: L143+, October 1997.

[31] P. M. Chadwick, M. K. Daniel, K. Lyons et al. *VHE gamma ray observations of Centaurus X-3*. Astronomy and Astrophysics, **364**: 165–169, December 2000.

[32] P. M. Chadwick, M. R. Dickinson, N. A. Dipper et al. *TeV gamma rays from PSR 1706-44*. Astroparticle Physics, **9**: 131–136, August 1998.

[33] P. M. Chadwick, K. Lyons, T. J. L. McComb et al. *Very High Energy Gamma Rays from PKS 2155-304*. Astrophysical Journal, **513**: 161–167, March 1999.

[34] P. Cherenkov. Dokl. Akad. Nauk, SSSR, **2**: 451, 1934.

[35] G. Colla, C. Fanti, R. Fanti et al. *The B2 Catalogue of radio sources - second part*. Astronomy and Astrophysics, Supplement Series, **7**: 1+, September 1972.

[36] J. E. Conway and J. M. Wrobel. *A helical jet in the orthogonally misaligned BL Lacertae object Markarian 501 (B1652 + 398)*. Astrophysical Journal, **439**: 98–112, January 1995.

[37] P. S. Coppi and F. A. Aharonian. *Constraints on the Very High Energy Emissivity of the Universe from the Diffuse GeV Gamma-Ray Background*. Astrophysical Journal Letters, **487**: L9+, September 1997.

[38] G. Cowan. *Statistical Data Analysis*. Clarendon Press, Oxford, 1998.

[39] CRC. *Handbook of Chemistry and Physics*. CRC Press, 77 edition, 1996.

[40] A. Dar and A. Laor. *Hadronic Production of TeV Gamma-Ray Flares from Blazars*. Astrophysical Journal Letters, **478**: L5+, March 1997.

[41] A. Daum, G. Hermann, M. Hess et al. *First results on the performance of the HEGRA IACT array*. Astroparticle Physics, **8**: 1–2, December 1997.

[42] B. Dawson and A. Smith. *Hybrid Operation Under Moonlight*. Technical Report GAP-96-034, University of Adelaide, October 1996.

[43] O. C. de Jager, F. W. Stecker and M. H. Salamon. *Estimate of the Intergalactic Infrared Radiation Field from Gamma-Ray Observations of the Galaxy Markarian 421*. Nature, **369**: 294+, May 1994.

[44] T. Deckers. *Messung von hochenergetischer γ-Strahlung aus der Richtung des Krebsnebels und der aktiven Galaxie Markarian 501 mit einem Cherenkov-Teleskop*. Ph.D. thesis, Christian-Albrechts-Universität Kiel, 1997.

[45] O. C. deJager, D. Kranich, E. Lorenz et al. *Central black hole mass estimates for Mkn 501 from shot noise-like X-ray and TeV flares during 1997*. In *26th International Cosmic Ray Conference (Salt Lake City)*, volume 3, pages 346+, 1999.

[46] C. D. Dermer. *Variability in blazars*. Astroparticle Physics, **11**: 1–2, June 1999.

[47] C. D. Dermer and R. Schlickeiser. *Model for the High-Energy Emission from Blazars*. Astrophysical Journal, **416**: 458+, October 1993.

[48] C. D. Dermer, S. J. Sturner and R. Schlickeiser. *Nonthermal Compton and Synchrotron Processes in the Jets of Active Galactic Nuclei*. Astrophysical Journal Supplement, **109**: 103+, March 1997.

[49] A. Djannati-Ataı , F. Piron, A. Barrau et al. *Very High Energy Gamma-ray spectral properties of MKN 501 from CAT Cherenkov telescope observations in 1997*. Astronomy and Astrophysics, **350**: 17–24, October 1999.

[50] M. Dopita. *Towards a truly unified model of AGN: Aspect, accretion and evolution*. Publications of the Astronomical Society of Australia, **14**: 230–245, November 1997.

[51] S. S. Eikenberry, K. Matthews, E. H. Morgan et al. *Evidence for a Disk-Jet Interaction in the Microquasar GRS 1915+105*. Astrophysical Journal Letters, **494**: L61+, February 1998.

[52] J. L. Elliot and S. L. Shapiro. *On the Variability of the Compact Nonthermal Sources*. Astrophysical Journal Letters, **192**: L3+, August 1974.

[53] R. P. Fender and G. G. Pooley. *Infrared synchrotron oscillations in GRS 1915+105*. Monthly Notices of the Royal Astronomical Society, **300**: 573–576, October 1998.

[54] E. J. Fenyves, S. N. Balog, N. R. Davis et al. *Electromagnetic component of* $10^{14}-10^{16}$ eV *air showers*. Physical Review D, **37**: 649–656, February 1988.

[55] L. Ferrarese, H. C. Ford and W. Jaffe. *Evidence for a Massive Black Hole in the Active Galaxy NGC 4261 from Hubble Space Telescope Images and Spectra*. Astrophysical Journal, **470**: 444+, October 1996.

[56] C. E. Fichtel, D. L. Bertsch, J. Chiang et al. *The first energetic gamma-ray experiment telescope (EGRET) source catalog*. Astrophysical Journal Supplement, **94**: 551–581, October 1994.

[57] I. Frank and I. Tamm. Dokl. Akad. Nauk, SSSR, **14(3)**: 109+, 1937.

[58] H. Frauenfelder and E. M. Henley. *Teilchen und Kerne*. Oldenbourg, 1987.

[59] U. Fritze v.-Alvensleben. In C. Leitherer et al. (editors), *ASP Conf. Ser. 98: From Stars to Galaxies*, pages 496+, 1996.

[60] T. K. Gaisser. *Cosmic Rays and Particle Physics*. Cambridge University Press, 1990.

[61] K. Gebhardt, J. Kormendy, L. C. Ho et al. *Black Hole Mass Estimates from Reverberation Mapping and from Spatially Resolved Kinematics*. Astrophysical Journal Letters, **543**: L5–L8, November 2000.

[62] G. Ghisellini. *Extreme Synchroton Blazars: the Case of MKN 501*. In *The Active X-ray Sky: Results from BeppoSAX and RXTE*, pages 397+, 1998.

[63] G. Giovannini and et al. *VLBI Observations of Mrk421 and Mrk501*. In *ASP Conf. Ser. 159: BL Lac Phenomenon*, pages 439+, 1999.

[64] K. Greisen. Prog. Cosmic Ray Physics, **3**: 1+, 1956.

[65] K. Greisen. Annual Review of Nuclear Science, **10**: 63+, 1960.

[66] U. Grenander and M. Rosenblatt. *Statistical Analysis of Stationary Time Series*. Almqvist & Wiksell, 1956.

[67] C. group. *Minuit users guide, Program Library D506*. CERN, 1994.

[68] D. E. Gruber, P. R. Blanco, W. A. Heindl et al. *The high energy X-ray timing experiment on XTE*. Astronomy and Astrophysics, Supplement Series, **120**: C641+, December 1996.

[69] R. C. Hartman, D. L. Bertsch, S. D. Bloom et al. *The Third EGRET Catalog of High-Energy Gamma-Ray Sources*. Astrophysical Journal Supplement, **123**: 79–202, July 1999.

[70] N. Hayashida, H. Hirasawa, F. Ishikawa et al. *Observations of TeV Gamma Ray Flares from Markarian 501 with the Telescope Array Prototype*. Astrophysical Journal Letters, **504**: L71+, September 1998.

[71] HEGRA Collaboration, A. Konopelko, F. Aharonian et al. *Detection of gamma rays above 1 TeV from the Crab Nebula by the second HEGRA imaging atmospheric Cherenkov telescope at La Palma*. Astroparticle Physics, **4**: 199–215, February 1996.

[72] W. Heitler. *The Quantum Theory of Radiation*. Oxford University Press, 1960.

[73] G. Henri, G. Pelletier, P. O. Petrucci et al. *Active galactic nuclei as high energy engines*. Astroparticle Physics, **11**: 347–356, July 1999.

[74] A. M. Hillas. In *17th International Cosmic Ray Conference (Paris)*, volume 8, pages 193+, 1981.

[75] A. M. Hillas. *Cerenkov light images of EAS produced by primary gamma*. In *NASA. Goddard Space Flight Center 19th Intern. Cosmic Ray Conf., Vol. 3 p 445-448 (SEE N85-34862 23-93)*, volume 3, pages 445–448, August 1985.

[76] A. M. Hillas. *Differences between Gamma-Ray and Hadronic Showers*. Space Science Review, **75**: 17–30, January 1996.

[77] A. M. Hillas. *Initial modeling of TeV spectra observed at the Whipple Observatory*. Astroparticle Physics, **11**: 27–34, June 1999.

[78] R. Hillier. *Gamma Ray Astronomy*. Clarendon Press, Oxford, 1984.

[79] S. Inoue and F. Takahara. *Electron Acceleration and Gamma-Ray Emission from Blazars*. Astrophysical Journal, **463**: 555+, June 1996.

[80] J. D. Jackson. *Klassische Elektrodynamik*. Walter de Gruyter, 2 edition, 1983.

[81] J. V. Jelley. *Cherenkov radiation and its applications*. Pergamon Press, 1958.

[82] A. Karle. *Entwicklung eines neuartigen atmosphärischen Tscherenkovdetektors und Messungen an hochenergetischer Kosmischer Strahlung zwischen 15 und 1000 TeV*. Ph.D. thesis, Ludwig-Maximilians-Universität München, June 1994. MPI-PhE/94-17.

[83] J. Kataoka, J. R. Mattox, J. Quinn et al. *High-Energy Emission from the TeV Blazar Markarian 501 during Multiwavelength Observations in 1996*. Astrophysical Journal, **514**: 138–147, March 1999.

[84] A. K. Kembhavi and J. V. Narlikar. *Quasars and Active Galactic Nuclei*. Cambridge University Press, 1999.

[85] M. Kestel. *The TeV γ-Emission of the AGN Mkn 421 in 1999/2000 as observed with the HEGRA Cherenkov Telescope CT1*. Ph.D. thesis, Technische Universität München, 2001.

[86] R. Khanna and M. Camenzind. *The gravitomagnetic dynamo effect in accretion disks of rotating black holes*. Astrophysical Journal Letters, **435**: L129–L132, November 1994.

[87] T. Kifune, T. Tanimori, S. Ogio et al. *Very high energy gamma rays from PSR 1706-44*. Astrophysical Journal Letters, **438**: L91–L94, January 1995.

[88] J. G. Kirk and A. Mastichiadis. *Variability patterns of synchrotron and inverse Compton emission in blazars*. Astroparticle Physics, **11**: 45–48, June 1999.

[89] D. Kranich. *Verbesserung der Gamma/Hadron-Trennung in der Hochenergie Gamma-Astronomie mit Cherenkov Teleskopen*, April 1997. Diplomarbeit, MPI-PhE/97-11.

[90] D. Kranich, O. C. deJager, M. Kestel et al. *Evidence for a QPO structure in the TeV and X-ray light curve during the 1997 high state γ emission of Mkn 501*. In *26th International Cosmic Ray Conference (Salt Lake City)*, volume 3, pages 358+, 1999.

[91] D. Kranich, R. Mirzoyan, D. Petry et al. *TeV gamma-ray observations of the Crab and MKN 501 during moonshine and twilight*. Astroparticle Physics, **12**: 65–74, October 1999.

[92] H. Krawczynski, P. S. Coppi, T. Maccarone et al. *X-ray/TeV-gamma-ray observations of several strong flares of Mkn 501 during 1997 and implications*. Astronomy and Astrophysics, **353**: 97–107, January 2000.

[93] F. Krennrich. *Beobachtung von TeV-Photonen aus der Richtung des Krebsnebels mit dem 5 m^2-Tscherenkovteleskop des HEGRA-Detektors*. Ph.D. thesis, Ludwig-Maximilians-Universität München, October 1995. MPI-PhE/96-03.

[94] A. Krys, E. Krys and A. Wasilewski. *High-energy photoproduction in air showers*. Journal of Physics G, **17**: 1261–1269, August 1991.

[95] R. W. Lessard. *VERITAS: the Very Energetic Radiation Imaging Telescope Array System*. Astroparticle Physics, **11**: 243–246, June 1999.

[96] A. M. Levine, H. Bradt, W. Cui et al. *First Results from the All-Sky Monitor on the Rossi X-Ray Timing Explorer*. Astrophysical Journal Letters, **469**: L33+, September 1996.

[97] T. Li and Y. Ma. *Analysis methods for results in gamma-ray astronomy*. Astrophysical Journal, **272**: 317–324, September 1983.

[98] N. R. Lomb. *Least-squares frequency analysis of unequally spaced data*. Astrophysics and Space Science, **39**: 447–462, February 1976.

[99] M. S. Longair. *High Energy Astrophysics*, volume 1, Particles, Photons and their Detection. Cambridge University Press, 2 (1997) edition, February 1992.

[100] E. Lorenz and The MAGIC Collaboration. *The MAGIC Telescope Project*. In *GeV-TeV Gamma Ray Astrophysics Workshop : towards a major atmospheric Cherenkov detector*, pages 510+, 2000.

[101] D. J. Macomb, C. W. Akerlof, H. D. Aller et al. *Multiwavelength Observations of Markarian 421 During a TeV/X-Ray Flare: Erratum*. Astrophysical Journal Letters, **459**: L111+, March 1996.

[102] K. Mannheim. *The proton blazar*. Astronomy and Astrophysics, **269**: 67–76, March 1993.

[103] K. Mannheim and P. L. Biermann. *Gamma-ray flaring of 3C 279 - A proton-initiated cascade in the jet?*. Astronomy and Astrophysics, **253**: L21–L24, January 1992.

[104] K. Mannheim, S. Westerhoff, H. Meyer et al. *Beacons at the gamma ray horizon*. Astronomy and Astrophysics, **315**: 77–85, November 1996.

[105] L. Maraschi, G. Fossati, F. Tavecchio et al. *Correlated variability of MKN 421 at X-ray and TeV wavelengths on time scales of hours*. Astroparticle Physics, **11**: 189–192, June 1999.

[106] L. Maraschi, G. Ghisellini and A. Celotti. *A jet model for the gamma-ray emitting blazar 3C 279*. Astrophysical Journal Letters, **397**: L5–L9, September 1992.

[107] A. P. Marscher and W. K. Gear. *Models for high-frequency radio outbursts in extragalactic sources, with application to the early 1983 millimeter-to-infrared flare of 3C 273*. Astrophysical Journal, **298**: 114–127, November 1985.

[108] A. Mastichiadis and J. G. Kirk. *Models of variability in blazar jets*. In G. F. and G. Mannocchi (editors), *Frontier Objects in Astrophysics and Particle Physics (Vulcano 1998)*, March 1998.

[109] I. F. Mirabel, V. Dhawan, S. Chaty et al. *Accretion instabilities and jet formation in GRS 1915+105*. Astronomy and Astrophysics, **330**: L9–L12, February 1998.

[110] R. Mirzoyan, J. Fernandez, E. Lorenz et al. *A direct method of measuring the single photoelectron to ADC counts conversion factor for Cherenkov Telecopes and determination of the Telescope trigger threshold*. In C. Cresti (editor), *Towards a Major Atmospheric Cherenkov Detector IV (Padua)*, sep 1995.

[111] R. Mirzoyan, V. Fomin and A. Stepanian. *On the optical design of VHE gamma ray imaging Cherenkov telescopes*. In C. Cresti (editor), *Towards a Major Atmospheric Cherenkov Detector IV (Padua)*, sep 1995.

[112] R. Mirzoyan, R. Kankanian, P. Sawallisch et al. *The first Imaging Air Cherenkov Telescope of the HEGRA collaboration*. Nuclear Instruments and Methods, **A 351**: 513+, 1994.

[113] R. Mirzoyan and E. Lorenz. *Measurement of the Night Sky Light Background at La Palma*. Technical Report MPI-PhE/94-35, Max-Planck-Institut für Physik (Werner-Heisenberg-Institut), December 1994.

[114] R. Mirzoyan and E. Lorenz. *On the Calibration Accuracy of Light Sensors in Atmospheric Cherenkov, Fluorescence and Neutrino Experiments*. In *25th International Cosmic Ray Conference (Durban)*, volume 7, pages 265+, 1998.

[115] M. Mori. *Status of the CANGAROO-III Project*. In H. J. Voelk and F. Aharonian (editors), *to appear in the Proc. of the Heidelberg International Symposium on High Energy Gamma-Ray Astronomy*. AIP Conf. Proc, 2000.

[116] S. L. Mufson, D. J. Hutter, K. R. Hackney et al. *Coordinated multifrequency observations of the BL Lacertae objects MRK 180 and MRK 501*. Astrophysical Journal, **285**: 571–579, October 1984.

[117] H. Muraishi, T. Tanimori, S. Yanagita et al. *Evidence for TeV gamma-ray emission from the shell type SNR RX J1713.7-3946*. Astronomy and Astrophysics, **354**: L57–L61, February 2000.

[118] Y. I. Neshpor, A. A. Stepanyan, O. P. Kalekin et al. *Blazar 3C 66A: Another extragalactic source of ultra-high-energy gamma-ray photons*. Astronomy Letters, **24**: 134–138, March 1998.

[119] J. Nishimura and K. Kamata. Progress in Theoretical Physics, **7**: 185+, 1952.

[120] T. Nishiyama, N. Chamoto, M. Chikawa et al. *Detection of a new TeV gamma-ray source of BL Lac object 1ES 1959+650*. In *Proc. 26th ICRC (Salt Lake City), vol 3*, pages 370+, 1999.

[121] S. Oser, D. Bhattacharya, L. M. Boone et al. *High energy gamma-ray observations of the Crab Nebula and pulsar with the Solar Tower Atmospheric Cherenkov Effect Experiment*. Astrophysical Journal, **to be submitted**, 2001.

[122] P. Padovani and P. Giommi. *The connection between x-ray- and radio-selected BL Lacertae objects*. Astrophysical Journal, **444**: 567–581, May 1995.

[123] E. Pare et al. In *22th International Cosmic Ray Conference (Dublin)*, volume 1, pages 492+, 1991.

[124] T. J. Pearson, S. C. Unwin, M. H. Cohen et al. *Superluminal expansion of quasar 3C273*. Nature, **290**: 365–368, April 1981.

[125] B. M. Peterson. *An introduction to active galactic nuclei*. Cambridge University Press, 1997.

[126] D. Petry. *Beobachtung hochenergetischer γ-Strahlung (E>1 TeV) aus Richtung der aktiven Galaxien Mkn 421 und Mkn 501*. Ph.D. thesis, Technische Universität München, September 1997. MPI-PhE/97-27.

[127] D. Petry, S. M. Bradbury, A. Konopelko et al. *Detection of VHE γ-rays from MKN 421 with the HEGRA Cherenkov Telescopes*. Astronomy and Astrophysics, **311**: L13–L16, July 1996.

[128] E. Pian, G. Vacanti, G. Tagliaferri et al. *BeppoSAX Observations of Unprecedented Synchrotron Activity in the BL Lacertae Object Markarian 501*. Astrophysical Journal Letters, **492**: L17+, January 1998.

[129] B. Povh, K. Rith, C. Scholz et al. *Teilchen und Kerne*. Springer-Verlag Berlin Heidelberg, 1994.

[130] W. H. Press, S. A. Teukolsky, W. T. Vetterling et al. *Numerical Recipes in C*. Cambridge University Press, 2 edition, 1997.

[131] J. Protheroe, C. L. Bhat, P. Fleury et al. *Very High Energy Gamma Rays from Markarian 501*. In *25th International Cosmic Ray Conference (Durban)*, volume 8, pages 317+, 1998.

[132] M. Punch, C. W. Akerlof, M. F. Cawley et al. *Detection of TeV photons from the active galaxy Markarian 421*. Nature, **358**: 477+, August 1992.

[133] J. Quinn, C. W. Akerlof, S. Biller et al. *Detection of Gamma Rays with $E > 300$ GeV from Markarian 501*. Astrophysical Journal Letters, **456**: L83+, January 1996.

[134] J. Quinn, I. H. Bond, P. J. Boyle et al. *The Flux Variability of Markarian 501 in Very High Energy Gamma Rays*. Astrophysical Journal, **518**: 693–698, June 1999.

[135] P. V. Ramana Murthy and A. W. Wolfendale. *Gamma-ray astronomy*. Cambridge University Press, 2 edition, 1993.

[136] A. R. Rao. *Inner Disk Oscillations and QPOs in Relativistic Jet Sources*. In *to be published in 'Proceedings of the Third Microquasar Workshop: Granada Workshop on galactic relativistic jet sources', Eds A.J. Castro-Tirado, J. Greiner and J.M. Paredes, Astrophysics and Space Science, in press Preprint no. mQSO TIII-07.*, December 2000.

[137] M. V. S. Rao and S. Sinha. *The origin of the hump in the Cerenkov lateral distribution in gamma-ray showers and a possible means of separating them from proton showers*. Journal of Physics G, **14**: 811–827, June 1988.

[138] B. C. Raubenheimer and H. J. Smit. *The source of TeV gamma-rays in CEN X-3 and VELA X-1*. Astroparticle Physics, **7**: 63–71, June 1997.

[139] G. Rauterberg et al. *A New 127 Pixel Camera for Cherenkov Telescopes of the HEGRA Array on La Palma*. In *24th International Cosmic Ray Conference (Rome)*, volume 3, pages 460+, 1995.

[140] M. J. Reid, J. A. Biretta, W. Junor et al. *Subluminal motion and limb brightening in the nuclear jet of M87*. Astrophysical Journal, **336**: 112–120, January 1989.

[141] P. T. Reynolds, C. W. Akerlof, M. F. Cawley et al. *Survey of candidate gamma-ray sources at TeV energies using a high-resolution Cerenkov imaging system - 1988-1991*. Astrophysical Journal, **404**: 206–218, February 1993.

[142] F. M. Rieger and K. Mannheim. *Implications of a possible 23 day periodicity for binary black hole models in Mkn 501*. Astronomy and Astrophysics, **359**: 948–952, July 2000.

[143] F. M. Rieger and K. Mannheim. *A possible black hole binary in Mkn 501*. In H. J. Voelk and F. Aharonian (editors), *to appear in the Proc. of the Heidelberg International Symposium on High Energy Gamma-Ray Astronomy*. AIP Conf. Proc, 2000.

[144] W. Roedel. *Physik unserer Umwelt: Die Atmosphäre*. Springer-Verlag Berlin Heidelberg, 1992.

[145] B. Rossi. *High Energy Particles*. Prentic-Hall, Englewood Cliffs, NJ, 3 (1961) edition, 1952.

[146] R. M. Sambruna, F. A. Aharonian, H. Krawczynski et al. *Correlated Intense X-Ray and TeV Activity of Markarian 501 in 1998 June*. Astrophysical Journal, **538**: 127–133, July 2000.

[147] R. M. Sambruna, L. Maraschi and C. M. Urry. *On the Spectral Energy Distributions of Blazars*. Astrophysical Journal, **463**: 444+, June 1996.

[148] F. W. Samuelson, S. D. Biller, I. H. Bond et al. *The TeV Spectrum of Markarian 501*. Astrophysical Journal Letters, **501**: L17+, July 1998.

[149] X. Sarazin, M. C. Chantell, P. Fleury et al. *Observation of the Crab Nebula with an ultraviolet Cherenkov camera*. Astroparticle Physics, **4**: 227–234, February 1996.

[150] J. D. Scargle. *Studies in astronomical time series analysis. II - Statistical aspects of spectral analysis of unevenly spaced data*. Astrophysical Journal, **263**: 835–853, December 1982.

[151] N. Schmitz. *Neutrinophysik*. B. G. Teubner, 1997.

[152] D. A. Schwartz, R. E. Griffiths, H. Gursky et al. *Identification of 4U 1651+39 with the BL Lacertae object Markarian 501 with the modulation collimator on HEAO 1*. Astrophysical Journal Letters, **224**: L103–L105, September 1978.

[153] A. Schwarzenberg-Czerny. *The distribution of empirical periodograms: Lomb-Scargle and PDM spectra*. Monthly Notices of the Royal Astronomical Society, **301**: 831–840, December 1998.

[154] J. C. Shields, H. Rix, D. H. McIntosh et al. *Evidence for a Black Hole and Accretion Disk in the LINER NGC 4203*. Astrophysical Journal Letters, **534**: L27–L30, May 2000.

[155] M. Sikora, M. C. Begelman and M. J. Rees. *Comptonization of diffuse ambient radiation by a relativistic jet: The source of gamma rays from blazars?*. Astrophysical Journal, **421**: 153–162, January 1994.

[156] D. Sobczynska and E. Lorenz. *Influence of peak sensitive discriminator on the collection area and flux calculations for air Cherenkov telescopes in γ astronomy*. Astronomy and Astrophysics, 2001. In preparation.

[157] M. Spada. *Rapid variability of gamma-ray blazars: a model for MKN 421*. Astroparticle Physics, **11**: 59–61, June 1999.

[158] F. W. Stecker. In J. L. Osborne and A. W. Wolfendale (editors), *Origin of Cosmic Rays*, pages 267+. Reidel, Dordrecht, 1975.

[159] F. W. Stecker and O. C. de Jager. *New Upper Limits on Intergalactic Infrared Radiation from High-Energy Astrophysics*. Astrophysical Journal Letters, **415**: L71+, October 1993.

[160] F. W. Stecker, O. C. de Jager and M. H. Salamon. *TeV gamma rays from 3C 279 - A possible probe of origin and intergalactic infrared radiation fields*. Astrophysical Journal Letters, **390**: L49–L52, May 1992.

[161] F. W. Stecker, O. C. de Jager and M. H. Salamon. *Predicted Extragalactic TeV Gamma-Ray Sources*. Astrophysical Journal Letters, **473**: L75+, December 1996.

[162] T. Takahashi, M. Tashiro, G. Madejski et al. *ASCA Observation of an X-Ray/TeV Flare from the BL Lacertae Object Markarian 421*. Astrophysical Journal Letters, **470**: L89+, October 1996.

[163] Y. Tanaka, K. Nandra, A. C. Fabian et al. *Gravitationally Redshifted Emission Implying an Accretion Disk and Massive Black-Hole in the Active Galaxy MCG:-6-30-15*. Nature, **375**: 659+, June 1995.

[164] T. Tanimori, Y. Hayami, S. Kamei et al. *Discovery of TeV Gamma Rays from SN 1006: Further Evidence for the Supernova Remnant Origin of Cosmic Rays*. Astrophysical Journal Letters, **497**: L25+, April 1998.

[165] Y. Tsai. *Pair production and bremsstrahlung of charged leptons*. Reviews of Modern Physics, **46**: 815+, 1974.

[166] M. Ulrich, T. D. Kinman, C. R. Lynds et al. *Nonthermal continuum radiation in three elliptical galaxies*. Astrophysical Journal, **198**: 261–266, June 1975.

[167] C. M. Urry and P. Padovani. *Unified Schemes for Radio-Loud Active Galactic Nuclei*. The Publications of the Astronomical Society of the Pacific, **107**: 803+, September 1995.

[168] A. Vikhlinin, E. Churazov and M. Gilfanov. *Quasi-periodic oscillations in the shot noise model of X-ray sources*. Astronomy and Astrophysics, **287**: 73–79, July 1994.

[169] M. Villata and C. M. Raiteri. *Helical jets in blazars. I. The case of MKN 501*. Astronomy and Astrophysics, **347**: 30–36, July 1999.

[170] T. C. Weekes. *Very high energy gamma-ray astronomy*. Physics Reports, **160**: 1–121, March 1988.

[171] T. C. Weekes. *Status of VHE Astronomy c.2000*. In *in proceedings of the International Symposium on High Energy Gamma-Ray Astronomy, Heidelberg, June 2000.*, October 2000.

[172] T. C. Weekes, M. F. Cawley, D. J. Fegan et al. *Observation of TeV gamma rays from the Crab nebula using the atmospheric Cerenkov imaging technique*. Astrophysical Journal, **342**: 379–395, July 1989.

[173] B. Wiebel. *Chemical Composition in High Energy Cosmic Rays*. Technical report, Bergische Universität Gesamthochschule Wuppertal, January 1994.

[174] T. Yoshikoshi, T. Kifune, S. A. Dazeley et al. *Very High Energy Gamma Rays from the VELA Pulsar Direction*. Astrophysical Journal Letters, **487**: L65+, September 1997.

[175] S. N. Zhang and D. Ramsden. *Statistical data analysis for gamma-ray Astronomy*. Experimental Astronomy, **1**: 145–163, 1990.

ACKNOWLEDGEMENT

I would like to thank Prof. N. Schmitz and Dr. E. Lorenz for the opportunity to carry out this Ph.D thesis at the MPI in Munich.

This thesis would not have been possible without the assistance of:

♦ Eckart Lorenz, who gave me this very interesting subject and triggered me to start with the timing analysis. I'd also like to thank Eckart for his great support in physics and non-physics concerns during all the years in Munich.

♦ Okkie de Jager, for his support and various discussions on time series analysis and physics in general. And last but not least

♦ Mkn 501, which was kind enough to start flaring 450 million years ago in order to deliver the γ-rays in good time.

I am very grateful that I got the opportunity to present my results on several leading international conferences of the field.

Furthermore, I would like to thank the HEGRA collaboration for the provision of first level data and all the HEGRA people who helped also in the data taking. Special thanks go to Sasha Konopelko and Dorota Sobczynska for the MC simulations, Henric Krawczynski for providing the CT system flux values and energy spectrum, Carol Magalow for English corrections and Okkie de Jager, Martin Kestel, Eckart Lorenz and Wolfgang Wittek for proof-reading the thesis. Many thanks go to the people at the MPI Munich: Ina Holl, Katja Müller, Sven Denninghoff for keeping the Alphas up and running, Martin Kestel for his work on the CT1 analysis programs, Razmik Mirzoyan, Jose Carlos Gonzalez, Jürgen Gebauer, Juan Cortina and Martin Kestel for useful discussions on physics and analysis subjects and Harald Kornmayer for all the discussions on the really important topics — Formula 1 and soccer.

I would like to thank Okkie, Estie and Danel de Jager and the people from Potchefstroom University for their kind hospitality during my visit in September 1999.

Finally, I'm very grateful to my whole family for the great support during the last years: Angelo, Harald and Pat Kranich, Susi and Sepp Antretter, my mother in law Hilde Schneider, my mother Paula Kranich and last but not least my two children Veronika and Antonia and my wonderful wife Anja for her assistance and existence.